

# Aeromechanics and Aeroacoustics Analysis of Active Camber Morphing Rotor Systems using a Vortex Particle Method

Sumeet Kumar

Vollständiger Abdruck der von der TUM School of Engineering and Design der Technischen Universität München zur Erlangung eines  
Doktors der Ingenieurwissenschaften (Dr.-Ing.)  
genehmigten Dissertation.

Vorsitz: Prof. Dr. Ilkay Yavrucuk

Prüfende der Dissertation:

1. Prof. Dr.-Ing. Manfred Hajek
2. Prof. Dr. Juergen Rauleder

Die Dissertation wurde am 09.10.2024 bei der Technischen Universität München eingereicht  
und durch die TUM School of Engineering and Design am 17.12.2024 angenommen.



# Kurzfassung

Verschiedene aktive Rotorkonzepte waren in der jüngeren Vergangenheit Gegenstand intensiver Untersuchungen. Experimentelle und theoretische Studien haben gezeigt, dass eine aktive Steuerung einen erheblichen Einfluss auf das aeromechanische Verhalten und die Effizienz des Rotors haben kann. Im Rahmen der weiteren Erforschung des Potenzials der aktiven Rotortechnologie wurde in der vorliegenden Arbeit eine simulationsbasierte Untersuchung verschiedener Rotorsysteme mit einem neuartigen aktiven Mechanismus zur Anpassung der Profilwölbung, dem sogenannten Fish-Bone-Active-Camber-Konzept (FishBAC), durchgeführt. Ziel war es, die Vorteile des FishBAC-Konzepts im Hinblick auf die Rotorleistung, die Vibrationslasten am Rotorkopf und die aeroakustischen Lärmemissionen zu untersuchen. Aus Gründen der Recheneffizienz beschränkte sich der Schwerpunkt dieser Arbeit auf mid-fidelity Modellierungsmethoden.

Um den gewünschten Grad an Modellgenauigkeit zu erreichen, wurde ein angepasstes Simulationsframework für die Simulation der aktiven Rotorstrukturmechanik, der Aerodynamik und des aeroakustischen Lärms entwickelt. Der Open-Source-Rotorcode Dymore wurde für die Strukturmechanik des Rotorsystems und die Blattaerodynamik genutzt. Um den Einfluss des Rotornachlaufs in allen Flugzuständen genau erfassen zu können, einschließlich der Interaktion zwischen Rotorblatt und Blattwirbel, wurde die aerodynamische Analysefähigkeit des Simulationsframeworks erweitert. Ein neuartiger Wake-Vorticity-Löser, basierend auf einer Vortex-Particle-Methode (VPM), wurde implementiert und mit dem Strukturmechanik-Löser gekoppelt. Die Implementierung des Wake-Lösers wurde durch bestehende analytische Testfälle aus der Literatur verifiziert. Darüber hinaus wurden Testfälle mit zunehmend komplexem stationären und instationären Flügelnachlauf verwendet, um das gekoppelte Dymore+VPM-Simulationsframework zu validieren. Das gesamte Analyse setup wurde schließlich für die Durchführung von aeroakustischen Simulationen unter Verwendung des Akustik-Lösers PSU-WOPWOP erweitert.

Um die Anwendbarkeit des aeromechanisch-aeroakustischen Frameworks über die gesamte Flugvelope eines Hubschrauberrotors zu demonstrieren, wurden verschiedene Flugfälle unter Verwendung unterschiedlicher Rotormodelle untersucht - HART II, Bo 105 Rotor und UT Austin Einzel-/Koaxialrotor. Mit dem HART II Rotor wurde das aeroakustische Analyseframework sowie die Fähigkeit von VPM zur Modellierung von BVI-Flugzuständen validiert. Der Passiv Bo-105-Rotor wurde umfassend anhand von Messdaten aus Windkanaltests validiert. Dies war erforderlich, um die Zuverlässigkeit der Simulationemethode nachzuweisen, da für den aktiven Bo-105-Rotor keine experimentellen Messdaten verfügbar waren. Es wurden getrimmte aktive Rotor-simulationen bei unterschiedlichen harmonischen Amplituden der Wölbungsanpassung unter variation des Phasenwinkels durchgeführt. Durch die Verwendung einer aktiven 1/rev oder 1P-Wölbungsanpassung konnte der Leistungsbedarf des Rotors um 9,6% und die Rotorkopfvibrationen um 32% reduziert werden. Der Einfluss auf die Lärmemissionen des Rotors war stark rich-

tungsabhängig, wobei eine maximale Lärmreduzierung von etwa 2 dB unterhalb der Rotorebene erreicht wurde. Abschließend wurde die Untersuchung des aktiven Rotors auf koaxiale Rotorsysteme ausgeweitet, die aufgrund des Blattdurchgangseffekts starke Vibrationslasten aufweisen. Auch hier konnte gezeigt werden, dass das Konzept der aktiven Wölbungsanpassung die Rotorschwingungen erheblich reduzieren und gleichzeitig die aeroakustischen Lärmemissionen des Rotorsystems verringern kann.

# Abstract

Different active rotor concepts have been the subject of immense scrutiny in the recent past. Experimental and theoretical investigations have revealed that active control can have a significant impact on rotor aeromechanical response and efficiency. Continuing to further look into the promise of active rotor technology, in the current work, a computational investigation of different rotor systems with a novel active camber morphing mechanism, called the fish bone active camber (FishBAC) concept, was conducted. The objective was to investigate the benefit of the FishBAC concept towards rotor performance, hub vibration loads, and aeroacoustic noise emissions. For computational efficiency, the focus of this work was limited to mid-fidelity modeling methods.

In order to achieve the desired degree of modeling fidelity, an appropriate simulation framework was established for simulating the active rotor structural dynamics, aerodynamics, and aeroacoustic noise. The open-source, comprehensive aeromechanics code Dymore was used for the rotor system structural dynamics and blade aerodynamic solutions. In order to accurately capture the effects of rotor wake in all flight conditions, including blade-vortex interaction, the aerodynamic analysis capability of the simulation framework was augmented. A novel wake vorticity solver, based on a vortex particle method (VPM) formulation, was implemented and coupled to the structural dynamics solver. Implementation of the standalone wake solver was verified using established analytical verification cases from the literature. Furthermore, test cases with incrementally complex steady and unsteady wing wakes were used to validate the coupled Dymore+VPM simulation framework. The entire analysis toolchain was ultimately extended to undertake aeroacoustic noise simulations using the solver PSU-WOPWOP.

In order to demonstrate the validity of the aeromechanics-aeroacoustics framework over the entire operating envelope of a helicopter rotor, various flight cases were investigated using different rotor models - HART II, Bo 105 rotor, and UT Austin single/coaxial rotors. Using the HART II rotor, the aeroacoustic analysis framework, as well as the capability of VPM to model BVI flight conditions, was validated. The baseline full-scale Bo 105 rotor was extensively validated using measurement data from tests in the wind tunnel. This was required in order to render confidence in the results of the active Bo 105 rotor investigation in lieu of experimental measurement data. Trimmed active rotor simulations were conducted at different amplitudes of camber morphing input over a sweep of input phase angles. Using just 1/rev (1P) active camber actuation, rotor power consumption was reduced by 9.6%, and rotor hub vibrations were reduced by 32%. The effect on rotor noise was highly directional, with a maximum noise reduction of about 2 dB achieved below the rotor disk. Finally, the active rotor investigation was extended to coaxial rotor systems that suffer from vibration loads due to the blade passage effect. Here, too, it was shown that the active camber morphing concept can reduce rotor shaft vibrations considerably as well as simultaneously reduce the aeroacoustic footprint of the rotor system.



# Acknowledgments

The work within this dissertation was entirely carried out by me. It would, however, be very remiss of me not to acknowledge the people who, to no small degree, influenced the trajectory and quality of this work through their frequent feedback and supported me in different ways throughout my doctoral journey. I would like to take this opportunity to thank Prof. Juergen Rauleder who hired me at the Institute and was always approachable for problems of any nature. He continued to stay in touch and held discussions with me despite having made the move to Georgia Tech halfway through the duration of my PhD. I am thankful to my doctoral supervisor, Prof. Manfred Hajek for the incredible freedom he provided me to not just pursue research areas of my own choosing but also entrusted me with the incredible responsibility of designing and delivering course lectures. This experience was as rewarding as it was challenging, and would not have come to fruition if not for his support. I would also like to thank Prof. Jayant Sirohi who spent some time at the Institute and freely interacted with us during that time. His easygoing manner made him very approachable. The insights he shared on understanding complex ideas through simple, intuitive approaches were enlightening and something I've tried to inculcate in my own work. Prof. Ilkay Yavrucuk, who took over the professorship of the Institute ensured that the transition was a smooth one and became just as much of a supervisory figure as Prof. Hajek, and for that, I'm thankful.

The bond I developed with my colleagues Amine and Dominik has been special because we spent most of the past few years in the company of one another. We've traveled to project meetings together and spent endless hours discussing rotors, project goals, and vegetarian food. I am grateful for their company and sharing the office with them. I'd like to thank Bastian for dropping by time and again with constructive criticisms of my coding style and constantly urging me to port the particle code to the GPU. I have to admit that I was very reluctant to take on the extra work at the time, but if not for those suggestions, I might have still been waiting on my simulations to end. I'd also like to thank Stefan and Markus who selflessly offered their valuable time to ensure that some of their know-how percolated to the next generation of graduates at the institute. I'm thankful to Willem, whose perseverance and patience while working with comprehensive rotor analysis motivated me to imbibe some of the same qualities in my work ethic. A special thanks to Ms. Martina Thieme, not least for always being on top of my work contracts and related (tiresome) paperwork. As someone whose work visa expired as frequently as it did, Ms. Thieme was always patient and took extra care to push matters through the university HR department in record times. Her jolly presence in the Institute and frequent drop-bys to the office always served as a source of contagious cheer, particularly in times of approaching deadlines.

I'd also like to thank Puneet Singh, whose own work on the vortex particle method inspired me to take it up for my PhD, for taking the time to discuss some of the nuances of modeling rotor

wake. I've known Puneet since my undergraduate days in India and he has been a constant source of inspiration over the years. I'd like to thank my parents, who've been incredibly patient and supportive all through my PhD. Seven years, after all, is an incredibly long time! Which is why I couldn't be more glad that my journey was not a solitary one. My wife Aditi was always by my side during this time. The emotional support and mental balance I found in her company have been crucial for me all through these years. *I just couldn't have done it without you.*

Last but not the least, a special thanks to Dr Gene Hammond, Messrs Oliver Dieterich and Rainer Heger for kindly granting me permission to reproduce pictures from their works.



# Contents

<b>Abbreviations and Symbols</b>	<b>V</b>
<b>List of Figures</b>	<b>XV</b>
<b>List of Tables</b>	<b>XXI</b>
<b>1. Introduction</b>	<b>1</b>
1.1. Motivation . . . . .	1
1.2. Active Rotor Concepts . . . . .	2
1.2.1. Higher harmonic control (HHC) . . . . .	4
1.2.2. Individual blade control (IBC) . . . . .	5
1.2.3. Trailing-edge flap (TEF) . . . . .	8
1.2.4. Miscellaneous concepts . . . . .	12
1.2.4.1. Active twist . . . . .	12
1.2.4.2. Leading-edge slats . . . . .	12
1.2.4.3. Gurney flaps . . . . .	13
1.2.5. Active camber morphing . . . . .	13
1.3. Rotor Wake Modeling . . . . .	15
1.3.1. Momentum theory . . . . .	16
1.3.2. Dynamic inflow model . . . . .	16
1.3.3. Free wake model . . . . .	17
1.3.4. Vortex particle method . . . . .	18
1.4. Rotor Aeroacoustics . . . . .	19
1.5. Objectives of Present Work . . . . .	22
1.6. Key Contributions of Present Work . . . . .	24
1.7. Organization of the Dissertation . . . . .	25
<b>2. Rotor Comprehensive Analysis</b>	<b>27</b>
2.1. Blade Structural Dynamics . . . . .	28
2.2. Blade Aerodynamics . . . . .	30
2.2.1. Theodorsen theory . . . . .	33
2.2.2. Peters 2D unsteady model . . . . .	34
2.3. Wake-induced Inflow . . . . .	36
2.3.1. Peters-He inflow model . . . . .	37
2.4. Trim . . . . .	39
2.5. Model Description . . . . .	40
2.5.1. Two-dimensional wings and finite span wings . . . . .	40
2.5.2. Full-scale Bo 105 rotor . . . . .	42

2.5.3. HART II rotor . . . . .	46
2.5.4. UT Austin rotors . . . . .	49
2.5.5. Active FishBAC rotors . . . . .	51
<b>3. Vortex Particle Method . . . . .</b>	<b>53</b>
3.1. Formulation . . . . .	54
3.1.1. Vortex particle evolution . . . . .	55
3.1.2. Regularization functions . . . . .	56
3.2. Conservation Laws . . . . .	57
3.3. Verification . . . . .	59
3.4. Coupling with Comprehensive Analysis Solver . . . . .	64
3.4.1. Bound vorticity-based induced velocity . . . . .	67
3.4.2. Vortex stretching divergence problem . . . . .	69
3.5. Code Acceleration . . . . .	69
<b>4. Aeroacoustic Noise . . . . .</b>	<b>71</b>
4.1. Theoretical Principles . . . . .	71
4.2. Aeroacoustics Solver . . . . .	73
4.3. Post-processing Framework . . . . .	75
4.3.1. Validation cases . . . . .	77
<b>5. Results and Discussion . . . . .</b>	<b>79</b>
5.1. Airfoil Unsteady Aerodynamics . . . . .	80
5.1.1. Description . . . . .	80
5.1.2. Validation results . . . . .	81
5.2. Static Elliptical Wing Aerodynamics . . . . .	84
5.2.1. Description . . . . .	84
5.2.2. Validation results . . . . .	85
5.3. Finite Wing Unsteady Aerodynamics . . . . .	87
5.3.1. Description . . . . .	87
5.3.2. Validation results . . . . .	87
5.4. Full-scale Bo 105 . . . . .	90
5.4.1. Description . . . . .	90
5.4.2. Blade natural frequencies and mode shapes . . . . .	90
5.4.3. Rotor aeromechanical results . . . . .	91
5.4.4. Aeroacoustic noise . . . . .	100
5.5. HART II . . . . .	101
5.5.1. Blade natural frequencies and mode shapes . . . . .	102
5.5.2. Rotor aeromechanical results . . . . .	104
5.5.3. Aeroacoustic noise . . . . .	107
5.6. Active Bo 105 Rotor . . . . .	109
5.6.1. Impact on performance and loads . . . . .	110
5.6.2. Impact on aeroacoustic noise . . . . .	115
5.7. UT Austin Rotors . . . . .	118
5.7.1. Fountain effect at blade root . . . . .	118
5.7.2. Two-bladed/four-bladed isolated rotors . . . . .	119
5.7.3. Coaxial rotor . . . . .	123

5.8. Active UT Austin Coaxial Rotor . . . . .	124
5.8.1. Impact on blade passage loads . . . . .	126
5.8.2. Impact on aeroacoustic noise . . . . .	127
<b>6. Summary and Conclusions</b>	<b>131</b>
6.1. Summary . . . . .	131
6.2. Key Conclusions . . . . .	135
<b>7. Outlook</b>	<b>139</b>
<b>A. Bo 105 Rotor</b>	<b>143</b>
<b>B. HART II Rotor</b>	<b>147</b>
<b>C. UT Austin Rotors</b>	<b>149</b>
<b>D. VPM</b>	<b>151</b>
<b>Bibliography</b>	<b>155</b>



# Abbreviations and Symbols

## Acronyms

ACSR	Active Control of Structural Response
ADASYS	Adaptives Dynamisches System (German acronym)
ARES	Aeroelastic Rotor Experimental System
ATR	Advanced Technology Rotor
AVCS	Active Vibration Control System
BPF	Blade Passage Frequency
BVI	Blade-vortex Interaction
ccr	coaxial contra-rotating
CA	Comprehensive Analysis
CAMRAD	Comprehensive Analytical Model of Rotorcraft Aerodynamics and Dynamics
CFD	Computational Fluid Dynamics
CTR	Controllable Twist Rotor
CSD	Computational Structural Dynamics
DARPA	Defense Advanced Research Projects Agency
eVTOL	Electric Vertical Take-off and Landing
ERA	Eigensystem Realization Algorithm
IBC	Individual Blade Control
ISA	International Standard Atmosphere
FEM	Finite Element Method
FVL	Future Vertical Lift
FW-H	Ffowcs Williams-Hawkings
GEBT	Geometrically Exact Beam Theory
GPU	Graphics Processing Unit
HART	Higher Harmonic Control Aeroacoustic Rotor Test
HHC	Higher Harmonic Control
HOA	Higher Order Algebraic
HOST	Helicopter Overall Simulation Tool
I/O	Input/Output
FishBAC	Fish Bone Active Camber
LED	Leading-edge Deflection
MFW	Maryland Free Wake
NACA	National Advisory Committee for Aeronautics

NASA	National Aeronautics and Space Administration
NFAC	National Full-scale Aerodynamics Complex
NS	Navier-Stokes
NURBS	Non-uniform Rational B-splines
OASPL	Overall Sound Pressure Level
OBC	On-blade Control
OKID	Observer/Kalman Filter Identification
ONERA	Office National d'Études et de Recherches Aérospatiales
PDE	Partial Differential Equation
RCAS	Rotorcraft Comprehensive Analysis System
RHS	Right Hand Side
SMART	Smart Material Actuated Rotor Technology
TCP	Transmission Control Protocol
TED	Trailing-edge Deflection
TEF	Trailing-edge Flap
UPM	Unsteady Panel Method
URANS	Unsteady Reynolds-averaged Navier-Stokes
VABS	Variational Asymptotic Beam Sectional Analysis
YAML	Yet Another Markup Language
1D	One-dimensional
2D	Two-dimensional
3D	Three-dimensional

## List of symbols

### Non-Roman

Symbol	Description	Unit	Formula/Value
$\alpha_p$	Particle strength vector	$\text{m}^3 \text{s}^{-1}$	
$\alpha$	Angle of attack	rad	
$\alpha_{L/D}$	Angle of attack at best airfoil aerodynamic efficiency	rad	
$\alpha_{L=0}$	Angle of attack at zero airfoil lift	rad	
$\alpha_0$	Zero-lift angle of attack	deg.	
$\alpha_j^q$	Expansion coefficients for induced inflow on actuator disk	-	Eq. 2.23
$\beta$	Trailing-edge flap deflection angle (downward positive)	rad	
$\beta_p$	Precone angle	rad	
$\beta_j^q$	Expansion coefficients for induced inflow on actuator disk	-	Eq. 2.23
$\gamma$	Rotor shaft angle of attack (positive aft)	rad	
$\Gamma$	Circulation bound to the airfoil/blade section; Vortex ring circulation	$\text{m}^2 \text{s}^{-1}$	
$\Gamma_w$	Circulation in the airfoil/wing wake	$\text{m}^2 \text{s}^{-1}$	
$\delta$	Dirac delta function		
$\delta$	FishBAC deflection (downward positive)	rad	
$\delta_{ij}$	Kronecker delta	-	
$\Delta$	Change in quantity	-	
$\Delta z$	Inter-rotor spacing	m	
$\epsilon_i$	Beam section strain components	-	
$\zeta$	Cutoff function	-	Table 3.1
$\zeta_\sigma$	Vorticity regularization function	$\text{m}^{-3}$	Table 3.1
$\eta_\sigma$	Regularization function for vortex diffusion	$\text{m}^{-3}$	Table 3.1
$\theta$	Pitch angle; Polar angle of spherical coordinate system	rad	
$\theta_0$	Collective pitch angle	rad	
$\theta_{1c}$	Longitudinal cyclic pitch angle	rad	
$\theta_{1s}$	Lateral cyclic pitch angle	rad	
$\theta_s$	Pitch angle oscillation amplitude	rad	
$\kappa_i$	Beam bending curvature components ( $i = \{1, 2, 3\}$ )	$\text{m}^{-1}$	

Symbol	Description	Unit	Formula/Value
$\lambda$	Induced inflow velocity due to 2D unsteady wing section wake	$\text{m s}^{-1}$	
$\lambda_n$	Coefficients of $\lambda$ -expansion ( $n = [0, \infty)$ )	$\text{m s}^{-1}$	Eq. 2.11
$\mu$	Rotor advance ratio	-	$= V_\infty / \Omega R$
$\mu$	Dynamic viscosity	Pa s	
$\nu$	Kinematic viscosity	$\text{J kg}^{-1} \text{s}$	$= \mu / \rho$
$\nu, \eta, \psi$	Non-dimensional confocal ellipsoidal coordinates	-	
$\rho$	Fluid density	$\text{kg m}^{-3}$	$= 1.225 \text{ kg m}^{-3}$
$\rho$	Particle displacement normalized by smoothing radius	-	$=  \mathbf{x} - \mathbf{x}_p  / \sigma$
$\sigma$	Rotor solidity	-	$= N_b c / (\pi R)$
$\sigma$	Particle smoothing radius	m	
$\tau_n^{mc}, \tau_n^{ms}$	Coefficients of pressure function $\Phi$	-	Eq. 2.22
$\phi$	Inflow angle; Phase angle, phase difference; Glauert angle; Rotation angle in spherical coordinate system	rad	
$\phi_j^q$	Radial expansion shape function	-	Eq. 2.23
$\Phi$	Non-dimensionalized pressure function	-	$= p / \rho V_{\text{tip}}^2$
$\psi$	Rotor blade azimuth angle	rad	
$\psi_\sigma$	Regularized stream function	$\text{m}^2 \text{s}^{-1}$	
$\omega$	Frequency of oscillation, natural or forced	$\text{s}^{-1}$	
$\omega_1$	Pitching angular velocity of the wing section about the mid-chord	$\text{rad s}^{-1}$	
$\omega_i$	Angular velocity vector components ( $i = \{1, 2, 3\}$ )	$\text{rad s}^{-1}$	
$\omega_x, \omega_y, \omega_z$	Vorticity vector components	$\text{s}^{-1}$	
$\boldsymbol{\omega}$	Vorticity vector	$\text{s}^{-1}$	$= \nabla \times \mathbf{v}$
$\boldsymbol{\omega}_\sigma$	Regularized vorticity vector	$\text{s}^{-1}$	
$\Omega$	Rotor rotational angular velocity	$\text{rad s}^{-1}$	
$\mathbf{\Omega}$	Total particles-based vorticity strength vector	$\text{m}^3 \text{s}^{-1}$	Eq. 3.21
$\Omega_{ref}$	Reference rotor rotational angular velocity	$\text{rad} \cdot \text{s}^{-1}$	
$\nabla$	Gradient operator	$\text{m}^{-1}$	
$\nabla$	Divergence operator	$\text{m}^{-1}$	
$\nabla^2$	Laplacian operator	$\text{m}^{-2}$	



## Roman

Symbol	Description	Unit	Formula/Value
$\mathbf{a}$	Acceleration vector	$\text{m s}^{-2}$	Eq. 2.15
$a$	Airfoil pitch axis location from mid-chord location (in semi-chords; positive aft)	-	
$a_s$	Speed of sound	$\text{m s}^{-1}$	$= 340 \text{ m s}^{-1}$
$\mathbf{A}$	Angular impulse of particle simulation field	$\text{m}^5 \text{ s}^{-1}$	Eq. 3.22
$A$	Rotor disk area	$\text{m}^2$	$= \pi R^2$
$AR$	Aspect ratio	-	$= c/s$
$b$	Airfoil semi-shord	$\text{m}$	$= c/2$
$c$	Rotor blade chord length	$\text{m}$	
$c$	Airfoil flap hinge location from mid-chord (in semi-chords; positive aft)	-	
$C$	Theodorsen's lift deficiency function	-	Eq. 2.7
$C_l$	Section aerodynamic lift coefficient	-	
$C_d$	Section aerodynamic drag coefficient	-	
$C_m$	Section aerodynamic moment coefficient	-	
$C_P$	Rotor power coefficient	-	$= P/\rho A(\Omega R)^3$
$C_T$	Rotor thrust coefficient	-	$= T/\rho A(\Omega R)^2$
$C_Q$	Rotor torque coefficient	-	$= Q/\rho A(\Omega R)^2 R$
$\mathcal{C}$	6x6 Beam section stiffness matrix	-	Eq. 2.2
$d$	Parametric variable	-	
$D'$	Aerodynamic drag on blade section	$\text{N}$	
$dF$	Section force per unit span	$\text{N m}^{-1}$	
$\mathbf{e}$	Strain vector	-	
erf	Gaussian error function	-	
$E_\sigma$	Semi-regularized kinetic energy of all particles in domain	$\text{m}^5 \text{ s}^{-2}$	Eq. 3.24
$E_{\sigma f}$	Divergence-free kinetic energy of all particles in domain	$\text{m}^5 \text{ s}^{-2}$	Eq. 3.25
$\mathcal{E}_\sigma$	Semi-regularized enstrophy of all particles in domain	$\text{m}^3 \text{ s}^{-2}$	Eq. 3.26
$\mathcal{E}_{\sigma f}$	Divergence-free enstrophy of all particles in domain	$\text{m}^3 \text{ s}^{-2}$	Eq. 3.27
$f$	Surface of integration for acoustic disturbances	-	
$f$	Prandtl wing tip loss factor	-	Eq. 2.6
$f_{\text{rev}}$	Reverse flow parameter in Peters 2D inflow theory	-	

Symbol	Description	Unit	Formula/Value
$F_i$	Beam section force components ( $i = \{1, 2, 3\}$ )	N	Eq. 2.3
$F$	Net aerodynamic force on blade section	N	
$F_\sigma$	Regularization function for vortex stretching	$\text{m}^{-5}$	Eq. 3.19
$F_{N_b x}$	$N_b$ P lateral rotor shear force	N	
$F_{N_b x 0}$	$N_b$ P lateral rotor shear force on baseline rotor	N	
$F_{N_b y}$	$N_b$ P longitudinal rotor shear force	N	
$F_{N_b y 0}$	$N_b$ P longitudinal rotor shear force on baseline rotor	N	
$F_{N_b z}$	$N_b$ P vertical rotor thrust	N	
$F_{N_b z 0}$	$N_b$ P vertical rotor thrust on baseline rotor	N	
$F_{PLi}$	Pitch link load at $i$ th blade	N	
$F_y$	Wing section aerodynamic drag force per unit span	$\text{N m}^{-1}$	
$F_{yi}$	Wing section aerodynamic induced drag force per unit span	$\text{N m}^{-1}$	
$F_Y$	Blade section aerodynamic drag force (rotor in-plane) per unit span	$\text{N m}^{-1}$	
$F_z$	Wing section aerodynamic normal force per unit span	$\text{N m}^{-1}$	
$F_Z$	Blade section aerodynamic normal force per unit span	$\text{N m}^{-1}$	
$g$	Acceleration due to gravity	$\text{m s}^{-2}$	$= 9.8 \text{ m s}^{-2}$
$h$	Generalized coordinate of wing section denoting plunge motion; generic variable for distance	m	
$h_i$	Angular momentum vector components ( $i = \{1, 2, 3\}$ )	$\text{kg rad s}^{-1}$	Eq. 2.3
$h_n$	Components of the airfoil generalized plunge motion ( $n = [0, \infty)$ )	m	
$h_{\text{res}}$	Particle-particle distance	m	Eq. 2.9
$H$	Heaviside function	-	
$H$	Mean rotor drag force	N	
$\mathcal{H}_\sigma$	Semi-regularized helicity of all particles in domain	$\text{m}^4 \text{ s}^{-2}$	Eq. 3.23
$\mathbf{I}$	Linear impulse of all particles in domain	$\text{m}^4 \text{ s}^{-1}$	Eq. 3.20
$J$	Jacobian of transformation of the panel surface	-	Eq. 4.4
$J_1$	Hub vibration index involving all components of forces and moments	-	Eq. 5.7

Symbol	Description	Unit	Formula/Value
$J_2$	Hub vibration index involving only thrust force and yaw moment	-	Eq. 5.8
$k$	Reduced frequency	-	$= \omega b / c$
$\mathbf{K}_\sigma$	Regularized Biot-Savart kernel	$\text{m}^{-2}$	Eq. 3.18
$\mathcal{K}$	Beam kinetic energy	J	Eq. 2.2
$l$	Aerodynamic force per unit area acting on the fluid	$\text{N m}^{-2}$	
$h_{\text{loss}}$	Finite wing tip loss function	-	Eq. 2.5
$L$	Aerodynamic lift on the wing; Rotor lift force in inertial reference frame	N	
$L^c, L^s$	Matrices of quasi-steady operators in dynamic inflow formulation	-	Eq. 2.24
$L/D$	Airfoil lift-to-drag ratio	-	$= C_l / C_d$
$L/D_e$	Rotor equivalent lift-to-drag ratio	-	$= L / (P / V_\infty + X)$
$m$	Harmonic number in solution of Laplace equation over actuator disk	-	Eq. 2.22
$M$	Aerodynamic pitching moment on the wing	N m	
$M$	Mach number	-	$=  \mathbf{v}  / a_s$
$\mathbf{M}$	Apparent mass matrix in dynamic inflow formulation	-	Eq. 2.24
$\mathcal{M}$	6x6 Beam section mass matrix		Eq. 2.2
$M_\beta$	Blade flap bending moment	N m	
$M_\zeta$	Blade chord bending moment	N m	
$M_\theta$	Blade twisting moment	N m	
$M_i$	Beam section bending moment components	N m	
$M_{N_b x}$	$N_b P$ rotor roll moment	N m	
$M_{N_b x0}$	$N_b P$ rotor roll moment on baseline rotor	N m	
$M_{N_b y}$	$N_b P$ rotor pitch moment	N m	
$M_{N_b y0}$	$N_b P$ rotor pitch moment on baseline rotor	N m	
$M_{N_b z}$	$N_b P$ rotor yaw moment	N m	
$M_{N_b z0}$	$N_b P$ rotor yaw moment on baseline rotor	N m	
$M_x$	Mean rotor pitch moment	N m	
$M_y$	Mean rotor roll moment	N m	
$M^2 C_m$	Blade section pitch moment coefficient	-	
$M^2 C_n$	Blade section normal force coefficient	-	
$n$	Parametric variable $\in [1, \infty)$	-	
$n_\phi$	Number of cross-section layers in discretized vortex ring along the azimuth	-	

Symbol	Description	Unit	Formula/Value
$n_c$	Number of layers in discretized vortex ring	-	
$n_{\text{res}}$	Wing spanwise discretization of wake using particles	-	
$N$	Number of points; Number of revolutions	-	
$N_b$	Number of rotor blades	-	
$N_p$	Number of particles in simulation domain	-	
$p$	Set of all particles in simulation domain	-	
$p$	Static pressure	Pa	
$p_i$	Linear momentum components	$\text{kg m s}^{-1}$	
$p'$	Total acoustic pressure perturbation	Pa	
$P$	Mean rotor power consumption	W	
$P_n^m$	Normalized Legendre functions	-	Eq. 2.22
PF	Mean rotor propulsive force	N	
$q$	Harmonic number in solution of induced in-flow over actuator disk	-	Eq. 2.23
$q_\sigma$	Regularization function for Biot-Savart kernel	-	Table 3.1
$Q$	Rotor torque	N m	
$Q_n^m$	Associated Legendre functions of second kind	-	Eq. 2.22
$\mathbf{r}$	Position vector	m	
$r$	Radial coordinate of the blade section, non-dimensionalized using rotor radius	-	$= y/R$
$r$	Radial distance in spherical coordinate system	m	
$r_a$	Blade root cut out	-	$= y_a/R$
$r_c$	Core radius of the vortex ring	m	
$r_l$	Layer half-width of the vortex ring	m	
$R$	Rotor radius; Vortex ring radius	m	
$Re$	Reynolds number	-	$= V_\infty c \rho / \mu$
$s$	Wing span	m	
$S$	Area	$\text{m}^2$	
$t$	Time; Observer time	s	
$t_i$	Initial time of simulation	s	
$t_f$	Final time of simulation	s	
$t_n$	$n$ th simulation time step	s	
$\bar{t}$	Non-dimensionalized time	-	$= \Omega t$
$T$	Time period	s	
$T$	Rotor thrust	N	
$T_{ij}$	Lighthill stress tensor	Pa	

Symbol	Description	Unit	Formula/Value
$\mathbf{u}$	Vector denoting beam section velocity and angular velocity components	-	
$u_0$	Velocity component along x-axis in Peters' 2D inflow theory	$\text{m s}^{-1}$	
$\mathbf{U}$	Quasi-steady free stream velocity vector	$\text{m s}^{-1}$	
$U$	Quasi-steady free stream velocity	$\text{m s}^{-1}$	
$U_2$	Velocity component along airfoil chord	$\text{m s}^{-1}$	
$U_3$	Velocity component perpendicular to airfoil chord	$\text{m s}^{-1}$	
$\mathbf{v}$	Velocity vector	$\text{m s}^{-1}$	
$\mathbf{v}_\sigma$	Induced velocity vector due to regularized vorticity field	$\text{m s}^{-1}$	Eq. 3.10
$\mathbf{v}'$	Perturbation velocity vector	$\text{m s}^{-1}$	
$\mathcal{V}$	Beam strain energy	J	Eq. 2.2
$\mathcal{V}$	Fluid volume domain with vorticity	$\text{m}^3$	
$v_0$	Velocity component along y-axis in Peters' 2D inflow theory	$\text{m s}^{-1}$	
$v_1$	Velocity gradient component over the airfoil in Peters' 2D inflow theory	$\text{m s}^{-1}$	
$v_i$	Velocity vector components ( $(i = \{1, 2, 3\})$ )	$\text{m s}^{-1}$	
$V_z$	z-component of induced velocity	$\text{m s}^{-1}$	
$V_c$	Self-induced convection velocity of the vortex ring	$\text{m s}^{-1}$	
$V_{\text{ind}}$	Wake-induced inflow velocity	$\text{m s}^{-1}$	
$V_{\text{tip}}$	Rotor tip speed	$\text{m s}^{-1}$	$= \Omega R$
$V_\infty$	Steady oncoming flow free stream velocity	$\text{m s}^{-1}$	
$w$	Non-dimensionalized induced inflow velocity normal to rotor disk	-	Eq. 2.23
$\mathcal{W}$	Work done (on beam) due to externally applied forces	J	Eq. 2.1
$\mathbf{x}$	Position vector of location in space	m	
$x$	Chordwise coordinate over wing section	m	
$\mathbf{x}_p$	Position vector of a particle	m	
$X$	Rotor drag force in the inertial reference frame	N	
$x, y, z$	Distance in Cartesian coordinate system	m	
$X, Y, Z$	Cartesian coordinate system axes	-	
$Y$	Mean rotor side force	N	
$y$	Radial coordinate of the blade section	m	

## Subscripts

Symbol	Description
$\sigma$	Regularized vortex particle attribute; semi-regularized diagnostic
0	Mean or quiescent property
$B$	Blade-fixed reference frame
F1A	Result based on the Farassat's formulation 1A
hpp	Half-peak-to-peak
$F$	Fuselage reference frame
$HF$	Hub-fixed reference frame
$HR$	Hub-rotating reference frame
$i$	Coordinate directions x,y and z; Airstation number
$I$	Inertial reference frame
$k$	Parametric variable for particle number
l	Lower rotor
L	Loading noise component
max	Maximum value during the entire simulation
mid	attribute at the mid-section of the wing
$M$	Dot product with velocity vector normalized with speed of sound
$n$	Dot product with unit normal vector; $n$ th simulation step
$r$	Dot product with unit radiation vector
$r1$	Upper rotor
$r2$	Lower rotor
ref	Reference
ret	Retarded time
$S$	Shaft reference frame
sim	Simulation
tip	Blade tip
tot	Total
$W$	Wing-attached or swashplate reference frame
x,y,z	Components along the direction of coordinate axes

## Superscripts

Symbol	Description
–	Average
'	Fluctuating part; Quantity per unit length
( $\dot{\phantom{a}}$ )	$\partial()/\partial t$

# List of Figures

1.1. The META rotor system from DLR for individual blade control via passive pitch links[1](CC BY-NC-ND 3.0 DEED). . . . .	2
1.2. Higher harmonic control (HHC) tests of the S-76 and XV-15 rotors in the NASA Ames 80- by 120-foot wind tunnel, and free flight test campaign onboard the OH-6A helicopter. . . . .	5
1.3. Individual blade control (IBC) rotor test campaign using the Bo 105 S1 demonstrator [226]. . . . .	7
1.4. Individual blade control (IBC) rotor test setups at the NASA Ames 40- by 80-foot wind tunnel. . . . .	7
1.5. The Boeing SMART rotor with trailing-edge flaps in the NASA Ames 40- by 80-foot wind tunnel [144]. . . . .	10
1.6. Trailing-edge flap-based active rotor free flight test campaigns at Airbus Helicopters using two different test bed helicopters. . . . .	11
1.7. Details of the FishBAC concept. [Courtesy of Ben Woods, University of Bristol] . . . .	14
1.8. Free wake simulation of a four-bladed rotor in forward flight using the Johnson model in CAMRAD II (oncoming free stream velocity from right to left). . . . .	17
1.9. Blue Edge rotor blade for passive noise reduction [14]. Photo taken by Nick Isaacs [CC BY-SA 4.0 DEED]. . . . .	20
2.1. Schematic of the aerodynamic flow conditions and aerodynamic loads at a typical blade section (looking outboard). . . . .	31
2.2. Effect of blade tip loss factor on lift distribution over the wing span. . . . .	32
2.3. Illustration of the modeled airfoil and wake features within Theodorsen theory. . . .	34
2.4. Illustration of the modeled airfoil and wake features within Peters theory. . . . .	35
2.5. Illustration of the multibody model of a wing used for the 2D and 3D steady and unsteady aerodynamics analyses. (Schematic inspired from Ref. [219]) . . . . .	40
2.6. Schematic showing the distribution of airstations on the different wing models. . . .	41
2.7. Static airfoil polars of the NACA0012 airfoil used on the elliptic wing and pitching finite wing models. . . . .	41
2.8. Illustration of the multibody dynamics model of the Bo 105 rotor (not to scale). Note that only one blade is shown, but four blades are modeled. . . . .	43
2.9. Illustration of the multibody dynamics model of the Bo 105 rotor used for obtaining the blade natural frequencies. . . . .	44
2.10. Schematic showing the distribution of airstations on the Bo 105 rotor blade. . . . .	44
2.11. Static airfoil polars of the NACA23012 airfoil for the Bo 105 rotor blade. . . . .	45
2.12. Illustration of the multibody dynamics models of the HART II rotor (not to scale). Note that only one blade is shown in (a) but four blades are modeled. . . . .	47

2.13. Illustration of the distribution of airstations on the HART II rotor blade. . . . .	47
2.14. Static airfoil polars of the NACA23012(tab) airfoil used on the HART II rotor blades. Based on data available on the DLR repository [8]. . . . .	48
2.15. Illustration of the multibody model of the UT Austin coaxial rotor model. . . . .	50
2.16. Schematic of the distribution of airstations on rotor blade used to model UT Austin single rotor and coaxial rotor system. . . . .	50
2.17. Static airfoil polars of the VR12 airfoil for the UT Austin rotor blade (obtained from Ref. [230]). . . . .	51
2.18. Illustration of the active camber morphing section modeled on the Bo 105 rotor blade. 52	
2.19. Airfoil profiles obtained for different degrees of FishBAC camber morphing. Adopted, with permission, from Ref. [141]. . . . .	52
3.1. Discretization of vortex rings using vortex particles. . . . .	61
3.2. Comparison of predicted centroid convection velocity for different vortex ring dis- cretizations using the current implementation and results available in Ref. [286](Winck- elmans). . . . .	62
3.3. Comparison of predicted linear diagnostics and convection velocity of 6by117 vor- tex ring versus results from Ref. [270](Valentin et al.) and, where available, Ref. [286](Winckelmans). . . . .	62
3.4. Comparison of predicted quadratic flow field diagnostics and convection velocity of 6by117 vortex ring versus results from Ref. [270](Valentin et al.) and, where available, Ref. [286](Winckelmans). . . . .	63
3.5. Illustration of the initialization of position and strength of particles for modeling trailing and shed vorticity. . . . .	65
3.6. Flow chart indicating the flow of information in the coupled Dymore+VPM analysis framework. . . . .	66
3.7. Illustration of the velocity induced by the bound circulation around a wing segment, which is modeled as a lifting-line element, on a particle located at $\mathbf{r}$ . . . . .	67
3.8. Snapshots of a diverging coupled Dymore+VPM simulation of the Bo 105 rotor in forward flight, with vortex stretching included. . . . .	69
4.1. Illustration of the rotor noise analysis toolchain comprising of the <i>HeliNoise</i> frame- work created to handle data output from the rotor aeromechanics analysis frame- work and convert into appropriate input for PSU-WOPWOP. . . . .	76
4.2. Illustration of the generated morphing wing surface and its discretization. . . . .	77
4.3. Illustration of the array of observers (or microphones) below and around the rotor used for acoustics analysis. . . . .	78
5.1. Section lift and moment coefficients for an airfoil pitching at $\theta = 6^\circ \sin(5 * 2\pi t)$ . . . .	81
5.2. Section lift and moment coefficients for a morphing airfoil with active camber actu- ation at $\delta = 9^\circ \sin(10 * 2\pi t)$ . . . . .	82
5.3. Section lift and moment coefficients for a pitching and morphing airfoil with $\theta =$ $6^\circ \sin(5 * 2\pi t)$ and $\delta = 0.5^\circ + 5.5^\circ \sin(10 * 2\pi t - 59^\circ)$ . . . . .	82
5.4. Section lift and moment coefficients for a pitching and morphing airfoil with $\theta =$ $4.5 + 5.75^\circ \sin(5 * 2\pi t)$ and $\delta = 5.0^\circ \sin(10 * 2\pi t - 196^\circ)$ . . . . .	82
5.5. Visualization of the 2D vortex wake of a wing section undergoing pitching ( $\theta = 6^\circ \sin(5 * 2\pi t)$ ) and camber morphing ( $\delta = 0.5^\circ + 5.5^\circ \sin(10 * 2\pi t - 59^\circ)$ ). . . . .	83



5.6. Spanwise distribution of the wake-induced inflow velocity for an elliptical wing at the quarter-chord location. . . . .	85
5.7. Visualization of the vortex wake of the an elliptical wing at static pitch angle $\theta = 5^\circ$ . .	86
5.8. Comparison of unsteady lift coefficient of a wing with aspect ratio $AR = 5$ with simulation and experimental measurements from Ref. [21]. . . . .	88
5.9. Visualization of the vortex wake of a rectangular finite wing of aspect ratio $AR=5$ pitching at $\theta = 3^\circ + 3^\circ \sin(2.05 * 2\pi t)$ . . . . .	89
5.10. Bo 105 rotor blade frequency fan plot at $0^\circ$ collective compared with data provided in Ref. [277](DLR) and Ref. [278](NASA). . . . .	91
5.11. Comparison of the mode shapes of the Bo 105 rotor blade obtained in the current study (solid lines) versus those provided in Ref. [99] (dashed lines). Note that only flap and lag mode shapes are provided in the reference study. . . . .	92
5.12. Comparison of rotor control angles obtained using Dymore and Dymore+VPM simulations against measurement data from Ref. [112] for the Bo 105 rotor over a sweep of advance ratios $\mu = 0.01-0.45$ . . . . .	93
5.13. Comparison of mean rotor shaft forces and moments, and power obtained using Dymore and Dymore+VPM simulations against measurement data from Ref. [112] for the Bo 105 rotor over a sweep of advance ratios $\mu = 0.01-0.45$ . . . . .	95
5.14. Comparison of half-peak-to-peak (HPP) dynamic blade loads and pitch link loads obtained using Dymore and Dymore+VPM simulations against measurement data from Ref. [112] for the Bo 105 rotor over a sweep of advance ratios $\mu = 0.01-0.45$ . . .	96
5.15. Comparison of aerodynamic parameters and blade section loads over the disk of the Bo 105 rotor obtained using standalone Dymore and Dymore+VPM simulation frameworks for the case of Run 42 point 7 ( $\mu = 0.1$ ) from Ref. [112]. . . . .	97
5.16. Comparison of aerodynamic parameters and blade section loads over the disk of the Bo 105 rotor obtained using standalone Dymore and Dymore+VPM simulation frameworks for the case of Run 26 point 11 ( $\mu = 0.3$ ) from Ref. [112]. . . . .	98
5.17. Visualization of the vortex wake of the Bo 105 rotor for the Run 42 point 7 case [112] obtained using VPM-based wake model. . . . .	99
5.18. Visualization of the vortex wake of the Bo 105 rotor for the Run 26 point 11 case [112] obtained using VPM-based wake model. . . . .	99
5.19. Comparison of Bo 105 rotor noise prediction at Run 42 point 7 ( $\mu = 0.1$ ) using Dymore and Dymore+VPM simulations with experimental measurement data from Ref. [112]. . . . .	101
5.20. HART II rotor blade frequency fan plot at $0^\circ$ collective compared with data from Ref. [256]. . . . .	103
5.21. Comparison of the mode shapes obtained in the current study (solid lines) versus results from DLR provided in Ref. [256] (dashed lines). . . . .	103
5.22. Comparison of azimuthal time-history of section blade coefficients of the HART II rotor at $r = 0.87$ obtained in the current work versus experimental measurements reported in Ref. [256]. . . . .	105
5.23. Visualization of the vortex wake of the HART II BL case obtained using VPM-based wake model. . . . .	105
5.24. Comparison of blade section loads and aerodynamic parameters over the disk of the HART II rotor obtained using standalone Dymore and Dymore+VPM simulation frameworks. . . . .	106

5.25. Comparison of the predicted noise levels for the HART II BL case using the different simulation frameworks used in the current work and the experimental data reported in Ref. [256]. . . . .	108
5.26. Re-scaled predicted noise levels for the HART II BL case for a qualitative assessment of the results obtained using the different simulation frameworks used in the current work. . . . .	108
5.27. Comparison of rotor control angles, thrust, mean hub moments, and power obtained using Dymore (solid lines) and Dymore+VPM (dashed lines) simulations. The results are obtained at the trim condition of Run 26 point 11 ( $\mu = 0.3$ ) case for different amplitudes ( $\delta = 0.5^\circ, 1.0^\circ, 1.5^\circ$ ) and phase angles ( $\phi = [0^\circ, 360^\circ]$ ) of active camber actuation at 1P. . . . .	112
5.28. Comparison of the change in aerodynamic quantities and blade section loads, obtained using standalone Dymore and Dymore+VPM simulation frameworks, for active rotor input of $\delta = 1.5^\circ \sin(2\pi * t / T + 270^\circ)$ with respect to the baseline results of Run 26 point 11 in Fig. 5.16. . . . .	113
5.29. Comparison of rotor 4P hub forces, moments and vibration indices, obtained using Dymore (solid lines) and Dymore+VPM (dashed lines) simulations. The results are obtained at the trim condition of Run 26 point 11 ( $\mu = 0.3$ ) case for different amplitudes ( $\delta_0 = 0.5^\circ, 1.0^\circ, 1.5^\circ$ ) and phase angles ( $\phi = [0^\circ, 360^\circ]$ ) of active camber actuation at 1P (see Fig. 5.27(a) for legend). . . . .	114
5.30. Comparison of the total noise at observer locations A, B, and C (see Fig. 4.3(a)), obtained using Dymore (solid lines) and Dymore+VPM (dashed lines) simulations. The results are obtained at the trim condition of Run 26 point 11 case for different amplitudes ( $\delta_0 = \{0.5^\circ, 1.0^\circ, 1.5^\circ\}$ ) and phase angles ( $\phi = [0^\circ, 360^\circ]$ ) of active camber actuation at 1P. . . . .	116
5.31. Baseline rotor noise at Run 26 point 11 conditions obtained using standalone Dymore output. . . . .	117
5.32. Baseline rotor noise at Run 26 point 11 conditions obtained Dymore+VPM output. . . . .	117
5.33. Variation in rotor total acoustic noise footprint over a hemisphere and a plane below the rotor, at different actuation profiles of active camber mechanism, obtained using Dymore+VPM output. . . . .	117
5.34. VPM simulation of the two-bladed UT Austin isolated rotor, at 1200 RPM and $6^\circ$ collective, exhibiting fountain effect when no special treatment is undertaken to solve for the rotor wake. . . . .	119
5.35. Comparison of predicted rotor performance, obtained using the different simulation strategies used in the current work, against measurement data from Ref. [113] for prescribed collective inputs to the UT Austin two- and four-bladed single rotors. . . . .	120
5.36. Comparison of blade spanwise variation of rotor simulation quantities for the UT Austin two-bladed single rotor case at rotation rate of 1200 RPM and $12^\circ$ collective. . . . .	121
5.37. Visualization of the vortex wake of the UT Austin two-bladed single rotor case, at rotation rate at 1200 RPM and $12^\circ$ collective, obtained using VPM wake modeling. . . . .	121
5.38. Comparison of predicted rotor aerodynamic parameters and blade section loads using standalone Dymore and Dymore+VPM simulation frameworks for the UT Austin two-bladed single rotor case at 1200 RPM and $12^\circ$ collective input. . . . .	122
5.39. Comparison of rotor thrust and torque variation for the baseline coaxial contra-rotating rotor. . . . .	124

5.40. Comparison of predicted rotor simulation quantities obtained using Dymore+VPM framework for the baseline coaxial contra-rotating rotor system. . . . .	125
5.41. Actuation profile of the FishBAC concept on the upper and lower rotor blades of the coaxial contra-rotating rotor system. . . . .	126
5.42. Comparison of rotor thrust and torque variation for the active coaxial contra-rotating rotor. . . . .	126
5.43. Comparison of predicted rotor simulation quantities obtained using Dymore+VPM framework for the active coaxial contra-rotating rotor system. . . . .	128
5.44. Baseline coaxial rotor noise hemispheres obtained using PSU-WOPWOP and Dymore+VPM. . . . .	129
5.45. Active coaxial rotor noise hemispheres obtained using PSU-WOPWOP and Dymore+VPM.	129
5.46. Comparison of the baseline and active coaxial contra-rotating rotor total noise results from a top view of the hemisphere. . . . .	129
5.47. Baseline coaxial contra-rotating rotor noise results over the ground plane obtained using PSU-WOPWOP and Dymore+VPM output results. . . . .	130
5.48. Active coaxial contra-rotating rotor noise results over the ground plane obtained using PSU-WOPWOP and Dymore+VPM output results. . . . .	130
D.1. Quadratic flow field diagnostics of 4by80 vortex ring predicted using VPM. . . . .	151
D.2. Linear flow field diagnostics of 4by80 and 5by100 vortex rings predicted using VPM. . . . .	152
D.3. Quadratic flow field diagnostics of 5by100 vortex ring predicted using VPM. . . . .	153



# List of Tables

3.1. Different kernel expressions based on the high order algebraic and the Gaussian smooth cutoff functions. . . . .	57
3.2. Vortex ring parameters used to verify the VPM solver setup. . . . .	59
3.3. Comparison of diagnostic quantities for different vortex ring discretizations (see Table 3.2) across different studies from the literature. . . . .	60
5.1. Rectangular wing geometry and simulation parameters for 2D wake analysis. . . . .	80
5.2. Elliptical wing geometry and simulation parameters for steady 3D wake analysis. . . . .	84
5.3. Finite wing geometry and simulation parameters for unsteady 3D wake analysis. . . . .	87
5.4. Acoustic sensor locations with respect to the hub in the shaft reference frame (see Fig. 2.8). . . . .	100
5.5. Acoustic sensor locations in the rotor shaft frame (see Fig. 2.12(a)). . . . .	102
A.1. Details of the Bo 105 rotor system multibody model. . . . .	143
A.2. Reference frames used to construct the Bo 105 multibody model of Fig. 2.8. Fixed points represented as •, joints as □. . . . .	144
A.3. Baseline Bo 105 rotor trim conditions for cases from Ref. [111] investigated in this work. . . . .	145
B.1. Reference frames used to construct the HART II multibody model of Fig. 2.12(a). Fixed points represented as •, joints as □. . . . .	147
B.2. Details of HART II rotor system multibody model. . . . .	148
C.1. Model parameters used for the construction of the UT Austin two- and four-bladed single rotors, and the coaxial contra-rotating rotor. . . . .	149
C.2. Details of the UT Austin coaxial rotor multibody model of Fig. 2.15. Fixed points represented as • and joints as □. . . . .	150



# 1. Introduction

## 1.1. Motivation

Conventional rotors impose several limitations on the performance of rotorcraft. Fundamentally, they can be ascribed to the design constraint whereby each rotor blade section has to operate in continuously varying aerodynamic conditions as the blade undergoes one rotor revolution. Given the inherent unsteady aerodynamics experienced by the rotor blade, different mechanisms have been proposed and studied to various extent in the past to improve rotor performance, lower hub vibrations, and reduce acoustic noise emissions. The fundamental idea behind these concepts, or active rotor technologies, is the ability to control blade section aerodynamics. By controlling local blade lift, drag, and moment over the rotor azimuth, the blade section lift-to-drag ratio can be improved, leading to lower required power. The local blade response can also be controlled to some extent. If such control can be implemented at different frequencies then there is potential to tailor blade response at those specific frequencies. This makes active rotor concepts attractive from the point of view of vibrations and noise reduction since the drivers of these two phenomena, i.e. unsteady aerodynamic loads, can be influenced at the source itself.

Modeling active rotor systems in some form has been in pursuit for more than half a century. The research in this field started with higher harmonic control of the rotor swashplate in the non-rotating frame to obtain higher harmonic changes to blade pitch angles. The fundamental idea behind the strategy was to control the high-frequency blade loads by directly influencing the blade pitch angle at the root. Rotor blades are generally slender in design, making them susceptible to structural twisting and flapping motion, which makes direct control of the pitch angle along the entire blade span difficult. To that end, a number of additional mechanisms have been computationally and experimentally investigated since then, with the fundamental objective of greater blade motion and loads control. A majority of these mechanisms have involved placement and actuation of the active mechanism in the rotating frame of the rotor. They include trailing-edge tabs, trailing-edge flaps, leading-edge droop, active twist, etc., which provide greater freedom of controlling blade motion and loads along the blade span.

The current work was motivated by past investigations to explore the potential of a novel biologically inspired camber morphing mechanism as an active rotor mechanism. The functioning of this mechanism, called the Fish Bone Active Camber (FishBAC) concept, stands in stark contrast to the trailing-edge flap mechanism that has been installed and tested on full-scale rotors in wind tunnel as well as in free-flight campaigns. Computational and wind tunnel studies of the FishBAC concept showed sufficient improvement over the trailing-edge flap concept to merit detailed rotor analysis of its impact on rotor operation. In addition to that, it is worth mentioning that new ac-

tive rotor concepts are always being investigated. Some of the most recent examples include the DLR META rotor (see Fig. 1.1) with individual blade control system and the STAR rotor system for active twist control. These ongoing efforts emphasize the need for updated and improved modeling techniques for such systems. To that end, an extensive framework with relevant modeling fidelity was created as part of this work. The comprehensive analysis solver Dymore was used to construct a detailed multibody model of the rotor and the associated control systems. The simulation toolchain was augmented using a vortex particle method-based formulation to solve for the inflow induced by the rotor wake system, and a post-processing framework for acoustics analyses. A number of rotor and wing test cases were adopted from the literature in order to incrementally verify and validate different components of the entire simulation framework.



**Figure 1.1.:** The META rotor system from DLR for individual blade control via passive pitch links[1](CC BY-NC-ND 3.0 DEED).

## 1.2. Active Rotor Concepts

A number of investigative campaigns have been conducted over the years in order to identify the effects of the different active rotor control mechanisms on rotor performance, hub vibratory loads, and aeroacoustic noise emissions. These campaigns include experimental tests, both scaled rotors and full-scale rotors, as well as mid- to high-fidelity computational investigations. The literature in this domain is fairly extensive. Bibliographical completeness in this regard would be a challenging endeavor and one that is not necessarily meaningful in the current context. So, this section covers only the most relevant studies and highlights the most prominent outcomes.

Stated below are some examples of the different active rotor technology investigations available in open literature-

1. Higher harmonic control (HHC)

Full-blade feathering systems that are capable of higher harmonic pitch control of the rotor blades, i.e., at frequencies that are multiples of the rotor rotation frequency. Here, the actuation system is placed in the non-rotating frame.



2. Individual blade control (IBC)

Full-blade feathering system similar to HHC, except that the actuator system is placed in the rotating frame of the rotor. With IBC, a greater number of blade frequencies can be influenced than the HHC concept.

3. On-Blade Control concepts (OBC)

These are similar to the IBC mechanism and are collectively referred to as IBC concepts by some authors because of their fundamental ability to actuate independently on each blade. The control mechanisms involved—for example, gurney flap, trailing-edge flap (TEF) or trailing-edge deflection (TED), active twist, leading-edge deflection (LED), etc.—are located on the rotating blades.

Fundamentally, HHC, IBC, and OBC mechanisms operate by influencing the blade section aerodynamic properties of lift, drag, and moment beyond the 1/rev (1P) pitch angle variation by the swashplate for primary rotor control. The HHC and IBC mechanisms differ in the frequencies at which control is afforded. Since the blade section profile does not deform, they do not result in any decrease in blade profile drag, and consequently, have limited use towards improving blade section  $L/D$ . The on-blade control mechanisms of TEF, TED/active camber, and LED can be separately operated for each blade at any given frequency within the limit of the actuation system. Based on the amplitude of actuation, a corresponding change in the blade section lift, drag, and moment properties results. Clearly, OBCs allow a greater degree of flexibility when it comes to tailoring blade aeromechanical loads and response since multiple such mechanisms can be located throughout the span of the blade, allowing different actuation profiles in different span sections of the blade. Adding active control capability, especially via OBCs, is likely to lead to an increase in the number of component parts that make up the rotor system. The *raison d'être* of installing such mechanisms is to improve rotor efficiency such that any potential increase in maintenance costs or increase in blade design complexity is justified.

The following details work carried out in the past on the different active rotor technologies. Special attention was paid to experimental investigations involving active rotors. This is because physical measurements of improvements in performance, hub vibration, and noise emissions are relatively more credible benchmarks, for the potential of different active rotor mechanisms, compared to computational studies. Once the benefits of active rotors are established, simulation studies can be useful to help identify the blade dynamics and flow phenomenology responsible for said potential improvements. Ref. [133] and its companion publication Ref. [132] provide a thorough yet concise review of the development of active rotor control technologies. The former provides a good overview of the development cycle of the HHC concept as well as experimental test campaigns that were carried out using it. The latter provides a review of the different active rotor concepts with control based in the rotating frame. These include IBC, active twist, TEF, and swashplateless rotor control concepts. Additionally, Ref. [81] provides a good background of nearly four decades of research activities into active rotors. Altogether, the three studies provide a good overall review of the state of the art. The following sections discuss the most important outcomes from a number of active rotor investigations, some of which have already been documented in sufficient detail in Refs. [133], [132], and [81]. The purpose of doing this is twofold—(i) highlighting only those aspects of the results that are relevant in the context of the current study and (ii) completeness of the literature review. In addition to this, a few active rotor investigations conducted since

the publication of the aforementioned review studies have also been discussed.

### 1.2.1. Higher harmonic control (HHC)

The HHC mechanism is arguably the simplest active rotor control mechanism to implement. It is likely that this is the reason why many full-scale rotor wind tunnel test campaigns and free flight test demonstrations have been conducted investigating this concept. These were conducted using both full-scale and scaled model rotors.

Ref. [145] details a full-scale S-76 rotor wind tunnel test (see Fig. 1.2(a)<sup>1</sup>), that were carried out in conjunction with the flight tests study of Ref. [180]. It was reported that substantial reductions in high-frequency hub loads were obtained for a range of advance ratios, and BVI noise reduction of up to 5 dB was measured for low forward speed operation. However, the effect of 2P control on reducing rotor power consumption did not yield clear trends. In Ref. [188], a full-scale rotor investigation where the XV-15 rotor (Fig. 1.2(b)) was tested in helicopter mode to independently control rotor noise and vibrations. It was observed that the HHC mechanism was capable of reducing BVI noise by up to 12 dB and a vibration controller led to a 50% reduction in vibratory loads. Preliminary exploration test campaigns conducted at Boeing using model rotors [237][238], demonstrated the potential of the HHC mechanism to reduce vibratory loads over a range of advance ratios. Ref. [237] demonstrated the viability of the HHC mechanism to suppress vibratory loads during maneuvers or gusts using a scaled Model 179 helicopter rotor with a closed-loop system. In Ref. [238], the HHC mechanism was shown to be capable of influencing vibratory loads along all three axes of the dynamically scaled CH-47D helicopter rotor for the entire range of rotor advance ratios.

A number of major helicopter manufacturers, by far the most of any active control concept, have conducted free flight tests using the HHC mechanism. For example, open-loop and closed-loop HHC controlled flight tests on the OH-6A helicopter (Fig. 1.2(c)) at McDonnell Douglas Helicopter Systems (currently Boeing) [290] and on the SA 349 Gazelle helicopter at Aerospatiale [18], and open-loop flight tests on the S-76 at Sikorsky Aircraft [180]. During the OH-6A helicopter tests, vibration reduction was achieved over a sweep of advance ratios  $\mu = 0-0.25$ , and vibrations in the aircraft frame below the pilot seat could be brought to below 0.05 g for all forward flight speeds tested. On the SA 349 and S-76, closed-loop and open-loop tests, respectively, demonstrated a significant reduction in measured vibrations both in level cruise flight and during maneuvers.

Rotating systems exhibit a characteristic behavior whereby only  $(nN_b - 1)P$ ,  $nN_bP$ ,  $(nN_b + 1)P$  frequencies, where  $n$  is a positive integer, pass on from the rotating system into the non-rotating frame. The frequencies in question can refer to the spectral components of the pitching motion of the blades or the structural/aerodynamic loads acting on the blades. Similar behavior is exhibited during HHC operation where  $nN_bP$  actuation of the stationary swashplate components can only induce  $(nN_b - 1)P$ ,  $nN_bP$ ,  $(nN_b + 1)P$  frequencies in blade pitching motion. This means that for rotors consisting of four blades or more, the HHC mechanism does not have the ability to excite

---

<sup>1</sup>Images in Figs. 1.2(a) and 1.2(c) are a work of the U.S. Government and free from copyright protection [55]; image in Fig. 1.2(c) is reproduced with permission from the author of Ref. [94].



(a) S-76 [5]



(b) XV-15 [188]



(c) OH-6A [94]

**Figure 1.2.:** Higher harmonic control (HHC) tests of the S-76 and XV-15 rotors in the NASA Ames 80- by 120-foot wind tunnel, and free flight test campaign onboard the OH-6A helicopter.

or control all the spectral components of blade motion responsible for vibratory hub loads in the non-rotating frame. In order to overcome this limitation, the IBC mechanism was invented. Ref. [116] cites the lack of HHC input scheduling, which simultaneously reduces BVI noise as well as vibration, as one of the driving factors for IBC research.

### 1.2.2. Individual blade control (IBC)

Many authors make the distinction of rotor technologies only as HHC or IBC. All mechanisms operating in the rotating frame, with the capability to individually influence blade behavior at all frequencies, get clubbed in the latter category; see, for example, Refs. [228] and [132]. However, IBC has come to be referred to a specific active rotor control technology—that of using active actuators in place of passive pitch links. With the IBC mechanism, each blade can be controlled independently of all other blades and at any given frequency within the operating limit of the actuation mechanism. This grants a greater degree of freedom to control the rotor compared to the HHC system. Thereby allowing, in principle, operational control of a rotor even with dissimilar

blades [224].

Unlike multiple HHC flying demonstrators, as mentioned earlier, full-scale rotor flight tests involving IBC were only conducted in Europe. At Eurocopter (now Airbus Helicopters Deutschland) many free flight tests were conducted using an IBC demonstrator test bed based on the Bo 105 helicopter rotor system. The free flight tests carried out in 1990-1991 were the first to demonstrate the potential of IBC to reduce hub vibrations [262]. However, the control authority of the IBC actuators, the input harmonic frequency range, as well as the helicopter operating speed were limited in these tests for safety reasons. Thereafter, an extensive test campaign of the full-scale rotor was carried out in the NASA Ames 40- by 80-foot wind tunnel. In the first stage of the campaign in 1993 [220], the influence of IBC on rotor noise and vibrations was tested at low-speed conditions, and up to 70% reduction in hub vibratory loads and 7 dB reduction in BVI noise was obtained. In the second stage, a fortified test stand was used to further conduct IBC tests at up to  $\mu = 0.45$  in 1994 [114]. It was observed that performance gains of up to 7% could be obtained at  $\mu = 0.4$  and  $\mu = 0.45$ , while none was measured at  $\mu = 0.3$  for 1-g level flight simulation conditions ( $C_T/\sigma = 0.075$ ) [115, 116]. Significant reductions in the vibratory loads and pitch link loads were measured, particularly for low-speed descent flight cases. The test campaign of 1993 [220] involved open-loop IBC inputs where it was later realized that IBC input, particularly 2P input for performance input, led to a sufficient change in the rotor trim state. As a consequence, the obtained performance gains were rendered suspect. The issue was rectified in the 1994 test campaign, and the rotor was re-trimmed after every IBC input. Therefore, the results of the test campaign of 1994 [115] are more physical. The measurement data from these tests are also used within this work to validate the Bo 105 model.

Another free-flight test campaign of the IBC systems onboard a Bo 105 S1 demonstrator (see Fig. 1.3<sup>2</sup>) was conducted with advanced algorithms for closed-loop control for BVI noise reduction [226]. A maximum reduction of 5 dB was achieved using on-ground filtered measurements and with only 2P actuation. In a later series of tests, vibration reduction was also demonstrated [228]. At ZF Luftfahrttechnik (now Airbus Helicopters Technik), free flight tests of the heavy lift CH-53G using a closed-loop vibration controller were conducted [22]. They showed varying levels of success based on the number of components of vibratory forces that were simultaneously controlled. An earlier study involving open loop control flight tests on the same test bed had shown that rotor noise during BVI in descent flight decreased by 3 dB and power consumption reduced by 6% [23]. Ref. [132] provides a detailed review of the outcome of further free flight tests conducted, which were particularly focused on BVI-induced noise and vibration.

In Ref. [95], the IBC system was tested to alleviate retreating blade stall on a scaled rotor model. This was successfully achieved using 2P and 3P control inputs at certain phases such that loading in the fore and aft portions of the rotor disk was increased and reduced on the lateral sides. Ref. [189] presents a computational study into automatic stall suppression on rotors using IBC. A modern Bo 105 rotor was simulated, with HH-10 airfoil sections instead of NACA23012, and with a control input of less than  $1^\circ$ , stall suppression was demonstrated for advance ratios of  $\mu = 0.3$  and 0.35. The study concluded that, using IBC inputs, it was difficult to simultaneously achieve reduction in power as well as alleviate stall.

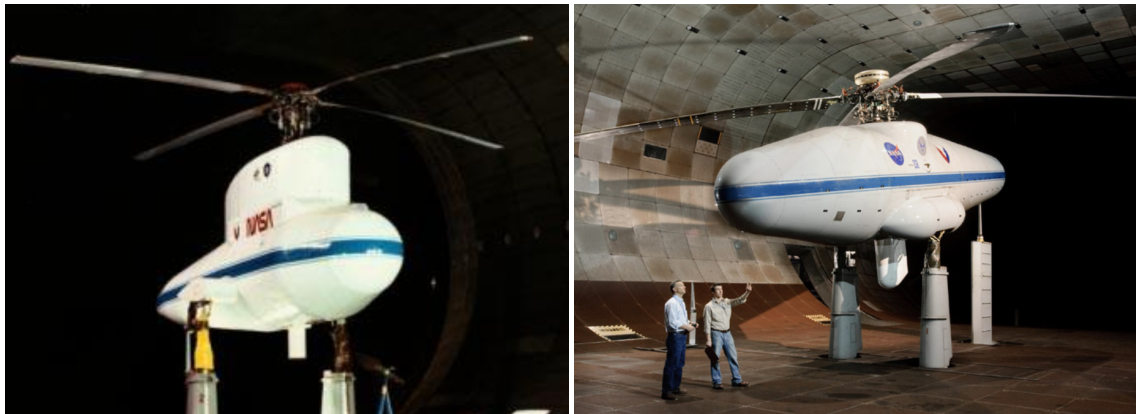
---

<sup>2</sup>Image reproduced from its original source with permission from Airbus Helicopters Deutschland.



**Figure 1.3.:** Individual blade control (IBC) rotor test campaign using the Bo 105 S1 demonstrator [226].

In Ref. [116], full-scale Bo 105 rotor tests were conducted in the NASA Ames 40- by 80-foot wind tunnel (see Fig. 1.4(a)<sup>3</sup>) to measure the effect of 2P IBC input via pitch links on rotor performance. No performance gain was measured for  $\mu = 0.3$  over a phase sweep of IBC input. At  $\mu = 0.4$  and 2P IBC input of  $1.0^\circ$  amplitude, the required power was decreased by 4% such that IBC input peaks occurred close to  $\psi = 100^\circ$  and  $\psi = 280^\circ$ . The pitch link loads remained almost unaffected at the phase angles of best power reduction. A similar experimental setup was used to investigate the effect of IBC on the rotor performance of a full-scale UH-60A rotor (see Fig. 1.4(b)) [190]. While the investigation involved a range of test conditions based on measurement data published in Refs. [190] and [294], the maximum reduction in rotor power achieved was 5% at 2P IBC input amplitudes of  $2^\circ$  and  $1.5^\circ$ . The input phase was such that peak IBC pitch input occurred at  $\psi = 112.5^\circ$  and  $\psi = 292.5^\circ$  on the advancing and the retreating sides, respectively. This, again, indicates a pattern of loading redistribution from the front and aft sections to the lateral sides of the rotor disk in both sets of rotor tests.



(a) Bo 105 [111].

(b) UH-60A [13].

**Figure 1.4.:** Individual blade control (IBC) rotor test setups at the NASA Ames 40- by 80-foot wind tunnel.

<sup>3</sup>Figures 1.4(a) and 1.4(b) are a work of the U.S. Government and free from copyright protection [55].

The requirement of placing hydraulically actuated systems either in the non-rotating frame (HHC) or in the rotating frame within the pitch links (IBC) is considered a disadvantage due to the mechanical complexities involved [243]. It is not an efficient technology for vibration reduction since the pitch link actuators have to move the entire blade in order to operate, even though the in-board blade sections are not effective towards vibration or noise suppression [81]. The advent of active materials introduced concepts such as the piezoelectrically actuated trailing-edge flaps and strain-induced rotor blade active twisting. This provided a means of individual blade control without the cumbersome setup necessary to transfer hydraulic power into the rotating system. Concepts such as the trailing-edge flap and active twist were realizable due to this technology and are discussed in the following sections.

### 1.2.3. Trailing-edge flap (TEF)

One of the earliest studies with a full-scale active rotor was carried out at NASA Ames 40- by-80-foot wind tunnel. A 40-foot diameter two-bladed teetering rotor (Dorand rotor) was controlled using higher harmonic control input of jet flaps with the objective of influencing hub vibratory loads. The details about the series of tests carried out on that rotor over the years are documented in Ref. [147]. These were some of the earlier studies with the practical application of the T-matrix approach [37] to identify multicyclic control that could lead to vibration minimization. Building up on those studies, work was carried out on the Dorand rotor by John L McCloud III [178], who also coined the term ‘multicyclic control’ for higher harmonic blade control (see Ref. [94]). The promise of this approach led to further studies such as the 56-foot diameter controllable twist rotor (CTR) where active control was achieved by twisting the rotor blades using servo flaps [179]. These early experimental studies provided some encouraging results towards using higher harmonic active control to reduce rotor-induced vibration.

A number of computational studies have established the potential of actively controlled trailing-edge flaps in influencing the 4P vibratory forces transferred from the rotating blade system to the hub-fixed system. Ref. [181] used a multicyclic controller on an S-76-like rotor to identify periodic TEF deflections. The objective was to identify the sensitivities of flap properties such as length, spanwise location, chord, etc., on influencing 4P hub vibratory forces and moments at a number of advance ratios. Different trends were identified for the investigated flap properties, but overall, it was established that the TEF is capable of affecting hub vibrations. Ref. [167] simulated a Bo 105-like hingeless full-scale rotor to identify the benefits of higher harmonic actuation of a trailing-edge flap. A closed-loop controller was used to reduce the power consumption of the rotor at high advance ratios of  $\mu = 0.35$  and above in single and dual trailing-edge flaps configurations on the blades. A peak reduction in power of 6.37% was obtained at an advance ratio of  $\mu = 0.4$ . However, the source of the savings was attributed to reduction in drag losses on the advancing side rather than stall alleviation on the retreating side. Simultaneous reduction in hub vibration and power consumption were also demonstrated to be possible. No substantial differences were obtained between the single and dual flap configurations simulated.

A number of scaled rotor tests have also been conducted in wind tunnels across the world. Active trailing-edge flaps were tested at ONERA as part of a cooperative partnership with Eurocopter

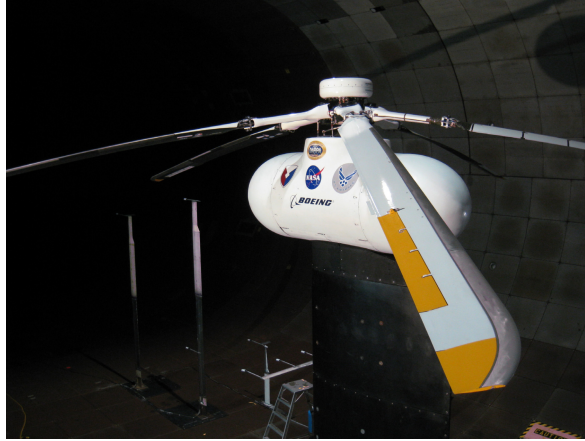
Deustchland (now Airbus Helicopters Deutschland) [64]. While the full-scale ADASYS rotor system was being built and tested out in Germany, the scaled active rotor tests in the ONERA Modane center were used to identify potential areas for further investigation by incrementally testing through a large matrix of operating conditions. One of the main observations from the test campaign was the lack of significant savings in rotor performance. It was observed, however, that there was scope for influencing rotor vibration using both open-loop and closed-loop tests. It is unlikely that this was a consequence of the high torsional stiffness of the blades. In such a scenario, any potential performance gains could only be achieved as a byproduct of improved 2D blade section aerodynamics and, therefore, be limited as observed during testing. Ref. [157] refers to this as the ‘direct-lift effect’, while the modification of blade loading via induced twist was referred to as the ‘servo-flap effect’ of the trailing-edge flap. In Ref. [157], the full-scale ATR rotor with active trailing-edge flaps was simulated, and it was shown that for both torsionally stiff and soft rotors a mix of both the aforementioned effects was responsible for the net blade response.

The Boeing Smart Material Actuated Rotor Technology (SMART) rotor was a full-scale five-bladed bearingless MD-900 helicopter rotor with piezoelectrically actuated flaps (see Fig. 1.5<sup>4</sup>). An extensive test campaign was carried out at the National Full-Scale Aerodynamics Complex (NFAC) 40- by 80-foot wind tunnel. The tests investigated the aerodynamic and structural loads, rotor performance, in-plane rotor noise, control power, and flow physics of the approximately 10 m diameter rotor. The active rotor setup included a flap located on the blades towards the outboard (from  $r = 0.74$ – $0.92$ ) with a relatively large flap chord of  $0.35c$ . Subsequently, high-fidelity computational studies were conducted in order to verify the capability of state-of-the-art modeling strategies to simulate the complex rotor physics. Ref. [209] carried out one such study using CFD/CSD coupling including flap gaps and rotor hub. Surprisingly, and much like the aforementioned preliminary investigations at ONERA [64], the experimental measurements as well as the high-fidelity simulations were in agreement that the flap actuation had negligible effect towards improving performance. The active flap mechanism was more successful in influencing rotor in-plane noise leading to a maximum reduction of about 2 dB, 5 dB and 5 dB for isolated 2P, 3P and 5P actuations, respectively. Overall, even the high-fidelity simulation setup was found incapable of accurately predicting the waveform and magnitude of the high frequency vibratory structural loads. Active vibration control using closed-loop control of flap deflection showed up to 95% reduction in 1-5P normal force vibratory loads in level cruise ( $\mu = 0.3$ ) and descent ( $\mu = 0.2$ ) flight conditions [92]. Comprehensive analyses using RCAS [62] and CAMRAD II [146] have both shown fairly similar ability to capture the time-history of the blade structural loads as well as their spectral composition.

Ref. [171] details the outcome of investigations carried out using the 4.191 m radius S-434 helicopter rotor by Sikorsky and United Technologies Research Center at the NFAC 40- by 80-foot wind tunnel. Closed-loop vibration control was demonstrated without significant effect on rotor efficiency, details of which have been summarized well in Ref. [81]. Active flap actuation at 2P and amplitude of  $4^\circ$  was found to be the most effective in reducing noise due to BVI. Further acoustics tests were carried out using this setup using harmonic and localized non-harmonic active flap actuation, as well as closed-loop acoustics control investigations. Measurements corresponding to the specific case of a forward cruise speed of  $\mu = 0.32$  and shaft tilt  $\alpha_s = -5^\circ$  were reported in

---

<sup>4</sup>Figure 1.5 is a work of the U.S. Government and free from copyright protection [55].



**Figure 1.5.:** The Boeing SMART rotor with trailing-edge flaps in the NASA Ames 40- by 80-foot wind tunnel [144].

Ref. [247]. They showed that approximately 2.0–8.0 dB reduction in low-frequency in-plane rotor noise was possible using either of the aforementioned approaches. Within the confines of the test parameters of the conducted study, it was observed that this reduction in noise occurred at the expense of rotor power consumption and vibratory loads.

Eurocopter has arguably the most extensive research experience with active rotor flight tests (IBC flight tests have already been detailed earlier) and active TEF investigations. In 2005, the first free flight tests of a full-scale active trailing-edge flap rotor were carried out [69]. This is commonly referred to as the ADASYS rotor (German acronym for ‘Adaptive Dynamic System’) and the BK117 helicopter was used as the experimental test bed, see Fig. 1.6(a)<sup>5</sup>. Based on the results reported in Ref. [227], the effect of TEF was qualitatively similar to IBC rotor for vibration suppression. Over a range of forward cruise speeds, between 50% and 90% reduction in 4P hub moments and forces was reported using TEF. In 2009, further work was carried out on this front using the ADASYS rotor system with improved instrumentation and using the EC145 airframe instead (see Fig. 1.6(b)). This test setup was referred to as the Blue Pulse demonstrator. Further investigations were also conducted into the use of TEF to improve rotor in-plane damping [176] as well as eliminate non-NP vibratory loads due to static dissimilarities among the different blades of the rotor [137]. Ref. [212] summarizes the achievement of the Blue Pulse tests, in particular showing a reduction in vertical vibratory hub loads across the entire advance ratio sweep of the helicopter. A maximum of 80% reduction in vibratory loads was measured at a fast cruise flight of 120 knots. The two flight test campaigns were used to successfully demonstrate active vibration control and BVI noise reduction and improved the technology readiness levels of critical technologies. This technology is also under development at Leonardo Helicopter where a AW139 baseline rotor was modified to include active TEF to address vibration control [258].

Investigations into trailing-edge morphing on a full-scale UH-60A rotor have reported performance gains for higher harmonic deflections with appropriate phasing over the rotor azimuth

---

<sup>5</sup>Figures 1.6(a) and (b) are reproduced from respective sources with permission from Airbus Helicopters Deutschland.





(a) BK117 ADASYS [212].

(b) EC145 Blue Pulse Demonstrator [212].

**Figure 1.6.:** Trailing-edge flap-based active rotor free flight test campaigns at Airbus Helicopters using two different test bed helicopters.

[117, 118, 217]. Ref. [117] used comprehensive analyses with free wake modeling as well as CFD/CSD coupled analyses to simulate a UH-60A helicopter rotor with a continuous TE deflection in forward flight. The airfoil was parameterized so that the upper and lower surfaces deformed smoothly to induce a TE deflection. The highest increments in rotor  $L/D_e$  of 7.6% and 4.4% were obtained using TE actuation at 1P and 2P, respectively. Using 1P actuation, performance gains were obtained when peak negative (upward) TE deflection occurred in a limited azimuth range about  $\psi = 90^\circ$ , leading to increased disk loading on the rotor advancing side. 2P actuation yielded performance gains when peak positive (downward) TE deflection occurred at the fore and aft sections of the rotor disk. These actuation profiles led to a positive pitch-up moment on the advancing side, increasing the angle of attack near the blade tip region and, consequently, increasing the blade loading there without any corresponding increase in drag. In Ref. [118], the deforming trailing edge was modeled to be more representative of a TEF but without spanwise or chordwise gaps. An extensive parametric study of active mechanism sizing and control parameters suggested that with a non-harmonic actuation, an improvement of 7.3% in rotor  $L/D_e$  could be obtained while keeping control loads within acceptable limits. The non-harmonic actuation cycle (or scheduling) involved a negative deflection on the advancing side and a high positive deflection on the retreating side of the rotor. Ref. [217] also reported similar effects of optimal combinations of 1P and 2P harmonic TEF actuation on the UH-60A rotor performance.

In reality, a small gap can exist between the main rotor blade section and TEF, both in the spanwise direction as well as the chordwise direction, depending on the angle of deflection. This gap can have a significant influence on the aerodynamic efficiency of the airfoil. Quasi-steady modeling of such gaps is possible via the standard procedure of obtaining C81 format airfoil tables for a range of flap deflections. However, potential flow theory-based unsteady aerodynamic models, commonly used in comprehensive analysis codes, are incapable of modeling the unsteady effects of TEF gaps. Therefore, proper accountability of flap-gap effects on overall blade performance can only be achieved via CFD/CSD studies. Studies, detailed in Refs. [210] and [209], carried out within the realm of the Boeing SMART rotor program, were one of the few studies that included this aspect, which has been missing from most studies on TEFs mentioned above. In Ref. [128], CFD analysis and CFD/CSD coupled investigation were carried out on an airfoil with TEF and a

fictional UH-60A rotor with active TEF, respectively. The presence of chordwise gaps was shown to have a detrimental effect on the airfoil performance. In the case of the UH-60A rotor analysis, results showed that chordwise gaps, depending on the flap deflection, reduce the thrust-generation capability of the rotor. Similarly, spanwise gaps also have an influence on blade thrust and pitching moment but to a lesser extent.

#### 1.2.4. Miscellaneous concepts

##### 1.2.4.1. Active twist

The NASA/Army/MIT active twist rotor was a concerted multi-organizational effort targeted towards the construction of a scaled active twist rotor system [284]. Wind-tunnel tests were conducted using this rotor to ascertain potential benefits in order to reduce rotor vibration and noise, as well as improve performance. Based on preliminary wind-tunnel testing, rotor-induced forces in the fixed system were reduced by 60% to 95% depending on the operating condition. The computational study of Ref. [44], investigating the impact of active twist on rotor noise, showed that it was possible to reduce BVI noise using 3P input without incurring higher vibrations. However, rotor performance was found to deteriorate. Experimental tests on the ARES testbed using the ATR rotor demonstrated that the ability of the active twist concept to reduce rotor noise is similar to that of the HHC concept [40]. A maximum reduction in rotor BVI noise of 2.8 dB and a maximum reduction of 90% in hub vibrations was registered. It was observed that it was generally possible to identify active twist actuation inputs that simultaneously led to noise reduction and vibration reduction to various degrees.

Aeromechanical simulations were conducted using a 40% Mach-scaled Bo 105 rotor (but with articulation and no precone) as part of the Smart-Twisting Active Rotor (STAR) program [164]. Another set of results from a simulation campaign of the same rotor are available in lieu of experimental measurement data from Ref. [68]. Using a number of different comprehensive analysis frameworks, overlapping conclusions from both studies confirmed successful reduction in power consumption reduction, BVI noise reduction and reduced vibratory loads using up to 3P actuation. Hover performance improvements, in terms of rotor FM, were limited due to the actuation limits of the actual physical active twist mechanism. Numerical simulations of a full-scale UH-60A with active twist in Ref. [117] showed similar performance trends as those obtained for the UH-60A rotor IBC test results of Ref. [294]. CFD/CSD coupled analysis was used to show that using a 2P active-twist scheduling with maximum outboard blade pitch increase of  $4^\circ$  occurring at  $\psi = 90^\circ$  a power reduction of 3.3% was possible. Ref. [296] also arrived at similar conclusions based on comprehensive analysis of a modified AH-64 Apache main rotor with active twist.

##### 1.2.4.2. Leading-edge slats

Multi-element airfoils have been explored in order to improve rotor stall boundary without incurring much drag penalty [170]. Applying the concept to an existing airfoil profile SC2110 and

simulating on the UH-60A rotor in an open-loop study, showed that this concept had potential to have a significant impact on rotor performance [218]. Rotor required power could be reduced by 10%-20% at various forward speeds during high blade loading conditions but the corresponding vibratory loads were always impacted negatively in that study. The general trend with multi-element airfoil designs is that they are beneficial at high thrust conditions where they lower the demand for power consumption [293]. However, the drag penalty associated with the airfoil in low thrust conditions makes them impractical. Ref. [293] further goes on to suggest that the benefits of slotted airfoils are similar to a passive blade with a wider chord design. The experimental measurements from the test campaign of Ref. [244] corroborated this assertion.

The variable-droop leading-edge device is another concept involving a change of profile of the blade airfoil section at the leading-edge. Ref. [25] used CFD/CSD coupled results from the high thrust flight counter C9017 of the UH-60A rotor to show that it can be used for favorable results in the dynamic stall regime of the rotor and reduce dynamic stall-induced loads. In Ref. [296], comprehensive analysis of the Apache main rotor using CAMRAD II showed that this concept could help increase maximum blade loading in a given flight state. This improvement was achieved by increasing disk loading on the retreating side of the rotor disk. However, this concept was never investigated further using an experimental test setup.

#### 1.2.4.3. Gurney flaps

Extending the idea of multi-element airfoils, a number of active rotor studies were carried out using active deployable gurney flaps. These are also referred to as microflaps [168] or miniature trailing-edge effectors [136]. These devices are attractive due to their small size and low inertia properties, thereby requiring low power to actuate them at high frequencies. Their influence on the blade section unsteady aerodynamics, and even post-stall airloads shows that they can be used to expand the rotor operating envelope [135], reduce hub vibrations [168], and reduce rotor noise [192]. Their utility in improving rotor cruise performance is, however, questionable since they generate more drag per unit amount of lift than TEF [175]. This technology is also under development at Leonardo where a AW139 baseline rotor was modified to include active gurney flaps for performance enhancement [258].

#### 1.2.5. Active camber morphing

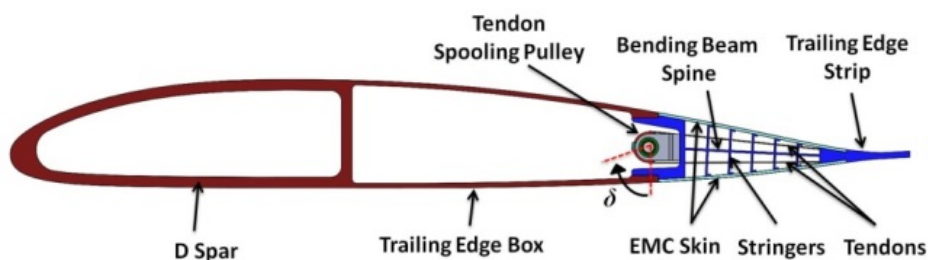
Each of the different active mechanisms discussed above allows a different degree of freedom to control the rotor response. The HHC mechanism works by higher harmonic control of the blade pitch angle input at the root. However, there is no control over the overall blade response due to its elastodynamics. The IBC mechanism is similar to the HHC except in its ability to effect blade pitch changes over larger spectrum of frequencies. On-blade mechanisms such as the LED, TED, TEF, gurney flap-type mechanisms, etc., work similarly by affording more direct control of the blade airloads. The differences in each of these mechanisms emerge from differences in 2D airfoil aerodynamics on the active blade sections. The mechanisms also differ from each other in terms

of their power requirements in order to have a meaningful influence on rotor behavior. Gurney flaps, for example, stand out as they need much lower power in order to operate compared to TEF [193]. However, studies in this regard are not conclusive since no single study compares all the different mechanisms, owing to the lack of maturity of the concepts.

A CFD/CSD coupled investigation in Ref. [119] showed that the presence of chordwise gaps between the blade and the flap mechanism leads to reduced effectiveness of TEF. This was quantified in terms of lower lift improvement and higher drag increase upon deflection. The degree of this degradation depends on the size of the chordwise gap but Ref. [119] reported that, for the study carried out on the UH-60A rotor, no performance benefit was observed if the gap size increased to  $1.2\%c$ . This makes concepts that involve smooth, continuous deformation of the airfoil profile more desirable. Therefore, an active camber mechanism appears more suitable than a TEF for active rotor applications. Ref. [288] demonstrates the feasibility of the Fish Bone Active Camber (FishBAC) concept (see Fig. 1.7), as an alternative to TEF, to deform the camber smoothly in the aft section of an airfoil. A previous limited-scope investigation of a full-scale rotor with active camber morphing showed that it could be used to improve performance both in hover and in forward flight [216].



(a) Scaled physical model



(b) Schematic of the structural details

**Figure 1.7.:** Details of the FishBAC concept. [Courtesy of Ben Woods, University of Bristol]

Ref. [41] showed that rotor efficiency  $L/D_e$  was related to the aerodynamic efficiency  $L/D$  of the airfoil sections that make up the rotor blades. In order to improve rotor efficiency, airfoil efficiency needs to be maximized while making sure that the drag divergence boundaries and maximum lift

performance do not deteriorate. Airfoil sections are the fundamental building blocks of aerodynamic performance of rotors, and an exercise in improving rotor performance is directly linked to improving airfoil performance. Using wind tunnel tests in Ref. [221], the FishBAC mechanism was demonstrated to be aerodynamically more efficient compared to an airfoil with an equivalent size TEF because of a more streamlined, continuous aft profile. 2D quasi-steady CFD analysis in [16] also confirmed that camber morphing resulted in improvement in airfoil aerodynamic efficiency.

The concept of using smooth deformation of the airfoil profile using camber deformation rather than a discrete trailing-edge is not necessarily new. Ref. [150] investigated the effect of deforming the camber of the entire airfoil section, and not just the aft 25%, which is the subject of the current work. The subject of investigation was a HART II-like rotor, with a NACA0012 airfoil instead of NACA23012, at  $\mu = 0.25$ . The blade aerodynamics, in this case, could not be based on airfoil tables obtained using 2D CFD simulations, but rather the potential flow theory-based formulation of Ref. [201] was used. Consequently, the effect of camber morphing on viscous drag could not have been captured. Overall, a reduction in mean rotor torque (i.e. power consumption) of 0.28% and about a 50% reduction in vibrations was reported. Ref. [82] studied a conformable airfoil design with a setup consisting of compliant mechanisms to allow deformation of the airfoil profile for rotary-wing applications. While Refs. [69] and [227] report the experimental test campaign at Eurocopter involving rotor tests with discrete active TEF, a trailing-edge deflection concept was also involved in preliminary investigations [90]. In this concept the active section was integrated into the airfoil so that a more smooth deformation of the airfoil could take place. Similar work was also carried out in Ref. [240] for rotorcraft applications and later full-scale rotor analysis results were presented in Ref. [70].

In that context, it is worth noting that the nature of camber morphing generated by the FishBAC mechanism, at least qualitatively, is not unlike the aforementioned concepts. However, the current work differs from previous investigations in the scope of analysis undertaken and the underlying simulation tools that are utilized. The current work investigated the impact of active FishBAC actuation on rotor performance, vibratory loads, and aeroacoustic noise. For this purpose an extensive mid-fidelity framework was established using a combination of methodologies that, to the extent of the author's knowledge, was unique to the current work. The following sections discuss the different available modeling strategies with regard to simulating rotor wake physics and aeroacoustic emissions. Since these two aspects of the rotor analysis framework were under special focus within this work, it is worthwhile to discuss alternate modeling strategies that are also available in literature.

### 1.3. Rotor Wake Modeling

It is a fundamental phenomenon of fluid dynamics that the flow field around a finite wing or blade is rendered circulatory due to the generation of lift. Therefore, it is an inescapable fact that a thrust-producing rotor is operating in a 'sea' of vorticity introduced by its own blades. The effect of this wake vorticity can be accounted for by estimating the induced inflow on the wing using

the Biot-Savart law [109](Section 5.2.2), provided that the strength and position of all the vortex elements is known at every time step as the simulation progresses. Solution strategies that are capable of modeling this degree of fidelity of the flow field are generally more time-consuming than their counterpart strategies that solve for the effect of the rotor wake purely through momentum balance or inviscid flow approximations. A short description of a few inflow modeling strategies, relevant in the context of the current work, is provided next.

### 1.3.1. Momentum theory

In its simplest form, this theory states that the thrust produced by the rotor is a consequence of momentum imparted to the surrounding fluid in the opposite direction, and the corresponding velocity of the fluid is called the induced velocity. This leads to a uniform distribution of the induced velocity over the rotor disk, which may not necessarily conform to real flow conditions on a rotor. A number of extensions to momentum theory have been proposed, including combining it with a blade aerodynamics model to give the blade element momentum theory. Since no rotor vorticity or discrete physical blades are modeled, this theory is incapable of reproducing all their effects. Overall, this inflow model is capable of predicting the inflow distribution over the rotor disk reasonably well once any empirical parameters involved have been judiciously chosen. The advantage of this strategy is that it is computationally fast and, therefore, used to identify parametric trends and is usually adopted in preliminary design stages for quick estimation of rotor power consumption. Refs. [122](Chapters 3–5) and [161](Chapter 2) cover the basics of momentum theory in the form that is applied to analysis of thrust-producing rotors. Ref. [149] provides a detailed historical overview of the development of ideas that led to the momentum theories in this current form that is commonly used today. Additionally, it provides extensive computational background to put actuator disk modeling strategy in context by showing comparisons with real rotors. Even though this reference is dedicated to modeling wind turbines, the physical principles also apply to the thrust-producing rotors.

### 1.3.2. Dynamic inflow model

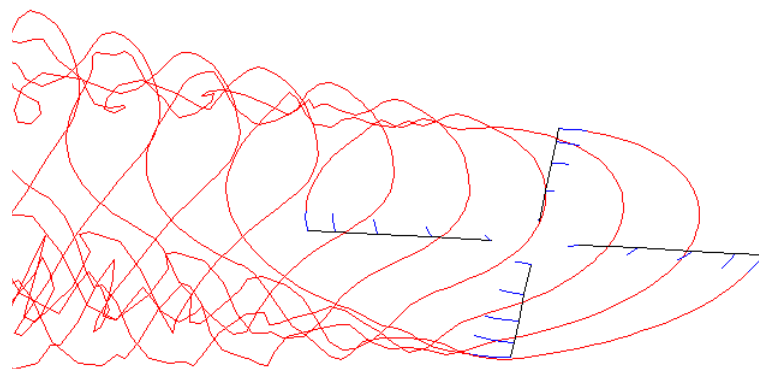
Dynamic inflow models are a class of rotor-induced inflow calculation strategies that relate the rotor aerodynamic loads to the wake flow velocities using hierarchical ordinary differential equations [205]. The Peters-He inflow model [202] is arguably the most popular dynamic inflow model. It is based on potential flow theory and, much like momentum theory, it cannot capture BVI phenomenon since it does not model vortices. Instead, it captures the dominant effects of wake vorticity by satisfying only the mass and momentum conservation laws for fluid flow. For this purpose, a number of modeling strategies have emerged in order to model the wake-induced inflow—free wake (linear and curved filaments), vortex lattice, panel methods, etc. The following section briefly describes the free wake model in order to contrast it with the vortex particle method that is used in this work. Later iterations of dynamic inflow models have incrementally incorporated more capabilities to model phenomena such as the effect of wake curvature, swirl velocity, ground plane obstruction (for a review, see Ref. [205]), multiple rotors [143], etc. However, vortex-based meth-

ods are more commonly adopted for rotor aeromechanical studies when computation speed, real-time simulation capability in particular, is not a high priority.

### 1.3.3. Free wake model

Modeling rotor wake distortion due to wake self-induced velocities is often required in order to obtain an accurate assessment of the wake-induced inflow velocity on the rotor blades. In such a scenario, it is common practice to employ free wake models for mid-fidelity simulations. These models are used to simulate the rotor wake in an inviscid manner, and the effects of viscosity on vortex generation, roll-up, and evolution of the vortices are modeled empirically. Ref. [122](Section 9.7) details a number of physics-based models available for this purpose. The discrete vortex element entities are modeled as filaments that move as material lines in a fluid. Figure 1.8 illustrates the wake of the four-bladed Bo 105 rotor in forward flight, simulated using the commercial code CAMRAD II.

The free wake formulation is based on the solution of a coupled non-linear system of equations that arise due to the dependence of the velocity of each filament on the velocity induced by every other filament [35]. The two major different formulations that exist include representation of the vortex filaments using curved elements, for example, in CHARM [39], or linear segments, for example, in Johnson's model [125] or Maryland Free Wake (MFW) [24]. CHARM uses curved vortex elements to model contours of constant vorticity [273] and has been demonstrated to be capable of modeling rotor wake effects for a number of different rotor configurations (see Ref. [211]). Ref. [222] presents a comparison of CHARM and MFW codes for a scaled rotor model and compares the peculiarities, particularly filament transient behavior, arising out of the different modeling strategies used in the two solvers.



**Figure 1.8.:** Free wake simulation of a four-bladed rotor in forward flight using the Johnson model in CAMRAD II (oncoming free stream velocity from right to left).

### 1.3.4. Vortex particle method

Particle methods were first introduced in Ref. [59] to solve the time-dependent Navier-Stokes equations for two-dimensional flow past a cylinder. The underlying assumptions include unbounded simulation domain (i.e., simulation domain boundaries extend to  $\infty$ ) and incompressibility. The method has since been extended to three-dimensional flows by including vortex stretching terms. The vorticity in the simulation domain is represented using Gaussian blobs with small support, and their strength is zero outside the support. Each vortex blob or particle interacts with every other particle. The biggest differentiating feature between the vortex particle and the free wake method is that the particles are not connected to one another. They convect with the local flow velocity, which is a superposition of the free stream flow velocity and the combined velocity induced by all the other particles.

The vortex particle method, or VPM, models the evolution of vorticity and belongs to the class of Lagrangian methods. This makes it particularly attractive for modeling wake systems since it does not require the generation of a mesh specific to the geometry of the model being investigated. This feature also makes them computationally inexpensive compared to grid-based Eulerian solvers since the domain of investigation of fluid flow around a body of interest is limited to the region where vorticity in the flow, represented using particles, dominates. Similar to free wake methods, the vorticity in the flow evolves in time based on the local flow velocity, which is a combination of the far-field flow velocity and vortex-induced velocity.

Some of the earliest studies involving rotorcraft simulations using VPM include Refs. [160] and [191]. In Ref. [160], a hovering rotor was simulated where the rotor was slowly started from rest, and a good correlation with experimental measurement data was established. In Ref. [191], the viability of the method was demonstrated using the NASA/ARMY/MIT ATR and the scaled UH-1H rotor, simulated in hover and forward flight conditions. Both the aforementioned studies were based on a panel method modeling of the blade aerodynamics. Recently, there has been a renewed focus on the application of vortex methods to rotor wake studies. Most of this work has been carried out in the field of distributed electric propulsion or eVTOLs, but investigations have also focused on the analysis of compound rotorcraft configurations [74]. The use of vortex particle formulation for modeling rotor wakes was largely revived through the work in Ref. [97]. They referred to their implementation as viscous VPM, but the physical processes modeled and the equations used to implement them are no different from those of vortex particle formulations traditionally referred to as VPM in literature. This viscous VPM wake modeling strategy has since been used to simulate rotors in hover, forward flight, ground effect [97], and multi-rotor configurations [98] where rotor-rotor interaction was shown to be reasonably captured by the wake solver. The potential for the use of vortex particle methods for dynamic stall and unsteady aerodynamics calculation was suggested in Ref. [28] and implemented for helicopter rotors in [252]. Vortex particle methods have been implemented in combination with panel methods in Refs. [54], [250] and [267]. Ref. [267], in particular, details the open-source rotor aerodynamics solver called DUST [2] that uses a combination of surface panel method and particles for the wake in order to generate a complete aerodynamic solution.



## 1.4. Rotor Aeroacoustics

Due to their ability to takeoff and land vertically, helicopters occupy a niche utility purpose for use in the military as well as civilian applications. Reducing helicopter noise has clear tactical advantages for military applications. Given that civilian applications involve helicopters operating over cities, greater community acceptance is likely if quieter operations could be ensured. Excessive rotorcraft noise remains an issue that needs to be addressed by rotary-wing community for greater acceptance in society. Ongoing industry excitement and intrigue over eVTOLs, envisaged as a ubiquitous mode of intra-city transport, has only brought on additional scrutiny to the noise generated by lifting rotors.

Fixed-wing aircraft generally tend to rely on a number of noise control measures that work towards reducing the noise at the source where it originates, i.e., aerodynamically designing the engine and fan for reduced noise, as well as controlling it thereafter using features such as engine cowling design and noise-absorbing rotor casings [272]. Unlike their fixed-wing counterparts, rotary-winged aircraft rely exclusively on mechanisms that can lead to reducing the noise at the source itself. A helicopter's main rotor can be a major source of noise in conventional designs. It is, therefore, natural that most efforts to reduce the acoustic footprint of helicopters have focussed on some form of modification of the main rotor itself. At normal cruise flight conditions, helicopter main rotor noise is primarily due to displacement of the air due to the finite thickness of the airfoil sections and due to pressure perturbations from blade airloads. The former contributes to the thickness noise, and the latter to the loading noise. BVI noise is a special case of loading noise where high-frequency changes to the blade loading, which occur from close passage of the tip vortices, act as a major contributor to overall rotor noise. Both passive design modifications and active rotor control strategies have been explored to reduce rotor noise emissions in different operating conditions.

Ref. [100] provides a good overview of the different studies that investigated the physics of rotor noise reduction. It summarizes different full-scale and scaled rotor tests that were conducted for this purpose. This includes the Bo 105 rotor IBC tests in the NASA Ames 40- by 80-Foot Wind Tunnel as well as the HART I rotor tests in the DNW. The paper concludes by ruling out some of the more obvious solutions, such as decreasing rotor RPM or blade thickness, that could help reduce the acoustic footprint of helicopter rotors. It rather emphasizes the following three approaches—path planning, passive blade shape optimization, and active rotor control. While the last approach forms the subject of this work, the first and second approaches are beyond the scope of this dissertation. However, a brief background of passive design approaches to reduce rotor noise is provided since it stresses the advantage of active control designs over passive design solutions. Since this report, the HART II rotor test campaign has successfully demonstrated the ability to reduce rotor noise using HHC [256]. Rotor noise measurements were also part of a number of active rotor test campaigns in the US—for example, the SMART rotor [144], the UH-60A rotor with IBC [190], S-76 rotor with HHC [145], etc. The acoustic benefits measured during these test campaigns have already been summarized in Sec. 1.2.

Passive rotor noise reduction techniques have focussed on blade designs which help lower the rotor acoustic footprint. Ref. [275] describes the ERATO double-swept blade design that has been

put into production at Airbus as the Blue Edge blade (see Fig. 1.9). The design reduced the impact of blade-vortex interactions, and consequently, lower noise was generated in BVI conditions. The acoustic benefits of a novel rotor with modulated blade spacing were studied in Ref. [49]. The motivation behind that investigation was to spread the rotor acoustic energy over a wider spectrum compared to a uniformly spaced rotor. While some improvements in rotor acoustics were shown using an analytical study, significant performance losses arising from rotor blades with uneven spacing were reported. While not reported in that study, it is expected that the rotor hub vibration resulting from uneven blade spacing would have to be critically examined as well. Subjective tests on participants performed in a companion study [261], using digitally constructed audio signals, failed to corroborate the acoustic benefits reported in Ref. [49]. While not strictly falling under the category of passive rotor design, the preliminary investigation of Ref. [232] is also worth mentioning. Here, using a simple analytical approach, the potential of 'X-force' or longitudinal force controllers was investigated. It was shown that they influence the tip-path plane of the rotor disk during descent approaches and help avoid rotor noise due to blade-vortex interaction.

Modern rotor designs such as the Blue Edge have shown promising advancements toward reducing acoustic noise and vibratory loads [215][255]. However, these are still passive rotor designs and their performance cannot be tweaked at a given advance ratio. Based on the results reported in Ref. [215], the Blue Edge rotor is more efficient compared to existing designs in hover only at high blade loadings. In forward flight, it exhibited no performance improvement over the baseline reference rotor.



**Figure 1.9.:** Blue Edge rotor blade for passive noise reduction [14]. Photo taken by Nick Isaacs [CC BY-SA 4.0 DEED].

During normal cruise flight conditions, the highest acoustic noise is generated in the plane of the rotor, with blade thickness noise being the major contributing component. Ref. [88] presents the first computational study of its kind, exploring the possibility of reducing helicopter thickness noise by generating ‘anti-noise’ pulses using on-blade active controls. Using linear acoustic theory, the FW-H equation was converted to an explicit algebraic equation for a rotor [87]. Upon exploring the functional behavior of the different parameters using simplified equations, it was found that the effect of in-plane thickness noise can be completely eliminated using in-plane force (drag) increase on the advancing side of the rotor. This is because the characteristic negative thickness acoustic pressure pulse, which is particularly strong on the advancing side of the rotor due to high Mach number, can potentially be nullified by the pressure pulse from harmonic in-plane force generation. Full-scale rotor experiments in Ref. [248] using on-blade control have reported a reduction of low-frequency in-plane rotor noise by exploiting essentially the same physics as laid out in Ref. [88]. Optimization strategies were presented in Ref. [292] to obtain an optimal on-blade loading solution that minimizes the rotor noise over a range of the rotor azimuth instead of just minimizing it for a single observer. The study, however, did not account for the loading due to the baseline rotor and just used the delta loading input due to the on-blade active mechanism in its formulation for the loading noise component. Since active blade actuation can significantly affect the baseline trim state of the rotor, it appears necessary to include the effect of the overall blade loading for a more accurate solution. The effect of active actuation on blade thickness noise due to changing section profile needs to be included as well.

The use of direct CFD numerical simulation for long-range external acoustics radiation is generally dismissed due to the challenges associated with the modeling process. Acoustic noise is caused due to aerodynamic perturbations, which are less than 0.01% of the free stream pressure. So, any errors incurred due to numerical dissipation/dispersion can be of the same order of magnitude as the perturbations, or even greater. This issue is less conspicuous in conditions where the acoustic signal is stronger, for example close to the rotor, and a better ‘signal-to-noise ratio’ is obtained. Another challenge in CFD also involves satisfying the inherently large spectral bandwidth requirement and addressing the disparity between acoustic pressure perturbations and mean flow pressures. This necessitates a grid spacing constraint in CFD implementations that must be sufficiently small to represent the smallest wavelength (i.e., highest frequency) of interest associated with the noise sources. However, smaller grid spacing leads to a large number of grid points. This was highlighted in the simulations of the Boeing SMART rotor as well as the free flight test simulation of the MD-902 helicopter rotor in Ref. [246]. The direct CFD simulation was only capable of capturing low-frequency sound; mid-to-high-frequency content could not be predicted due to the aforementioned modeling and grid constraints.

An alternative approach to direct CFD acoustic simulations is to simulate rotor aerodynamics using CFD and either prescribe blade motion using known measurement data or couple the framework to a CSD code. The trimmed rotor simulations obtained using either procedure can then be used to carry out aeroacoustic computations using the Ffowcs Williams-Hawkings (FW-H) equation [80]. This is a differential equation obtained from an exact rearrangement of the Navier-Stokes equations. A number of different strategies have been proposed to solve for rotor noise based on the FW-H equation, but the most popular strategy in the context of rotor noise investigations has been the formulation proposed in Ref. [79]. Additionally, formulations proposed in Refs. [158] and [101] are also commonly used. Their advantage derives from the fact that the differential

equation form of the FW-H equation is converted into an integral form, which is easier to solve. Once physically meaningful information, such as the pressure distribution over the surface of the noise source, relative flow velocity, etc., is known, time-domain acoustic pressure solutions can be obtained with reasonable accuracy. This strategy has been shown to yield results on par with CFD direct acoustic predictions, especially in the case of an isolated rotor; for example, see Ref. [26]. HART II rotor noise predictions were also made with good accuracy using prescribed blade motion+CFD aerodynamics and coupled CFD/CSD strategy in Refs. [291] and [43], respectively. Based on results published in Ref. [210] for the five-bladed full-scale MDART rotor, CFD/CSD coupled simulations together with the integral FW-H equation formulation were also able to capture the acoustic time histories very well.

Some of the difficulties associated with direct CFD simulations for acoustic predictions have already been detailed above. The strategy of using one of the integral formulations of the FW-H equation together with CFD/CSD coupled simulations can also be rendered impractical when a large number of simulations are desired—for example, the influence of geometric or control variables via parameter sweeps. For this purpose, the ‘compact loading’ assumption has long been used to predict rotor noise using simulations based on the lifting-line model. Within this modeling framework, the loading acoustic pressure integral equation is modified to include integration only over the spanwise component of the blade [48]. In Ref. [50], it was shown that this was a reasonable assumption especially for predicting loading noise away from the rotor tip path plane. Given that rotor comprehensive analyses usually employ a lifting-line model for obtaining blade aerodynamics solutions, the compact loading assumption is a natural strategy to obtain noise emissions from rotor aeromechanic simulations conducted using a mid-fidelity simulation setup.

A number of studies that have successfully employed the compact loading integral formulation of the FW-H equation include Refs. [134], [51] and [298]. In Ref. [298], for example, an FW-H equation-based solver was used to predict the acoustic pressure using data from HOST+UPM coupled simulations. The baseline HART II rotor flight state in BVI condition, as well as the full-scale Bo 105 rotor in descent, climb, and level flight conditions, were modeled, and the acoustic pressure prediction matched very well with measurement data. A previous limited investigation carried out by the author using CAMRAD II and PSU-WOPWOP also used the compact loading FW-H formulation. It showed promising results towards using active camber morphing to reduce rotor noise footprint. An extensive post-processing and visualization framework called *HeliNoise* was created for this purpose and has since been made open source [9].

## 1.5. Objectives of Present Work

Investigating complex rotor aeromechanical phenomena with high-fidelity CFD/CSD coupled rotor simulations remains challenging. The process is hampered by the time-consuming process of setting up the simulation framework as well as the slow computational speed, making routine use of these advanced frameworks impractical. Resorting to low-fidelity, but fast, analysis methods is not ideal since the physics corresponding to unsteady aerodynamics or the structural elastodynamics may not be accurately captured. Even with mid-fidelity analysis tools, it is prudent that

appropriate modeling strategies be adopted so that the relevant dominant physical effects are captured. For example, a prescribed wake-based solution may lead to acceptable accuracy of global quantities like rotor forces, moments, power, etc., but considerable inaccuracies could result in oscillatory blade loads and airloads distribution. This, in turn, can also lead to inaccurate aeroacoustic noise predictions.

The objective of the present work was to propose and apply state-of-the-art rotor mid-fidelity analysis methods to investigate the power requirement, hub vibration loads, and aeroacoustic noise emissions of passive and active rotors. The active rotor mechanism studied here is a novel camber morphing concept called FishBAC. As detailed earlier in Sec. 1.2.5, there have been past investigations into active concepts that work via morphing of the blade section camber on helicopter rotors. However, the FishBAC mechanism stands out in contrast to those concepts. It is based on a biologically inspired compliant structure that makes it capable of large, continuous changes in the airfoil camber and, consequently, in its aerodynamic characteristics [287]. Previously, limited scope investigations in this direction have been carried out by the author using the commercial comprehensive rotor aeromechanics solver CAMRAD II [140][141][152][153]. An entirely new simulation toolchain was established in the current work, only parts of which were presented in an earlier study by the author in Ref. [154].

In this work, the impact of the active camber morphing concept on rotor aeromechanics and noise emissions was studied using isolated rotors as well as a coaxial rotor. Special attention was paid to model the rotor wake and blade section unsteady aerodynamics accurately. A novel vortex particle formulation was implemented for this purpose and coupled to the comprehensive analysis solver. This enhanced wake modeling strategy also served the dual purpose of capturing interaction across rotor wake systems, such as in the case of coaxial rotors. The unsteady aerodynamics effects refer to the effect of shed vortices due to the high-frequency actuation of blade camber on the active rotor or the effect of BVI. Therefore, in addition to a variety of wing and rotor cases with active camber morphing, the benchmark HART II rotor was also modeled in order to assess the potential of the current method to model BVI. While investigating the Bo 105 rotor, a detailed rotor multibody setup was defined together with the rotor control system in order to capture the effect on pitch link loads. This was done in order to correctly capture dual path load transfer from the blades to the non-rotating rotor hub.

With the different rotor and wing models in various operating conditions studied in this work, the predictive capability of the simulation methodology used herein was extensively validated. In addition to this, a post-processing aeroacoustics analysis framework was created to predict the noise emissions of active and passive rotors. The objective here was to validate the analysis framework using baseline rotor measurement data and use it to predict the influence of active camber morphing on rotor noise emissions. Overall, the complete mid-fidelity aeromechanics-aeroacoustics toolchain established in this study has been sufficiently tested. It can serve to reliably replace some aspects of time-consuming and expensive wind tunnel and flight tests for new rotor systems, both passive as well as active designs.

## 1.6. Key Contributions of Present Work

In pursuit of the ultimate goal of active rotor investigations, the current work details the steps that were undertaken to build simulation toolchains, incorporate new methodologies for robust implementation, and include programming interfaces for computationally fast execution. The following details key aspects of the current work that have helped advance the state of the art—

1. A vortex particle formulation, for rotor and wing wake analysis, was implemented and extensively verified using results available in literature. The particle solver was implemented to run on graphics processing units (GPUs) and has been made publicly available by the author. To the best of the author's knowledge, this is the first such implementation of a freely available rotor wake solver that is capable of running on GPUs.
2. The vortex particle solver was explicitly coupled to the lifting-line theory-based rotor multi-body solver, Dymore, for an enhanced rotor aeromechanics analysis framework. This augmented framework is referred to as Dymore+VPM throughout this work. In order to validate this simulation framework, incrementally complex aerodynamic scenarios involving pitching airfoils and finite wing cases were used. This helped validate the ability of the wake model to capture the effect of high-frequency actuation of the FishBAC concept as well as unsteady airfoil/wing motion. Such an exercise is unique to this work as the cases were chosen to systematically render confidence in the solution methodology as well as in the coupling strategy adopted.
3. Detailed multibody models of the rotor control system and flexible blades have been set up in order to accurately simulate both active and passive rotor designs. Such a comprehensive representation of rotor systems is generally not required when modeling isolated rotors. However, this was done in the current work to correctly capture dual path load transfer between the rotor blades via the pitch links and the rotor shaft.
4. The two different simulation frameworks used in this work—standalone Dymore and Dymore+VPM—have been extensively validated using a number of different rotor cases. Experimental measurement data from the full-scale Bo 105 rotor, the scaled HART II rotor, and the UT Austin two- and four-bladed isolated rotors in a diverse set of operating conditions were used to validate different aspects of the modeling frameworks. To the extent of the author's knowledge, this is the first time a thorough validation has been carried out using full-scale Bo 105 rotor measurement data from the 1994 test campaign in the NASA Ames 40- by 80-foot wind tunnel. Prior studies involving the Bo 105 rotor have been limited and only focused on a small set of test results from that campaign.
5. As part of this work, a modular aeroacoustics analysis and visualization framework was established in conjunction with the rotor noise solver PSU-WOPWOP. This framework, which is called *HeliNoise* and has been made open source, seamlessly takes the relevant output from comprehensive analysis simulations, carries out necessary post-processing, and gives acoustic pressure fluctuations at any given observer location.

6. A complete and robust aeromechanics-aeroacoustics analysis toolchain has been established that is capable of accounting for the effect of multiple rotors and interactional wake effects. A number of validation cases have been presented to showcase the efficacy of the entire mid-fidelity toolchain. With limited modifications, this toolchain can be used for analysis of future rotors, both active and passive designs.

## 1.7. Organization of the Dissertation

This dissertation is organised into seven chapters and four appendices. The outline is as follows.

Chapter 1, the current chapter, describes the background and motivation behind this work. It summarizes the state of the art in research on rotor aeromechanics analysis. First, a concise historical development of the most relevant active rotor concepts and their effects on rotor performance, loads and noise is provided. Next, the different rotor modeling frameworks are discussed with particular attention to the wake aerodynamics and aeroacoustics analysis. This is done due to the special focus on these two aspects of rotor physics modeling within this work. Thereafter, the objectives of the current work are laid down together with a brief overview of the different investigations undertaken herein. Finally, the key contributions of this dissertation that add novelty to this work have been stated.

Chapter 2 begins with a description of the comprehensive analysis code Dymore that is used as the rotor aeromechanics solver. The different component models that make up the entire code are delineated, including models for solving the blade aerodynamics, 2D unsteady aerodynamics, and wake-induced inflow velocity. This was done in order to establish an accurate understanding of the component models as well as to recall the underlying physics when discussing the results, presented later in Chap. 5. Any corrections, made to the existing Dymore source code for this work, have also been detailed. Lastly, multibody models of the different wings and rotor systems analyzed within this study are described.

The work described in Chap. 3 is an attempt at improving the fidelity of the comprehensive analysis solver by incorporating an improved rotor wake model. For this purpose, a vortex particle method-based (VPM) framework is described that is used for modeling vorticity in the wake of lifting bodies. The theoretical formulation of the method is laid down in detail for completeness. The test cases used to verify the VPM setup are described, and the results are presented. Finally, the approach adopted to establish coupling between the wake solver and the multibody rotor aeromechanics solver is elaborated. This coupled framework is referred to as Dymore+VPM.

Chapter 4 describes the aeroacoustic analysis framework between the FW-H equation-based rotor noise solver PSU-WOPWOP and two different simulation frameworks that form the subject of this work—standalone Dymore simulation framework detailed in Chap. 2 and the improved-fidelity coupled framework Dymore+VPM obtained in Chap. 3. The post-processing carried out using output from rotor aeromechanical simulations and its organization into suitable input files for the acoustic solver is also described.

Chapter 5 uses the complete rotor aeromechanics-aeroacoustics analysis framework established in the preceding chapters and validates it using a number of application cases - isolated wings, isolated rotors, and a coaxial rotor. Isolated wing cases include an elliptical wing at a fixed angle of attack, pitching+morphing 2D airfoils, and a pitching rectangular finite wing. These cases were all structurally modeled as rigid in order to validate the aerodynamics of the coupled Dymore+VPM framework by comparing the results to simple analytical models as well as measurement data. Next, the full-scale Bo 105 rotor was modeled, and a number of rotor simulation quantities were used to validate the modeling framework. In addition to that, code-to-code comparisons were made between predictions made using the two simulation frameworks used in the current work. In lieu of experimental measurement data for full-scale helicopter rotors with active camber morphing installed, this validation exercise was meant to render confidence to the active rotor results. The HART II rotor case was used to further identify the potential of the framework to capture rotor aerodynamics in BVI conditions. The acoustics analysis framework was validated using measurement data available from the HART II rotor test campaign. Using the validated isolated Bo 105 rotor simulation framework, a parametric investigation was carried out using the active FishBAC concept to assess its acoustic and aeromechanical impact on rotor operation. Finally, an active rotor study was conducted using a coaxial rotor in order to identify the potential of camber morphing to reduce vibratory loads at blade passage frequency and the associated aeroacoustic noise.

Chapter 6 summarizes the most relevant outcomes from the validation studies as well as simulation results presented in Chap. 5. The prominent capabilities of the entire analysis framework are identified, based on the quality of match obtained with experimental measurements or analytical models, and highlighted. Finally, key conclusions from the entire work are also summarized.

Chapter 7 brings to light some of the difficulties encountered during the current work and suggestions are presented with regard to improving the robustness of the analysis framework. Furthermore, recommendations are made about additions that can be made to the current framework to carry out mid-fidelity analysis for general/complex applications with improved accuracy.

Appendices A-C provide relevant details regarding the construction of the respective multibody rotor models. Appendix D contains additional results, obtained as part of the verification of the VPM solver, corresponding to which no data is available in the literature.



## 2. Rotor Comprehensive Analysis

Analysis of rotor performance requires knowledge of the aerodynamics as well as structural dynamics of the rotating wings or blades. Fundamentally, such a problem is one of fluid-structure coupled interaction and is generally referred to using the term ‘comprehensive analysis’. Ref. [122] defines this term to mean computer programs that are capable of simulations involving rotorcraft performance and trim, stability, vibrations, noise, flight dynamics, etc. Ref. [155] further provides an interpretation of what is expected of such analysis frameworks by tracing the origins of different codes that are considered comprehensive analysis solvers and their capabilities.

Ref. [103] states that in order to achieve good correlation with experimental measurements, the following are necessities relevant to comprehensive analysis—accurately measured blade properties, structural loads and airloads, and an analysis framework that solves the problem governing equations correctly. Any errors incurred in one of these criteria will have an influence on the quality of the correlation between simulation output and measurement data. According to Ref. [126], the process of construction of an effective comprehensive analysis model entails, among other things, refinement to accommodate shortcomings in the model compared to the experimental setup. This is not limited to adjustments in numerical parameters but sometimes extends to the rotor description itself. A major simplification is afforded when studying rotors in isolation compared to the full helicopter system [172]. In rotorcraft research, this is accomplished by mounting rotor systems on nearly rigid rotor test rigs, allowing investigation of the rotor structural dynamics and aerodynamics in great detail. The structural dynamics of the test rig fixed system have been shown to result in better prediction of rotor loads in Ref. [297]. However, this level of modeling detail is generally not included in mid-fidelity analyses or even most high-fidelity CFD/CSD analyses.

The comprehensive analysis solver Dymore [32], developed by Prof. Olivier Bauchau and his students, was used in the current work to model and analyze rotor aeromechanics. It has a wide variety of modeling capabilities for structural dynamics in particular so that complex multibody structures, can be modeled in Dymore, and dynamic analysis can be conducted. By judiciously using a set of rotating and non-rotating components, facilitated through a combination of constraints and joints, the entire rotor system setup can be simulated. Forced system response, as well as eigenvalue analyses, are possible. The former is used to obtain steady-state solution of the trimmed rotor setup, and the latter is used in order to verify the blade structural properties using natural response frequencies and mode shapes. The relevant modules within the Dymore analysis framework include C81 format airfoil aerodynamic characteristics, 2D unsteady airfoil aerodynamics and dynamic stall loads corrections, and 2D and 3D potential flow theory-based inflow models. For the structural dynamics solution, a library of fundamental multibody elements, including beam and cable modeling, is made available. The entire formulation is solved using

nonlinear finite-element methods. The equilibrium equations are assembled in a global cartesian frame of reference, and the constraints on the degrees of freedom of the multibody elements are modeled using Lagrange multipliers. This leads to a sparse representation of the system of equations even for arbitrarily complex topologies, thereby allowing the adoption of sparse solvers from FEM analyses [31].

Dymore is employed in industry [110][184] as well as academia [17][183][71] for conducting rotorcraft simulations. It has been used to model tiltrotor designs [239], scaled model rotors such as HART II [195], bearingless rotors [61], articulated rotors [159, 219, 177] etc. Dymore has also been used for active rotor investigations, including active twist rotor [242], and active TEFs [225, 71]. The internal aerodynamics capabilities within standalone Dymore are fairly limited and, therefore, are often extended by coupling it to external solvers for improved results—for example, Refs. [196, 213] and Refs. [225, 194] coupled Dymore to CFD and free wake solvers, respectively. This is a strategy that has also been employed in the current work, where special attention is paid to the unsteady aerodynamics and wake modeling of the rotor with the objective of capturing the high-frequency unsteady effects of active rotor operation. This is partly described in Sec. 2.2 and in the following chapter. Based on the usage in Ref. [67], the following convention was adopted throughout this work—blade loads refer to structural dynamic loads, airloads is used to refer to aerodynamic forcing on the blades, oscillatory or vibratory loads refer to high-frequency blade loads or airloads.

This chapter provides details of the comprehensive analysis framework, Dymore, that was used in the current work. Section 2.1 provides a brief description of the solution strategy adopted to solve the flexible blade dynamics. In Sec. 2.2, a concise overview of the airfoil tables-based lifting-line theory approach is provided. This is used to solve for the quasi-steady blade aerodynamic loads and requires the wake-induced inflow at the blade section as input. The latter is separately obtained using an inflow model that is detailed in Sec. 2.3. The different rotor models investigated in this work were trimmed using the Jacobian-based approach highlighted in Sec. 2.4. Finally, Sec. 2.5 describes the different wing and rotor multibody models studied in this work, together with the relevant geometric details and the reference frames employed.

## 2.1. Blade Structural Dynamics

Helicopter rotor blades tend to be highly flexible in nature due to their slender design. Therefore, it is important to solve for the blade structural dynamics in order to correctly predict the dynamic loads. Complete 3D FEM analysis of the rotor blades could be achieved by coupling the multibody model to an external FEM solver. A number of standalone software are available that are capable of delivering this objective, such as NASTRAN, Ansys, etc. Recently, there has been some success in demonstrating a novel periodic 3D FEM solver developed specifically for rotors exploiting the periodicity of rotor response to speed-up calculations [197]. When applied together with a CFD solver, the framework is powerful enough to deliver truly high-fidelity results, including detailed 3D unsteady wake results and 3D dynamic stresses [198]. Such results cannot be captured even by traditional CFD/CSD coupled frameworks since the ‘CSD’ component of such frameworks re-

lies on comprehensive analysis solvers that usually only solve the 1D beam equations. In fact, rotorcraft simulation studies are almost always carried out by solving the rotor blade structural dynamics using a 1D beam representation of the blades.

The methodology behind the structural dynamics solution is based on the premise that the full 3D elastic blade problem can be separated into a 2D linear cross-section analysis and a 1D non-linear beam analysis [206]. The 1D beam analysis relies on properties of the blade cross-section that are obtained using one of two ways. The first involves using a 2D FEM beam cross-section analysis tool, such as VABS [57], to obtain its mass and stiffness properties. The second involves obtaining these results via experimental measurements, for example, as demonstrated in Refs. [129] and [130] for the HART I and the HART II rotor blades, respectively. Analysis of the 2D section properties is a time-intensive process, but it only needs to be carried out once for a set of blades. Rotor aeromechanics analysis can then proceed by modeling the blade as a 1D beam. So the need to model the rotor blades using 3D FEM elements in order to obtain a good structural representation of the blades is bypassed without substantial loss in accuracy of the results. It is likely that this modeling strategy would be unsuitable for rotor blades that are not slender in character or have significant couplings across the different response axes. It was shown in Ref. [266] that this methodology is capable of delivering results on par with 3D FEM analysis as long as the blade beam does not have significant flap-torsion coupling, has an aspect ratio greater than  $AR = 10$  and the blade planform does not have large tip sweep or taper. High-fidelity CFD/CSD studies [34, 295] and even prescribed airloads studies [265, 66] carried out using 1D beam representations have shown good correlation with measurement data. Therefore, this strategy can be considered a valid approach for modeling convention rotor designs and has been adopted in the current work.

Once the blade 2D section properties are known, they are used as input within Dymore in order to solve the 1D blade beam model to obtain its response. The rotor blades are modeled as beams such that the volume of the blade is composed of translating the blade cross-section along a smooth reference line [33]. The beam reference line itself is parameterized using NURBS curves since they possess the unique characteristic that of staying invariant under rotation, translation, and scaling operations. The beam response is then obtained using the principle of virtual work and Eqs. 2.1 and 2.2.

$$\int_{t_i}^{t_f} \int_0^s (\delta \mathcal{K} - \delta \mathcal{V} + \delta \mathcal{W}) ds dt = 0 \quad (2.1)$$

$$\mathcal{K} = \frac{1}{2} \int_0^s \mathbf{u} \mathcal{M} \mathbf{u} ds; \quad \mathcal{V} = \frac{1}{2} \int_0^s \mathbf{e} \mathcal{C} \mathbf{e} ds \quad (2.2)$$

Here,  $\mathcal{K}$  and  $\mathcal{V}$  denote the beam kinetic energy and the strain energy, respectively, and  $\mathcal{W}$  is the work due to externally applied forces.  $\mathbf{u}$  and  $\mathbf{e}$  are vectors denoting the beam section velocity and strain components, respectively.  $\mathcal{M}$  is a 6x6 sectional mass matrix relating the linear velocity  $v_i$  and angular velocity  $\omega_i$  of the beam sections to the section linear momentum  $p_i$  and the angular momentum  $h_i$  components (Eq. 2.3). The entries within the  $\mathcal{M}$  matrix are based on the aforementioned beam sectional properties - mass, center of mass location, mass moments of inertia

along the different axes, etc. Similarly,  $\mathcal{C}$  is a 6x6 sectional stiffness matrix relating the sectional strains  $\epsilon_i$  and bending curvatures  $\kappa_i$  to sectional forces  $F_i$  and moments  $M_i$ . Additional kinematic relationships govern the interplay between the linear and angular displacement, velocity components, and the deformed beam curvatures. These kinematic relations are valid for arbitrarily large displacements and rotations, and hence, this beam model is referred to as the geometrically exact beam theory (GEBT). The GEBT is used in Dymore as well as in other popular comprehensive analysis tools such as CAMRAD II and RCAS [107](Page 20). Further details of the beam modeling framework implementation within Dymore can be referred from Ref. [32](Page 192), and the details of the theoretical basis of the GEBT itself can be referred from Refs. [33] and [108].

$$\begin{Bmatrix} p_1 \\ p_2 \\ p_3 \\ h_1 \\ h_2 \\ h_3 \end{Bmatrix} = \mathcal{M} \begin{Bmatrix} v_1 \\ v_2 \\ v_3 \\ \omega_1 \\ \omega_2 \\ \omega_3 \end{Bmatrix}; \quad \begin{Bmatrix} F_1 \\ F_2 \\ F_3 \\ M_1 \\ M_2 \\ M_3 \end{Bmatrix} = \mathcal{C} \begin{Bmatrix} \epsilon_1 \\ \epsilon_2 \\ \epsilon_3 \\ \kappa_1 \\ \kappa_2 \\ \kappa_3 \end{Bmatrix} \quad (2.3)$$

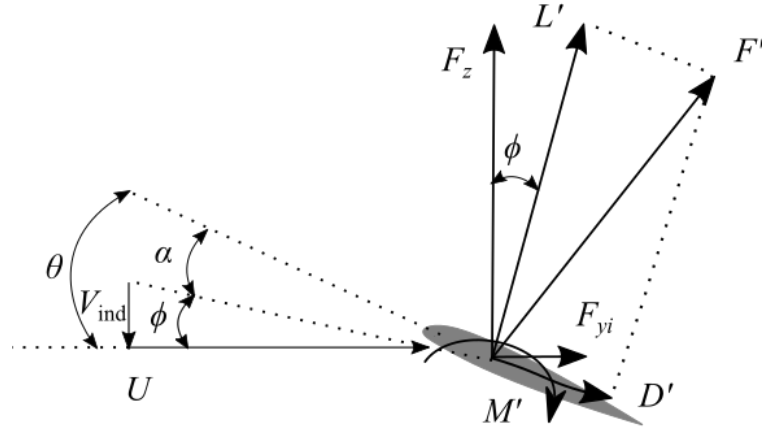
## 2.2. Blade Aerodynamics

As detailed in the preceding section, the slender geometry of rotor blades has important consequences towards simplifying the structural dynamics analysis. This characteristic, referred to as aspect ratio in the context of aerodynamics analysis, is also relevant to simplifying the blade aerodynamics analysis. Helicopter rotors comprise of sufficiently high aspect ratio blades such that the total aerodynamic solution of each blade can be split into a ‘wing model’ and a ‘three-dimensional wake problem’ [122](Page 307). Again, most well-known rotorcraft comprehensive analysis tools such as RCAS [104], CAMRAD II [124], FLIGHTLAB [72], etc., are known to also take advantage of this simplification. The wing model refers to the methodology of obtaining blade aerodynamic forces and moments, or airloads, at a given section of the wing or blade based on the local angle of attack at that section. This is also referred to as blade element theory in the context of rotary-wing analysis and is described in most rotorcraft engineering textbooks; for example, see Refs. [122], [161], and [84].

In order to obtain the angle of attack, the net oncoming flow velocity at each blade section is required, which in turn is the byproduct of rotor forward motion, angular rotation motion, blade elastic dynamic response, and the induced velocity due to vorticity in the wake. The contribution to oncoming flow velocity due to rotor forward motion and rotation of the blade is a straightforward kinematic addition that is taken care of by the multibody modules within Dymore. The blade elastic response is evaluated at each time step using beam analysis as described in Sec. 2.1. Usually, the effect of the wake vorticity is evaluated using a separate module within comprehensive analysis codes. In Dymore, the well-known Peters-He inflow model [202] is used and is detailed in Sec. 2.3. The quasi-steady implementation of the blade aerodynamics employed in the current work is given by Eq. 2.4. Here, the different components involved are also explained using

a schematic in Fig. 2.1.  $V_{\text{ind}}$  refers to the induced velocity at the blade quarter-chord due to circulation in the wake  $\Gamma_w$ , which in turn is a function of the history of bound circulation  $\Gamma$  on the blade.  $U$  is the net velocity magnitude at the given airfoil section due to blade kinematics as well as elastodynamics.

$$\frac{\Gamma}{\pi c} = \frac{U}{2\pi} C_l(\theta - V_{\text{ind}}(\Gamma_w)/U) \quad (2.4)$$



**Figure 2.1.:** Schematic of the aerodynamic flow conditions and aerodynamic loads at a typical blade section (looking outboard).

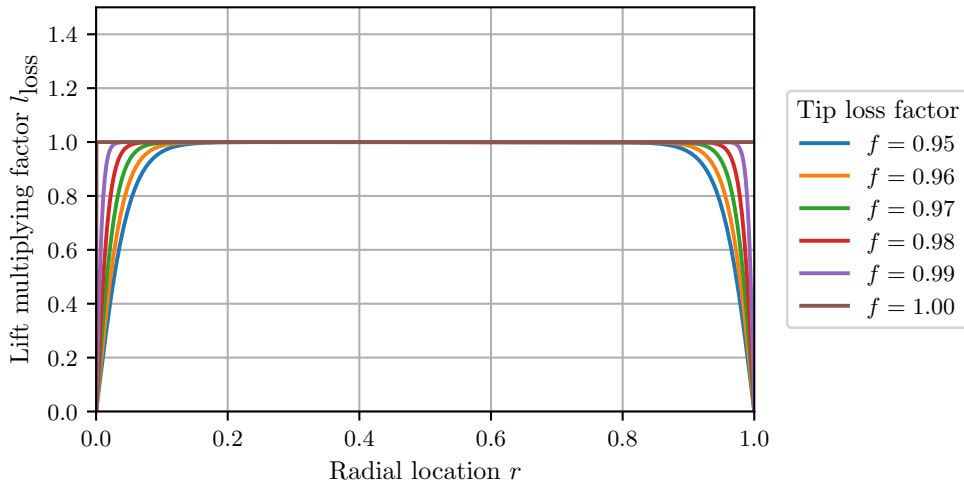
The blade aerodynamics were modeled using look-up tables populated with two-dimensional static airfoil aerodynamic coefficients of lift, drag, and moment. Airfoil tables in the standard C81 format are required where these aerodynamic coefficients are placed in a two-dimensional layout with the rows representing values at different angles of attack, and the columns denote Mach numbers (see Ref. [32](Page 64)). In order to cover the entire gamut of operating conditions encountered at any given blade section of a helicopter rotor over its entire operational envelope, the data within these airfoil tables is required for angles of attack  $\alpha = [-180^\circ, 180^\circ]$  and for Mach numbers from  $M = [0.0, 1.0]$ . In order to obtain a complete set of airfoil tables, it is common practice to use RANS-based CFD simulations of airfoils at different Mach numbers and angles of attack up to static stall. Beyond this, empirical expressions are used to augment the airfoil tables data since the aerodynamic behavior of airfoils beyond static stall is largely independent of the airfoil shape [161](Section 7.11.6). Ref. [166] showed that small differences in C81 airfoil table data could lead to differences in rotor aeromechanics results. For this purpose it is important to generate the aforementioned airfoil tables at the appropriate Reynolds number condition. In the current work, a number of different airfoils were used, of which only the NACA23012 airfoil of the full-scale Bo 105 rotor was generated in-house. This was part of the work carried out by Abdelmoula and Rauleder in Ref. [16]. Beyond that, no postdictive corrections were made to the airfoil tables in order to improve correlation with experimental measurement data. The aerodynamic characteristics of the different airfoils used within this work are shown later in Sec. 2.5 where the different multibody

models studied are described.

In order to ensure that the blade aerodynamic loads calculation using lifting-line theory was qualitatively congruent with the physical measurements, a tip loss factor was employed. This was done in order to facilitate lift dropoff towards the blade tip and is stated in Ref. [32](Page 45). Equation 2.5 shows the multiplying factor, which essentially leads to a loss in lift, that accomplishes this. Note that in the current study, Dymore source code was modified so that the tip loss function implementation was extended to also apply to the blade root. The parameter  $f$  in Eq. 2.5 is referred to as the tip loss factor; different empirical expressions exist that can be used to determine it for a given rotor. In this study, Eq. 2.6, obtained from Ref. [122](Page 63), and originally attributed to Ref. [282], was used to evaluate  $f$ . Figure 2.2 shows the effective variation of the loss in the lift, compared to the uncorrected lifting-line calculation, over the span of the wing for different values of  $f$  commonly employed for rotary-wing analysis.

$$l_{\text{loss}} = \tanh \frac{1 - r/R}{1 - f} \quad (2.5)$$

$$f = 1 - \frac{c}{2R} \quad (2.6)$$



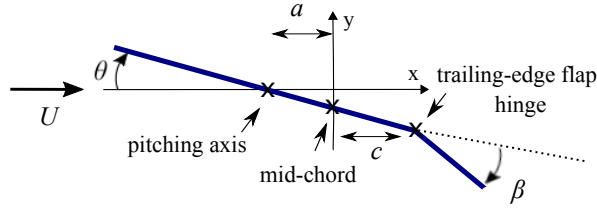
**Figure 2.2.:** Effect of blade tip loss factor on lift distribution over the wing span.

Based on Eq. 2.4 governing the blade aerodynamics, it is evident that knowledge of the quasi-steady modeling based on the airfoil tables uses the quarter-chord ( $c/4$ ) as the collocation point. So, if airfoil look-up tables are used, then the effect of the airfoil pitching about the feathering axis, i.e.,  $c/4$ , is not accounted for. In fact, if the rotor blades end up in elastic twisting motion during the rotor runup, then this twisting motion does not die down since no aerodynamic damping

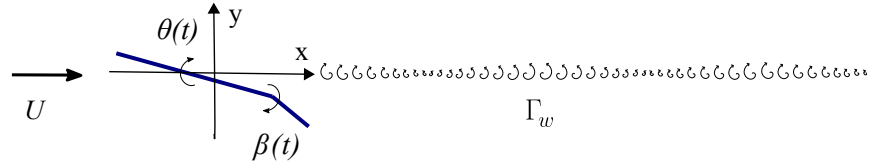
is afforded to a purely pitching oscillation of the blade about the feathering axis by quasi-steady aerodynamics modeling. However, aerodynamic damping would still exist for the lead-lag and the flapping motions. In any case, capturing the effect of unsteady blade motion on blade airloads is crucial to correctly predict their phase as well as their magnitude. It is common in comprehensive analysis tools to incorporate unsteady blade aerodynamic effects via analytical or semi-empirical theories. The 2D airfoil unsteady aerodynamics can also be modeled fairly accurately using indicial methods [96][127] or reduced order surrogate modeling techniques such as those shown in Refs. [187] and [169]. The latter modeling strategy is computationally intensive since it requires a number of high-fidelity 2D airfoil unsteady CFD simulations to be run. The obtained aerodynamic characteristics are then used to identify the terms within the transfer function relating the input unsteady motion to the output unsteady aerodynamic loads in the Laplace domain. The advantage of this strategy is the potential to also capture unsteadiness in airfoil drag. The current work utilizes two analytical theories—Theodorsen theory [263] and Peter’s theory for flexible airfoils [201]—in order to predict unsteady airfoil lift and moment. These are briefly detailed below.

### 2.2.1. Theodorsen theory

Theodore Theodorsen was the first to publish a complete and detailed solution to the problem of aerodynamic loads on an oscillating lifting surface with a trailing-edge flap [263]. The Theodorsen theory, or alternately the Theodorsen model, was developed in the frequency domain using potential flow theory and does not include unsteady viscous effects. In its most general form, it gives the variation of airfoil lift and moment using Eqs. 2.7 and 2.8. Figure 2.3(a) shows a schematic of the thin airfoil theory-based representation used within this theory, together with a description of the different parameters. The complete derivation is mathematically involved and requires meticulously solving a number of complex-valued integrals. Refs. [38] and [6] are a good source of understanding the derivation of the Eqs. 2.7 and 2.8. Ref. [6], in particular, contains a concise derivation as well as background information and exposition that is missing from the original work of Theodorsen, Ref. [263]. This theory only accounts for the pitching and flapping motions of the airfoil. The lead-lag motion of the airfoil, or alternately, the variation in the oncoming flow velocity, is not accounted for. Additionally, the wake vortices are assumed to lie along the  $x$ -axis, as shown in Figure 2.3(b), and not follow the trailing-edge tip as the airfoil undergoes pitching and flap actuation. Despite these simplifications, Theodorsen theory has found use in unsteady wing analysis due to the closed-form nature of the expressions for lift and moment obtained based on finite-state approximation of the deficiency function  $C(k)$ . It has been demonstrated to give a good match with experimental measurements in both phase and amplitude, especially for low reduced frequencies  $k$  [161](Section 8.7). In lieu of unsteady airfoil measurement data, this model was used in the current work to qualitatively compare the unsteady airfoil lift and moment against the higher fidelity wake modeling strategy proposed in the following Chap. 3. It is worth noting that an erratum in Ref. [200] has recently been published that highlights some of the mistakes in expressions present in Ref. [263]. None of the expressions relevant to this work were affected.



(a) Schematic of different parameters



(b) Assumed wake structure behind airfoil+TEF system

**Figure 2.3.:** Illustration of the modeled airfoil and wake features within Theodorsen theory.

$$\begin{aligned}
 L' = & \underbrace{\rho b^2 (U\pi\dot{\theta} - \pi b a \ddot{\theta} - UT_4\dot{\beta} - T_1 b \ddot{\beta})}_{\text{non-circulatory}} \\
 & + \underbrace{2\pi\rho U b C(k) \left\{ U\theta + b \left( \frac{1}{2} - a \right) \dot{\theta} + \frac{1}{\pi} T_{10} U \beta + b \frac{1}{2\pi} T_{11} \dot{\beta} \right\}}_{\text{circulatory}}
 \end{aligned} \tag{2.7}$$

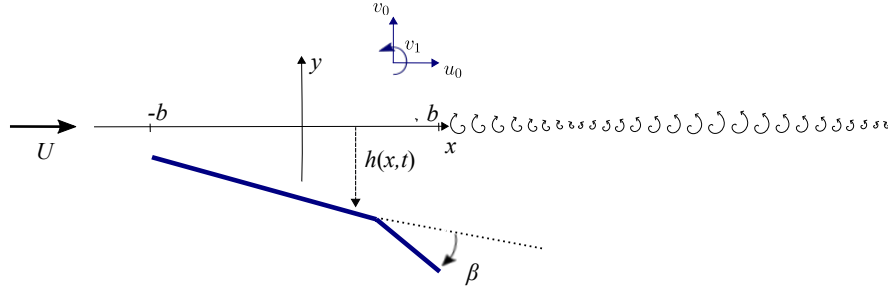
$$\begin{aligned}
 M' = & \underbrace{-\rho b^2 \left[ \pi \left( \frac{1}{2} - a \right) U b \dot{\theta} + \pi b^2 \left( \frac{1}{8} + a^2 \right) \ddot{\theta} + (T_4 + T_{10}) U^2 \beta \right]}_{\text{non-circulatory}} \\
 & + \underbrace{-\rho b^2 \left[ \left( T_1 - T_8 - (c - a) T_4 + \frac{1}{2} T_{11} \right) U b \dot{\beta} - (T_7 + (c - a) T_1) b^2 \ddot{\beta} \right]}_{\text{non-circulatory}} \\
 & + \underbrace{2\rho U b^2 \pi \left( a + \frac{1}{2} \right) C(k) \left[ U\theta + b \left( \frac{1}{2} - a \right) \dot{\theta} + \frac{1}{\pi} T_{10} U \beta + b \frac{1}{2} T_{11} \dot{\beta} \right]}_{\text{circulatory}}
 \end{aligned} \tag{2.8}$$

### 2.2.2. Peters 2D unsteady model

Motivated by the development of active rotor concepts, Ref. [201] proposed a more general theory of unsteady aerodynamics analysis. It is based on potential flow theory that accounts for arbitrary



deformation of airfoil cross-sections as well as variation in oncoming flow. It has been shown in Ref. [204] that Peters' results are similar to the finite-state Theodorsen theory, they separate the induced flow velocity estimation and the airloads calculation. This is a common theme across different theories proposed for unsteady airfoil analysis, such as Greenberg's theory for the case of a pulsating free stream [89], von Karman and Sears model for gust response [131], Küssner and Schwarz approach for modeling multi-element airfoils [156], etc. The Peters state-space airloads model fundamentally proceeds along similar lines as the Theodorsen model, even though the former is applicable for more general unsteady airfoil scenarios. While arbitrary motion of the complete airfoil system is modeled exactly, the local deformations of the coordinate system attached to the airfoil are assumed to be small. Figure 2.4 shows the relevant parameters used within this model. Arbitrary large motions are allowed in the  $x$ - $y$  frame, while the frame fixed to the airfoil (frame shown in blue) only permits small deformations. The net flow velocity at any point on the airfoil is obtained as a result of the velocity components  $u_0$  along the  $x$ -axis,  $v_0$  along the  $y$ -axis, and the component velocity  $v_1$  that is due to airfoil rotational motion leading to a velocity gradient over the chordwise direction.



**Figure 2.4.:** Illustration of the modeled airfoil and wake features within Peters theory.

The ability of the Peters model to simulate any airfoil motion makes it particularly attractive for rotary-wing analysis where the blade sections undergo flap, pitch, and surge (lead-lag) motions along with a harmonically pulsating free stream flow. In addition to using the unsteady Bernoulli's equation and the vorticity conservation equations, much like in Theodorsen's derivation, Peters theory proceeds to convert the resulting partial differential equations into a set of ordinary differential equations by casting the airfoil deformation using Glauert expansions (see Eqs. 2.9 and 2.10). The model assumes that principles of linearity apply since the relative airfoil deformations are assumed to be small, and the induced inflow velocity due to the shed vorticity can be written as Eq. 2.11.  $\lambda$  and  $h$  vary in the chordwise direction (denoted using  $x$ ) over the airfoil.

$$h = \sum_{n=0}^{\infty} h_n \cos(n\varphi) \quad (2.9)$$

$$\begin{aligned} x &= b \cos \varphi \\ -b \leq x \leq +b, \quad 0 \leq \varphi \leq \pi \end{aligned} \quad (2.10)$$

$$\lambda = \sum_{n=0}^{\infty} \lambda_n \cos(n\varphi) \quad (2.11)$$

Based on the derivation presented in Ref. [201], the bound circulation can be obtained as a result of airfoil motion parameters as given in Eqs. 2.12–2.14. Here  $u_0$  and  $v_0$  denote external flow perpendicular to the airfoil and parallel to the airfoil, respectively, in the airfoil-attached coordinate system.  $f_{\text{rev}}$  is referred to as the reverse flow parameter that is present to take into account reverse-flow effects by keeping track of where the Kutta condition is applied. For all the simulations carried out in this work, the Kutta condition is applied at the trailing-edge of the airfoil, and so in accordance with Ref. [201],  $f_{\text{rev}}$  is set to unity. Further details about the derivation of the Peters model can be obtained from Refs. [201] and [19]. In addition to that, Ref. [75] is a good resource for understanding the fundamentals of unsteady fluid modeling. Details about the implementation of the Peters model within the framework of Dymore are provided in Ref. [4]<sup>1</sup>.

$$\frac{\Gamma}{2\pi b} = -\alpha_{L=0} u_0 + f_{\text{rev}} (v_0 + \dot{h}_0 - \lambda_0) + \frac{1}{2} (v_1 + \dot{h}_1 - \lambda_1) + \frac{u_0}{b} \underbrace{\left[ f_{\text{rev}} \sum_{n=1,3,5}^{\infty} n h_n + \sum_{n=2,4,6}^{\infty} n h_n \right]}_{\Sigma} \quad (2.12)$$

$$\frac{\Gamma}{2\pi b} = \left[ f_{\text{rev}} U_3 + \frac{U_2}{b} \Sigma \right] + \left[ \frac{b}{2} \omega_1 + f_{\text{rev}} \dot{h}_0 + \frac{\dot{h}_1}{2} - \frac{\lambda_1}{2} \right] \quad (2.13)$$

$$\frac{\Gamma}{2\pi b} = [bUfC_l] + \left[ \frac{b}{2} \omega_1 + f_{\text{rev}} \dot{h}_0 + \frac{\dot{h}_1}{2} - \frac{\lambda_1}{2} \right] \quad (2.14)$$

### 2.3. Wake-induced Inflow

It is widely acknowledged that, in addition to the accurate unsteady airfoil aerodynamic characteristics, the effects of the three-dimensional rotor wake-induced inflow need to be correctly captured. This is composed of the ‘outer problem’ that was mentioned in the preceding section and is required to identify the blade section angle of attack. Dymore has a built-in implementation of the widely used Peters-He dynamic inflow model [202]. While the term ‘dynamic inflow’ is also used to refer to a wider class of finite-state inflow models [205], in the current work, it is used only to refer to the Peters-He model. The following describes the essential features of the Peters-He inflow model.

---

<sup>1</sup>These extra notes were obtained from the Dymore website which has now become defunct. These were collected by the author and are made available via the link in the references.

### 2.3.1. Peters-He inflow model

The Peters-He inflow model has been used successfully in a number of flight dynamics investigations, for example, Ref. [93], where the objective was to capture the global rotor unsteady inflow development. Ref. [30] demonstrated that the model is generally capable of capturing the variation of inflow over the rotor disk measured during experimental tests of a scaled rotor at different advance ratios. This inflow model continues to be of relevance to the flight dynamics community since it affords fast inflow calculations and is developed using a physics-based formulation [205]. The class of finite-state inflow models, under which the Peters-He model falls, are attractive for real-time simulation procedures due to their low computational expense and their ability to capture inflow perturbation due to changes in rotor thrust. The latter feature enables them to model transient flight states.

In general, the derivation of dynamic inflow theories is mathematically involved, and many assumptions that lead to simplifications are not thoroughly detailed in any one source. Ref. [99] serves as a helpful guide by providing intermediate steps and derivations that were skipped in the original publication Ref. [202], where the model was presented. Additionally, Refs. [186], [106], [27] and [105] were found to be helpful and are recommended. The development of actuator disk-based analysis given in Ref. [122](Section 11.4) and the references therein help trace the historical arc of contributions and changes to the analytical inflow theory over half a century and are also useful. The work of Kinner [138] is often cited as the source of dynamic inflow modeling strategy in the publicly available literature. This publication is in German and an English translation could not be found in open literature. Alternately, Ref. [223](Pages 249–251) could be consulted for a concise overview of the actuator disk modeling using acceleration potential methods, a subject that forms the basis of dynamic inflow strategies.

The following describes the mathematical framework of the Peters-He model in brief. An analytical solution of the rotor wake is not possible unless the rotor is modeled as an actuator disk [122](Page 308). An actuator disk is an infinitesimally thin abstract entity that is capable of sustaining a pressure difference but not a velocity difference. The Peters-He model builds on this concept by representing the rotor loading as a distribution of acceleration potential or pressure doublets on an actuator disk. The entire model is based on potential flow theory and gives inflow results based only on the loads acting normal to the rotor disk rather than the warped plane traced by the deforming blades. Some additional assumptions made within the model are compiled in Ref. [123](Page 301). Fluid behavior is governed based on Euler's equation, which can be written using Eq. 2.15 [223](Page 250). Here, the body force due to gravity has been ignored, and  $\mathbf{a}$  is the acceleration vector. Due to the incompressibility assumption, the rotor wake satisfies the divergence-free condition of Eq. 2.16. Based on Eq. 2.15,  $p$  ( $\rho$  is a constant) is the potential of the acceleration and can be denoted using the more conventional variable for potentials  $\Phi$ . This transforms Eq. 2.15 to Eq. 2.17, where all the quantities have been non-dimensionalized. Assuming that the rotor is lightly loaded<sup>2</sup>, the relation  $V_{\text{ind}} \ll |\mathbf{v}|$  is satisfied, as well as the thrust coefficient  $C_T \ll 1$  [173]. Using Eq. 2.18, this further simplifies Eqs. 2.16 and 2.17 to Eqs. 2.19 and 2.20, respectively. Eqs. 2.19 and 2.20 form the basis of dynamic inflow theories. Using the divergence operator on Eq. 2.20

---

<sup>2</sup>The concept of 'lightly loaded' rotors is also a recurring idea in rotor analysis using momentum theories because the wake contraction can be neglected for simplification without incurring much error [86](Page 255).

and the condition of Eq. 2.19 shows that the acceleration potential  $\Phi$ , i.e., pressure, satisfies the Laplace's equation Eq. 2.21.

$$-\frac{1}{\rho}\nabla p = \frac{D\mathbf{v}}{Dt} = \mathbf{a} \quad (2.15)$$

$$\nabla \cdot \mathbf{v} = 0 \quad (2.16)$$

$$\Rightarrow -\nabla\Phi = \frac{\partial\mathbf{v}}{\partial\bar{t}} + (\mathbf{U} \cdot \nabla)\mathbf{v} \quad (2.17)$$

$$\mathbf{v} = \mathbf{U} + \mathbf{v}' \quad (2.18)$$

$$\nabla \cdot \mathbf{v}' = 0 \quad (2.19)$$

$$-\nabla\Phi = \frac{\partial\mathbf{v}'}{\partial\bar{t}} + (\mathbf{U} \cdot \nabla)\mathbf{v}' \quad (2.20)$$

$$\nabla^2\Phi = 0 \quad (2.21)$$

Eq. 2.21 is a second-order differential equation with Dirichlet boundary conditions. The solution to any partial differential equation can be obtained either using an integral approach using Green's function or a separable variables approach. The choice of an ellipsoidal coordinate system helps obtain the solution of Eq. 2.21 in the form given by Eq. 2.22. The separable variables approach is adopted in the Peters-He model for solving the Laplace equation. Details about the solution of PDEs, and the Laplace equation in particular, can be referred to from Ref. [185](Chapter 5). Further information about the criteria for determining the coordinate systems in which a given PDE admits separable variable solutions can be obtained from that reference. Additionally, details about the nature of boundary conditions that ultimately help pick the most suitable coordinate system for a given problem are also provided. The boundary condition used to solve for the coefficients in Eq. 2.22 is the pressure distribution over the actuator disk. Ref. [186](Appendix 2.6) provides the intermediate steps leading from Eq. 2.21 to Eq. 2.22 as well as the form of the Legendre functions,  $P_n^m(v)$  and  $Q_n^m(i\eta)$ .  $C_n^m$  and  $D_n^m$  are arbitrary constants that are related to the pressure distribution and, by extension, the distribution of thrust, over the rotor disk. Using complete knowledge of the distribution of  $\Phi$  and integrating Eq. 2.20, the inflow velocity over the rotor disk is obtained in the form of Eq. 2.23 [99]. This transformation from Eq. 2.22 to Eq. 2.23 is commonly summarized using Eq. 2.24. It is worth noting that the representation of the basis Legendre functions across different sources—for example, Refs. [99], [186] and [202]—differ in some instances by a scaling parameter or change in sign of the basis functions. The final matrices of coefficients obtained, while consistent within the respective theoretical frameworks, are inconsistent across these different sources.

$$\Phi(v, \eta, \psi, \bar{t}) = \sum_{m=0}^{\infty} \sum_{n=m+1, m+3}^{\infty} P_n^m(v) Q_n^m(i\eta) [\tau_n^{mc}(\bar{t}) \cos m\psi + \tau_n^{ms}(\bar{t}) \sin m\psi] \quad (2.22)$$

$$w(r, \psi, \bar{t}) = \sum_{q=0}^{\infty} \sum_{j=q+1, q+3}^{\infty} \phi_j^q(r) [\alpha_j^q(\bar{t}) \cos(q\psi) + \beta_j^q(\bar{t}) \sin(q\psi)] \quad (2.23)$$

$$\begin{aligned}
[M] \begin{Bmatrix} \vdots \\ \left\{ \frac{\partial \alpha_j^q}{\partial \bar{t}} \right\} \\ \vdots \end{Bmatrix} + [L^c]^{-1} \begin{Bmatrix} \vdots \\ \left\{ \alpha_j^q \right\} \\ \vdots \end{Bmatrix} &= \begin{Bmatrix} \vdots \\ \left\{ \tau_n^{mc} \right\} \\ \vdots \end{Bmatrix}, \\
[M] \begin{Bmatrix} \vdots \\ \left\{ \frac{\partial \beta_j^q}{\partial \bar{t}} \right\} \\ \vdots \end{Bmatrix} + [L^s]^{-1} \begin{Bmatrix} \vdots \\ \left\{ \beta_j^q \right\} \\ \vdots \end{Bmatrix} &= \begin{Bmatrix} \vdots \\ \left\{ \tau_n^{ms} \right\} \\ \vdots \end{Bmatrix}
\end{aligned} \tag{2.24}$$

The problem of assessment of rotor wake-induced inflow boils down to identifying coefficients  $\alpha_j^r$  and  $\beta_j^r$  in Eq 2.23 by solving Eq. 2.24. These are also referred to as states or degrees of freedom of the model [260](Pages 8–14). Increasing the order of the model can improve the accuracy of inflow estimation. However, this improvement in the wake solution is restricted by the assumptions of Euler's equations. For example, no amount of increase in the order of the model will allow the Peters-He model to capture BVI effects since the inflow calculation is based on momentum balance rather than directly modeling the effects of vorticity. The theory is also restricted in terms of application to interacting systems, such as rotor-rotor interaction on coaxial rotors or propeller-wing interaction on wing-mounted propellers. It is worth mentioning that the Peters-He theory was only recently expanded to include mutual rotor interference effects [143]. In addition, several research groups have made progress towards including the effects of wake distortion, the effect of blockage due to surfaces, and the included the effect of swirl velocity. These refinements have been documented in Ref. [205] with appropriate references.

## 2.4. Trim

In order to validate the rotor setup, a number of trimmed rotor simulations at different advance ratios were conducted in this work. Active rotor investigations were carried out using a closed-loop strategy, i.e., the rotor was trimmed to the same conditions as the baseline passive rotor for comparison. To that end, the autopilot controller framework of Ref. [203], which has already been implemented in Dymore [32](Page 112), was used. This control law determines the configuration of the system in order to achieve given target outputs. It relies on identifying a Jacobian matrix, which is a derivative of the input controls with respect to the output measurements/configuration. In the current study, prescribed rotor forces and moments are used to achieve trim; alternately, rotor thrust and minimized blade flapping are also commonly used for rotor wind tunnel studies. Once the Jacobian is obtained, the control law drives the system to the desired state by proportionally changing the output by driving the input quantities to their targets.

Time-periodic systems often benefit from the harmonic balance analysis that takes advantage of the periodicity of the system response. In the case of a rotor these correspond to the deformed blade motion and the structural dynamic loads. However, Dymore uses implicit time stepping in

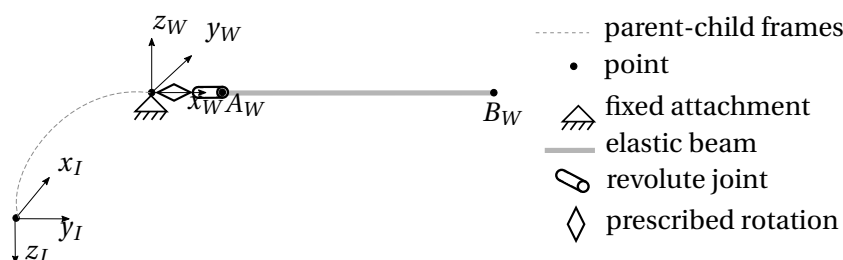
order to advance the simulation, so the periodicity in rotor dynamics was assumed after ensuring that the difference in cycle-to-cycle response was minimized after the controller had sufficient time to drive the system to the desired state. The rotor was then considered to be trimmed.

## 2.5. Model Description

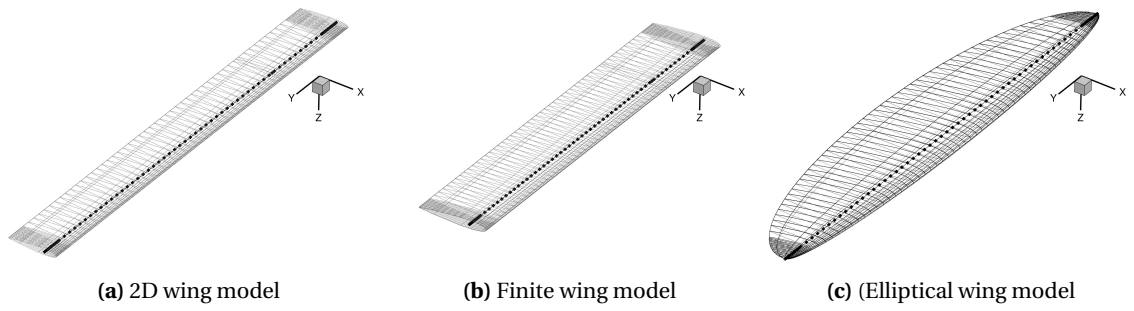
This section describes the multibody construction of the different rotor/wing models used in the current work. The ultimate goal of this work is to showcase the effect of active camber morphing on rotor performance, hub vibrations and noise emissions. Therefore, an approach was adopted whereby incrementally complex wing/rotor models were used to establish the validity of different simulation sub-models that make up the entire analysis framework. These are described below.

### 2.5.1. Two-dimensional wings and finite span wings

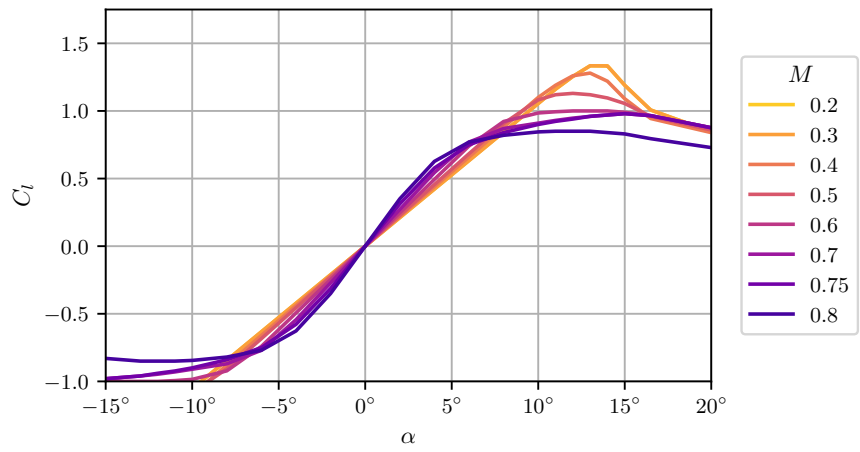
Figure 2.5 shows the simple multibody model in Dymore used to simulate finite wings or two-dimensional wing sections. The difference between the two types of models existed owing to the nature of wing wake modeling and whether or not the tip loss parameter  $f$  was invoked. While the wing was modeled as a flexible beam per se, idealized stiff structural properties were chosen that rendered the wing rigid for the purposes of this simulation. This enabled the isolation of the effect of aerodynamics modeling without the influence of structural dynamics. The wing aerodynamics was modeled using a lifting-line representation and a number of airstations distributed over its span. Figure 2.6 shows the distribution of airstations for the three different types of wings constructed using the multibody model of Fig. 2.5. The airfoil sections of all wings studied, except the morphing wing cases, comprised of the NACA0012 airfoil. Figure 2.7 shows the aerodynamic characteristics that were employed for this purpose. These airfoil polars were provided together with the Dymore source code and were not generated as part of the current work. The morphing wing cases utilized the NACA23012 airfoil and the corresponding airfoil tables are discussed later in Sec. 2.5.2.



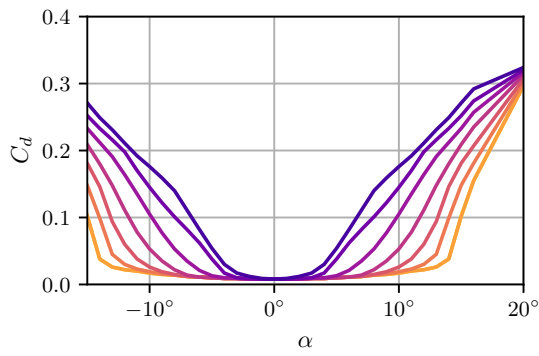
**Figure 2.5.:** Illustration of the multibody model of a wing used for the 2D and 3D steady and unsteady aerodynamics analyses. (Schematic inspired from Ref. [219])



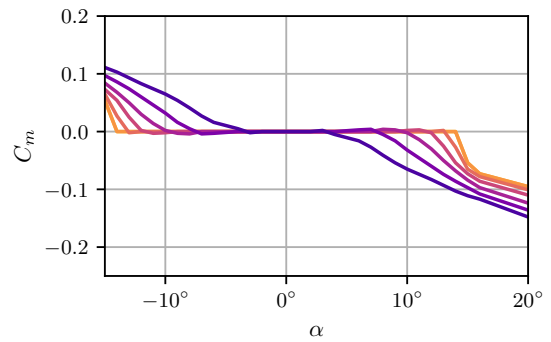
**Figure 2.6.:** Schematic showing the distribution of airstations on the different wing models.



**(a) Lift coefficient**



**(b) Drag coefficient**



**(c) Moment coefficient**

**Figure 2.7.:** Static airfoil polars of the NACA0012 airfoil used on the elliptic wing and pitching finite wing models.

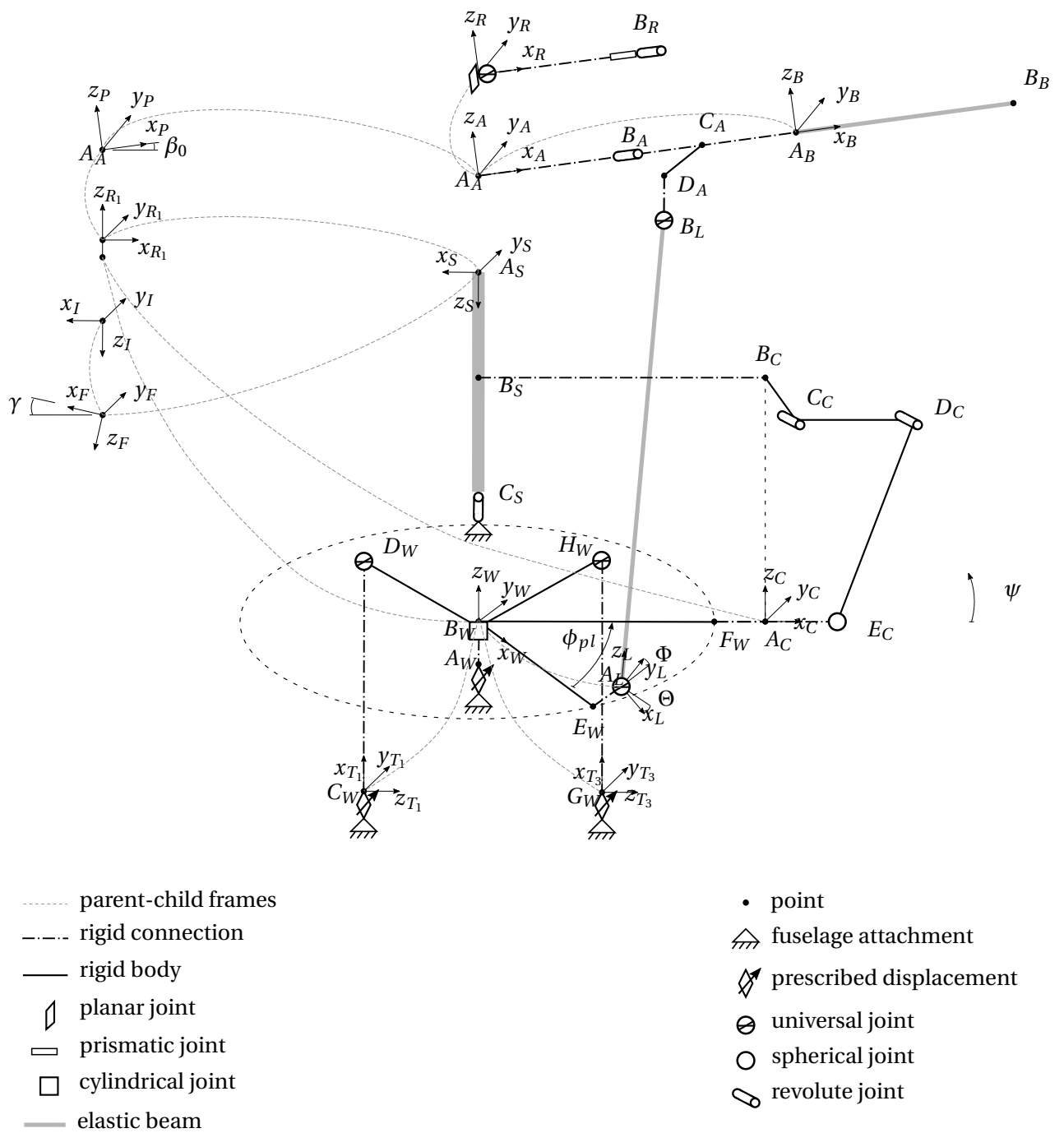
## 2.5.2. Full-scale Bo 105 rotor

The Bo 105 rotor was chosen as the baseline rotor in order to investigate the potential of active camber morphing towards performance improvement, as well as noise and vibration reduction. One of the motivations for choosing this rotor was that hingeless rotors are especially susceptible to increased levels of vibratory loads. Ref. [65] summarizes the experimental measurements of airfoil aerodynamic data necessary for rotorcraft airfoils tables-based analyses. In particular, measurements corresponding to airfoil lift, drag, and moment coefficients are available for tabbed as well as untabbed NACA23012 airfoils, among other airfoils used for rotary wing applications [259]. The full-scale Bo 105 rotor was used in this work. For this purpose, the isolated baseline rotor was constructed using data provided by DLR in Ref. [277]. Ref. [259] is another resource that contains a wealth of data needed to accurately model the Bo 105 rotor blade structural dynamics and control system kinematics. Additionally, information is available regarding airfoil 2D aerodynamic characteristics for the NACA23012 airfoil for angle of attack  $\alpha = [-180^\circ, 180^\circ]$ . Minor differences between the structural blade properties were identified between the data provided in Ref. [277] and that available in Ref. [259], but the former source is used throughout this work.

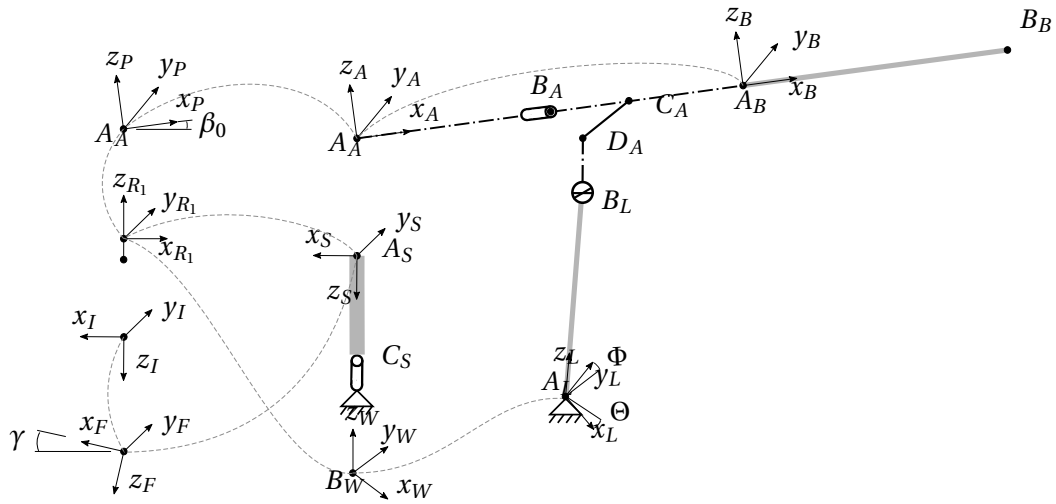
Figure 2.8 shows a schematic of the multibody model of the Bo 105 rotor used in this work. For simplicity, only the reference blade and the associated pitch link is shown. The Bo 105 model was validated using measurement test data from the Bo 105 IBC rotor test campaign of Ref. [111]. The rotor swashplate, static servo actuator links, scissor mechanism, etc., were represented but modeled as rigid entities. The objective of representing the Bo 105 rotor model using such a detailed setup was to accurately simulate the different load paths within the rotor head and control system. Detailed information about the different frames represented in the schematic, as well as relevant information related to the rotor setup is organized in Appendix A. Figure 2.9 shows the multibody model in Dymore that was used to verify the structural model of the Bo 105 rotor blades by obtaining the blade vibration natural frequencies at different rotation angular velocities. The blade was modeled as rigidly fixed at the root to a rigid non-rotating shaft, and the free end of the pitch link was also rigidly fixed to the ground. Similar to the HART II setup detailed in the preceding section, this entire assembly was subjected to an artificial centrifugal field using the concept of ‘rigid rotation’ in Dymore [32](Page 131). Eigenvalue analysis of the multibody setup at different ‘rotation’ rates yielded the blade natural frequencies and corresponding mode shapes. The blade aerodynamics was resolved using 81 lifting-line collocation points distributed over the span of the lifting surface of the blade ranging from  $r = 0.22-1.0$  (see Fig 2.10). While the HART II rotor is a scaled model of the Bo 105 rotor, one difference that stands out is that the zero twist section lies at  $0.7R$  for the latter while it is at  $0.75R$  for the former design.

Figure 2.11 shows the static airfoil polars of the NACA23012 airfoil used within the current study to model full-scale Bo 105 rotor blade aerodynamics. This was part of the work carried out by Abdelmoula and Rauleder in Ref. [16] and are presented here for completeness. A cursory comparison of the airfoil characteristics of the HART II blade (Fig. 2.14) and the Bo 105 blade (Fig. 2.11) show minor differences in the properties arising from the differences in the airfoil trailing-edge design (HART II rotor blade has a tab) as well as the operating Reynolds numbers.

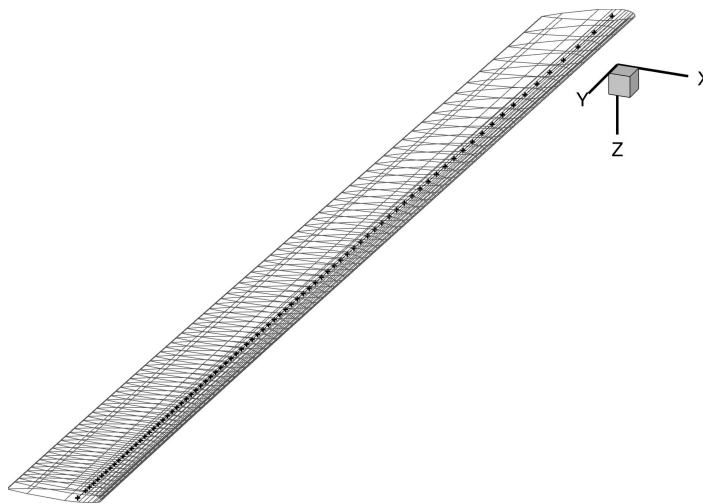




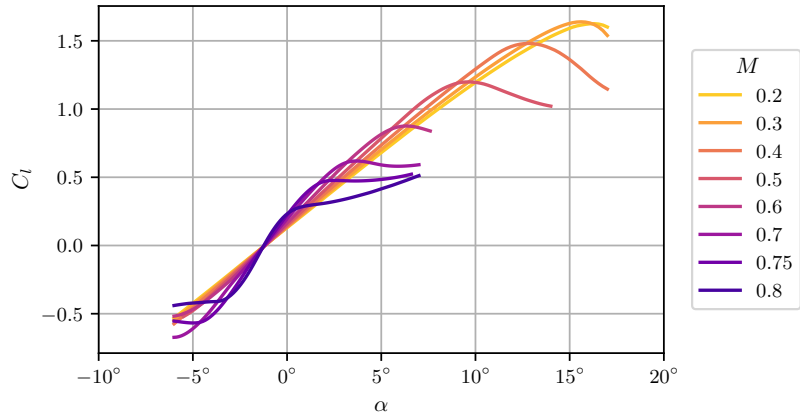
**Figure 2.8.:** Illustration of the multibody dynamics model of the Bo 105 rotor (not to scale). Note that only one blade is shown, but four blades are modeled.



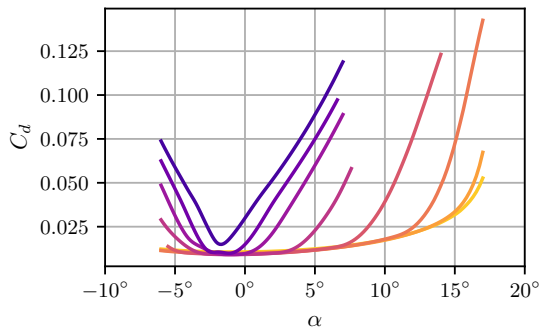
**Figure 2.9.:** Illustration of the multibody dynamics model of the Bo 105 rotor used for obtaining the blade natural frequencies.



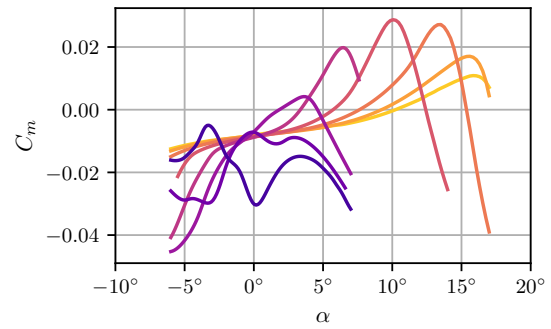
**Figure 2.10.:** Schematic showing the distribution of airstations on the Bo 105 rotor blade.



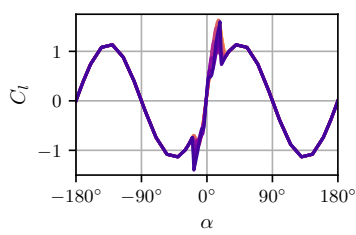
(a) Lift coefficient



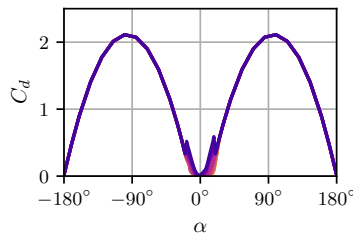
(b) Drag coefficient



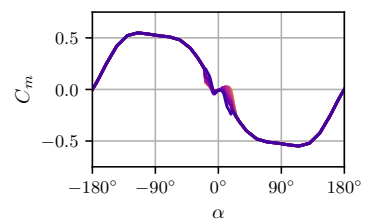
(c) Moment coefficient



(d) Lift coefficient



(e) Drag coefficient



(f) Moment coefficient

**Figure 2.11.:** Static airfoil polars of the NACA23012 airfoil for the Bo 105 rotor blade.

### 2.5.3. HART II rotor

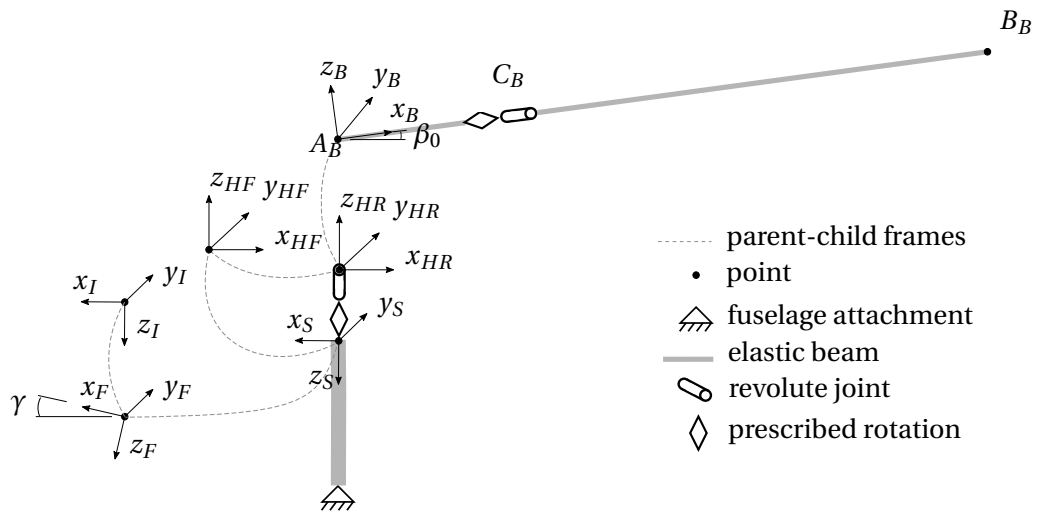
The HART II rotor is a Mach and dynamically scaled Bo 105 rotor that was used to conduct experimental tests using higher harmonic control. During an extensive measurement campaign in 2003, the effect of HHC was investigated using data obtained from rotor blade loads, airloads, vibratory loads, rotor wake, acoustics emissions, etc., [276]. These data from the HART II test campaign has been extensively used by a number of researchers to verify and validate their rotor analysis codes; examples include Refs. [256] and [257]. Ref. [10] maintains a full list of publications based on the HART II measurement data. In the current work, only the baseline (i.e. passive) rotor setup was simulated in order to validate the comprehensive analysis framework as well as the acoustic analysis framework.

Figure 2.12(a) shows the multibody model of the HART II rotor used for investigations in the current work. For simplicity, the schematic shows details corresponding only to the reference rotor blade. Additionally, the rotor swashplate mechanism and the control system were not modeled and instead direct harmonic control was prescribed using rotation control of the revolute joint that forms the feathering bearing in the model. As is evident in the figure, a number of inertial and non-inertial coordinate frames were defined with the origin of all the frames coincident at the rotor hub center. The equilibrium equations of the entire system were formulated in the inertial frame of reference  $I$ . Further details about the different reference frames and relevant rotor parameters needed are provided in Appendix B. Figure 2.12(b) shows the multibody model that was used to verify the structural model of the HART II rotor blades by obtaining the blade vibration natural frequencies at different rotation angular velocities. The blade was modeled as rigidly fixed on one end and was subjected to an artificial centrifugal field using the concept of ‘rigid rotation’ in Dymore [32] (Page 131). Eigenvalue analysis of the multibody setup at different ‘rotation’ rates yielded the blade natural frequencies and corresponding mode shapes. The HART II rotor blades are rectangular and have a modified NACA23012 airfoil (with tab). There are 81 airstations placed along the span of the lifting surface of the blade ranging from  $r = 0.22$ – $1.0$ . Figure 2.13 schematically shows their distribution.

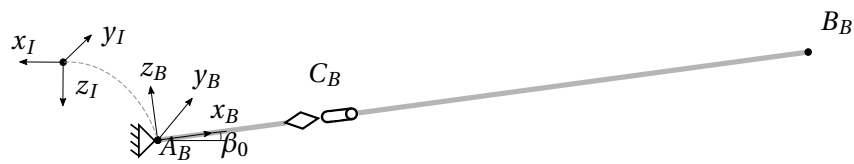
Figure 2.14 shows the coefficients of lift  $C_l$ , drag  $C_d$ , and moment  $C_m$  used in airfoil tables in order to evaluate the blade airloads. These airfoil data are publicly available from the DLR website [7]. Ref. [165]<sup>3</sup> highlights the minor differences in airfoil tables across the different research organizations involved in the HART II test campaign. The differences were largely in the airfoil moment coefficient values and had a negligible effect on the prediction of blade section lift but led to minor differences in the prediction of blade section moments. Figures 2.14(a)–(c) show airfoil  $C_l$ ,  $C_d$  and  $C_m$  over a narrow range of angle of attack which blade sections over the entire rotor predominantly experience. Airfoil coefficients over the entire angle of attack range of  $[-180^\circ, 180^\circ]$  are shown in Fig. 2.14(d)–(f). It is likely that Fig. 2.14(a)–(c) were obtained using two-dimensional CFD simulations and then extended using semi-empirical relations in Fig. 2.14(d)–(f) but this information is not provided in Ref. [7].

---

<sup>3</sup>Obtained via private communication with the author

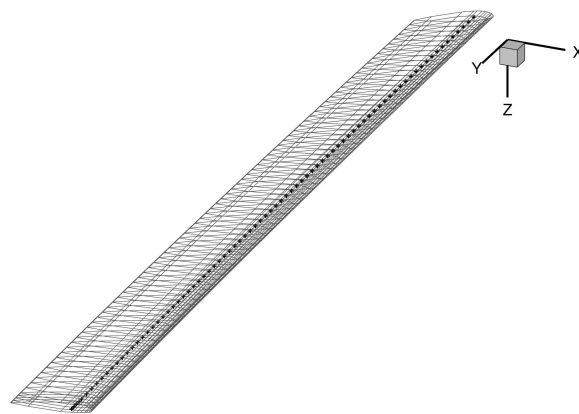


(a) (a) Rotor model

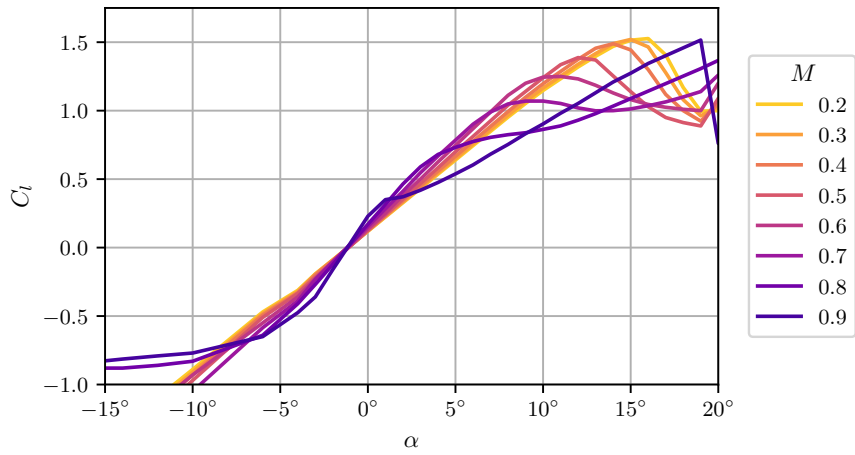


(b) (b) Blade model for fanplot analysis

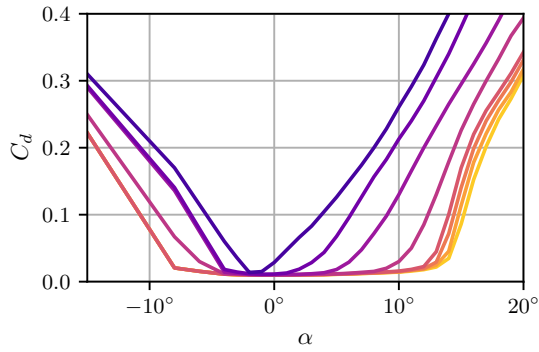
**Figure 2.12.:** Illustration of the multibody dynamics models of the HART II rotor (not to scale). Note that only one blade is shown in (a) but four blades are modeled.



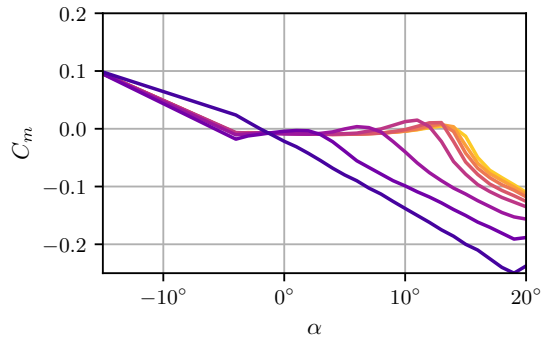
**Figure 2.13.:** Illustration of the distribution of airstations on the HART II rotor blade.



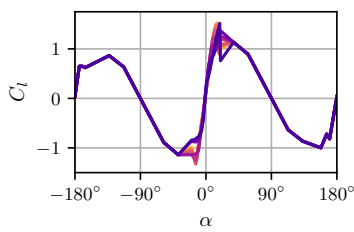
(a) Lift coefficient



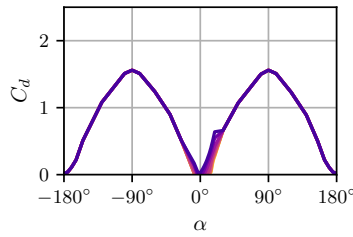
(b) Drag coefficient



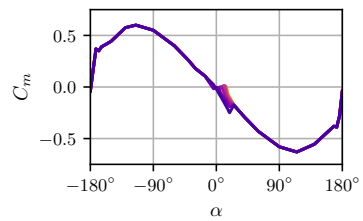
(c) Moment coefficient



(d) Lift coefficient



(e) Drag coefficient



(f) Moment coefficient

**Figure 2.14.:** Static airfoil polars of the NACA23012(tab) airfoil used on the HART II rotor blades. Based on data available on the DLR repository [8].

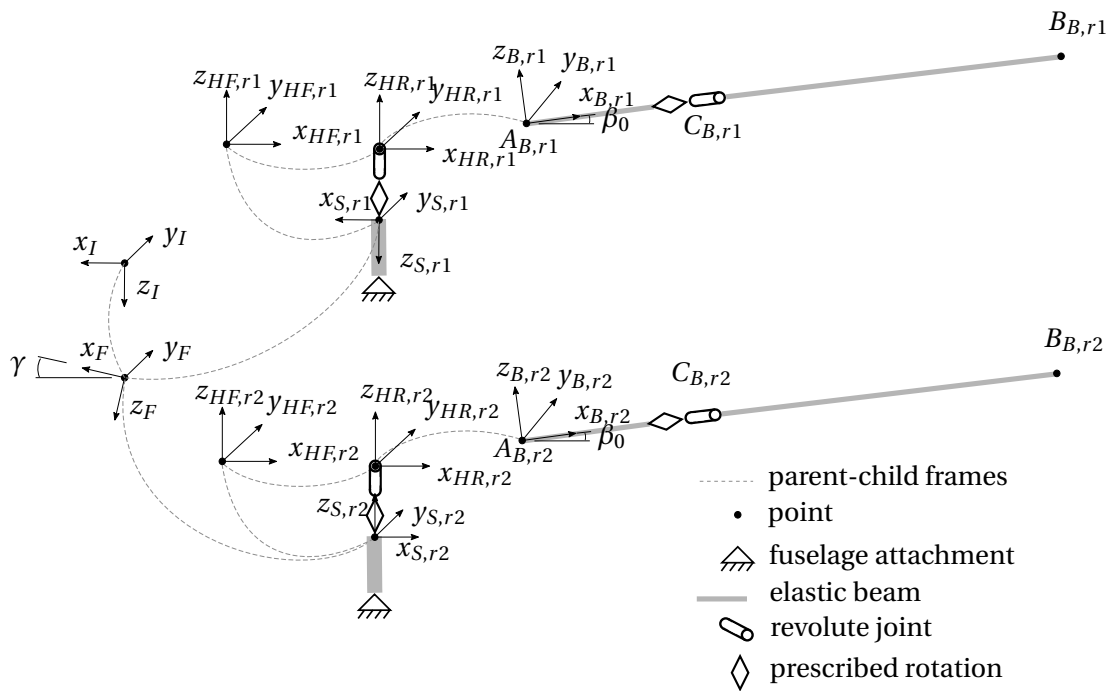
#### 2.5.4. UT Austin rotors

Coaxial rotors have recently been the subject of a number of investigations towards their performance and vibrations characteristics. This was in part motivated by the proposition from Sikorsky of a coaxial contra-rotating rotor design as part of the future vertical lift initiative (FVL) within the US Army [12, 11]. Coaxial contra-rotating rotors have also been sought by eVTOL industry in pursuit of improved rotor efficiency for future urban air mobility aircraft [36]. However, they tend to suffer from high harmonic vibratory loads occurring at the blade passage frequency due to interaction between the blades of the two rotors involved. These have been documented in, for example, Ref. [268].

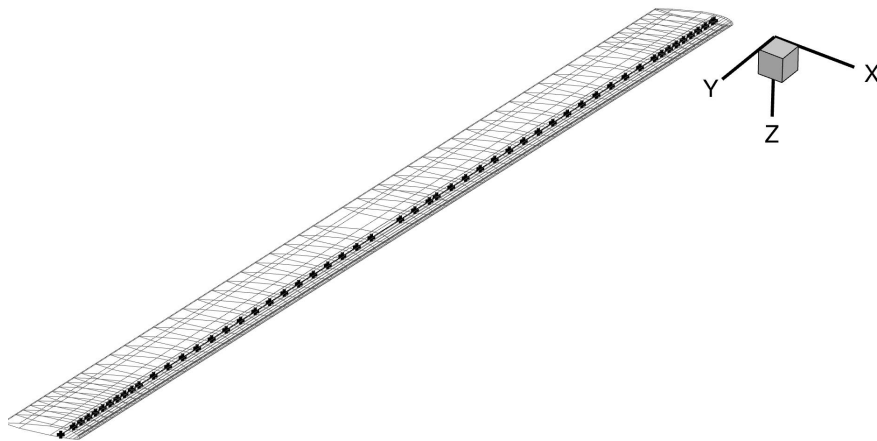
The benefit of the Dymore+VPM simulation framework is accentuated in the context of a multi-rotor design since the VPM formulation naturally lends itself to assessing rotor-rotor wake interactions. No additional changes are required to the simulation framework on the VPM side since it considers the entire wake vorticity in the simulation domain as a single entity. This is not the case with the Peters-He inflow model where a renewed formulation is needed to account for rotor-rotor effect [91][142]. This section provides details into the setup of a single rotor and a coaxial rotor system, henceforth referred to as the ‘UT Austin rotor’. The objective of simulating this rotor system is to serve the dual purpose of demonstrating the flexible utility of VPM to model multi-rotor systems as well as the potential of the FishBAC mechanism to reduce blade passage vibratory loads on the coaxial contra-rotating rotor. The single-rotor configuration is only used for validation purposes.

Figure 2.15 shows the multibody model of the coaxial design of the UT Austin rotor used for investigations in the current work. For single rotor analysis, only the upper rotor (rotor 1) is used. While the multibody model construction had little variation across the isolated and coaxial contra-rotating (ccr) rotors, the rotor radii varied slightly across the designs. The relevant model parameters are summarized in Appendix C for the different designs along with the different reference frames that make up the multibody model. Table C.2 details the frame definitions used for the multibody model construction, while Table C.1 summarizes the rotor parameters of the test setups of the single rotor and the ccr rotor. These model parameters were obtained from Refs. [269] and [113]. Again, for simplicity, the schematic of Fig. 2.15 shows details corresponding only to the reference rotor blade in each rotor. The rotor model construction is similar to the multibody model for the HART II rotor used in this work and detailed in Sec. 2.5.3. The rotor swashplate mechanism and the control system were not modeled, and instead, direct harmonic control was prescribed using rotation control of the revolutes joint that forms the feathering bearing in the model. The rotor itself is modeled as rigid. The blades have been modeled with sufficiently high stiffness values so that they can be considered as effectively rigid.

The UT Austin rotor blades are rectangular and have a VR-12 airfoil with tab [230](Page 129). To model the blade aerodynamics, 55 airstations were placed along the span of the lifting surface of the blade (see Fig. 2.16). Figure 2.17 shows the coefficients of lift  $C_l$ , drag  $C_d$ , and moment  $C_m$  used in airfoil tables in order to evaluate the blade aerodynamic loads. These airfoil data are taken from Ref. [230], and the data used are shown in their entirety for the sake of completeness.

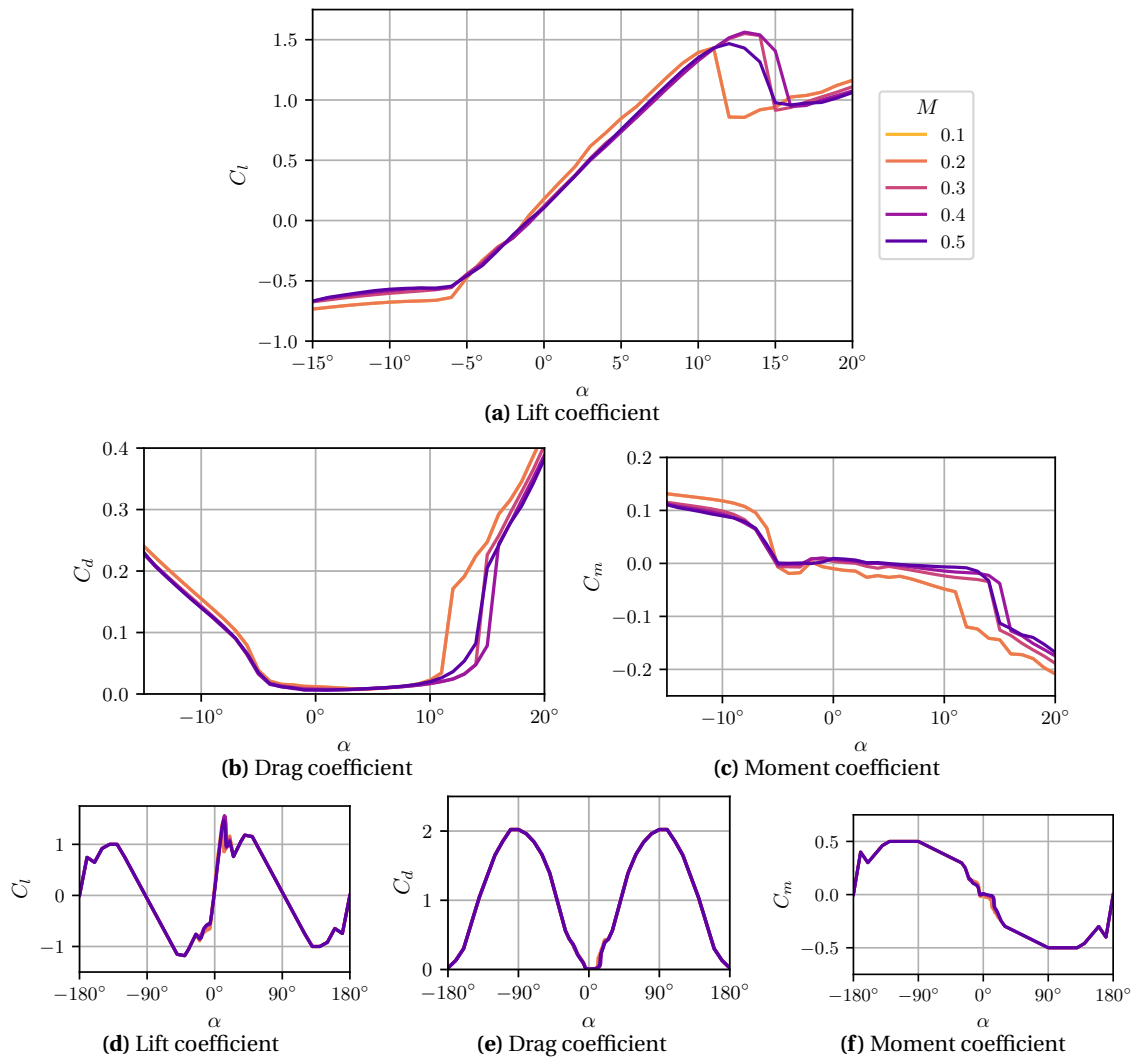


**Figure 2.15.:** Illustration of the multibody model of the UT Austin coaxial rotor model.



**Figure 2.16.:** Schematic of the distribution of airstations on rotor blade used to model UT Austin single rotor and coaxial rotor system.





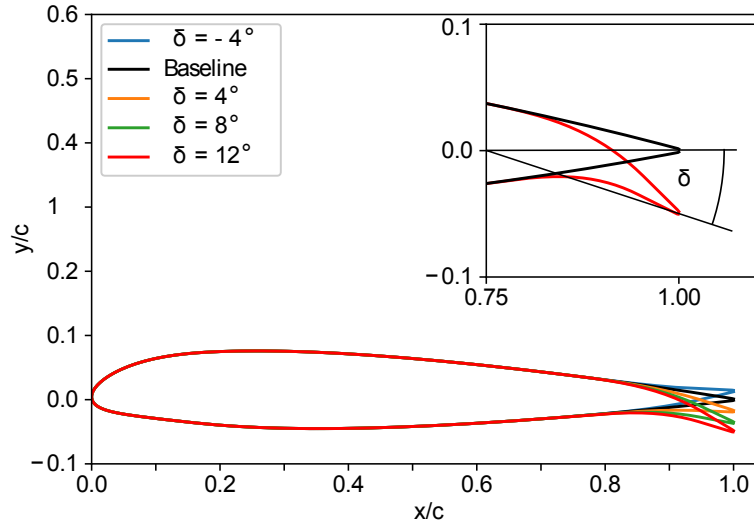
**Figure 2.17.:** Static airfoil polars of the VR12 airfoil for the UT Austin rotor blade (obtained from Ref. [230]).

### 2.5.5. Active FishBAC rotors

Rotor aeromechanics analysis, with an active camber morphing mechanism installed, forms one of the core investigative aspects of this work. For this purpose, the Fish Bone Active Camber (Fish-BAC) concept of Ref. [288] was modeled. In order to conduct active rotor investigations with the full-scale Bo 105 rotor, the same setup as the Bo 105 rotor was used with the difference that airfoil tables were represented as ‘compound’ airfoil tables in Dymore [3]. This definition was used only for radial location extending from  $r = 0.5$ – $0.9$ , which defined the location of the active camber morphing section, as shown in Fig. 2.18. A compound airfoil table is a three-dimensional matrix obtained by combining multiple two-dimensional matrices of airfoil tables at various degrees of camber morphing. As shown in Fig. 2.19, an equivalent deflection angle  $\delta$  was identified for the trailing-edge tip of the airfoil in order to denote the extent of camber morphing due to FishBAC actuation. The different two-dimensional matrices of airfoil tables making up the compound table were obtained at trailing-edge deflection angles  $\delta = [-9^\circ, 13.5^\circ]$ .



**Figure 2.18.:** Illustration of the active camber morphing section modeled on the Bo 105 rotor blade.



**Figure 2.19.:** Airfoil profiles obtained for different degrees of FishBAC camber morphing. Adopted, with permission, from Ref. [141].

Based on studies conducted using TEFs, this range of deflections was deemed sufficient to identify the influence of camber morphing on rotor power, vibrations, and noise. In addition, a time function definition [32](Page 238) was attached to the lifting-line definition for denoting the time variation of deflection angle. Together with the compound airfoil tables, the instantaneous morphing angle was responsible for obtaining the quasi-steady aerodynamic loads of all the airstations of the active rotor. The unsteady aerodynamic effects were modeled using the Peters 2D unsteady aerodynamics theory and the Peters-He inflow model. For simplicity, the aft 25% $c$  of the blade section was modeled as linear rigid segment, similar to a trailing-edge flap, in order to calculate the unsteady aerodynamic effects.

Two-dimensional fluid-structure interaction studies conducted in Refs. [289] and [301] using XFOIL and CFD, respectively, emphasize some of the practical issues associated with flexure of the morphing section. Additionally, it is likely that the structural properties in the active blade region, where the camber morphing mechanism is embedded, would be different from the baseline rotor properties. However, in the current study the blade structural properties of the baseline rotor are used without modification even for the active rotor analysis. Only the aerodynamic effects of the active camber mechanism are modeled, and the FishBAC section elastic dynamics are not accounted for. Design challenges such as the operation of the active mechanism in high centrifugal and dynamic loading conditions, friction at the hinges, the effect of the structural properties on the dynamics of the morphing section, etc., are beyond the scope of this work.

### 3. Vortex Particle Method

According to Ref. [163], the following quantities are critical to accurately model rotor wake—blade motion, blade loading, and the convection of vortices in the wake without numerical dissipation. Chapter 2 already provides sufficient details about the basic comprehensive analysis framework used in the current study. The structural dynamics and the blade aerodynamics models were already provided in sufficient detail in Secs. 2.1 and 2.2, respectively. In order to better capture the high-frequency unsteady airloads acting on the rotor blade, there is scope to improve the simulation capabilities of the framework of Chap. 2. This chapter details the steps adopted towards that goal.

Dynamic inflow models, and in particular the Peters-He model detailed in Sec. 2.3.1, are capable of predicting the induced flow velocity on and off the rotor reasonably well in both steady state and transient maneuvers. However, the assumption of irrotational flow inherent in potential flow theory, which these models are based on, makes the inflow model inaccurate when the effect of vorticity is pronounced. This can happen, for example, when the tip vortex from a preceding blade passes close to the following blade. Besides, rotational flow (or vortical flow) is the fundamental fluid phenomenon that is responsible for induced velocity in the case of lift-generating finite wings. This was postulated by Lanchester-Prandtl and later confirmed via careful wind tunnel experiments [53][76]. It has stood the test of time and forms the basis of the inner and outer problem strategy adopted in order to solve three-dimensional wing flow problems in a computationally efficient manner. For  $\mu < 0.2$ , it is critical for the rotor wake model to be able to simulate the effect of the trailing and shed vorticity since strong blade-vortex interactions are likely in this flight regime [125]. Additionally, lightweight construction and high aspect ratio of the blades lead to highly flexible structures. Low-fidelity dynamic inflow models are limited in their ability to accurately capture the resultant complex fluid-structure interactions. For this purpose, an improved wake modeling framework using the vortex particle method (VPM) is proposed in this chapter in order to accurately solve for the unsteady induced inflow velocity at the rotor blades.

Unlike Eulerian grid-based analyses, such as traditionally used URANS simulations in CFD/CSD coupled rotor investigations, VPM is Lagrangian in character. This makes this method particularly useful because computational resources can be utilized only in regions of high vorticity instead of solving flow field equations over an entire grid. Since the formulation is based on incompressible flows, a solution of the flow field vorticity directly yields the corresponding velocity field at any point in the region of interest—both on and off rotor blades. Vortex-induced velocity at the rotor disk is needed for LL-based blade aerodynamics solutions to obtain the effective section angle of attack. It might also be required in regions in the rotor wake, for example, surfaces surrounding the rotor, in order to account for interference effects. The vortex particle-based methodology has recently gained traction as an alternative to grid-based CFD techniques and was used to study

coaxial rotor systems [251] as well as rotor wake interference due to the presence of boundaries [97].

The focus of this chapter is to describe the VPM solver used in the current study to evaluate rotor wake-induced velocity. For this purpose, the theoretical formulation of the solver is detailed in Sec. 3.1. Essentially, this includes equations that describe the evolution of vorticity in the wake. Section 3.2 documents a number of diagnostic quantities. The evolution of these reference quantities in time is used to verify the model implementation and confirm the veracity of assumptions made. Section 3.5 briefly mentions techniques adopted in order to speed-up computations within the VPM solver. Section 3.3 describes the vortex ring analytical test cases used in order to verify the overall implementation of the solver. The theoretical formulation of the vortex particle method, the diagnostics, and the verification test cases have been adopted from Refs. [286], [285] and [253]. The VPM framework itself is largely built using the formulation presented in Ref. [253], which in turn is based on the formulation presented in Refs. [285] and [286]. Ref. [253] proposed new analytical expressions for vortex particle interaction with rotor blades and made corrections to typos in the original publications. Continuing in that spirit, the fundamental equations needed to construct the model are detailed in this chapter for the sake of completeness and with the objective of further correcting typos/errors that were present in the aforementioned original works.

### 3.1. Formulation

Ref. [139](Chapter 1) provides a concise modern review of the origins and the development of vortex methods with a particular focus on vortex particle methods. In the current study, the unsteady wake is modeled using the equations detailed in Refs. [253] and [285]. The most relevant elements of the formulation are detailed in this section for the sake of completeness and accuracy. VPM solves the momentum equation of the incompressible Navier-Stokes equations (Eq. 3.1). For this, it uses the vorticity formulation of Eq. 3.2 where the pressure variable has been eliminated by taking the curl of Eq. 3.1. An alternative formulation includes an additional term on the RHS of Eq. 3.2 representing the sub-grid scale model for large-eddy simulations using the particle method [56]. The issue of the validity of the VPM solution in the presence of a no-slip boundary has been raised in Ref. [139], but this does not concern the current work since only unbounded wake problems were investigated.

$$\rho \frac{\partial \mathbf{v}}{\partial t} + (\mathbf{v} \cdot \nabla) \mathbf{v} = -\nabla p + \mu \nabla^2 \mathbf{v} \quad (3.1)$$

$$\frac{\partial \boldsymbol{\omega}}{\partial t} + (\mathbf{v} \cdot \nabla) \boldsymbol{\omega} - \boldsymbol{\omega} \cdot \nabla \mathbf{v} = \nu \nabla^2 \boldsymbol{\omega} \quad (3.2)$$

Refs. [139](Section 2.5) and [63](Appendix A) describe the mathematical basis of discretizing a function, which is the vorticity field distribution in the current context, using particles. The fundamental idea revolves around using the Dirac delta distribution and appropriate weights to sample any given function over a domain—

$$\boldsymbol{\omega}(\mathbf{x}, t) \approx \sum_p \boldsymbol{\alpha}_p(t) \delta(|\mathbf{x} - \mathbf{x}_p(t)|) \quad (3.3)$$

where,

$$\int \boldsymbol{\omega}(\mathbf{x}, t) d\mathcal{V} \approx \sum_p \boldsymbol{\alpha}_p(t) \quad (3.4)$$

$\boldsymbol{\alpha}_p$  corresponds to the strength of the particles and is given by the vorticity vector at a given location  $\mathbf{x}_p$  multiplied by the volume  $\mathcal{V}$  associated with that particle. The volume, and by extension, the particle strength, is therefore based on the discretization scheme of the flow field. Based on Eq. 3.4, the total vorticity in a given volume domain is simply the sum of the strength of all particles in that domain. In order to avoid large unphysical induced velocities when two particles get close to each other, the standard practice involves ‘mollifying’ the Dirac delta function-based singular vorticity field using a smooth cutoff function  $\zeta$  and corresponding cutoff radius or ‘smoothing’ radius  $\sigma$ . The mollified or regularized vorticity field  $\boldsymbol{\omega}_\sigma$ , as it is often referred to in literature, is given by

$$\begin{aligned} \boldsymbol{\omega}(\mathbf{x}, t) \approx \boldsymbol{\omega}_\sigma(\mathbf{x}, t) &= \zeta_\sigma * \boldsymbol{\omega}(\mathbf{x}, t) \\ &= \sum_p \boldsymbol{\alpha}_p(t) \zeta_\sigma(|\mathbf{x} - \mathbf{x}_p(t)|) \end{aligned} \quad (3.5)$$

$$\begin{aligned} \zeta_\sigma(|\mathbf{x}|) &= \frac{1}{\sigma^3} \zeta\left(\frac{|\mathbf{x}|}{\sigma}\right) \\ &= \frac{1}{\sigma^3} \zeta(\rho) \end{aligned} \quad (3.6)$$

According to Ref. [63] (Section 2.2), the efficiency of the vortex methods is contingent on the choice of regularization function  $\zeta_\sigma$  and the initialization of particle strength and position. For the purposes of the current investigation, the choice of regularization functions was based on the suggestions in Ref. [285]. The Gaussian kernel was used for Dymore+VPM coupled analysis while the higher-order algebraic kernel was used to verify the VPM model. The particle initialization scheme is discussed later in Sec. 3.4.

### 3.1.1. Vortex particle evolution

The evolution of the vortex particles occurs with inter-particle interactions that lead to change in particle strengths  $\boldsymbol{\alpha}_{p_i}$ , as well as change in position  $\mathbf{x}_p$  due to velocity induced in accordance with the Biot-Savart law. Accordingly, the evolution equations can be written as follows—

$$\frac{d\mathbf{x}_{p_{ij}}}{dt} = \mathbf{K}_\sigma \times \boldsymbol{\alpha}_{p_j} \quad (3.7)$$

$$\frac{d\boldsymbol{\alpha}_{p_{ij}}}{dt} = \boldsymbol{v}_\sigma(\mathbf{x}_{p_i}) \quad (3.8)$$

$$\mathbf{x}_{p_{ij}} = \mathbf{x}_{p_i} - \mathbf{x}_{p_j} \quad (3.9)$$

Here,  $\mathbf{K}_\sigma$  is the Biot-Savart kernel used to obtain induced velocity due to a regularized particle. The total induced velocity on a given particle  $\mathbf{v}_\sigma(\mathbf{x}_{p_i})$  due to the regularized vorticity field and the rates of change in vortex particle strengths are given using Eq. 3.10 and Eqs. 3.11-3.13, respectively. In Eq. 3.10, the self-induction by a vortex particle has been discounted, and the effect of all particles  $N_p$  in the simulation domain is included. The change in vortex particle strength occurs as a consequence of the process of viscous diffusion and vortex stretching. Viscous diffusion is modeled using the Particle Strength Exchange (PSE) scheme, and vortex stretching is modeled using the transpose scheme. For more details, Ref. [286] can be consulted.  $\eta_\sigma$ ,  $q_\sigma$ , and  $F_\sigma$  are the different kernel functions that depend on the choice of the regularization function  $\zeta$  and are detailed in the following section.

$$\mathbf{v}_\sigma(\mathbf{x}_{p_i}) = \sum_{\substack{j=1 \\ i \neq j}}^{N_p} \mathbf{K}_\sigma(\mathbf{x}_{p_{ij}}) \times \boldsymbol{\alpha}_{p_j} \quad (3.10)$$

$$\frac{d\boldsymbol{\alpha}_{p_i}}{dt} = \left( \frac{d\boldsymbol{\alpha}_{p_i}}{dt} \right)_{\text{viscous diffusion}} + \left( \frac{d\boldsymbol{\alpha}_{p_i}}{dt} \right)_{\text{vortex stretching}} \quad (3.11)$$

$$\left( \frac{d\boldsymbol{\alpha}_{p_i}}{dt} \right)_{\text{viscous diffusion}} = \nu \nabla^2 (\mathcal{V} \boldsymbol{\omega}_{\sigma_i}) = \frac{2\nu}{\sigma^2} \sum_{j=1}^{N_p} (\mathcal{V}_{p_i} \boldsymbol{\alpha}_{p_j} - \mathcal{V}_{p_j} \boldsymbol{\alpha}_{p_i}) \eta_\sigma(|\mathbf{x}_{p_{ij}}|) \quad (3.12)$$

$$\left( \frac{d\boldsymbol{\alpha}_{p_i}}{dt} \right)_{\text{vortex stretching}} = \sum_{j=1}^{N_p} \left[ \frac{q_\sigma(|\mathbf{x}_{p_{ij}}|)}{x_{p_{ij}}^3} (\boldsymbol{\alpha}_{p_i} \times \boldsymbol{\alpha}_{p_j}) + \{\mathbf{x}_{p_{ij}} \cdot (\boldsymbol{\alpha}_{p_i} \times \boldsymbol{\alpha}_{p_j})\} \mathbf{x}_{p_{ij}} F_\sigma(|\mathbf{x}_{p_{ij}}|) \right] \quad (3.13)$$

### 3.1.2. Regularization functions

From Sec. 3.1.1, the different kernel functions involved in Eqs. 3.7-3.13 are related to the cutoff function  $\zeta$ , or the corresponding regularization function  $\zeta_\sigma$ . The choice of  $\zeta$  governs the stability and convergence properties of the vorticity field simulation [286]. The relevant kernels are related by the following relationships—

$$-\frac{1}{\rho} \frac{d}{d\rho} \zeta(\rho) = \eta(\rho) \quad (3.14)$$

$$\eta_\sigma(|\mathbf{x}|) = \eta(|\mathbf{x}|/\sigma) / \sigma^3 \quad (3.15)$$

$$\frac{1}{\rho^2} \frac{d}{d\rho} q(\rho) = \zeta(\rho) \quad (3.16)$$

$$q_\sigma(|\mathbf{x}|) = q(\rho) \quad (3.17)$$

$$K_\sigma(\mathbf{x}) = \frac{q_\sigma(\mathbf{x})}{|\mathbf{x}|^3} \quad (3.18)$$

$$F_\sigma(|\mathbf{x}|) = \frac{1}{|\mathbf{x}|} \frac{\partial}{\partial s} \left( \frac{q_\sigma(|\mathbf{x}|)}{|\mathbf{x}|^3} \right) = \frac{1}{s^2} \left[ \zeta_\sigma(|\mathbf{x}|) - 3 \frac{q_\sigma(|\mathbf{x}|)}{|\mathbf{x}|^3} \right] \quad (3.19)$$

Based on the type of function used to represent the smooth cutoff function for the particle-based discretization of the vorticity field, the aforementioned kernels can take different forms as shown in Table 3.1. Here, the regularization functions are based on those proposed in Ref. [285] for their good convergence properties. The high order algebraic (HOA) kernels are used for verification of the methodology in the following sections, while the Gaussian kernels are used for the coupled Dymore+VPM analysis. This is done because HOA kernels allow closed-form solutions of the diagnostics, discussed in the following section, that need to be evaluated in order to verify the simulation setup. Such verification cannot be carried out using the Gaussian kernels since the corresponding diagnostics expressions cannot be obtained in a closed analytical form. However, the Gaussian smoothing function is used in the rest of this work due to their good convergence properties, as stated in Ref. [286].

Higher-order algebraic (HOA)	Gaussian
$\zeta(\rho) = \frac{15}{8\pi} \frac{1}{(\rho^2+1)^{7/2}}$	$\zeta( \mathbf{x} ) = \frac{1}{(2\pi)^{3/2}} e^{- \mathbf{x} ^2/2}$
$\zeta_\sigma( \mathbf{x} ) = \frac{15}{8\pi} \frac{\sigma^4}{( \mathbf{x} ^2+\sigma^2)^{7/2}}$	$\zeta_\sigma( \mathbf{x} ) = \frac{1}{(2\pi)^{3/2}\sigma^3} e^{- \mathbf{x} ^2/2\sigma^2}$
$\eta_\sigma( \mathbf{x} ) = \frac{105}{8\pi} \frac{\sigma^6}{( \mathbf{x} ^2+\sigma^2)^{9/2}}$	$\eta_\sigma( \mathbf{x} ) = \frac{1}{(2\pi)^{3/2}\sigma^3} e^{- \mathbf{x} ^2/2\sigma^2}$
$q_\sigma( \mathbf{x} ) = \frac{ \mathbf{x} ^3}{4\pi} \frac{\left( \mathbf{x} ^2 + \frac{5\sigma^2}{2}\right)}{( \mathbf{x} ^2+\sigma^2)^{5/2}}$	$q_\sigma( \mathbf{x} ) = \frac{1}{4\pi} \operatorname{erf}\left(\frac{ \mathbf{x} }{\sqrt{2}\sigma}\right) - \frac{ \mathbf{x} }{(2\pi)^{3/2}\sigma} e^{- \mathbf{x} ^2/2\sigma^2}$

**Table 3.1.:** Different kernel expressions based on the high order algebraic and the Gaussian smooth cutoff functions.

To summarize, the VPM formulation solves Eqs 3.8 and 3.11 using the regularization functions from Table 3.1. The next section lays down the expressions for diagnostic or invariant quantities that can help verify the correctness of the VPM solver.

## 3.2. Conservation Laws

Simple analytical test cases are desired where the results of the test case are known exactly so that comparison with the VPM prediction can be used to verify the latter. The following section describes the analytical test case of vortex rings as well as the relevant diagnostic quantities of interest. A number of diagnostic quantities or invariants or conserved quantities, as they are called, from Ref. [286] are used to verify the VPM model setup:  $\mathbf{I}$  - linear impulse;  $\mathbf{\Omega}$  - total vorticity;  $\mathbf{A}$  - angular impulse;  $\mathcal{H}_\sigma$  - semi-regularized helicity;  $E_\sigma$  and  $E_{\sigma f}$  - semi-regularized and divergence-free kinetic energy, respectively;  $\mathcal{E}_\sigma$  and  $\mathcal{E}_{\sigma f}$  - semi-regularized and divergence-free enstrophy, respectively. These are detailed in the following expressions below for the sake of completeness. Note that both Refs. [286] and [253]<sup>1</sup> contained typos in the expression for  $\mathcal{E}_\sigma$  and this has also been addressed below; this expression is also correctly stated in Ref. [270]. These diagnostic quantities are classified into linear and quadratic diagnostics based on whether the diagnostics have a linear

<sup>1</sup>Confirmed via private communication with the author

dependence on the particle strength  $\alpha_p$ , i.e.  $\mathbf{I}$ ,  $\mathbf{\Omega}$ ,  $\mathbf{A}$ ,  $\mathcal{H}_\sigma$ , or a quadratic dependence, i.e.  $E_\sigma$ ,  $E_{\sigma f}$ ,  $\mathcal{E}_\sigma$ ,  $\mathcal{E}_{\sigma f}$ .

$$\mathbf{I} = \frac{1}{2} \sum_{i=1}^{N_p} (\mathbf{x}_{p_i} \times \alpha_{p_i}) \quad (3.20)$$

$$\mathbf{\Omega} = \sum_{i=1}^{N_p} \alpha_{p_i} \quad (3.21)$$

$$\mathbf{A} = \frac{1}{3} \sum_{i=1}^{N_p} \mathbf{x}_{p_i} \times (\mathbf{x}_{p_i} \times \alpha_{p_i}) \quad (3.22)$$

$$\mathcal{H}_\sigma = \int (\boldsymbol{\omega} \cdot \mathbf{v}_\sigma) d\mathcal{V} = \sum_{i,j=1}^{N_p} \frac{q_\sigma(\mathbf{x}_{p_{ij}})}{|\mathbf{x}_{p_{ij}}|^3} [\mathbf{x}_{p_{ij}} \cdot (\alpha_{p_i} \times \alpha_{p_j})] \quad (3.23)$$

$$\begin{aligned} E_\sigma &= \frac{1}{2} \int (\mathbf{v} \cdot \mathbf{v}_\sigma) d\mathcal{V} \\ &= \frac{1}{16\pi} \sum_{i,j=1}^{N_p} \frac{(|\mathbf{x}_{p_{ij}}|^2 + 2\sigma^2) \alpha_{p_i} \cdot \alpha_{p_j} + (\mathbf{x}_{p_{ij}} \cdot \alpha_{p_i})(\mathbf{x}_{p_{ij}} \cdot \alpha_{p_j})}{(\sigma^2 + |\mathbf{x}_{p_{ij}}|^2)^{3/2}} \end{aligned} \quad (3.24)$$

$$\begin{aligned} E_{\sigma f} &= \frac{1}{2} \int \boldsymbol{\psi}_\sigma \cdot \boldsymbol{\omega} d\mathbf{x} \\ &= \frac{1}{2} \sum_{i,j=1}^{N_p} G_\sigma(\mathbf{x}_{p_i} - \mathbf{x}_{p_j}) \alpha_{p_i} \cdot \alpha_{p_j} \\ &= \frac{1}{8\pi} \sum_{i,j=1}^{N_p} \frac{\left(|\mathbf{x}_{p_i} - \mathbf{x}_{p_j}|^2 + \frac{3}{2}\sigma^2\right)}{\left(|\mathbf{x}_{p_i} - \mathbf{x}_{p_j}|^2 + \sigma^2\right)^{\frac{3}{2}}} \alpha_{p_i} \cdot \alpha_{p_j}. \end{aligned} \quad (3.25)$$

$$\begin{aligned} \mathcal{E}_\sigma &= \int (\boldsymbol{\omega} \cdot \boldsymbol{\omega}_\sigma) d\mathcal{V} \\ &= \frac{1}{8\pi} \sum_{i,j=1}^{N_p} \frac{1}{(|\mathbf{x}_{p_{ij}}|^2 + \sigma^2)^{9/2}} \left[ (|\mathbf{x}_{p_{ij}}|^2 + \sigma^2) (2|\mathbf{x}_{p_{ij}}|^4 + 7\sigma^2|\mathbf{x}_{p_{ij}}|^2 + 20\sigma^4) (\alpha_{p_i} \cdot \alpha_{p_j}) \right. \\ &\quad \left. - 3(2|\mathbf{x}_{p_{ij}}|^4 + 9\sigma^2|\mathbf{x}_{p_{ij}}|^2 + 7\sigma^4) (\mathbf{x}_{p_{ij}} \cdot \alpha_{p_i})(\mathbf{x}_{p_{ij}} \cdot \alpha_{p_j}) \right] \end{aligned} \quad (3.26)$$



$$\begin{aligned}
\mathcal{E}_{\sigma f} &= \int \boldsymbol{\omega} \cdot \boldsymbol{\omega}_{\sigma} d\mathbf{x} \\
&= \sum_{i,j=1}^{N_p} \zeta_{\sigma}(\mathbf{x}_{p_i} - \mathbf{x}_{p_j}) \boldsymbol{\alpha}_{p_i} \cdot \boldsymbol{\alpha}_{p_j} \\
&= \frac{1}{4\pi} \sum_{i,j=1}^{N_p} \frac{15}{2} \frac{\sigma^4}{\left(|\mathbf{x}_{p_i} - \mathbf{x}_{p_j}|^2 + \sigma^2\right)^{\frac{7}{2}}} \boldsymbol{\alpha}_{p_i} \cdot \boldsymbol{\alpha}_{p_j}
\end{aligned} \tag{3.27}$$

### 3.3. Verification

In order to verify the VPM solver set up using the governing equations in Sec. 3.1, model vortex rings based on Eq 3.28 were used. The corresponding discretization parameters used for the particle simulation of the vortex rings are given in Table 3.2. These simulation parameters were adopted from Ref. [286] and are detailed here for completeness.

$$\boldsymbol{\omega}(\mathbf{x}, 0) = \omega(r, \theta, 0) \hat{\mathbf{e}}_{\varphi} = \frac{\Gamma}{2\pi\sigma_R^2} \left(1 + \frac{r}{R} \cos\theta\right) e^{-r^2/2\sigma_R^2} \hat{\mathbf{e}}_{\varphi} \tag{3.28}$$

Parameter	Isolated vortex ring
Vortex ring radius, $R$	1.0
Circulation, $\Gamma$	1.0
Ring core radius, $r_c$	0.35
Ring layer half-width, $r_l$	[0.03889, 0.03182, 0.02692]
Azimuthal discretization, $n_{\phi}$	[80, 100, 117]
Azimuthal discretization, $\Delta\phi$	[4.50°, 3.60°, 3.08°]
Number of layer, $n_c$	[4, 5, 6]
Time step, $\Delta t$	0.025
Kinematic viscosity, $\nu$	$2.50 \times 10^{-3}$

**Table 3.2.:** Vortex ring parameters used to verify the VPM solver setup.

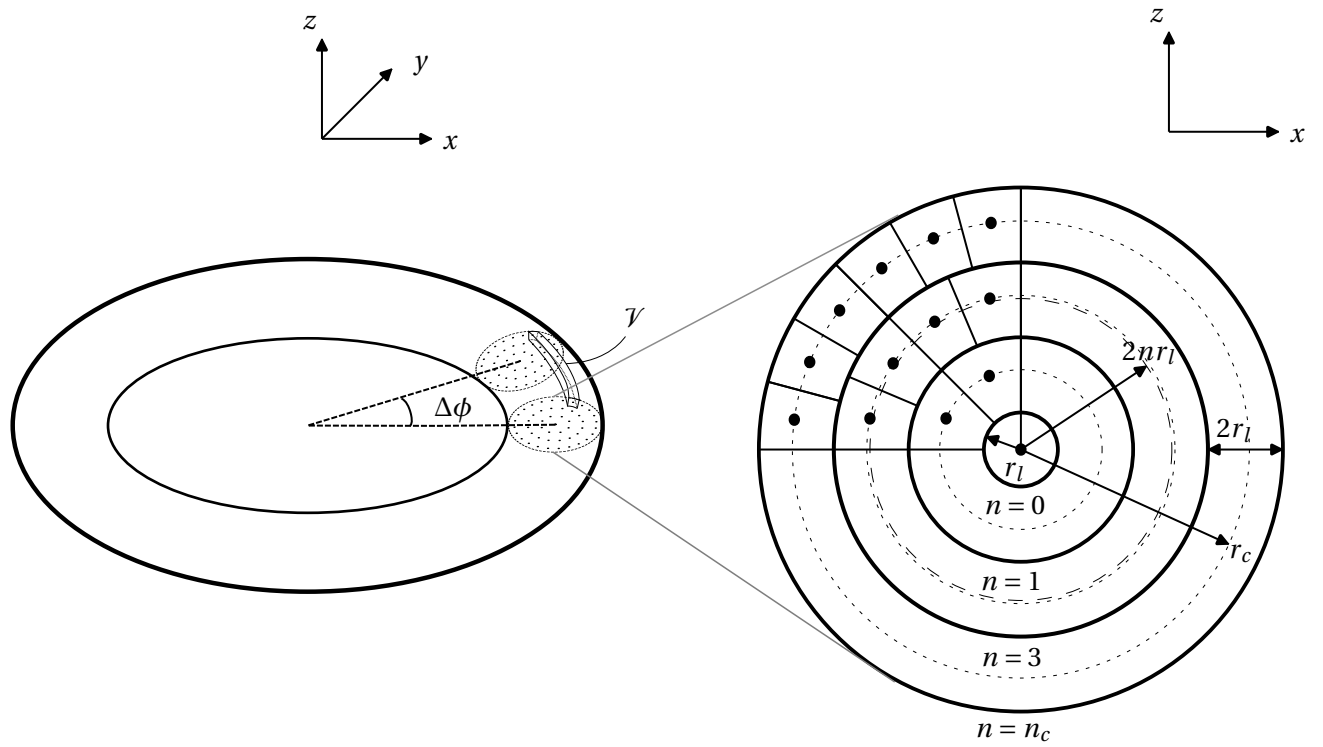
Figure 3.1 shows the analytical vortex ring of Eq. 3.28 modeled using VPM. The discretization strategy adopted is the same as suggested in Ref. [286]. The number of particles in each layer is  $8n$ , where  $n$  is the order of the layer, as shown in the figure, with a single particle forming the innermost layer. The entire vortex ring is represented using a number of cross-section layers and azimuthal layers; Fig. 3.1(a) shows two such azimuthal layers along with a pop-up showing the cross-section details. Three different discretizations of vortex rings were studied to verify the VPM implementation. The discretized rings are denoted using the number of cross-section layers they have and the number of azimuthal layers used. For example, the vortex ring with the coarsest

discretization in Table 3.3 with  $n_c = 4$  and  $\Delta\phi = 4.5^\circ$  is written as ‘4by80’. Figure 3.1(b) shows the complete discretized 4by80 vortex ring.

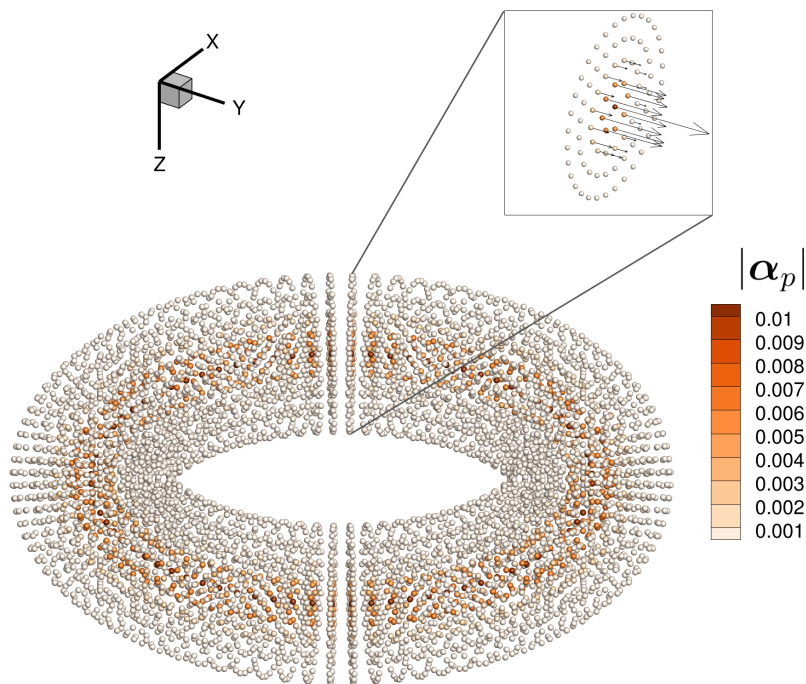
Using the discretization scheme illustrated in Fig. 3.1, the vortex ring of Eq. 3.28 was simulated with the VPM solver set up using the equations laid down in Sec. 3.1. The different diagnostic quantities from Sec. 3.2 were evaluated at each time step of the simulation, including the initial time step  $t = 0$ . The results at the initial time step are available from a number of studies in literature—Refs. [286], [253] and [270]. They are compiled together in Table 3.3 and compared to the results from the current study. The minor differences in the results across the different studies can be attributed to the different initialization processes adopted to allocate particle strengths. The current study used the same scheme as that adopted in Ref. [253]. The evolution of the diagnostic quantities over time is compared with the corresponding data available from Refs. [286] and [270]. Figure 3.2 compares the self-induced velocity of the 4by80 and 5by100 vortex rings. Figures 3.3 and 3.4 compare the linear flow field diagnostics and the quadratic flow field diagnostics, respectively. Based on the results presented in Table 3.3 and Figs. 3.2–3.4, the current VPM formulation stands verified.

Layers $n_c$	$\Delta\phi$	$\sigma$ [m]	Diagnostic	Current Study	Ref. [286]	Ref. [253]	Ref. [270]
4	4.50°	0.1	$ \mathbf{I} $	3.1655	3.2139	3.1654	3.1654
			$E_{\sigma f}$	1.0168	1.0476	1.0167	1.0167
			$E_\sigma$	1.0167	1.0475	1.0166	1.0166
			$\mathcal{E}_{\sigma f}$	60.4148	62.3842	60.4121	60.4120
			$\mathcal{E}_\sigma$	61.4135	61.3464	61.4109	61.4108
			$V_c$	0.2601	0.2660	0.2496	0.2495
			$dE_\sigma/dt$	-0.1223	-0.1276	-0.1496	-0.1235
5	3.60°	0.084	$ \mathbf{I} $	3.1785	3.2154	3.1785	3.1731
			$E_{\sigma f}$	1.0137	1.0365	1.0136	1.0103
			$E_\sigma$	1.0137	1.0364	1.0136	1.0103
			$\mathcal{E}_{\sigma f}$	57.6523	58.9907	57.6503	57.5490
			$\mathcal{E}_\sigma$	58.3194	58.3052	58.3174	58.3068
			$V_c$	0.2627	0.2660	0.2510	0.2505
			$dE_\sigma/dt$	-0.1225	-0.1268	-0.1526	-0.1234
6	3.08°	0.073	$ \mathbf{I} $	3.1865	3.2184	3.1864	3.1731
			$E_{\sigma f}$	1.0121	1.0314	1.0121	1.0103
			$E_\sigma$	1.0121	1.0314	1.0121	1.0103
			$\mathcal{E}_{\sigma f}$	56.0832	57.1632	56.0819	57.5490
			$\mathcal{E}_\sigma$	56.6203	56.6137	56.619	58.3068
			$V_c$	0.2632	0.2662	0.2519	0.2505
			$dE_\sigma/dt$	-0.1230	-0.1268	-0.1534	-0.1234

**Table 3.3.:** Comparison of diagnostic quantities for different vortex ring discretizations (see Table 3.2) across different studies from the literature.

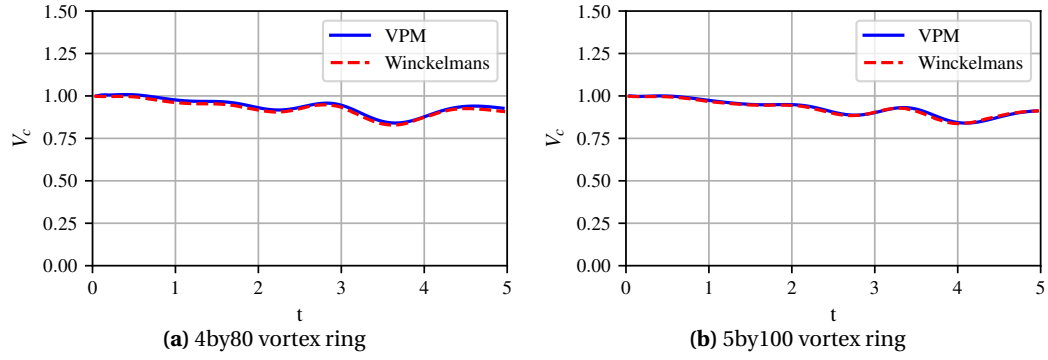


(a) Discretization details of a three-layer vortex ring.

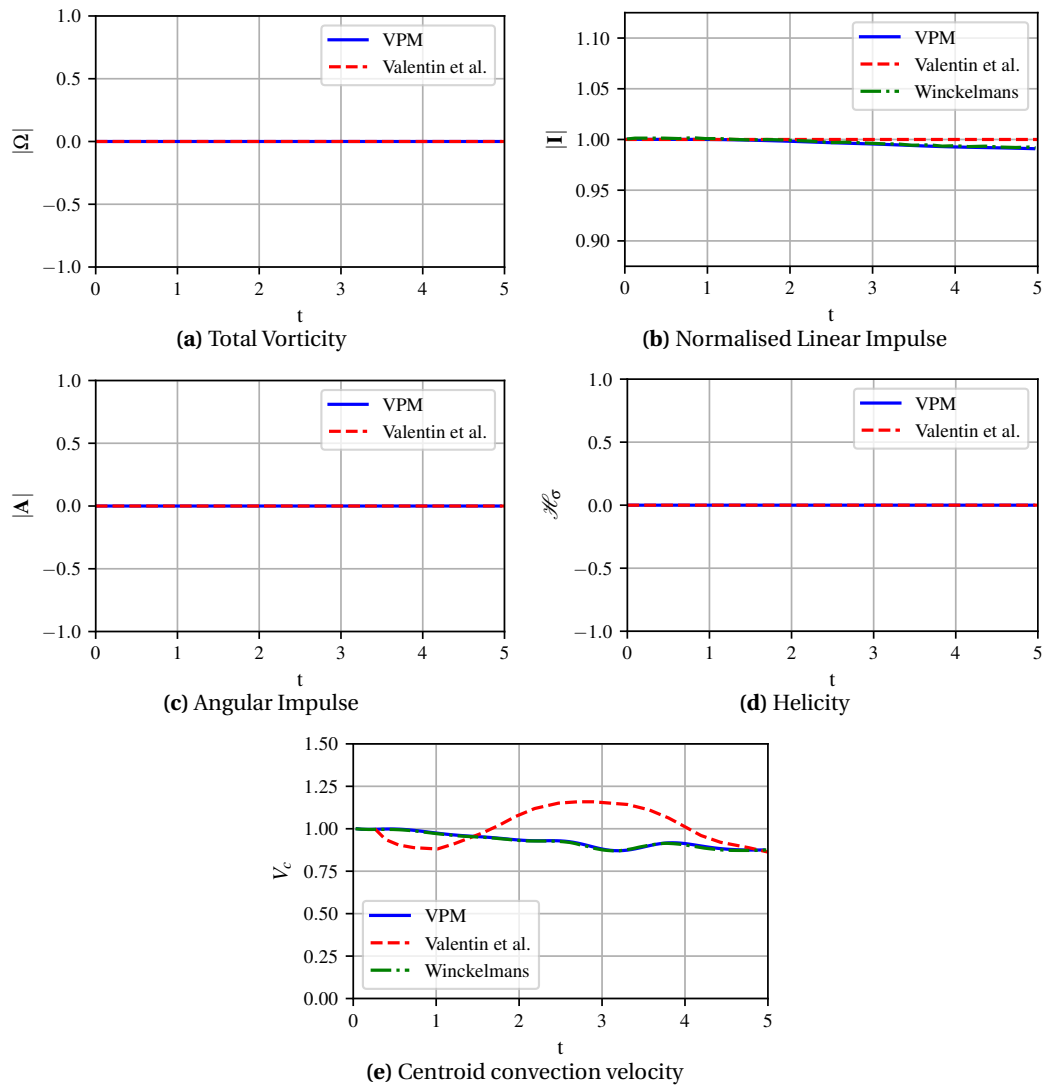


(b) Fully discretized 4by80 vortex ring. Inset shows particles with strength vectors.

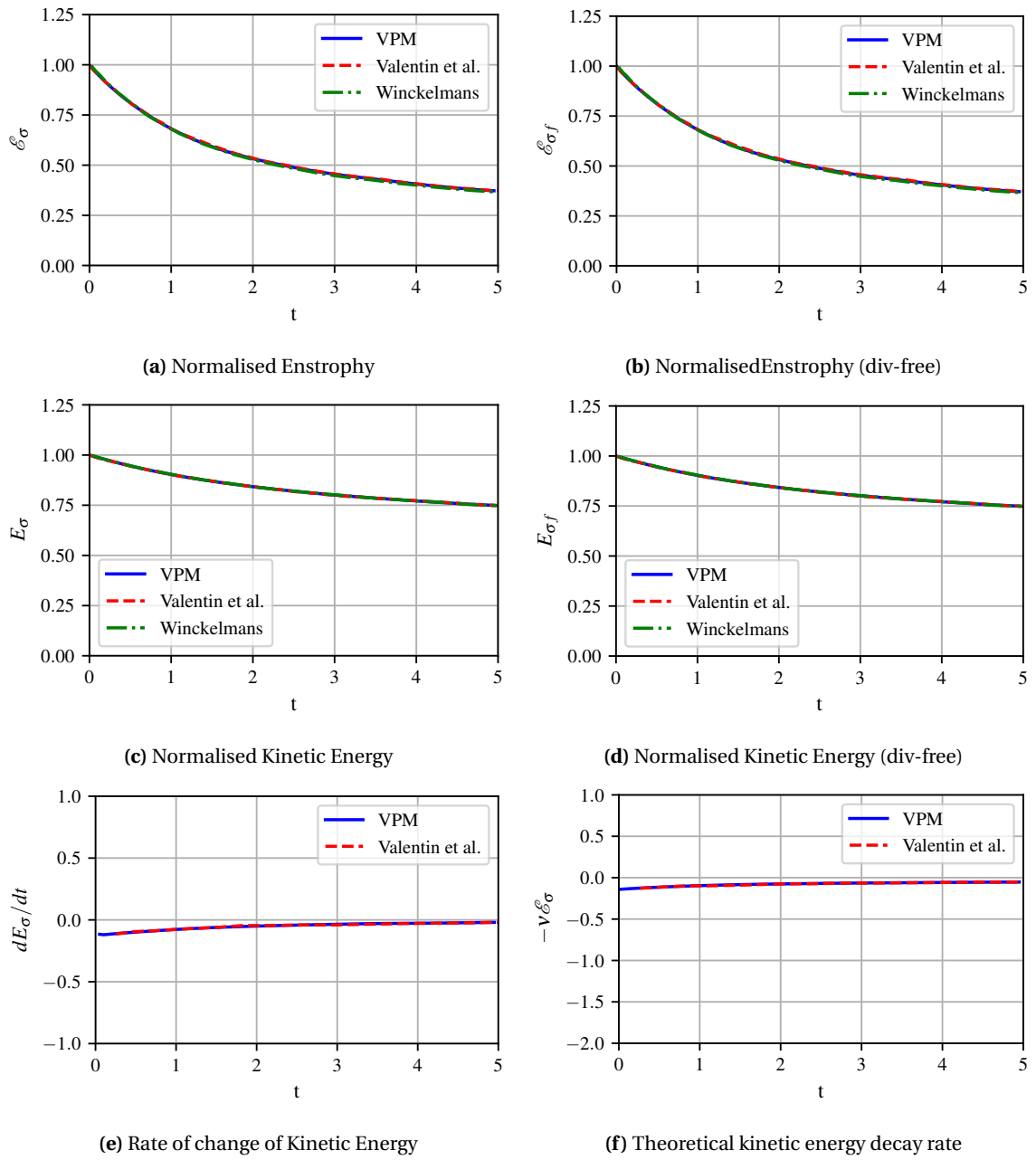
**Figure 3.1.:** Discretization of vortex rings using vortex particles.



**Figure 3.2.:** Comparison of predicted centroid convection velocity for different vortex ring discretizations using the current implementation and results available in Ref. [286](Winckelmans).



**Figure 3.3.:** Comparison of predicted linear diagnostics and convection velocity of 6by117 vortex ring versus results from Ref. [270](Valentin et al.) and, where available, Ref. [286](Winckelmans).



**Figure 3.4.:** Comparison of predicted quadratic flow field diagnostics and convection velocity of 6by117 vortex ring versus results from Ref. [270](Valentin et al.) and, where available, Ref. [286](Winckelmans).

### 3.4. Coupling with Comprehensive Analysis Solver

The verified VPM formulation detailed above was coupled to the comprehensive analysis code Dymore by replacing the inflow analysis module of Peters-He in Dymore with the VPM solver. That way, the blade aerodynamics analysis using lifting-line and airfoil tables is carried out using the internal aerodynamics of Dymore, while the wake system is solved using VPM. The equations governing the evolution and transport of the particles were already stated in Sec. 3.1 in sufficient detail. At each time step of the simulation, the inflow velocity induced by all the particles in the wake at a given airstation, or collocation point, can be obtained using Eq. 3.10 and using  $\mathbf{x}_{p_i} = \mathbf{x}_{ast_i}$ . This section deals with the initialization process implemented at the interface of Dymore and VPM, which led to birth of the particles at specific positions with prescribed strength.

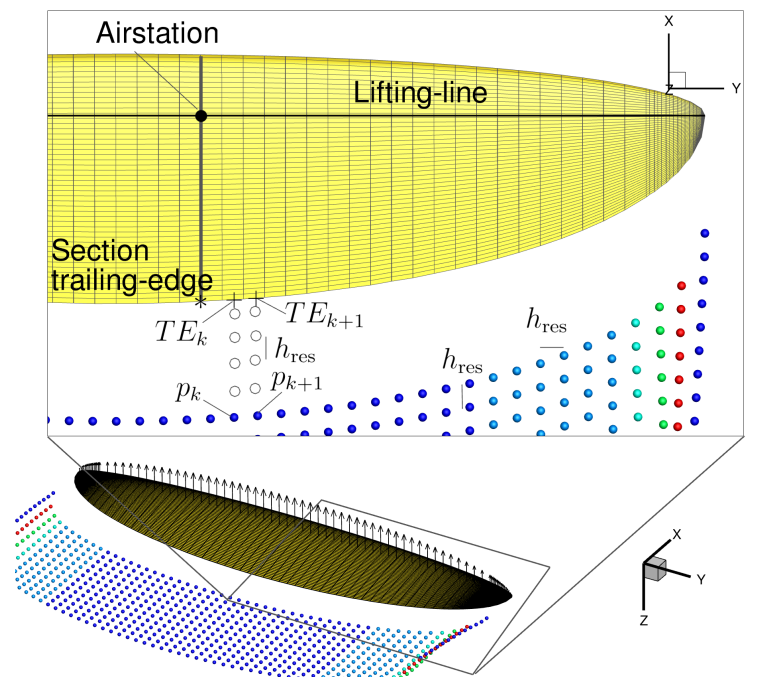
As detailed in Sec. 2.2, the blade aerodynamics model in Dymore uses the lifting-line theory. Each blade section cross-section has an airstation defined at its quarter-chord location with a single bound vortex. Based on the wing kinematics and flow field conditions, the section angle of attack is obtained using flow conditions at these airstations. Thereafter, the blade aerodynamic forces and moments are evaluated using the data provided by airfoil tables. However, it is the aerodynamic lift  $L'$  that is of interest for wake modeling since it is related to the bound circulation  $\Gamma$  at each airstation via Eq. 3.29. The generation of rotationality or fluid vorticity is governed by Kelvin's theorem of irrotationality [235](Section 2.11) and Helmholtz's theorems [235](Section 4.3). The former relates the time rate of change of bound circulation to the vorticity introduced in the flow field, and the latter dictates the spatial variation of vorticity in the case of finite wings. Ref. [6](Chapter 'Review') provides a more detailed description of the two theories and how they apply to airfoils and finite wings. Overall, the rate of vorticity generation at each airstation can be obtained using Eq. 3.30 and can be ascribed to each particle.

$$L' = \rho V_\infty \Gamma \quad (3.29)$$

$$\boldsymbol{\omega} = \underbrace{-\frac{d\Gamma}{dt}}_{\text{Kelvin's theory}} + \underbrace{\mathbf{v} \nabla \cdot \Gamma}_{\text{Prandtl's circulation theory}} \quad (3.30)$$

Since the airstations can be arbitrarily defined during model construction, an interpolation scheme was adopted so that particles were released not behind each airstation but rather uniformly across the span of the lifting-line. This was required in order to satisfy the requirement of uniform overlap of particles [286][253]. In order to separate the spatial and temporal dependence of the vortex particles, a new scheme was implemented to ensure that at the birth of the particles, the overlap remains constant irrespective of their spatial resolution or the time step size of the simulation. Figure 3.5 shows that this discretization was achieved not by placing particles between the current and the past trailing-edge positions, but rather the interpolated trailing-edge positions  $TE_k(t_n)$  at the current time step and the position of the last particle that was generated from that trailing-edge point. New particles were then linearly added until the distance between  $TE_k(t_n)$  and the latest particle became less than  $h_{res}$ —where  $h_{res}$  is the resolution parameter used to denote the distance between centroids of two neighboring particles at the time of their birth. Different studies tend

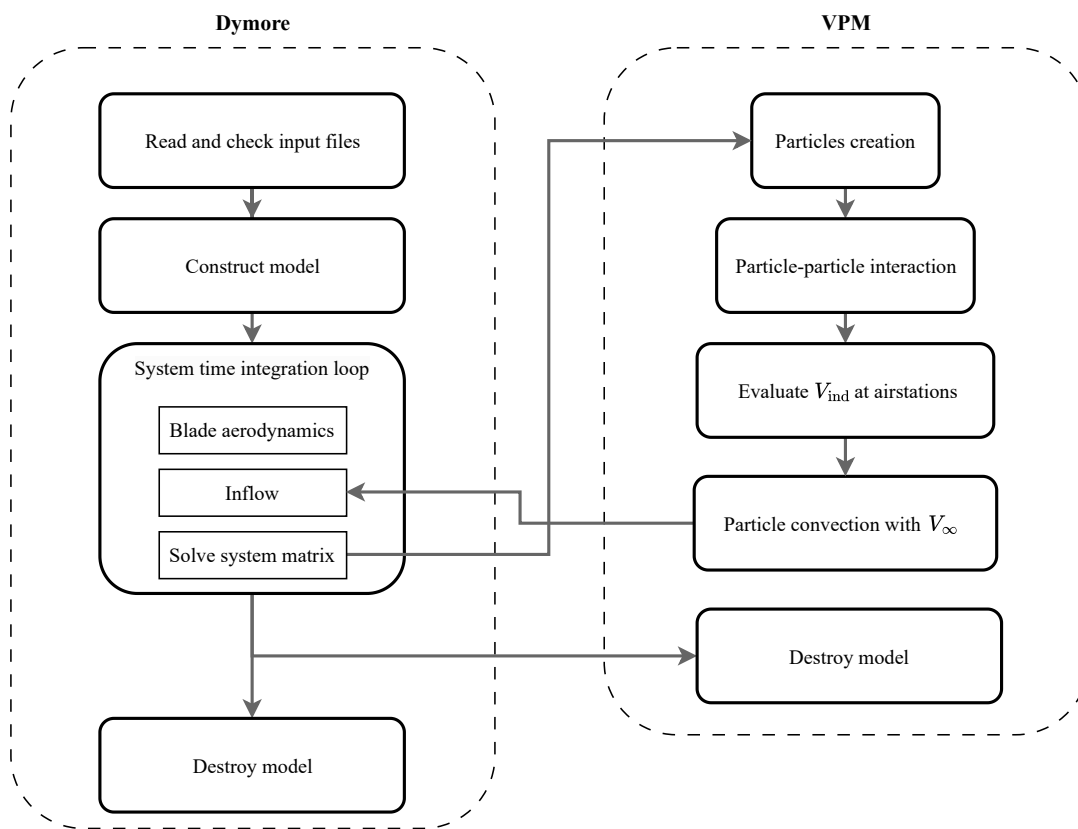
to use different approaches for the generation of particles; for example, in Ref. [253] vortex particles representing trailing vorticity were generated at the trailing-edge between the wing tips at a separation of  $2h_{\text{res}}$  and particle representing shed vortices were placed in between them, thereby bringing the overall wake resolution to  $h_{\text{res}}$ . In the current study, the shed and trailing vorticity were ascribed to a single particle by vectorially adding the two vorticities. In case only trailing vorticity or only shed vorticity needs to be modeled, the number of particles stays constant for a given wake resolution  $h_{\text{res}}$ . Note that this strategy of initializing the vortex particles is similar to that proposed in Ref. [271] but was devised independently. In the current work, the particle smoothing radius was chosen such that the overlap ratio was  $\sigma/h_{\text{res}} = 1.3$ .



**Figure 3.5.:** Illustration of the initialization of position and strength of particles for modeling trailing and shed vorticity.

The explicit time step coupling between Dymore and the VPM solver was established such that the exchange of information occurred at each time step. Any number of lifting-lines and corresponding airstations could be defined within the Dymore standalone model. For the purposes of coupling with VPM, the airstation positions were augmented with additional position information at the corresponding blade section from where vortex particles can originate. In the case of static analysis, the latter location corresponds to the lifting-line itself. In the case of unsteady aerodynamics analysis using the Peters unsteady model, it corresponds to the trailing-edge location of the wing/blade sections. This information was needed in order to solve for the instantaneous blade/wing trailing-edge positions accounting for an elastic deformation and blade/wing motion. Corresponding to each airstation, the following quantities were passed to the VPM solver so that interpolated results could be obtained at any given spanwise location—bound circulation,

trailing-edge position, far field oncoming flow velocity, and the wing/blade section span in order to carry out interpolation. All the passed information was evaluated in the inertial frame of reference. In turn, the wake solver returned the induced flow velocity due to all the particles in the wake, which were also evaluated in the inertial frame of reference at each airstation location. Instead of using file I/O, direct communication between the server (i.e., where the VPM solver runs) and the client machine (i.e., where Dymore runs) was established using transmission control protocol-based (TCP) sockets. The data that was set up to be exchanged was of modest size; only a few kilobytes were exchanged at each time step. However, the benefit of a TCP connection is that the two solvers can be made to run on different machines, and if they are connected via the internet, the coupled simulation could progress seamlessly. As detailed in Sec. 2.4, the rotor/wing simulations were run until the transient response phase was over. This was identified by ensuring that the cycle-to-cycle response variations were minimized. Figure 3.6 illustrates the overall Dymore-VPM analysis framework. It is worth noting that particles were convected with the mean flow velocity  $V_\infty$  after the induced velocity evaluation step; otherwise, an incorrect (lower) value of  $V_{ind}$  was obtained. The inability to correctly predict the induced velocity for the static elliptical wing case in Ref. [154] by the author was later found to be due to interchange of these two steps in that study.



**Figure 3.6.:** Flow chart indicating the flow of information in the coupled Dymore+VPM analysis framework.



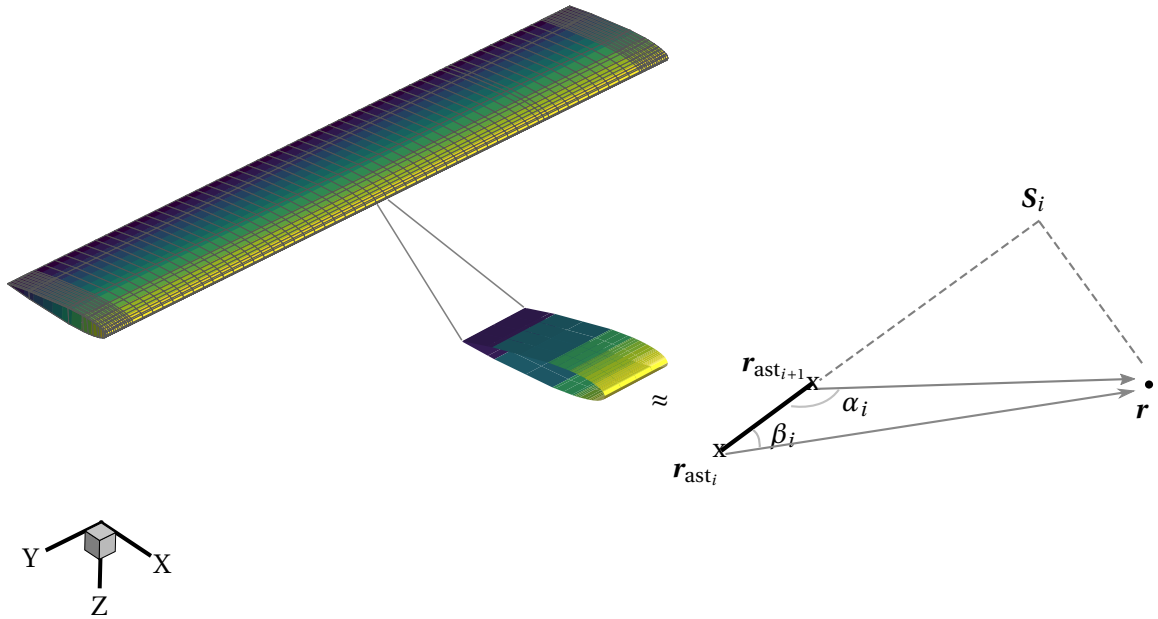
### 3.4.1. Bound vorticity-based induced velocity

One component of vorticity in the entire flow field that is not modeled using particles is the bound vorticity. This can have a non-negligible effect on the overall induced velocity at a given particle or another blade element when the bound vortex element, i.e., the blade section in question, is in close proximity. So, the effect of bound vortex elements is separately accounted for, as detailed below.

The Biot-Savart law relates the velocity induced by an elemental vortex tube at a given point in the fluid domain to the vorticity strength, as given in Eq. 3.31. The derivation of this expression can be referred from Ref. [235](Page 142). The velocity induced due to a finite vortex segment at a location of interest  $\mathbf{r}$  can be derived to be given by Eq. 3.32. In the context of the current modeling strategy in Dymore, the bound circulation was known at the airstations and assumed to vary linearly across the lifting-line segments connecting the closest pairs of airstations. Figure 3.7 schematically illustrates the different relevant parameters involved in Eqs. 3.33–3.42, which were used to obtain the total induced velocity given by Eq. 3.43.

$$dV_{\text{ind}} = \frac{\Gamma}{4\pi h^2} \sin\theta ds \quad (3.31)$$

$$V_{\text{ind}} = \frac{\Gamma}{4\pi |\mathbf{S}_i - \mathbf{r}|} (\cos\alpha_i + \cos\beta_i) \quad (3.32)$$



**Figure 3.7.:** Illustration of the velocity induced by the bound circulation around a wing segment, which is modeled as a lifting-line element, on a particle located at  $\mathbf{r}$ .

$$\mathbf{S}_i = \mathbf{r}_{\text{ast}_1} + d(\mathbf{r}_{\text{ast}_{i+1}} - \mathbf{r}_{\text{ast}_i}) \quad (3.33)$$

$$\begin{aligned} (\mathbf{r}_{\text{ast}_{i+1}} - \mathbf{r}_{\text{ast}_i}) \cdot (\mathbf{r} - \mathbf{S}_i) &= 0 \\ \mathbf{S}_i \cdot (\mathbf{r}_{\text{ast}_{i+1}} - \mathbf{r}_{\text{ast}_i}) &= \mathbf{r} \cdot (\mathbf{r}_{\text{ast}_{i+1}} - \mathbf{r}_{\text{ast}_i}) \\ [\mathbf{r}_{\text{ast}_i} + d(\mathbf{r}_{\text{ast}_{i+1}} - \mathbf{r}_{\text{ast}_i})] \cdot (\mathbf{r}_{\text{ast}_{i+1}} - \mathbf{r}_{\text{ast}_i}) &= \mathbf{r} \cdot (\mathbf{r}_{\text{ast}_{i+1}} - \mathbf{r}_{\text{ast}_i}) \\ \Rightarrow d &= \frac{(\mathbf{r} - \mathbf{r}_{\text{ast}_i}) \cdot (\mathbf{r}_{\text{ast}_{i+1}} - \mathbf{r}_{\text{ast}_i})}{|\mathbf{r}_{\text{ast}_{i+1}} - \mathbf{r}_{\text{ast}_i}|^2} \end{aligned} \quad (3.34)$$

$$\mathbf{l}_i = \mathbf{r}_{\text{ast}_{i+1}} - \mathbf{r}_{\text{ast}_i} \quad (3.35)$$

$$\hat{\mathbf{l}}_i = \frac{\mathbf{l}_i}{|\mathbf{l}_i|} \quad (3.36)$$

$$\mathbf{s}_i = \mathbf{r} - \mathbf{S}_i \quad (3.37)$$

$$\begin{aligned} s_i &= |\mathbf{s}_i| \\ \hat{\mathbf{s}}_i &= \frac{\mathbf{s}_i}{s_i} \end{aligned} \quad (3.38)$$

$$\gamma_i^0 = \frac{\Gamma_i |\mathbf{r}_{\text{ast}_{i+1}} - \mathbf{S}_i| + \Gamma_{i+1} |\mathbf{S}_i - \mathbf{r}_{\text{ast}_i}|}{l_i^2} \quad (3.39)$$

$$\gamma_i^1 = \frac{\Gamma_{\text{ast}_{i+1}} - \Gamma_{\text{ast}_i}}{l_i} \quad (3.40)$$

$$\alpha_i = \cos^{-1} \frac{(\mathbf{r} - \mathbf{r}_{\text{ast}_{i+1}}) \cdot (\mathbf{r}_{\text{ast}_{i+1}} - \mathbf{r}_{\text{ast}_i})}{|\mathbf{r} - \mathbf{r}_{\text{ast}_{i+1}}| |\mathbf{r}_{\text{ast}_i} - \mathbf{r}_{\text{ast}_{i+1}}|} \quad (3.41)$$

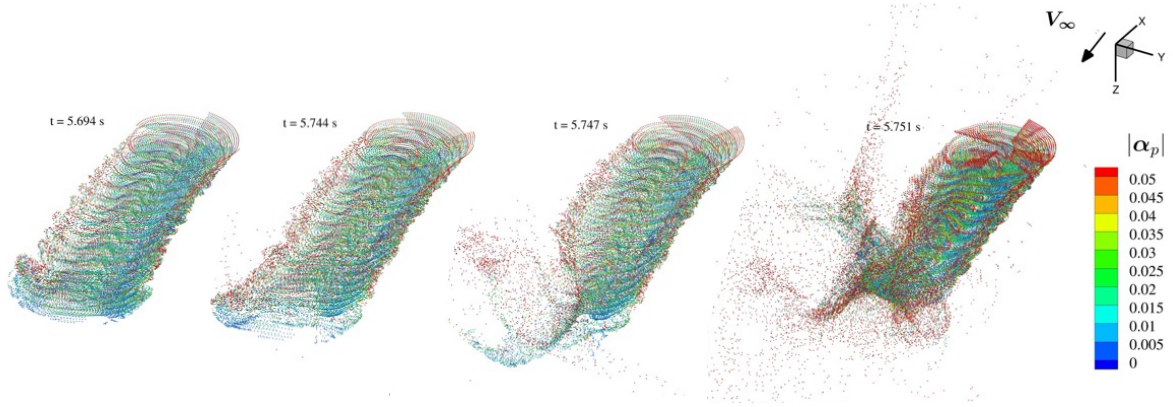
$$\beta_i = \cos^{-1} \frac{(\mathbf{r} - \mathbf{r}_{\text{ast}_i}) \cdot (\mathbf{r}_{\text{ast}_{i+1}} - \mathbf{r}_{\text{ast}_i})}{|\mathbf{r} - \mathbf{r}_{\text{ast}_i}| |\mathbf{r}_{\text{ast}_i} - \mathbf{r}_{\text{ast}_{i+1}}|} \quad (3.42)$$

Where  $i$  represents a blade element based on the spanwise discretization of the blade. The total induced velocity experienced by each particle due to all the elements combined can then be written as given in Eq. 3.43. Here,  $n_{\text{span}}$  is the number of spanwise segments on a given blade which is one less than the number of airstations. The induced velocity due to the bound vortex effect of the other blade panels can be obtained using this expression by replacing  $\mathbf{r} = \mathbf{r}_{\text{ast}_i}$ .

$$\mathbf{V}_{\text{ind}}(\mathbf{r}) = \sum_{N_b} \sum_{i=0}^{n_{\text{span}}} \frac{\hat{\mathbf{l}}_i \times \hat{\mathbf{s}}_i}{4\pi s_i} [l_i \gamma_i^0 (\cos \beta_i + \cos \alpha_i) + s_i \gamma_i^1 (\sin \beta_i - \sin \alpha_i)] \quad (3.43)$$

### 3.4.2. Vortex stretching divergence problem

During the course of the current work, it was encountered that VPM simulations diverged after a certain time before converged simulation results could be obtained. Figure 3.8 shows the sequence of simulation snapshots of the Bo 105 rotor in forward flight where the particles-based wake system eventually diverged. This divergence was attributed to unphysical vortex stretching being experienced by the oldest particles in the wake. Studies in literature have suggested some steps that can be undertaken in order to resolve this issue. Ref. [253] has suggested using particle split and merge techniques in order to avoid wake vorticity divergence. Ref. [303] has recommended relaxation of the vorticity field. However, the implementation of these strategies did not resolve this issue in the current work. Therefore, all the results presented in Chapter 5 involving the VPM solver were obtained by ‘turning off’ vortex stretching, i.e., Eq. 3.13 was excluded from the formulation. Ref. [20] discusses the effect of vortex stretching on wake development in the context of free wake methods and shows that these effects are present in all operating conditions, and the effects are not necessarily negligible. However, all results presented later in Chap. 5 using VPM model are devoid of the influence of vortex strain.



**Figure 3.8.:** Snapshots of a diverging coupled Dymore+VPM simulation of the Bo 105 rotor in forward flight, with vortex stretching included.

## 3.5. Code Acceleration

The problem of flow field solution using VPM is a classical  $N$ -body problem where  $N$  refers to the entity of interest within the formulation, i.e., vortex particles. Given that each particle influences every other particle within the domain of investigation, the computational complexity scales as  $\mathcal{O}(N^2)$ . As the simulation progresses new particles are continuously added at the blade/wing trailing-edge. This means that each time step progressively takes  $\mathcal{O}(N_p^2)$  time for execution, which can quickly slow down the overall simulation. For this purpose, VPM solvers generally implement a strategy to delete particles based on the criteria of age or distance from the location of interest where their influence needs to be calculated. This is an acceptable practice since the induced velocity contribution at a point scales inversely with square of the distance. In the current study, the

maximum number of particles within the simulation was capped to a reasonable value such that the wake structure in the near wake of the blade/wing was correctly represented. In all the cases investigated in this work, the wake eventually convected away as new particles were constantly introduced into the simulation flow field. Once a critical number of particles were reached, the simulation proceeded by deleting the oldest particles, which are likely to be far away from the region of interest and, therefore, of little consequence for the overall analysis.

Given that the number of particles in a simulation can reach up to  $N_p \approx 10^5$ , the computational cost of a direct VPM solver can still be prohibitive. There are algorithmic techniques such as the Barnes-Hut algorithm [174] and the Fast Multipole Method [299] available for accelerating  $N$ -body simulations. These strategies are necessary in order to perform simulations with good resolution, i.e., a large number of particles. Most well-known VPM solvers for rotary-wing simulations, such as VVPM[97], FLOWVPM[254] and DUST [2], use the FMM algorithm to achieve computational acceleration for well-resolved flows. In the current implementation, the process of particle-particle interaction was parallelized using multiple CPU cores using the OpenMP paradigm [15]. This demonstrated improved execution speeds compared to single CPU core execution. Additionally, another implementation was made for execution on a graphics processing unit GPU. In general, executing the VPM solver on GPU allowed the computation time to be an order of magnitude lower compared to a single/multi-core CPU implementation. The GPU version of the VPM solver was adopted for all simulations conducted within this study.

## 4. Aeroacoustic Noise

There is a constant effort in the rotorcraft community to minimize the aural footprint of rotors. Based on computational and experimental studies involving active rotors, discussed in Sec. 1.4, it is evident that higher harmonic blade section profile changes can influence rotor noise emissions. Due to the large variation in blade surface profile that the FishBAC mechanism is capable of delivering, it can potentially be used to modify noise emissions from the rotor. As already mentioned, a previous limited investigation carried out by the author using CAMRAD II and PSU-WOPWOP showed promising results towards this goal [153]. An extensive post-processing and visualization framework called *HeliNoise* was created for this purpose and has since been made open source [9]. In the current work, this framework was extended to carry out acoustic analysis using the comprehensive analysis output from Dymore (see Chap. 2) as well as the augmented framework obtained after coupling with VPM (see Sec. 3.4).

This chapter describes the toolchain established to carry out an acoustics analysis of an active or passive rotor. Section 4.1 first details the theoretical foundations of acoustics analyses that facilitate rotor noise prediction by post-processing the output from a comprehensive analysis solver. In this study, the rotor acoustics solver called PSU-WOPWOP [245] was used<sup>1</sup>. Section 4.2 provides a brief overview of this solver. Subsequently, Sec. 4.3 describes the framework that was created to ensure seamless processing of Dymore or Dymore+VPM simulation output and preparing appropriate input files for the acoustics solver. Once the acoustic simulation was carried out, this framework also allowed visualization of the resulting output in order to quickly generate a qualitative and quantitative overview of the output.

### 4.1. Theoretical Principles

The principles of mass, momentum, and energy conservation that govern fluid dynamics also govern the physics of aerodynamically generated noise by moving surfaces. The mathematical theory to quantify noise generated by such surfaces was first proposed by Ffowcs Williams and Hawkins (FW-H) using Eq. 4.1 [80], hereafter referred to as the FW-H equation. This equation is an exact rearrangement of the Navier-Stokes (NS) equations for arbitrarily moving surfaces. For this reason, solving the FW-H equation over the flow domain is no easier than solving the NS equations themselves. It is formulated in generalized function space so that it becomes valid in an unbounded fluid domain. This makes it amenable to solve using the free-space Green's function.

---

<sup>1</sup>The solver was provided as an executable file (no source code) by Prof. Kenneth Brentner of Penn State University.

One such integral solution in time and space was proposed in Ref. [77] and is commonly referred to as Formulation 1A (Eq. 4.2).

$$\begin{aligned}
\frac{1}{a_s^2} \frac{\partial^2 p'}{\partial t^2} - \nabla^2 p' &= \underbrace{\frac{\partial}{\partial t} [\rho v_n \delta(f)]}_{\text{monopole source term}} - \underbrace{\frac{\partial}{\partial x_i} [l_i \delta(f)]}_{\text{dipole source term}} + \underbrace{\frac{\partial^2}{\partial x_i \partial x_j} [T_{ij} H(f)]}_{\text{quadrupole source term}} \quad (4.1) \\
4\pi p'_{\text{F1A}}(\mathbf{x}, t) &= \int_{f=0} \left[ \underbrace{\frac{\rho (\dot{v}_n + v_n)}{r(1-M_r)^2} + \frac{\rho v_n (r\dot{M}_r + a_s(M_r - M^2))}{r^2(1-M_r)^3}}_{\text{monopole source term (thickness noise)}} \right]_{\text{ret}} dS \\
&+ \frac{1}{a_s} \int_{f=0} \left[ \underbrace{\frac{\dot{l}_r}{r(1-M_r)^2} + \frac{l_r - l_M}{r^2(1-M_r)^2} + \frac{l_r (r\dot{M}_r + a_s(M_r - M^2))}{r^2(1-M_r)^3}}_{\text{dipole source term (loading noise)}} \right]_{\text{ret}} dS \quad (4.2)
\end{aligned}$$

Based on Eq. 4.1, knowledge of  $\rho$ ,  $v_n$ , and  $p$  is required on the surface of the moving body. The stress tensor  $T_{ij}$  is required in the fluid domain beyond the surface in order to quantify the acoustic pressure perturbation  $p'$  produced by the body in motion [47]. These quantities can be difficult to obtain, so a direct solution of Eq. 4.1 is not used for rotor noise prediction. Instead, the integral approach of Eq. 4.2 is used. Here, integration is carried out over the impermeable surface responsible for perturbing the flow, i.e., the rotor blade, by evaluating the relevant quantities at retarded time, i.e. time when the sound originated at the blade. It is different from observer time  $t$  due to the finite speed of sound  $a_s$ .  $f$  denotes the surface over which the surface integral is evaluated; this is usually made to coincide with the blade surface since that is where the quantities within the integral are available from mid-fidelity simulations. The subscripts  $n$  and  $r$  correspond to the vector directions normal to  $f$  and the radiation vector from the surface grid cell to the observer, respectively.  $\rho_0$  refers to the quiescent flow density,  $v$  is the velocity of the surface  $f$ ,  $M$  is its Mach number, and  $l$  is the aerodynamic pressure acting on the fluid due to the surface element  $dS$ .

In Eq. 4.2, the total acoustic pressure perturbation is ascribed to physically relevant attributes such as the lifting-surface geometry and the blade airloads. The different source terms in Eq. 4.1 are categorized using monopole, dipole, and quadrupole terms based on their mathematical structure [47]. The monopole and dipole source terms are transformed to 'thickness noise' and 'loading noise' terms, respectively, while the quadrupole source terms have been dropped entirely. Thickness noise component refers to acoustic perturbations that depend on the blade geometry and the blade motion. In order to obtain the corresponding integration result, the blade geometry needs to be defined using a surface grid. The loading noise component requires, in addition to the airloads on the blade surface, the blade geometry and motion information. This grid-based blade airloads, geometry, and motion information is easily obtained when aerodynamics are evaluated using an Eulerian CFD analysis. In this study, since the blade airloads are obtained using a lifting-line solution from Dymore, an additional post-processing framework was required. Such a framework would take the local blade airfoil profile at a given spanwise station and, together with the elastic beam motion information over the azimuth, generate the blade surface configuration at each time step. This is a valid exercise since rotor blades are assumed to not undergo any chordwise section

deformation. This framework is detailed later in Sec. 4.3.

The quadrupole source term requires a volume flow field solution around the rotor blade and can only be obtained using a traditional CFD solution. This can also be surmised from Eq. 4.1 where the Dirac delta function  $\delta(f)$  in the monopole and the dipole terms indicate that the corresponding flow or loading information is required only at the surface  $f = 0$ . The quadrupole term has a Heaviside step function associated with it, which means that information regarding the stress tensor  $T_{ij}$  is desired in the entire source region extending beyond the integration surface  $f > 0$ . This term captures the noise due to turbulence in the flow, which, in certain scenarios, can become comparable to the loading and thickness noise components. This occurs when the blade tip Mach numbers are low, for example, in the case of multi-rotor eVTOLs, and various strategies have been suggested to simulate it using physics-based models [162]. When the blade tip Mach numbers are high, as is typical of conventional helicopters, this quadrupole component of noise can be ignored [231] (Page 90). For conventional helicopter rotors, the quadrupole term becomes dominant for flight conditions where the blade tip approaches the delocalization Mach number, so named because the transonic flow due to high blade tip speed causes shock waves to appear that detach from the blade. This happens typically when the blade tip Mach number approaches 0.9 [231] and leads to much higher noise than that predicted just using the monopole and dipole contributions. In such a scenario, the contribution due to the quadrupole term cannot be ignored without incurring a significant error in noise prediction. In the current study, the quadrupole source term was not evaluated or modeled. The reason for this is two-fold. The first is that the comprehensive analysis framework, together with the wake solution using VPM, is not capable of modeling flow field turbulence stresses. However, this is acceptable since, as already mentioned, the loading and the thickness noise dominate at the operating conditions encountered on a helicopter rotor. The second reason is that the flight conditions analyzed in the current work were chosen such that at no point on the blade section the Mach number exceeded 0.9. So, the quadrupole source term is expected to be much smaller in comparison to the dipole and the monopole source terms, and therefore, the error incurred from neglecting it is acceptable.

## 4.2. Aeroacoustics Solver

The FW-H formulation has been successfully applied in the past for post-processing comprehensive analysis output data in order to predict rotor aeroacoustic noise. The most common approach used is the Farassat's F1A formulation; for example, see Refs. [51], [120], [134], and [298]. The rotor noise prediction code PSU-WOPWOP [245], developed at Penn State University by Prof. Kenneth Brentner and his students, was used to predict the rotor acoustic noise in the present work. The theoretical basis of the code is Eq. 4.1. PSU-WOPWOP uses the F1A formulation and solves it numerically using schemes detailed in the Ref. [102]. It is capable of predicting periodic rotor noise, i.e., steady-state rotor operation, as well as noise during transient maneuvers [58][199]. It has been successfully used to study noise emissions from conventional rotors [229][245], compound helicopter designs [29][275], coaxial rotors [134][304], multirotor eVTOL aircraft [121][274], and active rotor designs [44][153][249].

The formulation F1A (Eq. 4.2) was later expanded in Ref. [101] to include the effect of changing surface area of the panels that make up the rotor blade surface. The source of such an effect could either be elastic deformation experienced by the blade or an active on-blade mechanism that influences the blade surface area itself—for example, an extendable tab mechanism that protrudes in and out of the blade trailing-edge, a chord extension mechanism that leads to change in blade solidity, etc. In the current study, in order to correctly include any effects of blade flexibility and camber deflection on blade surface deformation and, consequently, on noise emissions, the improved Farassat’s formulation 1A was used. It was proposed in Ref. [101] using Eq. 4.3 by assuming that each surface panel, over which integration is carried out, can itself undergo deformation. Here, the formulation includes two additional integrals that model the effect of change in the Jacobian (Eq. 4.4) that relates the panel area to the coordinates describing the blade surface.

$$p'(\mathbf{x}, t) = p'_{\text{F1A}}(\mathbf{x}, t) + \frac{1}{4\pi} \left[ \int_{f=0} \left( j \frac{\rho_0 v_n}{r|1-M_r|^2} \right)_{\text{ret}} + \frac{1}{a_s} \left( j \frac{l_r}{r|1-M_r|^2} \right)_{\text{ret}} du_1 du_2 \right] \quad (4.3)$$

$$dS = J du_1 du_2 \quad (4.4a)$$

$$J = \frac{1}{\left| \frac{\partial u_1}{\partial s_1} \right| \left| \frac{\partial u_2}{\partial s_2} \right|} \quad (4.4b)$$

The loading noise was obtained using the compact formulation of Eq. 4.5, proposed originally in Ref. [46], instead of the surface formulation of the loading noise from Eq. 4.2. This was necessary since comprehensive analyses in the current work were based on lifting-line blade aerodynamics analysis and were, therefore, capable of only predicting blade airloads at a single collocation point at each blade section.

$$4\pi p'_{\text{F1A,L}}(\mathbf{x}, t) = \frac{1}{a_s} \int_{f=0} \left[ \frac{\dot{l}_r}{r(1-M_r)^2} + \frac{l_r - l_M}{r^2(1-M_r)^2} + \frac{l_r(r\dot{M}_r + a_s(M_r - M^2))}{r^2(1-M_r)^3} \right]_{\text{ret}} dS \quad (4.5)$$

PSU-WOPWOP uses the integral approach, developed in Ref. [77], in order to obtain the acoustic pressure fluctuations in the time domain. From Eqs. 4.2 and 4.3, it is evident that complete information on the blade surface motion and elastic deformation is required to accurately predict the corresponding acoustic pressure. It was shown in Ref. [50] that the blade geometry and motion can have a critical influence on the acoustic prediction in certain regions around the rotor. For example, it was shown that the blade pitching motion and coning are relevant to capturing the noise below the rotor and in the tip-path plane. For this purpose, a post-processing framework is required to obtain blade surface motion information since this level of detail is lacking in mid-fidelity comprehensive analyses where the blade is aerodynamically and structurally modeled as a representative one-dimensional entity. This is described in the following section.

The acoustic analysis itself is computationally fast, on the order of one second per blade per observer location for blade surface discretization of the order of  $10^4$  panels per blade. When the



discretization resolution of the blade surface is increased, the integration in Eqs. 4.3–4.5 then needs to be carried out over a larger number of elements. This has an adverse effect on the computation speed. In addition to that, the duration of simulation time and the time step size can also have an impact on the computation time. Since the current work is concerned with trimmed rotor steady-state simulations, the resultant rotor acoustic output is always periodic. Therefore, only one revolution of the rotor needs to be simulated. The number of steps that make up the rotor revolution does not have to conform to the discretization time step used in the comprehensive analyses. Instead, the temporal discretization in acoustic simulations is dictated by the range of acoustic pressure frequencies that are of interest. For example, in order to capture the high-frequency acoustic pressure perturbations due to a rotor operating in BVI state, the temporal discretization of the acoustic simulations needs to be appropriately adjusted.

The blade airloads could be obtained from comprehensive analysis using a lifting-line model or a blade element momentum theory model, or using CFD simulations. The premise is that the closer the source terms on the right-hand side of Eq. 4.2 represent the true physics, the more accurate is the predicted acoustic noise. However, this is valid only when the quadrupole term of Eq. 4.1, which was dropped in Eq. 4.2, is comparably lower than the other two source terms. For the maximum advance ratio of  $\mu = 0.30$  used for acoustics investigation in this work, the advancing blade tip Mach number does not exceed 0.835 in ISA conditions. Given that the NACA23012 is a 12% thick airfoil, it is reasonable to assume that no shocks occur throughout the investigated flight regime and that acoustic predictions based on flexible blade F1A formulation in PSU-WOPWOP are valid. Broadband noise is not modeled in the current study since it is usually relevant only for low RPM rotors [231].

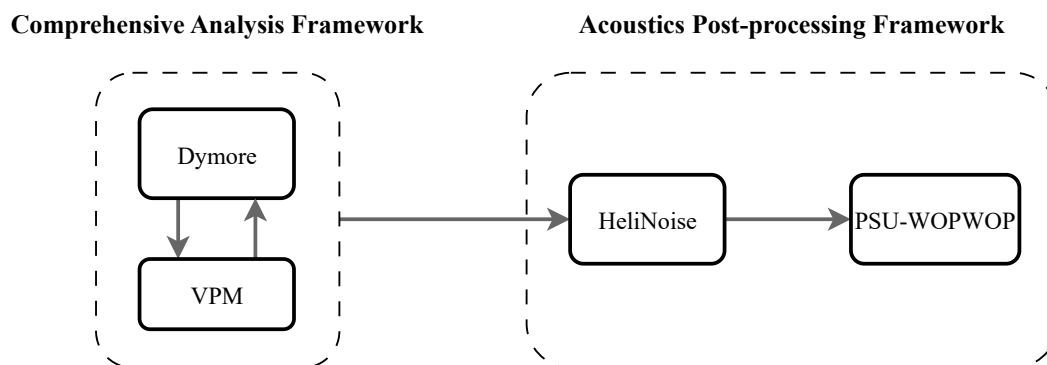
### 4.3. Post-processing Framework

As mentioned in Sec. 4.2, relevant output data from any comprehensive analysis framework can be used as input to PSU-WOPWOP for acoustics analysis. In the literature, studies often take the liberty of referring to this as a ‘coupling’. Since there is no flow of information back from the acoustics solver, the operation is merely one of post-processing of data. In that sense, PSU-WOPWOP has been coupled in Ref. [236] to the comprehensive analysis code RCAS to carry out acoustic analysis of different rotor configurations. A combined framework of CAMRAD II + PSU-WOPWOP was used in a previous study carried out by the author to analyze a full-scale Bo 105 rotor with an active camber morphing mechanism [153]. In the current work, a post-processing framework with Dymore was independently established. Since Dymore+VPM coupled analysis merely replaces the in-built lower order inflow model within Dymore, the same post-processing framework can be used for either the standalone Dymore or coupled Dymore+VPM simulations as long as the underlying rotor multibody model remains the same.

As is evident from Eq. 4.2, the acoustic pressure disturbance due to the lifting surface under investigation is obtained via a surface integration of relevant flow and aerodynamic quantities. These quantities can be obtained from either CFD simulations or from lifting-line-based analyses. Surface discretization is inherent to CFD simulations, and the same can be imported directly within the acoustic analysis framework. However, rotor comprehensive analyses generally use a lifting-line representation of the blade aerodynamics and a 1-D beam representation for structural analysis. So, a geometric discretization of the lifting surface is not inherent to comprehensive analyses

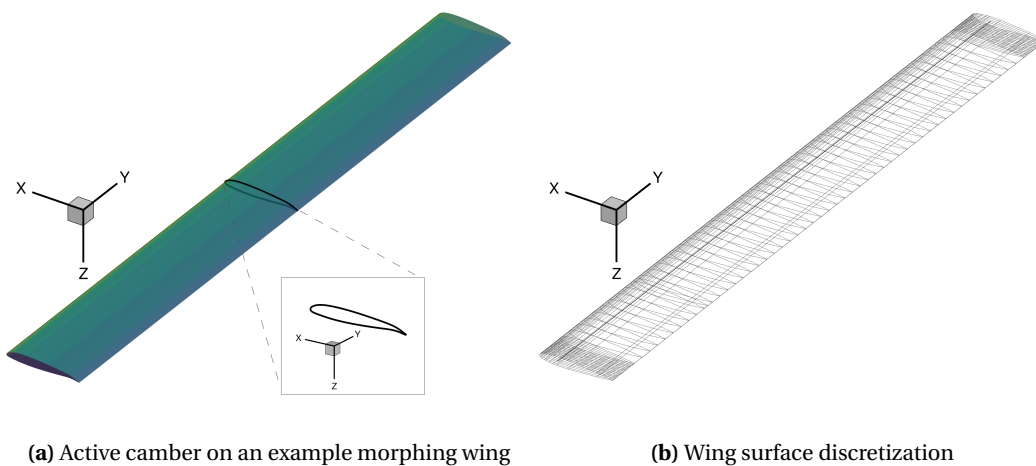
and needs to be generated separately. For the current work, involving analyses based on Dymore output results, a framework was created to generate a structured surface grid based on blade geometry data. For this purpose, the existing functionalities available for blade surface generation within the in-house open-source multidisciplinary blade design and optimization tool SONATA [206] were leveraged, and the framework was built on top of it. This also had the added benefit of future incorporation of acoustic footprint as an objective within blade design optimization.

Figure 4.1 illustrates the entire cycle of data processing and the corresponding tools used in order to prepare input files for acoustics analysis using PSU-WOPWOP. The blade geometry definition was provided as a YAML file. It contains information such as the airfoil profile, chord length, reference beam location, blade pitch, etc., at each spanwise location to generate the blade surface geometry. Based on this information and the custom methods introduced in SONATA to generate the lifting surface geometry for the purpose of acoustic analysis, a rigid blade geometry could be generated. The elastic blade deformation was obtained from the trimmed rotor Dymore simulation results at each blade section as a set of three displacements and three rotations at each time step. These were combined with the rigid blade definition to obtain the elastic blade surface definition and stored as a binary file, called a ‘patch’ file, in a format specific to PSU-WOPWOP [102]. The blade airloads were obtained from Dymore output files and stored without modification in a binary format within a ‘functional’ data file. While the blade deformation and airloads output in any reference frame could be utilized, in the current study, all the processed output was in the local blade frame. The entire toolchain, referred to as *HeliNoise*, was responsible for processing Dymore output, preparing input files for acoustics analysis, and visualizing the output noise. Note that a similar process of generating the surface geometry and loading files was used in an earlier study by the author, see Ref. [153].



**Figure 4.1.:** Illustration of the rotor noise analysis toolchain comprising of the *HeliNoise* framework created to handle data output from the rotor aeromechanics analysis framework and convert into appropriate input for PSU-WOPWOP.

Figure 4.2 shows the surface geometry of the active-camber morphing wing obtained using *HeliNoise* and the corresponding surface discretization generated. Note that the chordwise discretization resolution in Fig. 4.2(b) has been lowered for clarity purposes. The entire *HeliNoise* toolchain detailed above works seamlessly for isolated wings, rotors with any number of blades, or multi-rotor systems simulated using Dymore.



**Figure 4.2.:** Illustration of the generated morphing wing surface and its discretization.

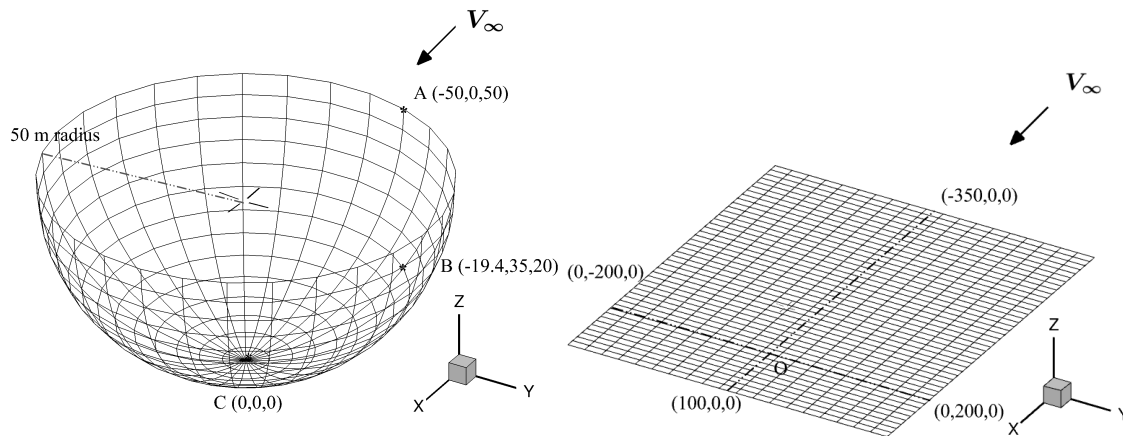
### 4.3.1. Validation cases

A majority of rotor acoustics investigations conducted with PSU-WOPWOP contain no corresponding validation study. This is either due to the novelty of the rotor system being analyzed or due to a lack of access to measurement data. Such studies usually rely on the physical nature of the results obtained since no comparison with experimental data is possible. The limited number of experimental measurement datasets, where acoustic pressure data was recorded, has also contributed to the limited number of validation studies.

The HART II rotor test campaign is the most widely used data set to validate aeroacoustic analysis tools. This is because the relevant rotor properties and test conditions have been made open source. Additionally, an extensive amount of research has been published using HART II measurement data that imbues confidence in the reported data [10]. Among the results of different comprehensive analysis frameworks reported in Ref. [256], CAMRAD II + PSU-WOPWOP acoustic results of the HART II rotor were in relatively good agreement. A corresponding CFD/CSD coupled study [43] showed a good correlation with the measurement data, both acoustic pressure fluctuations and overall sound pressure levels, across the three operating cases for which the data has been made public. Ref. [245] was one of the first studies where a good correlation was achieved with measured acoustic pressure of a model UH-60A rotor, a model Bo 105 rotor (HART I), and the full-scale XV-15 tiltrotor in maneuvering flight. The accuracy of acoustic pressure prediction in this study was, however, limited due to a lack of a good underlying comprehensive analysis model. CAMRAD II + PSU-WOPWOP simulations of the active flap SMART rotor also matched favorably with measurement data [248]. All these studies suggest that the underlying theory and algorithms, that PSU-WOPWOP is based on, are indeed capable of making accurate rotor noise predictions for both passive as well as active rotor designs. A separate validation exercise was carried out as part of this work in order to render confidence in the current implementation of the overall acoustics analysis framework. The corresponding results are presented and discussed in the following chapter in Secs. 5.4.4 and 5.5.3.

All rotor aeromechanic simulation results in the current study were obtained using either a standalone Dymore or Dymore+VPM framework. The rotor solutions were not strictly periodic since it can take a long simulation run in order for the cycle-to-cycle differences to *completely* die down. While these minor differences in rotor airloads and response from one revolution to the next could be ignored for aeromechanical analysis purposes, this is not true for acoustics analysis. For noise estimation, the rate of change of the aeromechanical state of the rotor blade elements is also relevant (see Eq. 4.2). A minor cycle-to-cycle change in the rotor state can lead to a large unphysical spike in acoustic pressure. For this purpose, up to three revolutions of rotor data were provided to PSU-WOPWOP for analysis, and only a one time period slice of acoustic pressure was finally used for overall sound pressure level (OASPL) calculations. It is worth mentioning that Ref. [73] suggested an alternate strategy of smoothing out the periodic rotor response so that the relevant parameters at the end of one cycle match those at the beginning of the next cycle.

In addition to the validation results, the acoustics framework was also used to assess the effect of active rotor actuation on noise emissions. Since there are no acoustic measurement data available for active rotors with FishBAC, the current work focused on a qualitative and quantitative variation in the noise emissions based on the camber actuation profile employed. For this purpose, the noise output was simulated over a hemisphere as well as a horizontal plane of observers. Figure 4.3 schematically shows the overall grid of the two different arrangements. Figure 4.3(a) additionally shows three individual observer locations denoted A, B, and C that were chosen for comparing the change in noise emission with FishBAC actuation. These locations were chosen due to the directivity of dominant components of noise along the radiation direction at each of these locations. Observer at C captures the variation in loading noise, observer at A captures the variation in thickness noise and observer at B captures a combination of the two. Figure 4.3(b) shows the horizontal plane grid of observers used to simulate the ground plane where the rotor is placed at a height of 50 m above it.



(a) Hemispherical distribution around rotor hub at 50 m. (b) Ground plane distribution 50 m below the rotor hub.

**Figure 4.3.:** Illustration of the array of observers (or microphones) below and around the rotor used for acoustics analysis.

## 5. Results and Discussion

Chapter 1 in this dissertation detailed selected outcomes from computational studies and test campaigns involving various active rotor mechanisms available in the literature. Operational aspects of the different active rotor control technologies were highlighted there to identify if any common thread exists between them in the manner in which they lead to a reduction in rotor power consumption, lower vibrations, and lower acoustic emissions. Chapter 2 described the modeling aspects of the baseline rotor/wing designs as well as active rotor systems/wings used in this study. The baseline rotors used were the HART II, Bo 105, and UT Austin single rotors; the active systems modeled include the active camber morphing concept installed on the Bo 105 and UT Austin coaxial rotor. Chapter 3 describes the methodology by which the VPM-based wake-induced inflow velocity calculation was used to augment the comprehensive analysis solver Dymore. The output obtained using simulations conducted using Dymore and Dymore+VPM were used as input to the acoustics solver PSU-WOPWOP in order to predict rotor noise emissions. The relevant post-processing framework was described in Chap. 4. The current chapter is dedicated to the presentation and discussion of results obtained using the models and methodology detailed in Chaps. 2-4.

The current chapter is organized as follows. First, the coupling between Dymore and VPM, as detailed in Chap. 3, was validated using a number of test cases. Section 5.1 shows results corresponding to pitching and pitching+morphing airfoils, obtained using VPM, and compared to results obtained using unsteady potential flow theory. Sections 5.2 and 5.3 compare the simulation results of an elliptical wing at static angle of attack to theoretical results and the results of a pitching finite wing to experimental measurement data, respectively. These test cases, together with the VPM verification cases, already presented in Chap. 3, were used to show the validity of the implemented solution strategy of using particles to represent the wake vorticity of lifting wings. Additionally, these results also helped establish the correctness of the Dymore+VPM coupling. Rotor simulation results are presented from Sec. 5.4 onwards. In Sec. 5.4, the full-scale baseline Bo 105 rotor was simulated using operating conditions over a range of advance ratios. The aeromechanical rotor loads, performance, and acoustic noise predictions were made at different operating conditions and compared to measurement data available in the literature. Next, the Mach-scaled Bo 105 rotor, called HART II, was simulated in BVI conditions, and Sec. 5.5 shows relevant aerodynamic and acoustics results and compares them to measurement data. Having established sufficient confidence in the simulation methods, Sec. 5.6 shows aeromechanical and aeroacoustic results corresponding to the active Bo 105 rotor with the FishBAC mechanism installed. In lieu of any measurement data, a comparison was made between the standalone Dymore and Dymore+VPM results here. Finally, Sec. 5.7 shows the effect of utilizing the FishBAC mechanism on coaxial rotor in order to suppress vibratory loads and noise emissions inherent to that design.

## 5.1. Airfoil Unsteady Aerodynamics

### 5.1.1. Description

The objective of this study was to simulate an airfoil undergoing sinusoidal pitching in oncoming flow and obtain the resulting unsteady aerodynamic lift and moment characteristics. Standalone Dymore and Dymore+VPM simulation frameworks were used for this purpose. The induced velocity due to the shed wake vorticity was modeled using the Peters 2D inflow theory, detailed in Ref. [201], in the former simulation framework. VPM was used in the latter setup while imposing *ceteris paribus* across the rest of the two simulation frameworks. A rectangular finite wing model was used for this study, but using Peters' model, by default, ensured that no 3D wake effects were modeled. Here, the wake was represented using eight states. For the VPM-based wake simulation too, only shed vorticity was considered during the initialization phase of the vortex particles and trailing vorticity was 'turned off'. Additionally, only the results corresponding to the mid-section of the wing were considered in order to minimize any effects due to the finite spanwise extent of the shed vortices.

In the VPM model, the shed wake was represented using a spanwise resolution of  $n_{\text{res}} = 100$  vortex particles while the total number of particles within the simulation flow field was set to  $N_{p,\text{max}} = 1.25 \times 10^5$ . Table 5.1 summarizes the wing geometry and simulation parameters used in this study. The quasi-steady wing aerodynamics were based on airfoil tables, and no tip loss correction was applied to the wing models. Three cases with different airfoil kinematic motions were simulated—pitching, camber morphing, and pitching+morphing. The airfoil motion parameters for the pitching+morphing study were adopted from the experimental test campaign of Ref. [148]. However, no attempt was made to compare the results obtained in this study with the measurement data since that reference study used the NACA0012 airfoil with a trailing-edge flap, while the current study used the NACA23012 airfoil with the FishBAC concept.

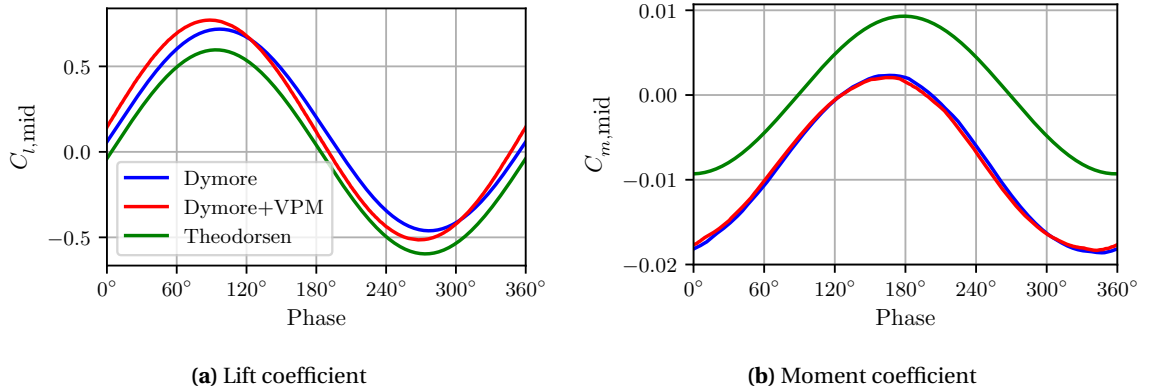
Parameter	Value
Span, $s$	1.6 m
Chord, $c$	0.18 m
Airfoil	NACA23012 + FishBAC morphing
Free stream velocity, $V_\infty$	50.0 m s <sup>-1</sup>
Spanwise particle resolution, $n_{\text{res}}$	100
Time step, $\Delta t$	$2.22 \times 10^{-4}$ s
Maximum total particles, $N_{p,\text{max}}$	$1.25 \times 10^5$

**Table 5.1.:** Rectangular wing geometry and simulation parameters for 2D wake analysis.

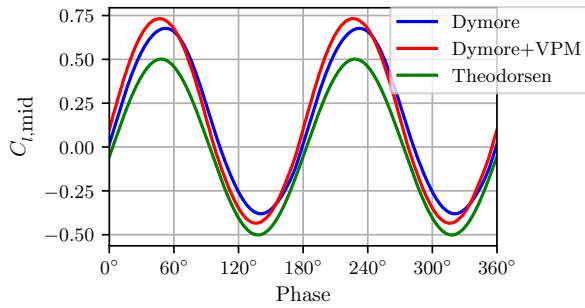
### 5.1.2. Validation results

Figure 5.1 shows the 2D coefficients of lift and moment obtained at the center of the wing undergoing pitching oscillations with an amplitude of  $6^\circ$  and frequency of 5 Hz. In addition to the Dymore and Dymore+VPM simulations, results obtained from Theodorsen theory are also shown for reference purposes. It is worth noting that the Theodorsen theory results were obtained using the original formulation proposed in Ref. [263], and summarized earlier in Sec. 2.2.1, which assumes the airfoil is thin and without any camber. Therefore, it exhibits a quasi-steady aerodynamic lift-curve slope of  $2\pi$  and zero moments about the quarter-chord. As a consequence, the predicted lift and moment show differences in magnitude compared to the Dymore or Dymore+VPM results, which use the NACA23012 airfoil tables to obtain the relevant aerodynamic characteristics. Despite this inherent disparity exhibited by the Theodorsen theory formulation, the objective was to use a simple analytical model in order to put the results obtained in this study in perspective. The results obtained using the VPM-based wake model as well as the Peters 2D inflow model compare reasonably well with each other over the entire actuation cycle. Understandably, both  $C_l$  and  $C_m$  results exhibit differences in magnitude compared to the Theodorsen theory prediction, but the general qualitative trends are captured. Small differences between Dymore and Dymore+VPM results can be attributed to two significant differences in underlying strategies used to model wake physics - (a) Peters' model assumes a flat wake behind the airfoil but VPM model doesn't (see Fig. 5.5(c)), (b) VPM model did not include infinitely many shed vortex particles to simulate a strictly 2D shed vorticity in the airfoil wake, unlike the analytical formulation of the Peters' model that automatically accounts for it.

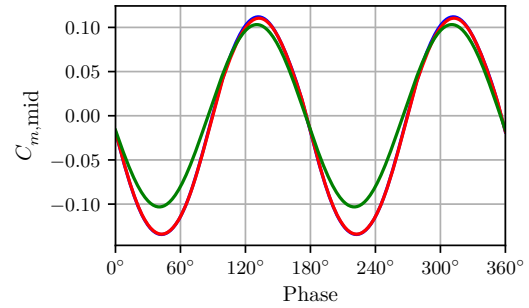
Figures 5.2-5.4 show further results obtained for different airfoil morphing and pitching profiles. Figure 5.2 shows results corresponding to a pure camber morphing case where the airfoil trailing-edge tip undergoes an oscillation with  $9^\circ$  amplitude at a frequency of 10 Hz. Note that the phase referred to in the figures is based on an actuation frequency of 5 Hz. Consequently, the results show two cycles of camber actuation. Figures 5.3 and 5.4 show results corresponding to combined pitching and morphing cases. All the results show trends similar to those in Fig. 5.1 described above. Overall, the quality of results obtained demonstrates that the VPM framework is able to predict 2D unsteady aerodynamic lift and moment correctly, both qualitatively and quantitatively.



**Figure 5.1.:** Section lift and moment coefficients for an airfoil pitching at  $\theta = 6^\circ \sin(5 * 2\pi t)$ .

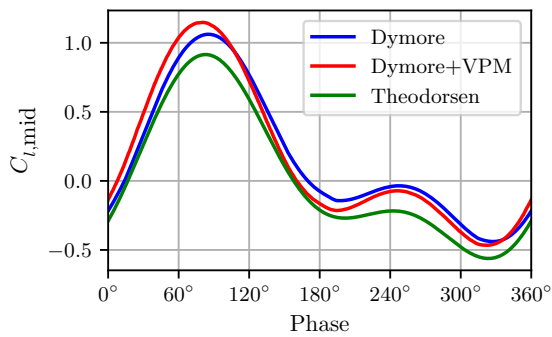


(a) Lift coefficient

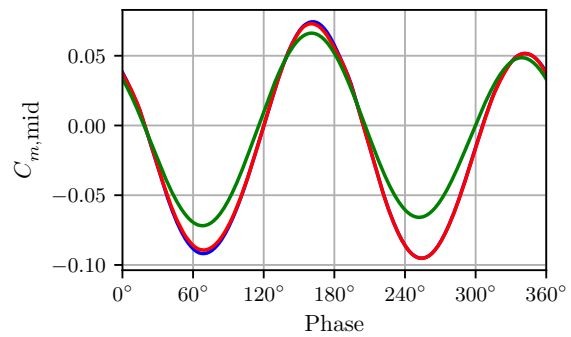


(b) Moment coefficient

**Figure 5.2.:** Section lift and moment coefficients for a morphing airfoil with active camber actuation at  $\delta = 9^\circ \sin(10 * 2\pi t)$ .

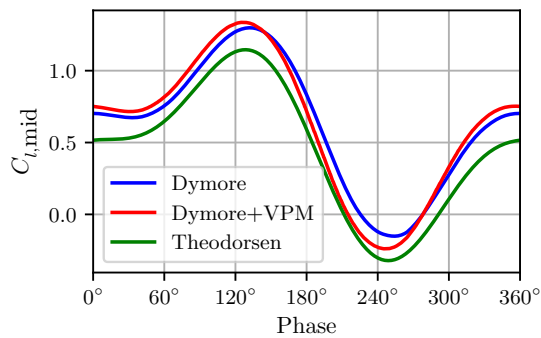


(a) Lift coefficient

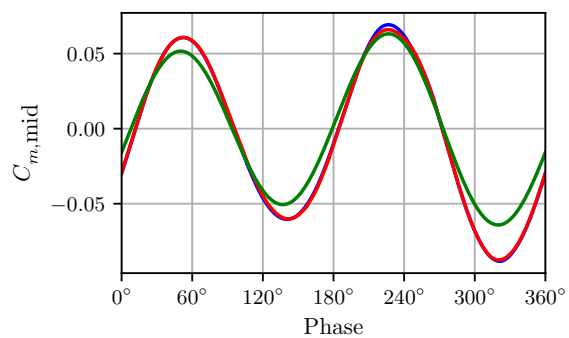


(b) Moment coefficient

**Figure 5.3.:** Section lift and moment coefficients for a pitching and morphing airfoil with  $\theta = 6^\circ \sin(5 * 2\pi t)$  and  $\delta = 0.5^\circ + 5.5^\circ \sin(10 * 2\pi t - 59^\circ)$ .



(a) Lift coefficient

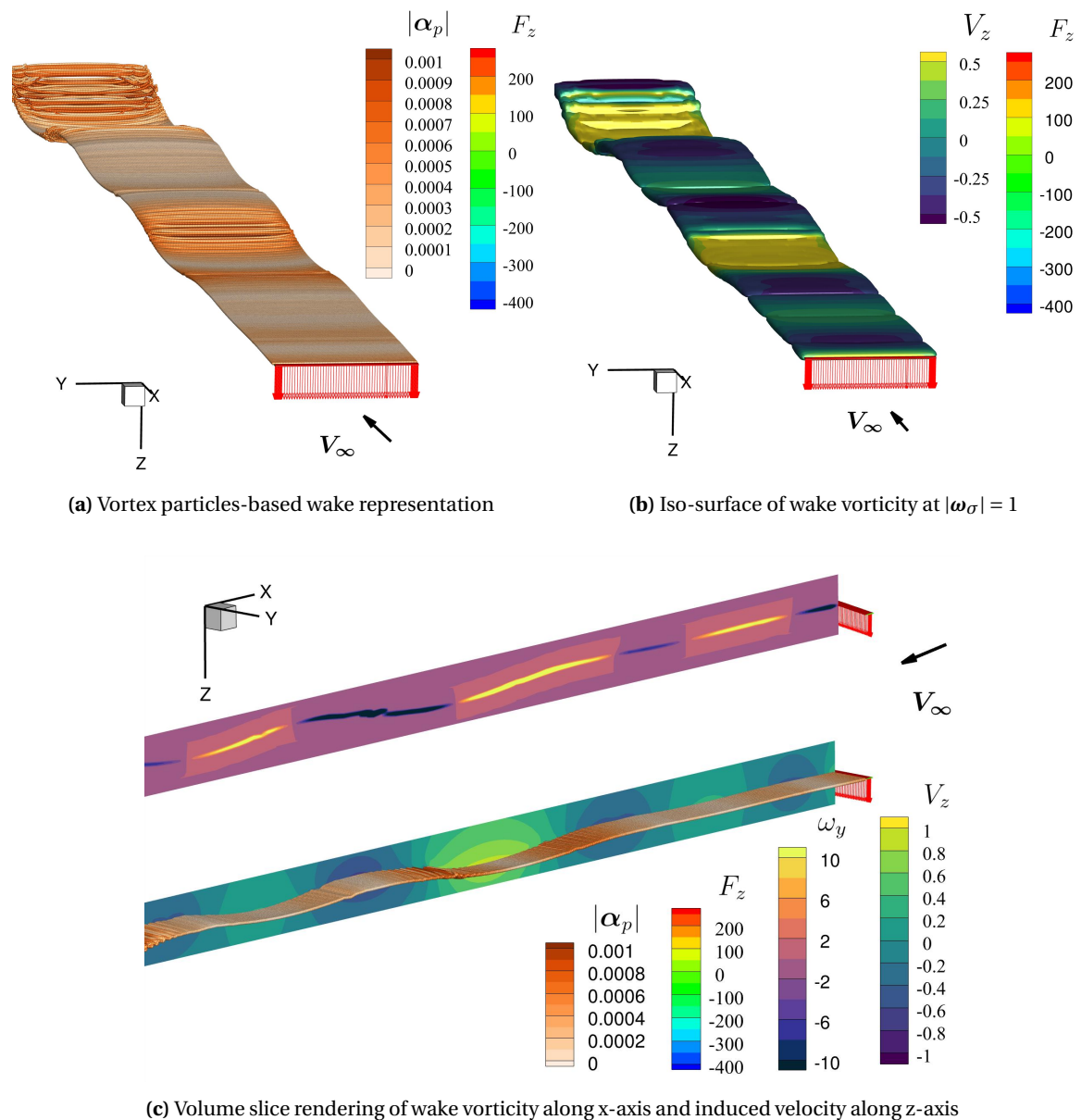


(b) Moment coefficient

**Figure 5.4.:** Section lift and moment coefficients for a pitching and morphing airfoil with  $\theta = 4.5 + 5.75^\circ \sin(5 * 2\pi t)$  and  $\delta = 5.0^\circ \sin(10 * 2\pi t - 196^\circ)$ .



Figure 5.5 shows the wing wake obtained using VPM for the representative pitching+morphing wing case. Fig. 5.5(a) shows the purely shed wake vorticity modeled in the wake of the wing using particles. Fig. 5.5(b) shows the corresponding iso-surface of vorticity inherent within the particles. This vorticity leads to the induced velocity obtained at each section of the wing as well as the volume surrounding the vortex sheet. This is exhibited in Fig. 5.5(c), which shows a composite image of two volume slices shown together. From the figure, it is evident that the shed vorticity is concentrated only within the thin vortex sheet comprising of shed vortices. Qualitatively similar results were obtained for the other cases simulated and are not shown here for conciseness.



**Figure 5.5.:** Visualization of the 2D vortex wake of a wing section undergoing pitching ( $\theta = 6^\circ \sin(5 * 2\pi t)$ ) and camber morphing ( $\delta = 0.5^\circ + 5.5^\circ \sin(10 * 2\pi t - 59^\circ)$ ).

## 5.2. Static Elliptical Wing Aerodynamics

### 5.2.1. Description

The suitability of the VPM method for use in wake analysis was further established by validating the Dymore+VPM setup against two finite wing test cases with different aerodynamic wake complexities. The first case investigated included an elliptical wing at a static angle of attack and forms the subject of this section. The second case investigated included a pitching wing, which is discussed in the following section. The objective of the static angle of attack wing investigation was to verify the implementation of trailing vortex particles as well as introduce another validation case toward the overall credibility of the VPM framework. An elliptical wing planform was chosen due to the key feature of uniform downwash over the entire span of the wing [235] (Section 4.11). This result can be analytically derived and can be referred to from the aforementioned source. Eqs. 5.1–5.4 summarize the key expressions used in order to obtain the theoretical uniform induced velocity over the wing. In the current study, the elliptical wing was modeled and simulated using the parameters summarized in Table 5.2.

$$L = C_L \frac{1}{2} \rho V^2 S \quad (5.1)$$

$$L = \frac{\rho V \Gamma_{\text{mid}} \pi s}{4} \quad (5.2)$$

$$\Rightarrow \Gamma_{\text{mid}} = \frac{2C_L V S}{\pi s} \approx \frac{2C_L V S}{\pi s} \quad (5.3)$$

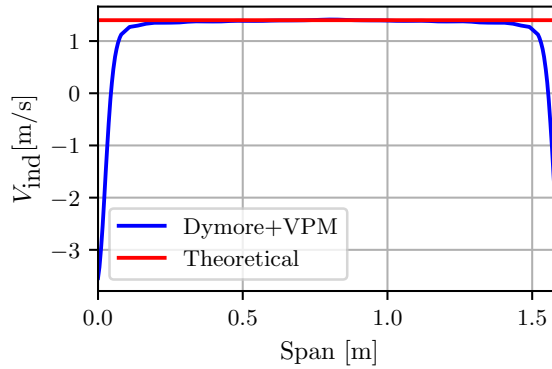
$$V_{\text{ind}} = \frac{\Gamma_{\text{mid}}}{2s} \quad (5.4)$$

Parameter	Value
Span, $s$	1.6 m
Mid-chord, $c_{\text{mid}}$	0.34 m
Airfoil	NACA0012
Freestream velocity, $V_{\infty}$	50.0 m s <sup>-1</sup>
Pitch angle, $\theta$	5°
Spanwise particle resolution, $n_{\text{res}}$	100
Time step, $\Delta t$	6.4 × 10 <sup>-4</sup> s
Maximum total particles, $N_{p,\text{max}}$	1.25 × 10 <sup>5</sup>

**Table 5.2.:** Elliptical wing geometry and simulation parameters for steady 3D wake analysis.

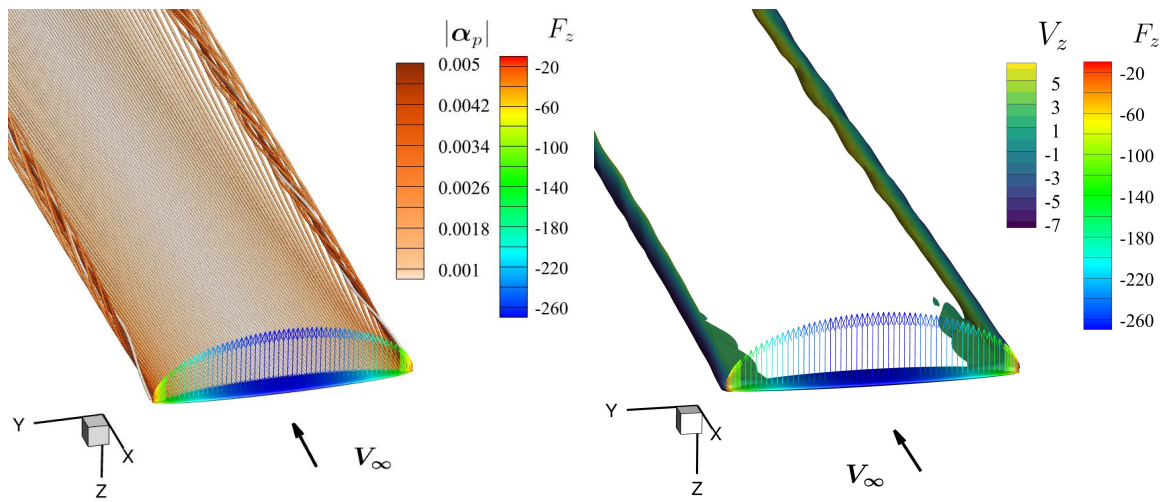
### 5.2.2. Validation results

Figure 5.6 compares the distribution of the wake-induced inflow over the span of the wing against the theoretical result obtained using Eq. 5.4.  $C_l = 0.527$  was used in Eq. 5.3, along with the parameters in Table 5.2, in order to arrive at the theoretical value. It is evident from the figure that VPM captures the general trend of uniform induced velocity over almost the entire wing span. It can be seen that close to the wing tips, the induced velocity drops rapidly. This is due to the formation of strong tip vortices, when using VPM, at a location slightly inboard of the wing tips. This led to a high negative induced velocity, i.e., induced velocity that leads to an increase in the local angle of attack. This was a consequence of the discretization resolution adopted for the simulation, and the spanwise sections where this occurs can be made smaller using a finer resolution. However, unlike the theoretical result, this drop in induced velocity persists in the VPM-based result since the wake formulation used in this method does not rely on a simplified analytical solution. Ref. [271] presents similar results from modeling an elliptical wing at a static angle of attack, using a slightly different formulation of the vortex particle method. Here, too, the characteristic drop in predicted induced velocity at the wing tips was obtained.



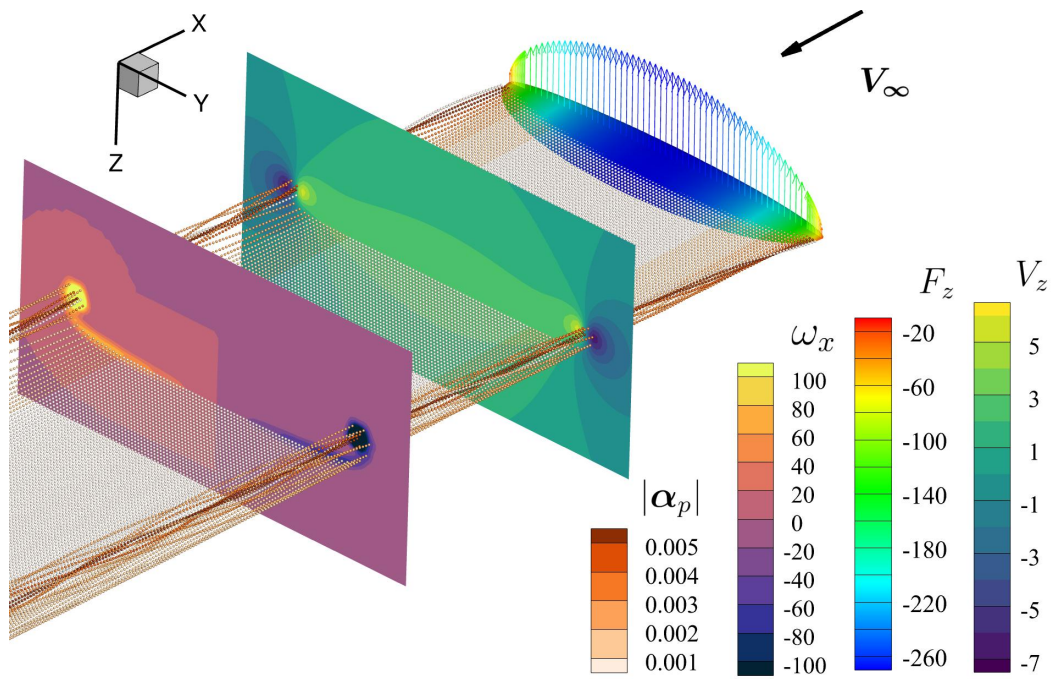
**Figure 5.6.:** Spanwise distribution of the wake-induced inflow velocity for an elliptical wing at the quarter-chord location.

Figure 5.7 shows the elliptical wing wake obtained for the static angle of attack wing simulation. In Fig 5.7(a), the particle representation of the wake is shown. Based on the contour map of the strength of the vortex particles, it is evident that the dominant vorticity resides in the trailing vortices emanating near the wing tips. Since the wing is not undergoing unsteady motion, there are no shed vortices. The resulting roll-up of the tip vortices was clearly captured by VPM. Figure 5.7(b) shows the corresponding wake generated using an iso-surface of vorticity manifested within the vortex particles. The contour map over the iso-surface represents the induced velocity distribution along the Z-axis. In Fig 5.7(c), slices of the volume in the wake show the vorticity concentration and induced velocity distribution in the YZ slicing planes. The elliptical distribution of loading over the wing is also indicated by the vectors denoting the normal force over the span of the wing. Overall, they show that the analysis framework is capable of capturing vortex wake results that are consistent with theory.



(a) Vortex particles-based wake representation

(b) Iso-surface of wake vorticity at  $|\omega_\sigma| = 100$



(c) Volume slice rendering of wake vorticity and induced velocity in the YZ plane

**Figure 5.7.:** Visualization of the vortex wake of the an elliptical wing at static pitch angle  $\theta = 5^\circ$ .

## 5.3. Finite Wing Unsteady Aerodynamics

### 5.3.1. Description

This study was an extension of the work in Sec. 5.2, which was carried out in order to assess the capability of VPM to accurately capture unsteady 3D wake structures. The objective was to be able to reliably predict the loads on a finite wing oscillating in oncoming flow. For this purpose, a rectangular wing of aspect ratio  $AR = 5$  was chosen and simulated in oncoming flow, based on the parameters provided in Ref. [21]. This reference contains results corresponding to a computational simulation that was conducted in that study as well as experimental measurements. Table 5.3 summarizes the wing geometry as well as the simulation parameters used in this study.

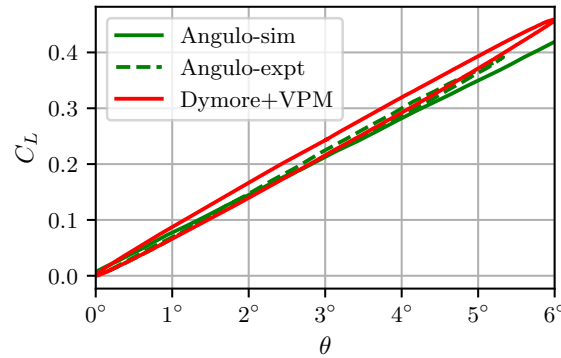
Parameter	Value
Span, $s$	1.054 m
Chord, $c$	0.211 m
Pitching frequency, $f$	2.053 Hz
Freestream velocity, $V_\infty$	27.2 m s <sup>-1</sup>
Mean pitch angle, $\theta_0$	3°
Amplitude of pitch, $\theta_s$	3°
Spanwise particle resolution, $h_{\text{res}}$	40
Time step, $\Delta t$	$5.42 \times 10^{-4}$ s
Maximum total particles, $N_{p,\text{max}}$	$7.5 \times 10^4$
Tip-loss parameter, $f$	0.95

**Table 5.3.:** Finite wing geometry and simulation parameters for unsteady 3D wake analysis.

### 5.3.2. Validation results

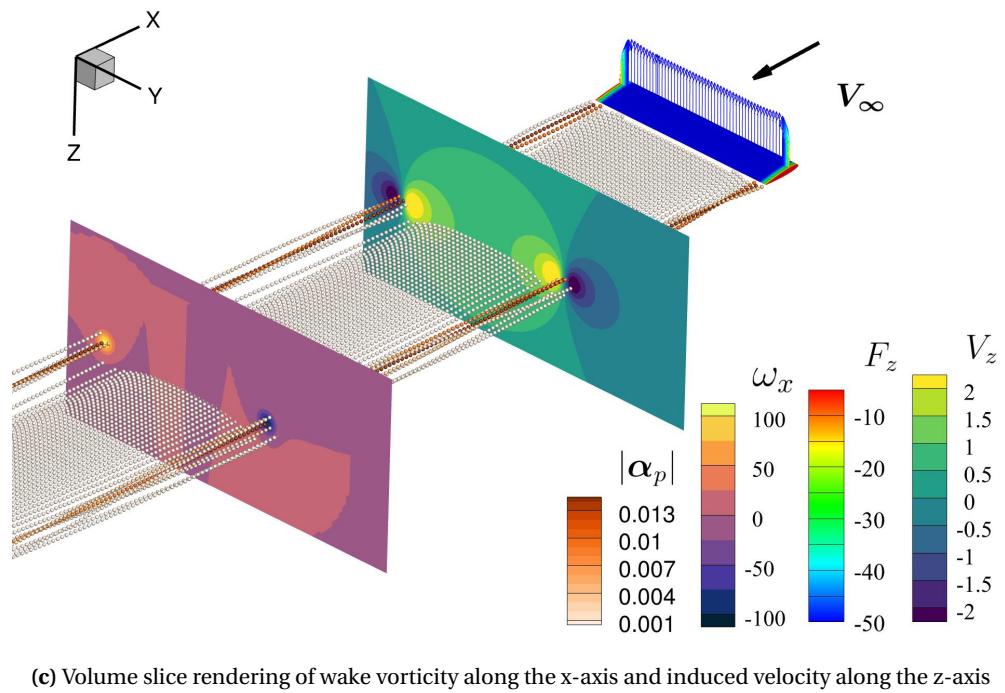
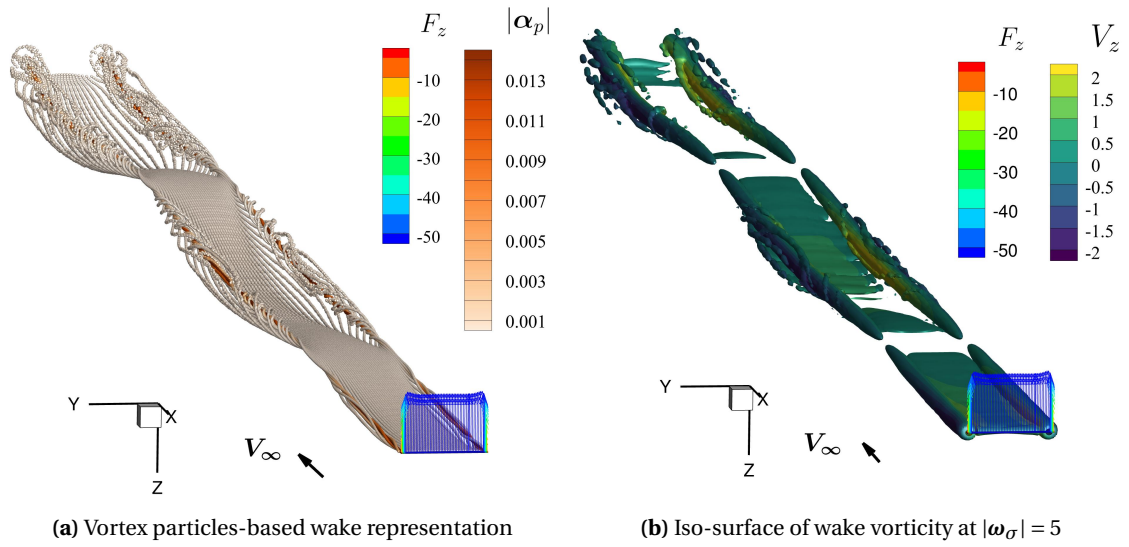
The validation of the unsteady pitching finite wing case is presented in Fig. 5.8. Here, the predicted total wing lift coefficient  $C_L$  is plotted over a complete oscillation cycle and compared with corresponding results from Ref. [21]. As mentioned earlier, the reference study contains results from a panel method-based simulation as well as measurement data. Both results have been shown in Fig. 5.8. The magnitude of the prediction matches fairly well with the results from Ref. [21], although cyclic hysteresis effects were slightly over-predicted by the VPM-based simulation. The overall lift curve slope of the predicted results is also higher. This could be attributed to a modeling deficiency in the Dymore+VPM framework. Since blade aerodynamics in Dymore are modeled using lifting-line theory, it is incapable of capturing the loss in lift-generating capability of finite wings towards the tip. Three-dimensional wake representation using VPM has a partial ameliorat-

ing effect, but the combined Dymore+VPM framework is still not capable of giving the characteristic drop in the sectional lift to zero at the tip of the wing. In order to rectify this, the tip loss factor described in Sec. 2.2 was used with an assumed value of  $f = 0.95$ . Different values of  $f$  would result in a different lift curve slope of the overall predicted  $C_L$  curves. For the purposes of the current study,  $f = 0.95$  was considered to be a reasonable value considering the low aspect ratio of the finite wing. This practice of assuming a tip loss factor in order to capture the 3D wing tip effects correctly is also employed in the case of rotor blades using Eq. 2.6 and has been used throughout the studies presented in the following sections.



**Figure 5.8.:** Comparison of unsteady lift coefficient of a wing with aspect ratio  $AR = 5$  with simulation and experimental measurements from Ref. [21].

Figure 5.9 shows the wake obtained for the pitching rectangular wing simulation. In Fig. 5.9(a), the particle representation of the wake is shown. Much like the elliptical wing case, it is evident that the dominant vorticity resides in the trailing vortices emanating near the wing tips. In addition to the resulting roll-up of vortices, the undulating pattern of the wake due to shedding vortex particles was also captured by VPM. Figure 5.9(a) shows the wake generated from two cycles of oscillation of the wing. Figure 5.9(b) shows the corresponding wake using iso-surface of vorticity manifested within the vortex particles. The contour map over the iso-surface represents the induced velocity distribution along the Z-axis. The discontinuities in the iso-surface are consistent with known fluid dynamics and kinematics principles. For example, there is high shed vorticity in the wake during the upstroke and the downstroke cycles and low vorticity at the end of each half-cycle. This is because the magnitude of shed vorticity is dictated by the rate of change of wing bound circulation, which is high during the upstroke and the downstroke motion and low at the end of each half-cycle of oscillation. In Fig 5.9(c), slices of the volume in the wake show the vorticity concentration and induced velocity distribution in the YZ slicing planes. It can be seen that the dominance of the trailing vorticity leads to a distribution pattern similar to the elliptical wing case. The instantaneous distribution of loading over the wing is also indicated by the vectors denoting the normal force over the span of the wing. Due to the use of the tip loss factor  $f = 0.95$ , the lift smoothly drops to zero at the wing tips.



**Figure 5.9.:** Visualization of the vortex wake of a rectangular finite wing of aspect ratio  $AR=5$  pitching at  $\theta = 3^\circ + 3^\circ \sin(2.05 * 2\pi t)$ .

## 5.4. Full-scale Bo 105

### 5.4.1. Description

This section details the validation of the full-scale Bo 105 rotor model detailed in Sec. 2.5.2. The objective of this exercise was to simulate and analyze the Bo 105 rotor over a spectrum of advance ratios. The predicted trimmed rotor results using the standalone Dymore and the Dymore+VPM frameworks were then compared with measurement data. This was done in order to render confidence in the multibody Bo 105 model setup as well as the simulation strategies adopted. Thereafter, the modeling framework was extended to simulate an active Bo 105 rotor with the FishBAC concept, and the results are presented in later sections.

The technical reports of Refs. [111] and [112] detail the rotor test setup and measured data from the full-scale Bo 105 rotor IBC test campaign. The objective of those tests was to evaluate the potential benefits of using IBC to improve rotor performance, reduce BVI noise, and alleviate helicopter vibrations. The wind tunnel tests reported in these two volumes of reports were conducted in two phases in 1993 and 1994. For the purpose of validating the current analysis framework, the results corresponding to the 1994 tests have been adopted. Ref. [112], in particular, concerns itself with aeromechanical and aeroacoustic measurements of an active IBC Bo 105 rotor for a range of different operating conditions. However, a few baseline rotor test measurements, i.e., without any IBC, have also been reported which form the basis for the validation exercise.

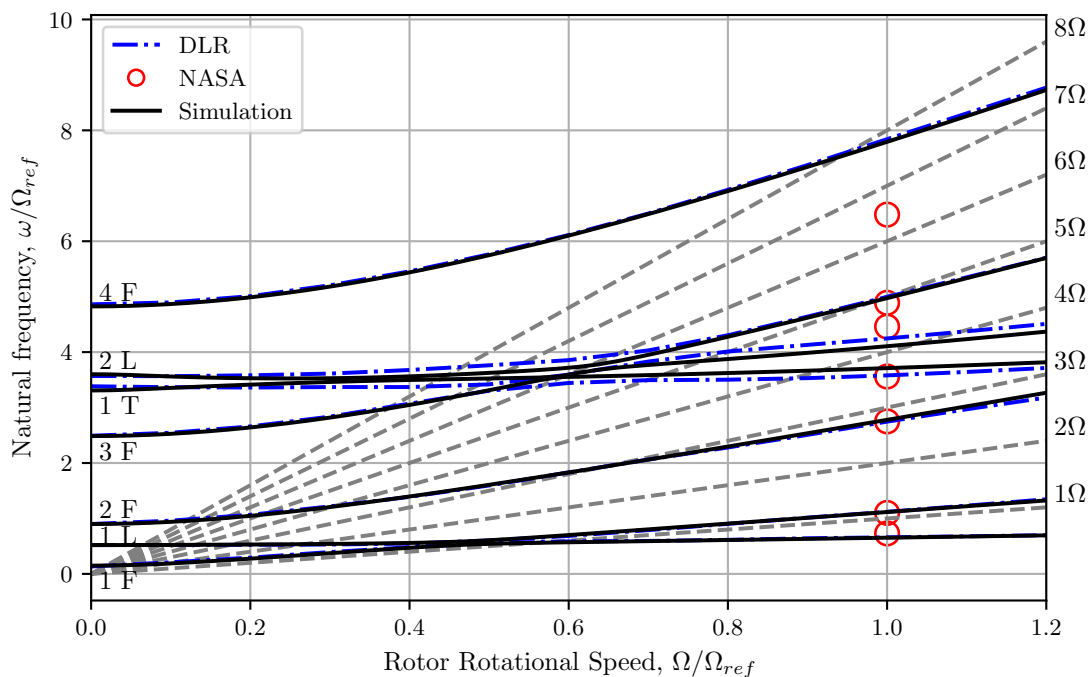
In this study, the trim state was specified using the following trim targets - rotor thrust, hub pitch moment and hub roll moment. This was because the measurement test campaign of Ref. [112] used the ‘constant moment trim state’ method in order to replicate free flight test conditions within the controlled environment of a wind tunnel. During the tests, the rotor thrust and hub moments were maintained at desired fixed values by tuning the collective and cyclic angles. In the current study, the rotor control angles—collective, longitudinal cyclic, and lateral cyclic—required in order to achieve these trim targets were obtained using the Jacobian-based controller in Dymore, described earlier in Sec. 2.4. Corrections were made to the rotor load balance and torque data, taking into account the rotor shaft angle, airspeed, and cross-coupling between the different load balance components. Ref. [111] can be referred to for further details pertaining to the basis of these corrections as well as how relevant transformations of data in different reference frames were achieved. The corrected rotor shaft angles, in order to account for the interference effects with the wind tunnel walls, from Ref. [112] were used in this study. Together with other trim conditions for all the simulated cases, they are detailed in the Appendix in Table A.3.

### 5.4.2. Blade natural frequencies and mode shapes

Since blade elastodynamics affect the overall blade loads as well as its motion, it is relevant to model the structural elastic properties correctly. Obtaining the blade natural frequencies at different rotation speeds, referred to as a fan plot, is a common technique employed as a check whether the elastic blade model has been setup correctly in the rotor simulation. Figure 5.10 shows the



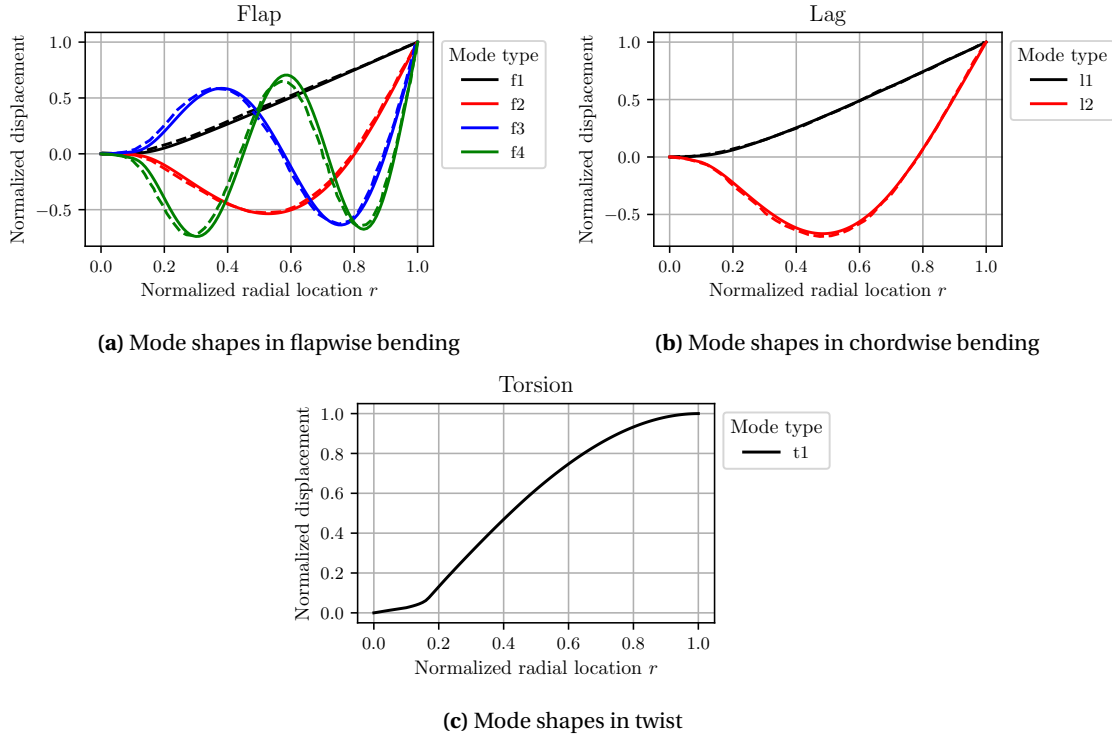
variation of blade natural frequencies as a function of the rotation angular velocity of the rotor. There is a good match between all the predicted blade natural frequencies with DLR data from Ref. [277]. Some differences can be observed with the calculated natural frequencies at the reference RPM available in the NASA report in Ref. [278]. However, there is little information in Ref. [278] about the blade structural properties used and the modeling strategy adopted to obtain the results. Therefore, the DLR results are assumed to be a more reliable source of information. Figure 5.11 shows the mode shapes of the Bo 105 rotor blade at the reference rotation angular velocity. The shape of these blade natural modes is relevant since it determines to what extent the blade can absorb the energy from the distributed airloads acting on the blade. The predictions made using Dymore have been compared to the mode shapes reported in Ref. [99]. It can be observed that the predicted mode shapes in flap and lag match the reported results very well. No torsion mode shapes were reported in Ref. [99].



**Figure 5.10.:** Bo 105 rotor blade frequency fan plot at  $0^\circ$  collective compared with data provided in Ref. [277](DLR) and Ref. [278](NASA).

### 5.4.3. Rotor aeromechanical results

This section is dedicated to the validation of the complete Bo 105 rotor aeromechanical model. For this purpose, the rotor model described in Sec. 2.5.2 was simulated at different advance ratios ranging from  $\mu = 0.01$ – $0.45$ . The different operating conditions and the corresponding measurement data were adopted from the wind tunnel study of Ref. [112] and are summarized in Table A.3. In all the simulations carried out on the baseline Bo 105 rotor, the blades were discretized into 81 airstation locations (see Fig. 2.10). A total of 540 integration time steps were used to cover one revolution, which corresponds to an azimuthal resolution of  $\Delta\psi = 0.67^\circ$ . The wake vorticity along



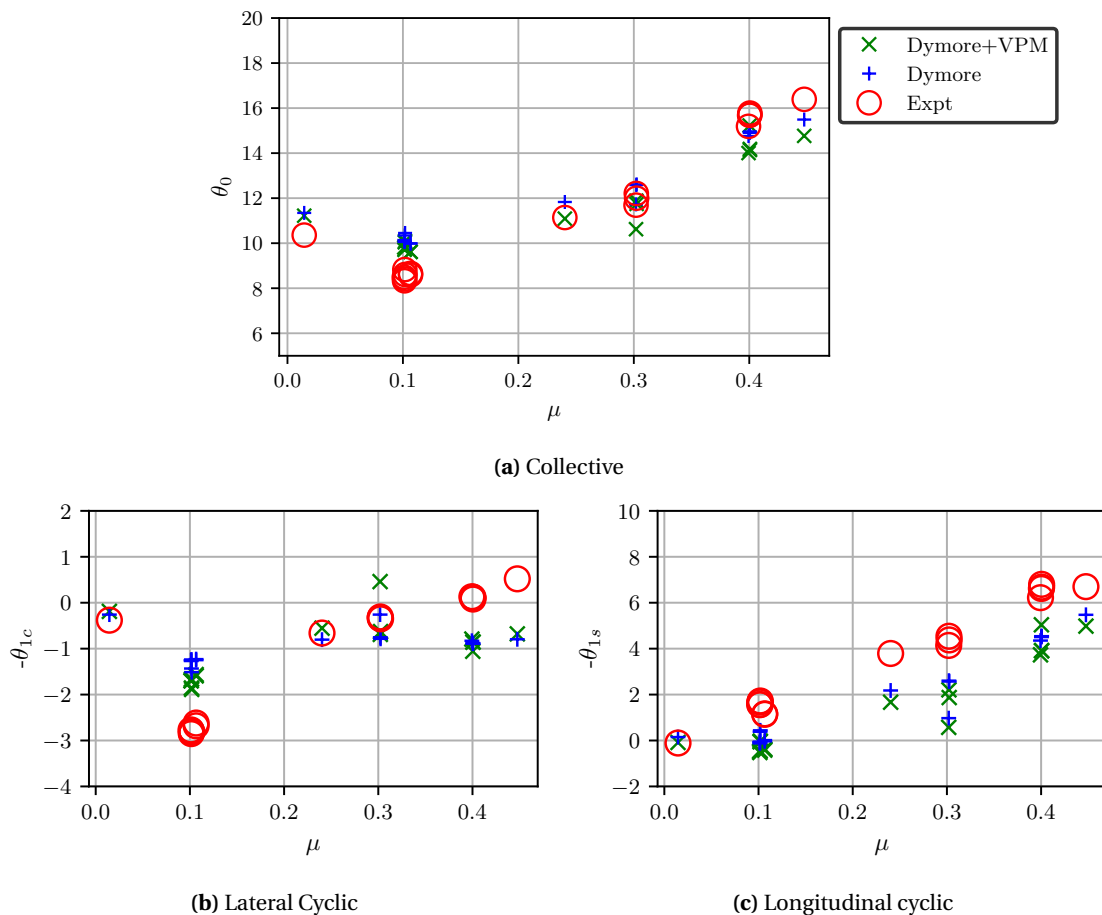
**Figure 5.11.:** Comparison of the mode shapes of the Bo 105 rotor blade obtained in the current study (solid lines) versus those provided in Ref. [99] (dashed lines). Note that only flap and lag mode shapes are provided in the reference study.

the blade span was discretized into particles using  $n_{\text{res}} = 35$ , and the rotor wake was limited to a total number of particles  $N_{p,\text{max}} = 10^5$ .

Figures 5.12-5.14 show the predicted rotor aeromechanical results and compare them with experimental measurement data. Figure 5.12 shows a comparison of the predicted rotor control trim angles with measured values. It can be seen that while the general trends over the advance ratio sweep were captured, there was an over-prediction or under-prediction of up to  $1^\circ$  in the collective and lateral cyclic values. In the case of longitudinal cyclic, too, the overall trend of increasing magnitude with advance ratio was captured but there was a near-constant offset of  $1.5^\circ$ . It is worth noting that, while there are some differences in the results obtained using standalone Dymore and Dymore+VPM frameworks, both simulation strategies qualitatively match the trend observed in the measurement data. The reason behind this is discussed later in the context of the low speed forward flight case simulated in this study.

Figure 5.13 shows the mean rotor loads and moments obtained at the rotor shaft, as well as the total power consumed. The quantities presented in Fig. 5.13(a)–(c) simply correspond to the trim objectives. These are presented to showcase the efficacy of the trim controller in arriving at the desired operating conditions starting from an initial set of reference conditions. In Fig. 5.13(f), it can be observed that there is an outlier measurement data point at  $\mu = 0.3$  which is likely due to a malfunctioning sensor during the test campaign. Overall, it can be observed from Figs. 5.13(d)–(g) that either simulation framework is able to predict the variation in mean rotor shaft loads with

advance ratio. In general, even when the predicted results differ from measurement data, results obtained using standalone Dymore closely match the Dymore+VPM simulation results. This is understandable since Fig. 5.13 shows mean rotor quantities, and the Peters-He inflow model-based simulations are generally able to capture the mean rotor loads very well. However, the VPM-based wake model is better able to capture the high-frequency fluctuations due to the rotor wake. So differences in the results from the two simulation frameworks would likely show up when analyzing higher harmonic loads and moments that are discussed next. It is worth mentioning that this difference between the modeling capability of the Peters-He model and VPM is highlighted further in the context of discussing the HART II rotor results later.



**Figure 5.12.:** Comparison of rotor control angles obtained using Dymore and Dymore+VPM simulations against measurement data from Ref. [112] for the Bo 105 rotor over a sweep of advance ratios  $\mu = 0.01$ – $0.45$ .

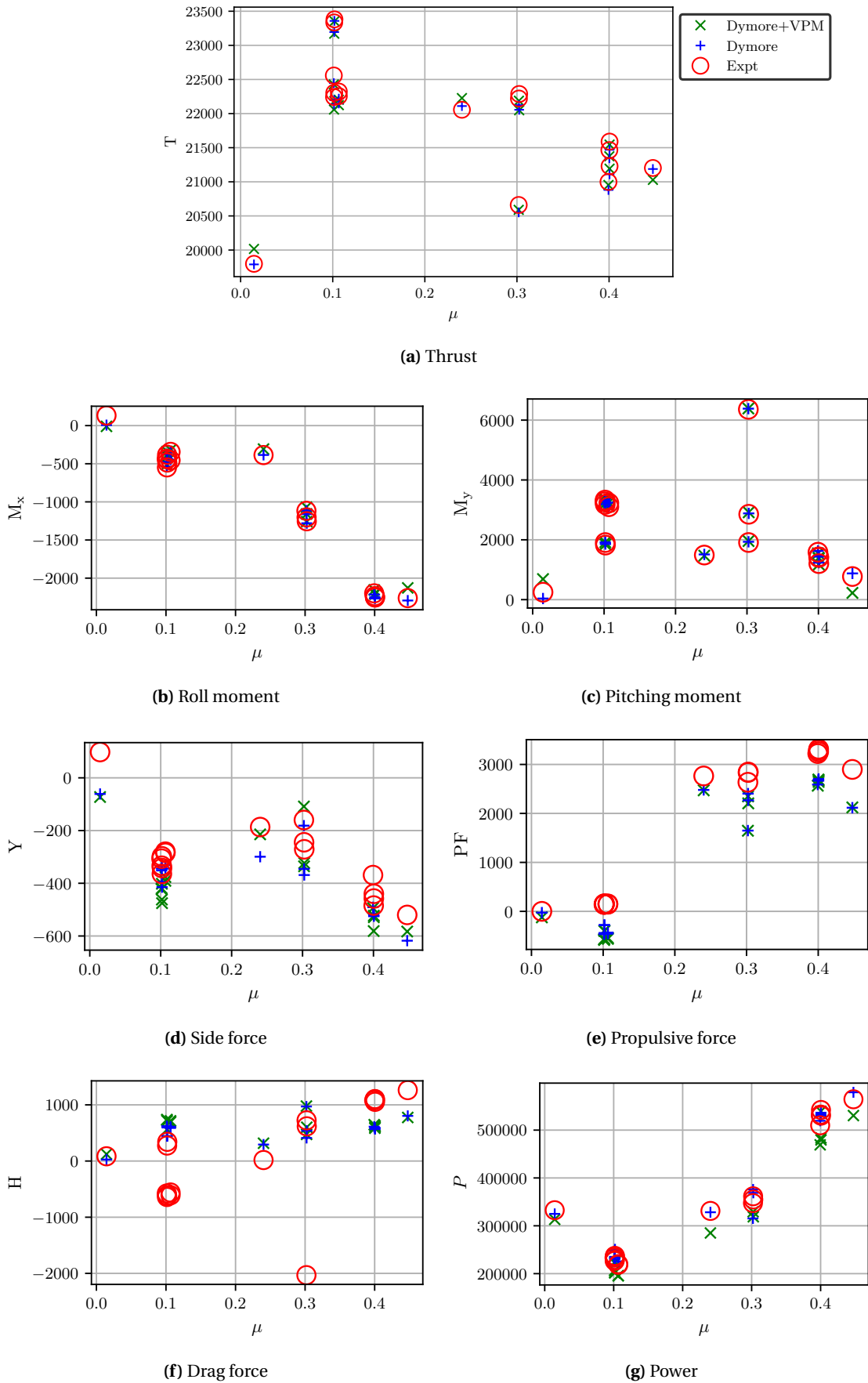
Figure 5.14 shows the half-peak-to-peak blade structural bending moment and twisting moment at different stations along the blade span, as well as the half-peak-to-peak pitch link loads. From Figs. 5.14(a)-(d) it is evident that, as expected, there is greater spread in the results obtained using Dymore and Dymore+VPM frameworks. The flap bending moments, close to the blade root were significantly over-predicted in Fig. 5.14(a). In contrast, the flap bending moments close to the mid-span of the blades were slightly under-predicted. The exact cause for this behavior in the

results of the simulation frameworks is difficult to pinpoint since they are an outcome of intricate fluid-structure interaction processes. A slightly improved correlation is obtained in the chord bending moment results shown in Figs. 5.14(c) and 5.14(d). In an effort to improve chord bending moment prediction of the UH-60A rotor, Ref. [297] had conducted a study that included a model of the rotor test stand in the NFAC 40- by 80-foot wind tunnel. This resulted in an improvement in the correlation between predicted and measured loads. Similar work was carried out in Refs. [280] and [279] where the effect of drivetrain dynamics on Bo 105 blade loads was investigated. The results presented therein suggest that the inclusion of a gearbox model is likely to improve the correlation presented in Figs. 5.14(c) and 5.14(d). Finally, pitch link load and blade twisting moment results are presented in Figs. 5.14(e)–(g). A good correlation was obtained between the measurement data and simulation results for the entire range of advance ratios except at  $\mu = 0.45$ . Lack of dynamic stall modeling could be one of reasons for this since it is likely to occur at high advance ratio operation and is characterized by an increase in blade twisting moments and pitch link loads.

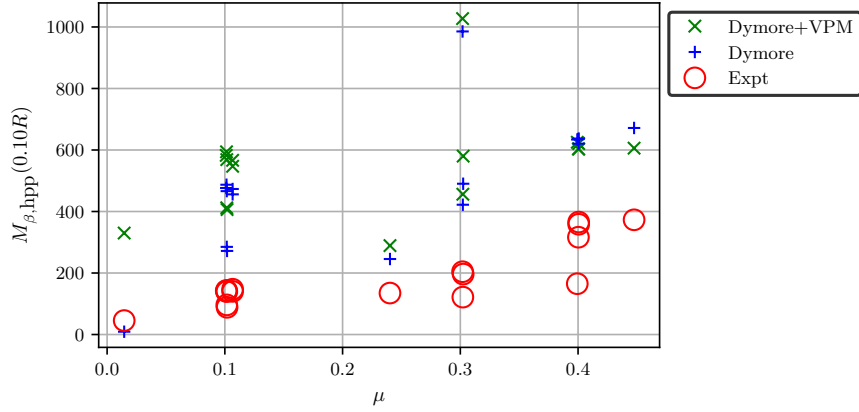
Figure 5.15 shows polar plots of different blade section quantities—angle of attack  $\alpha$ , induced inflow velocity  $V_{ind}$ , rotor thrust  $F_Z$  and rotor in-plane force  $F_Y$ . These correspond to  $\mu = 0.1$  case of Run 42 point 7 (see Table A.3), which is also used for acoustics validation in the following section. Due to the low forward speed and near-zero tilt of the shaft angle, the rotor undergoes BVI at these operating conditions. This can be seen in all the results in Fig. 5.15 obtained using VPM. The Peters-He inflow model is unable to capture the high-frequency effects of BVI; rather, it only captures the smoothed-out average effects. This is evident in all the different quantities shown in Fig. 5.15 obtained using the Dymore framework. The differences in physical modeling capabilities of VPM and Peters-He models, particularly highlighted in BVI conditions, are further discussed in the context of HART II rotor in the following section. Similar results are presented for the cruise speed  $\mu = 0.3$  case of Run 26 point 11 in Figs. 5.16. Here, unlike the results of  $\mu = 0.1$  case, there is greater match between the results from Dymore and Dymore+VPM frameworks. Due to the higher oncoming flow velocity, the rotor wake is washed quickly away from the rotor disk, resulting in a reduced impact of the induced inflow velocity on blade section angles of attack. Since the rest of the underlying simulation model is common to both frameworks, the final results obtained using the VPM-based wake and Peters-He inflow model exhibit a closer match.

Figure 5.17 illustrates the overall rotor wake, modeled using VPM, indicating the characteristic roll-up of the rotor wake into two distinct trailing vortices. In addition to that, the movement of trailing vortex particles, generated from preceding blades, close to the following blades can be seen. This is responsible for the undulations in induced velocity seen in Fig. 5.15(b), which consequently has a similar effect on other quantities shown in Fig. 5.15. Figure 5.18 illustrates the physical effect of the wake moving away from the rotor disk. Comparing Figs. 5.17 and 5.18, it is evident that in the former case the wake tends to stay close to the rotor disk and in the plane of the rotor itself. The inability of the Peters-He model to capture the effect of these vortices is the cause of the greater difference in the Dymore and Dymore+VPM results for the low advance ratio cases in the half-peak-to-peak results shown in Fig. 5.14.

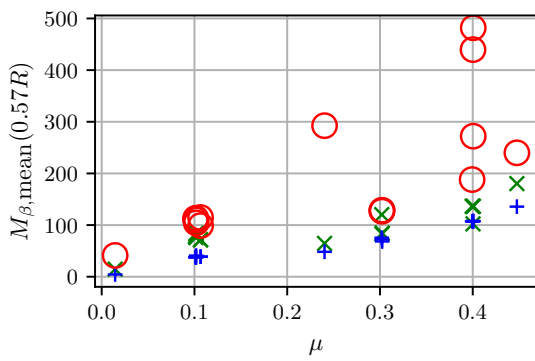
Based on the results presented in Figs. 5.12–5.18, the predictive accuracy of both comprehensive analysis frameworks is considered to be fair. In the following section, the simulation output results presented here were used for post-processing to predict rotor noise using PSU-WOPWOP.



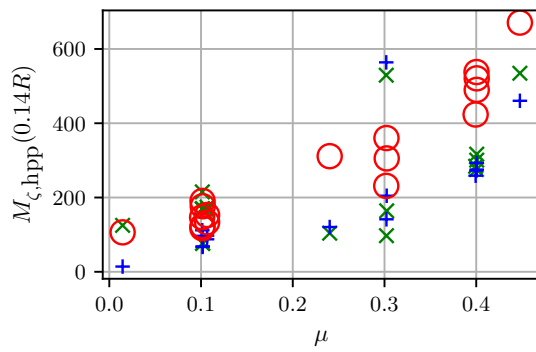
**Figure 5.13:** Comparison of mean rotor shaft forces and moments, and power obtained using Dymore and Dymore+VPM simulations against measurement data from Ref. [112] for the Bo 105 rotor over a sweep of advance ratios  $\mu = 0.01-0.45$ .



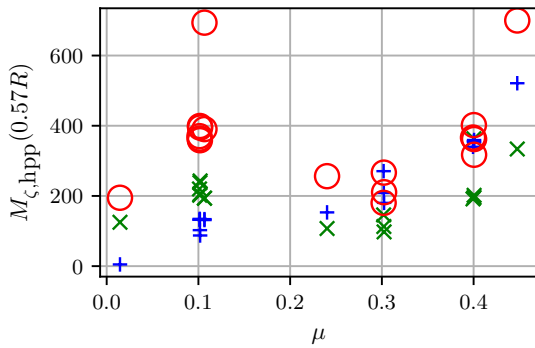
(a) Blade flap bending moment at  $r = 0.1034$



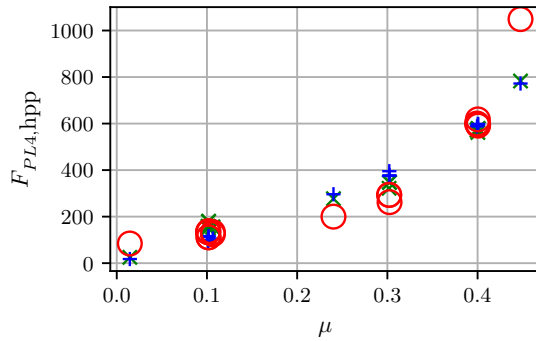
(b) Blade flap bending moment at  $r = 0.5688$



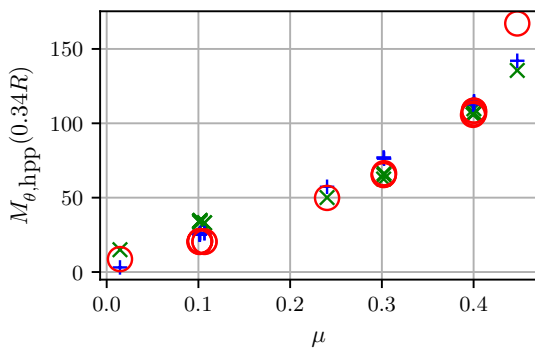
(c) Blade chord bending moment at  $r = 0.1447$



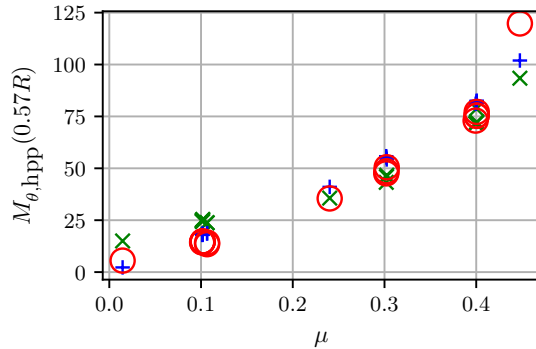
(d) Blade chord bending moment at  $r = 0.5688$



(e) Pitch link loads

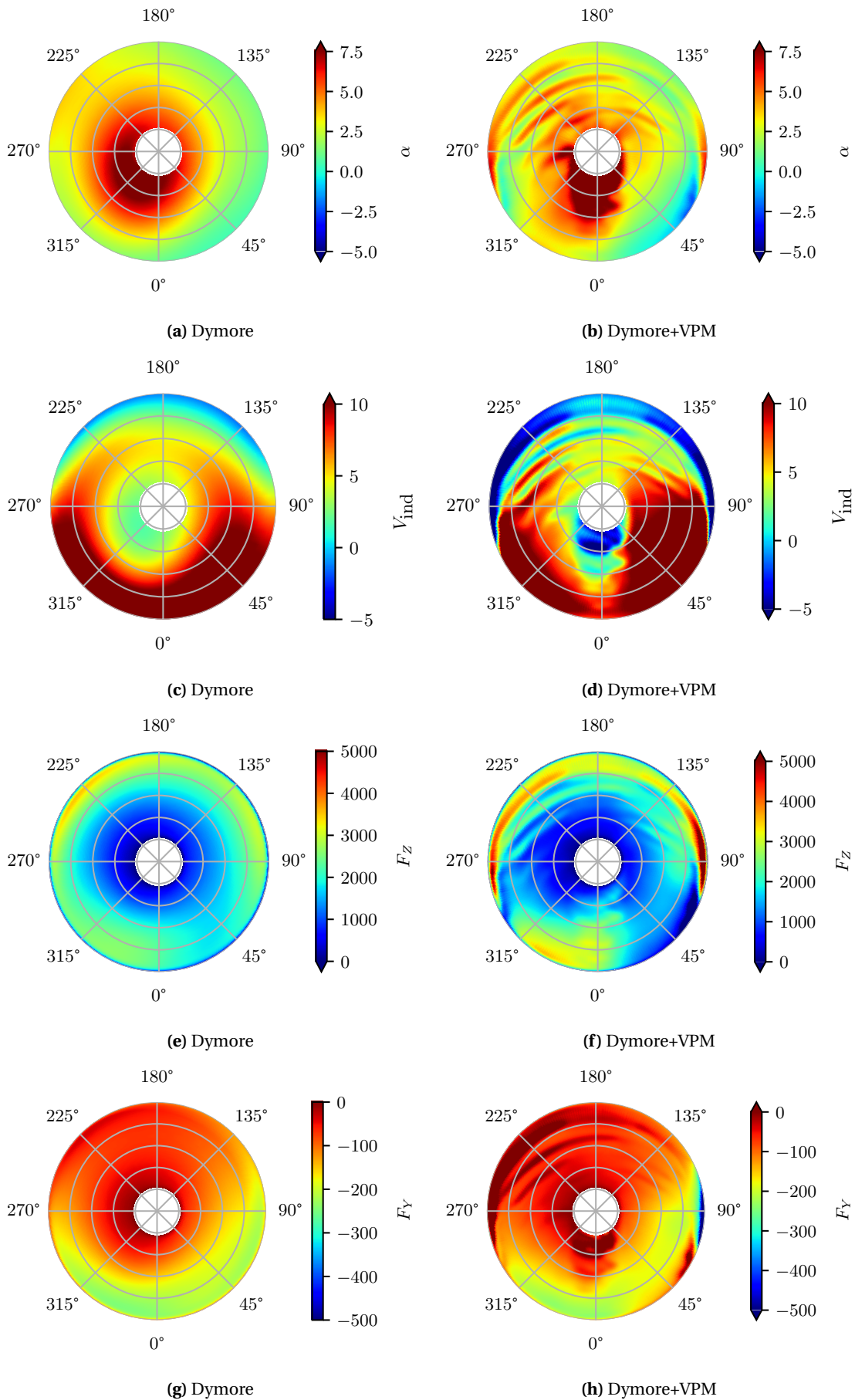


(f) Blade twisting moment at  $r = 0.3361$

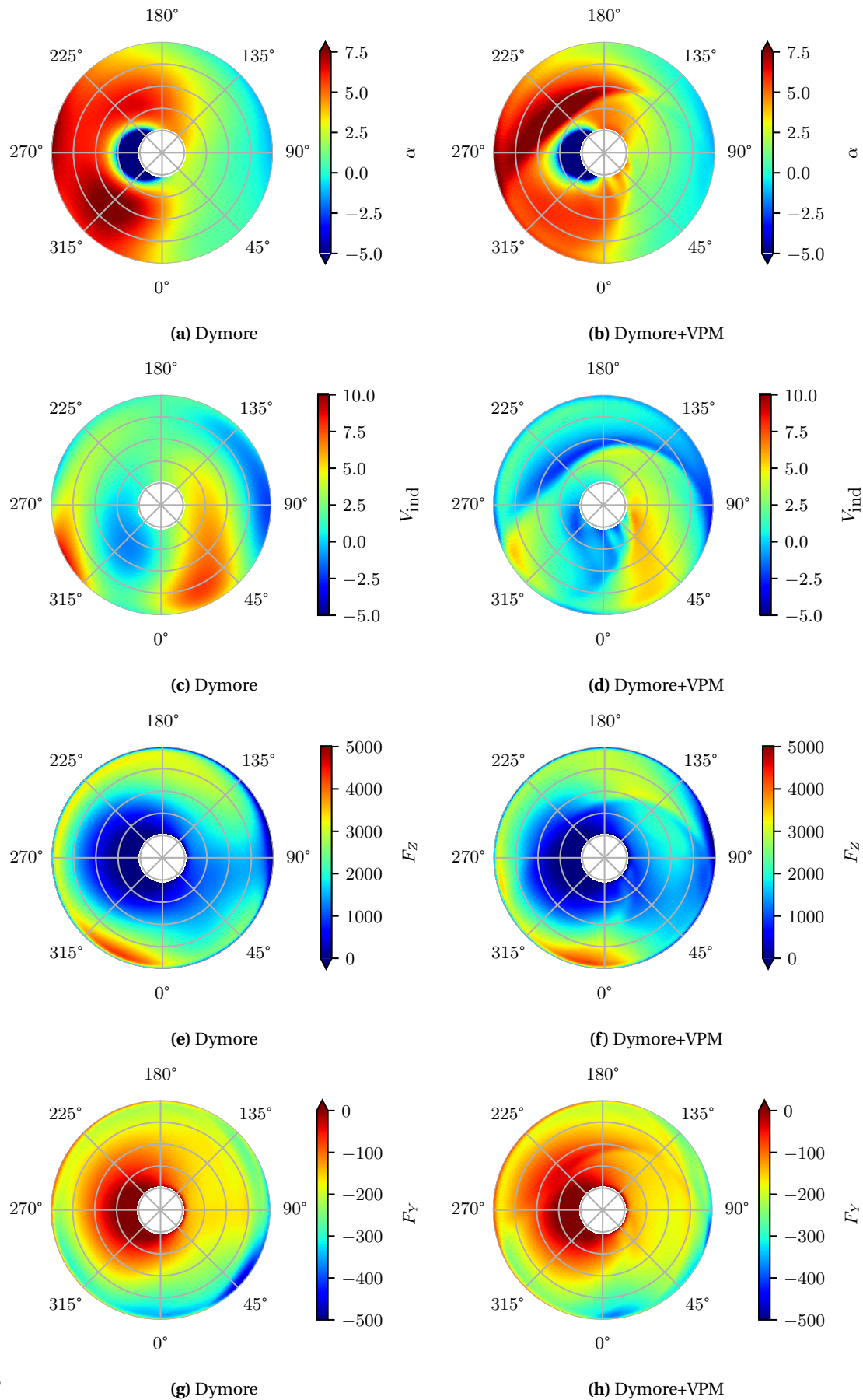


(g) Blade twisting moment at  $r = 0.5688$

**Figure 5.14.:** Comparison of half-peak-to-peak (HPP) dynamic blade loads and pitch link loads obtained using Dymore and Dymore+VPM simulations against measurement data from Ref. [112] for the Bo 105 rotor over a sweep of advance ratios  $\mu = 0.01$ – $0.45$ .

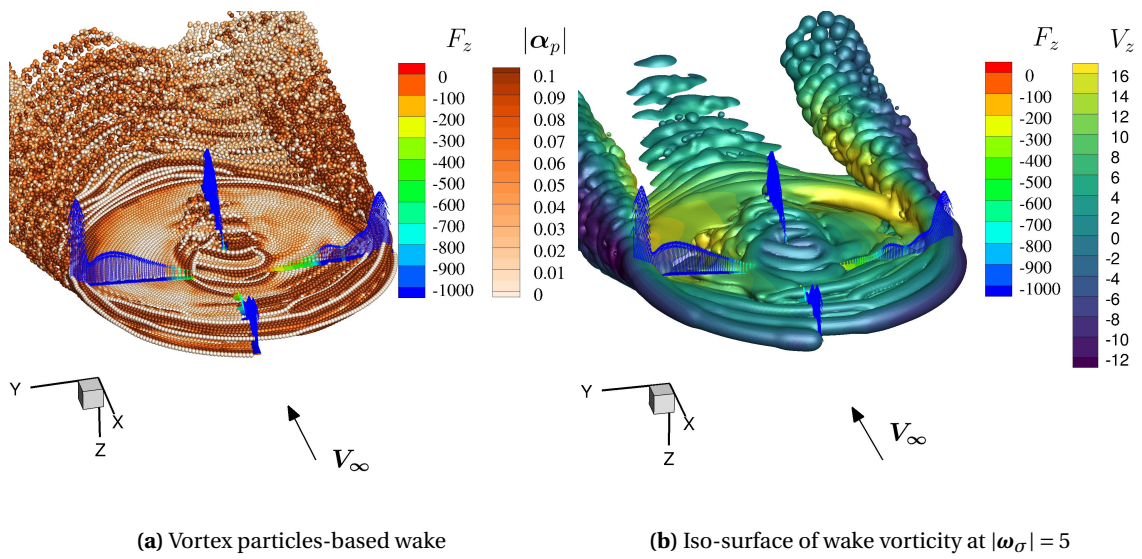


**Figure 5.15.:** Comparison of aerodynamic parameters and blade section loads over the disk of the Bo 105 rotor obtained using standalone Dymore and Dymore+VPM simulation frameworks for the case of Run 42 point 7 ( $\mu = 0.1$ ) from Ref. [112].

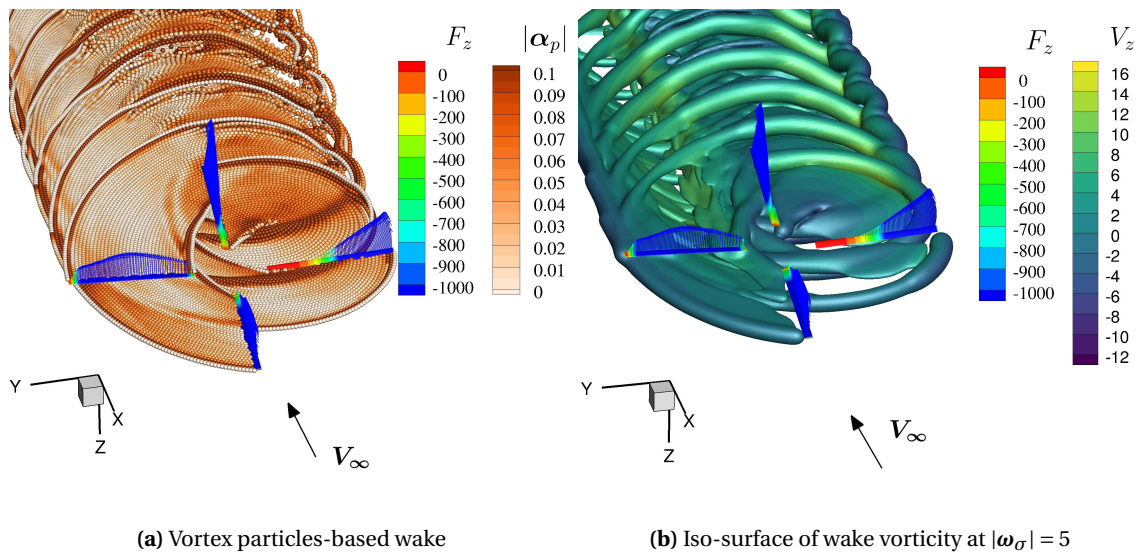


**Figure 5.16.:** Comparison of aerodynamic parameters and blade section loads over the disk of the Bo 105 rotor obtained using standalone Dymore and Dymore+VPM simulation frameworks for the case of Run 26 point 11 ( $\mu = 0.3$ ) from Ref. [112].





**Figure 5.17.:** Visualization of the vortex wake of the Bo 105 rotor for the Run 42 point 7 case [112] obtained using VPM-based wake model.



**Figure 5.18.:** Visualization of the vortex wake of the Bo 105 rotor for the Run 26 point 11 case [112] obtained using VPM-based wake model.

#### 5.4.4. Aeroacoustic noise

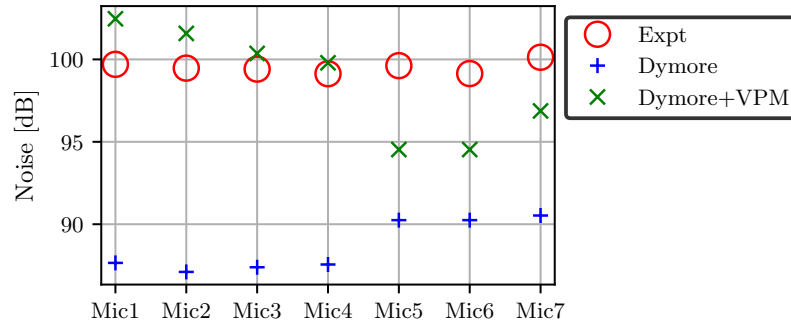
The rotor test campaign of Ref. [111] also focused on the impact of IBC actuation on BVI noise. For this purpose, rotor tests were conducted in the 40- by 80-foot wind tunnel at different advance ratios. Since the subject of the investigation was BVI noise, the rotor shaft tilt angle was held predominantly positive or close to zero. The case corresponding to Run 42 point 7 ( $\mu = 0.1$ ) was the only unique operating case, from a number of other cases at  $\mu = 0.1$ , for which baseline rotor noise measurements are available together with aeromechanical data. Therefore, this case was chosen to validate the aeroacoustics model of the baseline Bo 105 rotor.

Table 5.4 shows the locations of the different microphones placed beneath the rotor where acoustic measurements of the baseline Bo 105 rotor were made. The sensor locations are based on the shaft reference frame of the Bo 105 model; for reference, see Fig. 2.8 and Table A.2. It is worth noting that the arrangement in Table 5.4 corresponds to the 1994 Run 42 point 7 case only. Different microphone distributions were used for other operating conditions for which measurements were made in the test campaign, but they are not the subject of this study. The acoustic noise in dB reported in Ref. [112] was based on a frequency band of 6-40 BPF. This is standard practice adopted when only BVI noise is of interest; for example, see Ref. [40]. However, there is inconsistency in the reported range of frequencies used for filtering. Ref. [112] reports that filtering was carried out between 150 Hz to 1500 Hz or 6-40 BPF. However, given the angular rotation rate of the Bo 105 of 7 Hz, 6-40 BPF translates to 170 Hz - 1133 Hz. The latter range was used in the current study to filter the acoustic pressure perturbation and evaluate the overall sound pressure level (OASPL).

Mic. no.	x	y	z
1	5.0	5.40	5.748
2	5.0	4.05	5.748
3	5.0	2.7	5.748
4	5.0	2.02	5.748
5	-2.0	-4.05	4.304
6	-4.456	-4.05	4.304
7	-4.456	-2.7	4.304

**Table 5.4.:** Acoustic sensor locations with respect to the hub in the shaft reference frame (see Fig. 2.8).

Figure 5.19 shows a comparison of the predicted rotor noise using Dymore and Dymore+VPM with the measured data. The effect of the fidelity of the comprehensive rotor modeling framework is apparent. The Peters-He inflow model-based simulation framework significantly under-predicted the rotor noise at all microphone locations. This can be attributed to the inability of the Dymore simulation framework to capture the high-frequency induced inflow variations that are the source of corresponding variations in airloads. Consequently, the term in the Farassat's formulation (see Eq. 4.5) that relies on a derivative of airloads is incorrectly calculated. The correlation between measured data and BVI noise predicted using VPM-based wake solution is fair for microphones Mic1-Mic4. For the remaining microphones, Mic5-Mic7, the noise is under-predicted by 3-5 dB. Since the measurement test campaign did not report any airloads measurements, which are re-



**Figure 5.19.:** Comparison of Bo 105 rotor noise prediction at Run 42 point 7 ( $\mu = 0.1$ ) using Dymore and Dymore+VPM simulations with experimental measurement data from Ref. [112].

quired for predicting noise using the Farassat’s F1A formulation, it is difficult to ascertain the exact source of the discrepancy for microphones Mic5-Mic7. Overall, the correlation of predicted rotor acoustic noise can be considered to be fair. However, for added measure, the HART II rotor was also simulated, and acoustic noise emissions were compared to measurement data for improved validation of the acoustics framework. These results are presented in the following section.

## 5.5. HART II

The HART II rotor is a Bo 105 Mach-scaled model rotor that was tested in the DNW wind tunnel in 2001 [256]. The measurement data from the test campaign have been extensively used for validating different rotor analysis codes in a number of publications [10]. In the current study, the HART II rotor was used primarily to validate the acoustics analysis framework detailed in Chap. 4. While the complete HART II rotor test campaign included an exhaustive range of experiments, only a limited data set has been made public online via the DLR website [7]. This data set includes a baseline rotor test in descent flight conditions experiencing BVI. This flight condition, referred to as ‘BL’, was simulated as part of the current acoustics study. Results presented in Ref. [78] show that when unsteady blade pressure measurement data were used as input for acoustic analysis, the predicted noise was very accurate even in BVI conditions. This suggests that the accuracy of the rotor aerodynamics are correlated with the predicted noise. Therefore, in addition to validating the acoustic framework, the BL case also serves as a validation for BVI modeling using the Dymore+VPM framework.

The rotor control input in the current study was prescribed, and the relevant input data needed to set the simulation up was obtained from Ref. [256]. The acoustics measurement data is available over a number of grid points on a plane. The exact coordinates of the microphone locations were obtained from Ref. [276] and shown in Table 5.5(a). Note that the coordinates are provided in Ref. [276] in a ‘wind tunnel’ coordinate system where the rotor hub location is given using Eq. 5.5. Table 5.5(b) contains the final microphone coordinates that were used based on the simulated rear tilt of the rotor shaft  $\gamma = 5.3^\circ$ .

Mic. no.	x	y	z
1	0.001	-2.686	-2.224
2	-0.019	-2.241	-2.225
3	-0.012	-1.797	-2.224
4	-0.010	-1.344	-2.219
5	-0.007	-0.894	-2.214
6	0.005	-0.456	-2.214
7	0.016	0.009	-2.217
8	0.007	0.455	-2.214
9	0.011	0.905	-2.205
10	0.013	1.360	-2.207
11	0.012	1.810	-2.202
12	0.019	2.268	-2.213
13	0.014	2.701	-2.208

(a)  $\gamma = 0^\circ$

Mic. no.	x	y	z
1	-0.118	-2.686	-2.224
2	-0.139	-2.241	-2.225
3	-0.132	-1.797	-2.224
4	-0.130	-1.344	-2.219
5	-0.127	-0.894	-2.214
6	-0.114	-0.456	-2.214
7	-0.103	0.009	-2.217
8	-0.112	0.455	-2.214
9	-0.108	0.905	-2.205
10	-0.106	1.360	-2.207
11	-0.107	1.810	-2.202
12	-0.100	2.268	-2.213
13	-0.105	2.701	-2.208

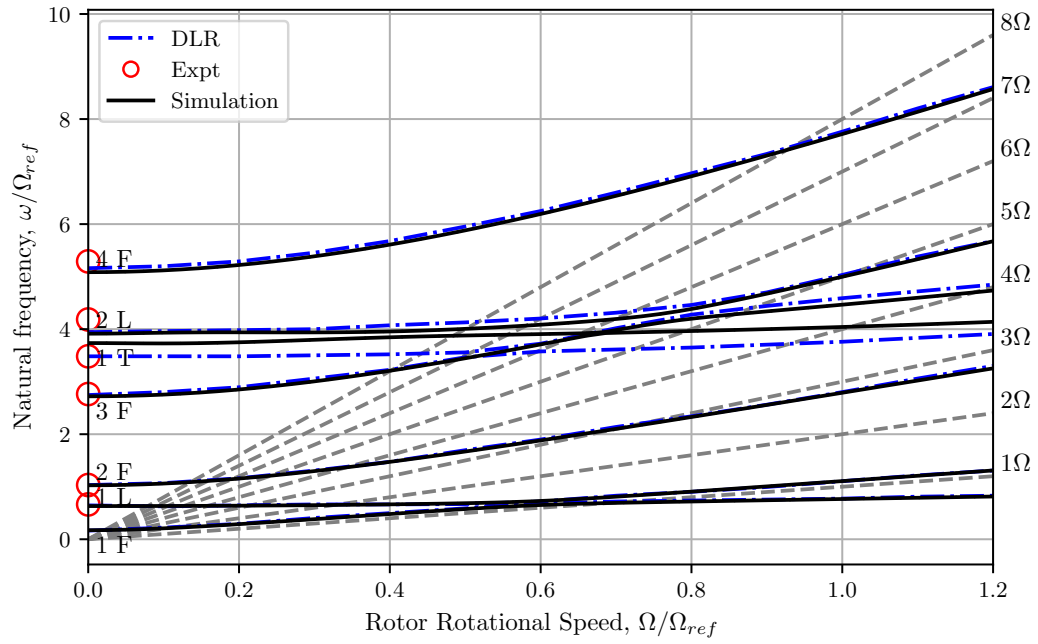
(b)  $\gamma = 5.3^\circ$

**Table 5.5.:** Acoustic sensor locations in the rotor shaft frame (see Fig. 2.12(a)).

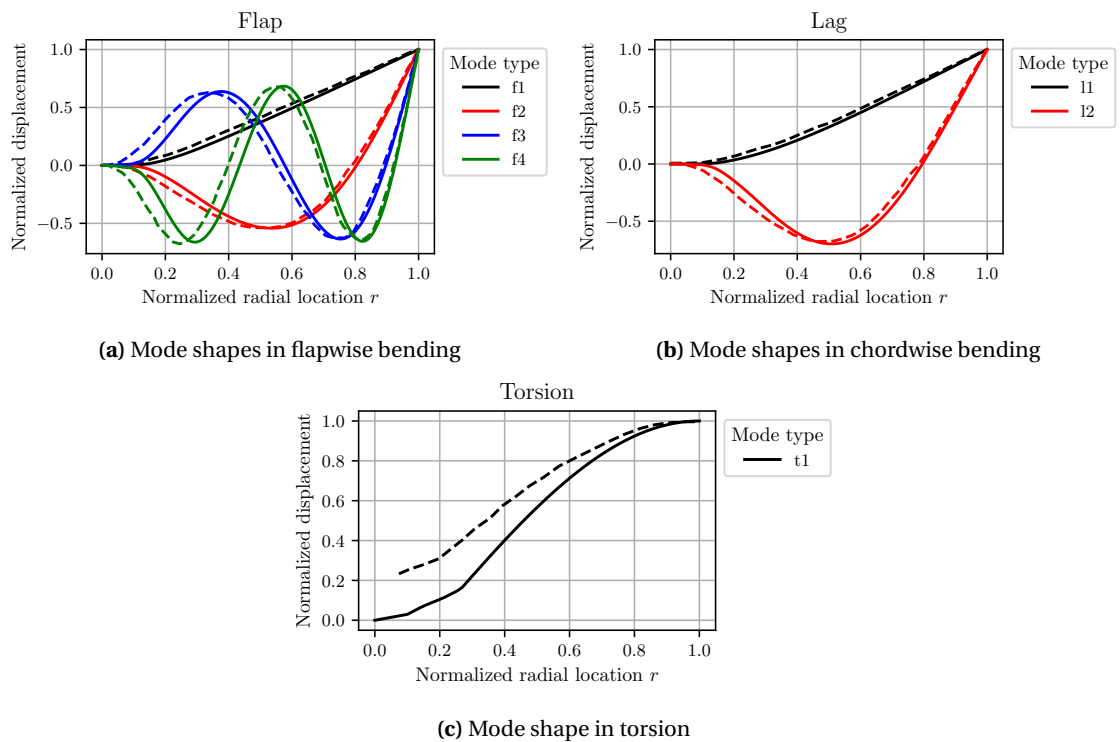
$$\begin{aligned}
 x_{\text{hub,WT}} &= 4.400 - 4.601 \cos(13.7^\circ + \gamma) \\
 y_{\text{hub,WT}} &= 0 \\
 z_{\text{hub,WT}} &= 0.915
 \end{aligned} \tag{5.5}$$

### 5.5.1. Blade natural frequencies and mode shapes

Figure 5.20 shows the frequency fan plot of the HART II rotor and compares the results obtained in the current study against those reported in Ref. [256]. There is a good match between all the predicted blade natural frequencies, except torsion, when compared to results reported by DLR in Ref. [256], over the entire range of rotor rotational speeds. It is worth noting that results from a number of other organizations are available in Ref. [256], but those provided by DLR were chosen arbitrarily in this study. The predicted torsion frequencies exhibit a near-constant offset compared to the experimental measurement data, at  $\Omega = 0$ , as well as the reported results from DLR. This could be the result of modeling the blade with a clamped condition at the blade rotor, as shown in Fig. 2.12(b), instead of a torsional spring. This also leads to differences in the corresponding blade mode shapes shown in Fig. 5.21. While the mode shapes for flap and lag are a good match with the corresponding results from Ref. [256], the predicted torsion mode shape differs due to the nature of the root condition. It is worth noting that different partner institutions, who reported their results in Ref. [256], modeled the blades differently. Consequently, there is considerable spread in the fan plot, as well as mode shapes, as reported by them. This indicates that the manner in which the blade root is modeled has a non-negligible effect on the blade natural frequencies as well as the torsion blade mode shape.



**Figure 5.20.:** HART II rotor blade frequency fan plot at  $0^\circ$  collective compared with data from Ref. [256].



**Figure 5.21.:** Comparison of the mode shapes obtained in the current study (solid lines) versus results from DLR provided in Ref. [256] (dashed lines).

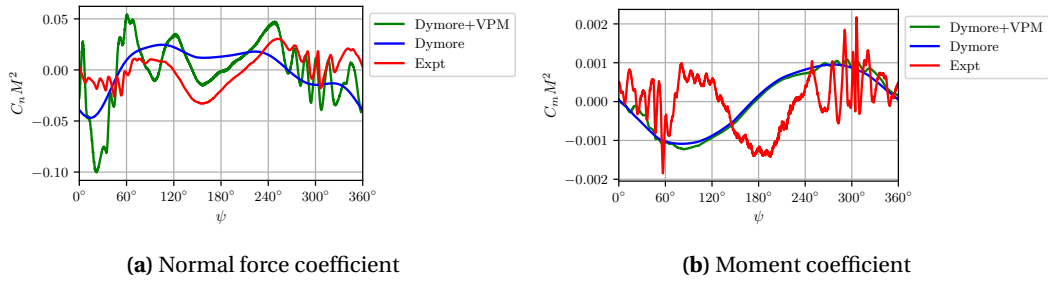
### 5.5.2. Rotor aeromechanical results

As mentioned earlier, the main purpose of this study involving the HART II rotor was to verify and validate the acoustics analysis framework. For this purpose, the baseline HART II rotor case BL was simulated. This corresponds to a simulated descent flight condition with rotor shaft tilt  $\gamma = 5.3^\circ$ , forward speed  $V_\infty = 32.8 \text{ m s}^{-1}$ , collective  $\theta_0 = 3.8^\circ$ , longitudinal cyclic  $\theta_{1s} = -1.34^\circ$  and lateral cyclic  $\theta_{1c} = 1.92^\circ$ . The simulation was conducted using a particle spanwise resolution of  $n_{\text{res}} = 40$  and a total number of particles  $N_{p,\text{max}} = 1.25 \times 10^5$  in the rotor wake.

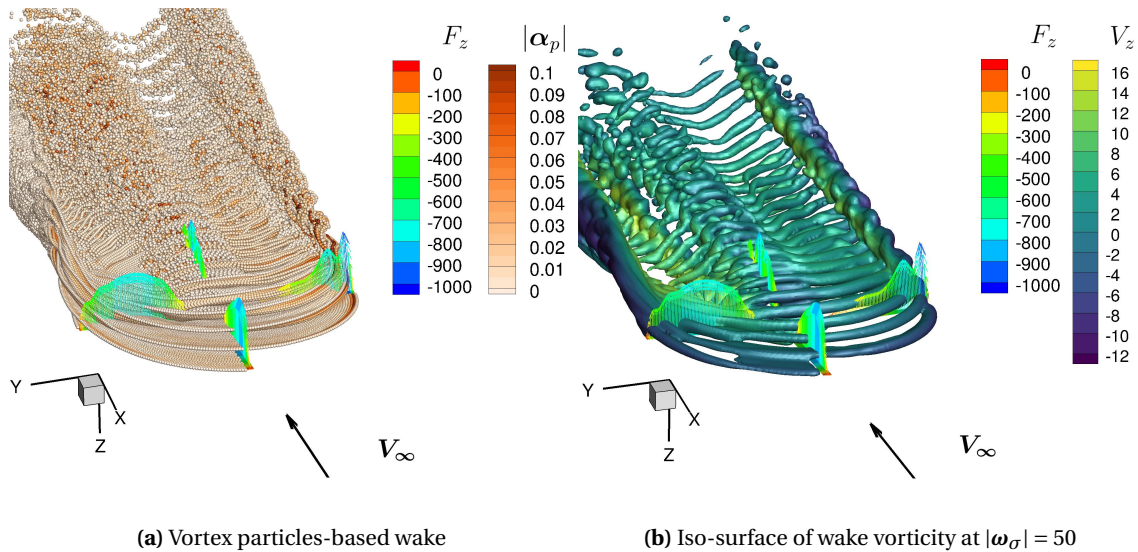
Figure 5.22 shows an extract of the aerodynamic normal force and moment at  $r = 0.87$  over the entire azimuth. The simulation results are compared to corresponding measurement data for a closer analysis of the BVI events and their direct effect on blade aerodynamic loads. From Fig. 5.22(a), it is evident that VPM-based simulation is able to accurately capture the BVI events but only those occurring on the retreating side. It also over-predicts the oscillating effect of vortex interaction on the normal force in the advancing side region. Unsurprisingly, the Peters-He model-based simulation was only able to capture the general trend of normal aerodynamic load. In contrast, the VPM-based simulation performs just as well as the Peters-He model-based simulation with regard to predicting the aerodynamic moment in Fig. 5.22(b). Both models were only able to capture the mean trend of measured moment data in this case. This can be attributed to the limitation of the blade aerodynamics analysis based on the lifting-line model. Small fluctuations in the section angle of attack due to the passage of trailing vortices in proximity to the blade register a corresponding fluctuation in the lift forces. This is because blade sections predominantly operate in the regime where lift is linearly proportional to the angle of attack. In contrast, the blade section pitching moment is predominantly constant over a significant range of angle of attack (see Fig. 2.14(c)). Consequently, fluctuations in the angle of attack do not necessarily lead to a proportional variation in sectional moment. This can also be observed in the results presented in Ref. [256], where free wake model-based simulations were able to capture the high-frequency fluctuations in normal force but not in moment oscillations. Since the vortices pass in close proximity to the lifting-line itself, the approximation of collapsing the chordwise airfoil representation to a point (i.e., quarter-chord collocation point) starts to break down and does not result in accurate aerodynamics calculation.

Figure 5.23 illustrates the overall rotor wake, modeled using VPM, clearly indicating the proximity of trailing tip vortices to the following blades. Figure 5.23(a) shows that the particles-based wake model was able to capture the dominant characteristics, including the coalescing of the individual trailing vortices into two large vortices forming at the lateral ends of the rotor disk. Figure 5.23(b) shows the iso-surface representation of the wake vorticity where the individual trajectories are more clearly evident.

Since the accuracy of the noise prediction depends on the accuracy of the aerodynamic loads and blade motion, it is worthwhile to examine the overall results obtained from the different simulation frameworks. Figure 5.24 shows the distribution of the angle of attack, induced velocity, thrust, and drag over the rotor disk obtained using Dymore and Dymore+VPM. The angle of attack distribution over the rotor azimuth is an insightful quantity that sheds light on the interplay between the rotor control angles, blade elastic deformation, and the wake-induced inflow. This quantity

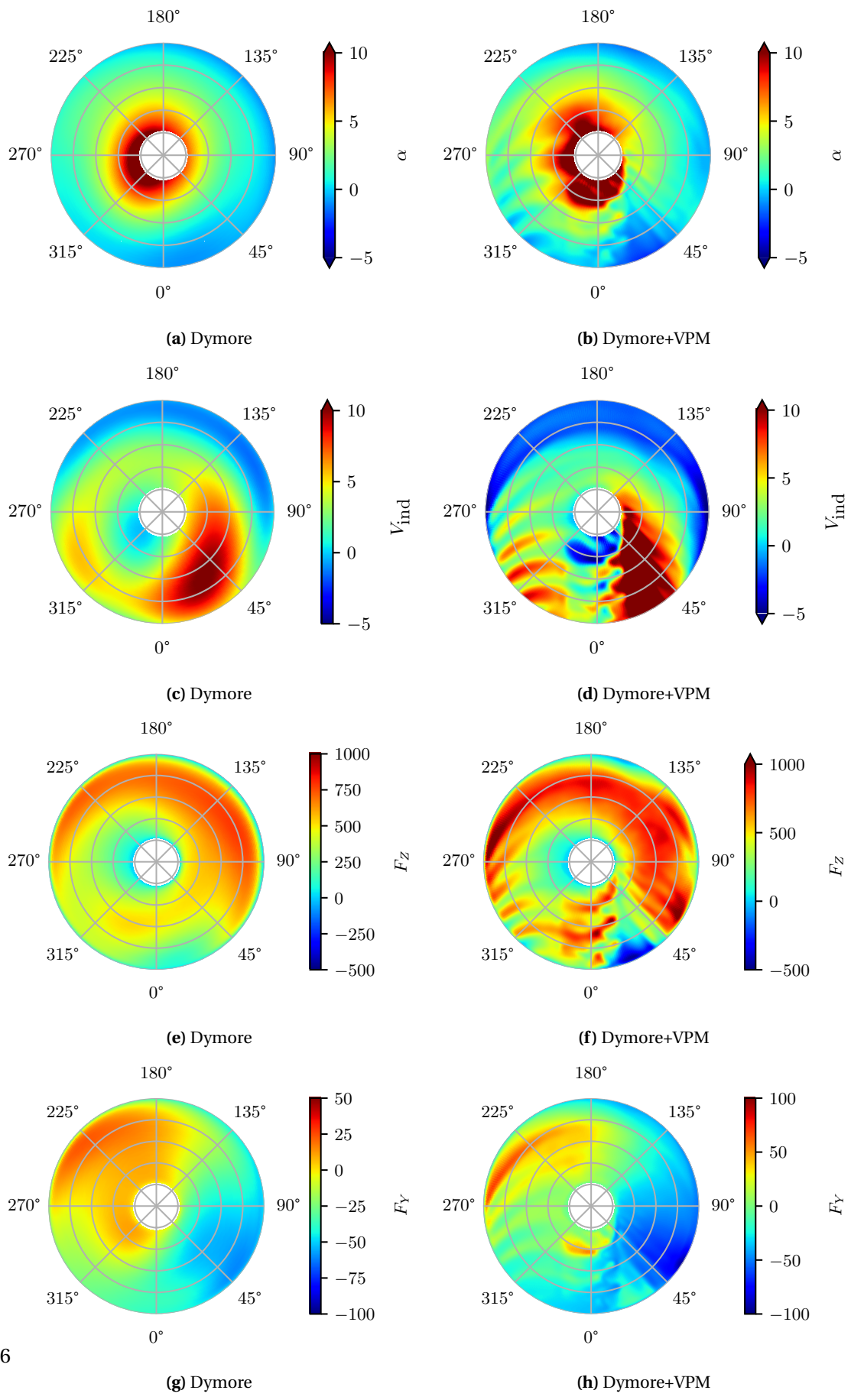


**Figure 5.22.:** Comparison of azimuthal time-history of section blade coefficients of the HART II rotor at  $r = 0.87$  obtained in the current work versus experimental measurements reported in Ref. [256].



**Figure 5.23.:** Visualization of the vortex wake of the HART II BL case obtained using VPM-based wake model.

is not usually available in any data set reported after a rotor measurement test campaign. In fact, Ref. [42] has rightly called out the lack of blade section angle of attack measurement capability to be ‘frustrating’. Overall, it is evident that the Peters-He inflow model is capable of capturing the dominant wake characteristics—for example, the higher angle of attack near the blade root on the retreating side in Fig. 5.24(a), lift in the first rotor quadrant in Fig. 5.24(c), thrust distribution in the region  $90^\circ < \psi < 270^\circ$  in Fig. 5.24(e), and drag in the third quadrant near the blade tips in Fig. 5.24(g). In contrast, VPM is capable of capturing the multiple BVI events that occur over the rotor disk. These are evident to a lesser degree in the angle of attack (Fig. 5.24(b)) and drag force (Fig. 5.24(h)) and more apparent in the induced velocity (Fig. 5.24(d)) and the thrust force (Fig. 5.24(f)).



**Figure 5.24.:** Comparison of blade section loads and aerodynamic parameters over the disk of the HART II rotor obtained using standalone Dymore and Dymore+VPM simulation frameworks.



### 5.5.3. Aeroacoustic noise

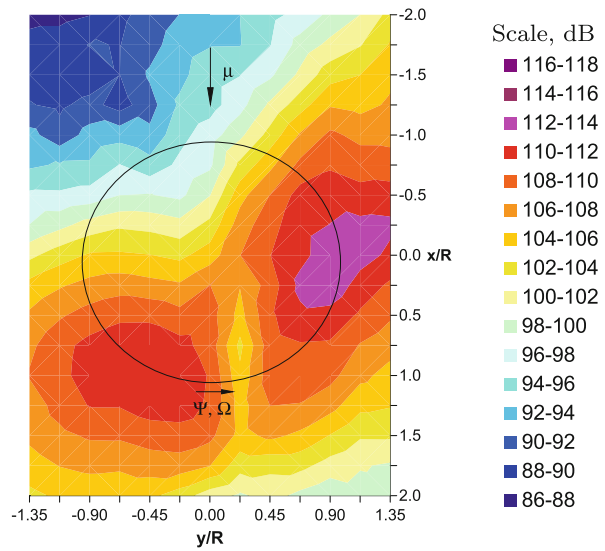
This section is dedicated to the presentation and discussion of acoustic noise results for the BL case of the HART II rotor. It is worth noting that the experimental test apparatus also included a fuselage, but only the isolated rotor was modeled in this study. Ref. [129] carried out a similar analysis of the HART I rotor, a precursor to the HART II, using CAMRAD II and indirectly included the effect of the fuselage used in that study by correcting the shaft tilt angle by  $0.2^\circ$ . The basis of this correction, however, was not detailed. Therefore, the current study was carried out without any shaft angle correction due to the presence of fuselage and no structural or aerodynamic effect of the fuselage was modeled. There was a shaft angle correction to account for wind tunnel wall effects, but this is already included in the shaft tilt angle  $\gamma$  taken from Ref. [256].

Figure 5.25<sup>1</sup> shows a comparison of the noise predictions made using PSU-WOPWOP, with the blade motion and aerodynamic loads output from Dymore (Fig. 5.25(b)) and Dymore+VPM (Fig. 5.25(c)) frameworks, against the experimental measurement data from the HART II test campaign (Fig. 5.25(a)). The experimental data were filtered to include only 6-40 BPF, so the simulation data presented were also appropriately filtered. The acoustics analysis framework described in Sec. 4.3 was used for this purpose in order to obtain acoustic pressure perturbations at a grid of observers locations given in Table 5.5(b). Based on the results presented in Fig. 5.25(b), it is evident that standalone Dymore-based results significantly under-predicted rotor noise. The reason behind this can be attributed to the inability of the Peters-He inflow model to capture any high-frequency aerodynamic fluctuations (see Fig. 5.22(a)) resulting from BVI. Consequently, the terms in the loading acoustic pressure in Eq. 4.5, that contain a derivative of the aerodynamic forces acting on the fluid, are inaccurately calculated. This is not the case with the VPM-based framework in Fig. 5.25(c), which shows a predominantly good match with the experimental predictions, especially below the rotor disk. In regions away from the rotor disk, only the qualitative trend could be captured.

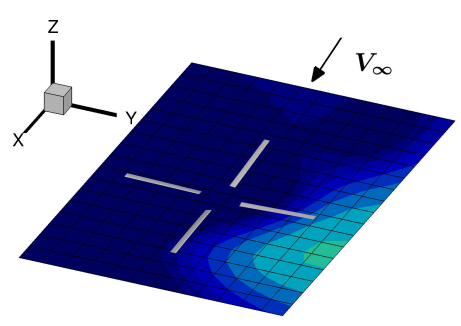
In order to better analyze the contour map of the acoustic emissions from the simulations, Fig. 5.26 shows the results where the colorbar was adjusted to accentuate the distribution in the respective cases. Figure 5.26(a) shows that the Peters-He model not only under-predicted the overall noise but was also unable to capture the qualitative trend of its distribution over the measurement domain when compared to Fig. 5.25(a). In contrast, Fig. 5.26(b) shows that the VPM-based framework was able to predict the qualitative distribution of rotor noise very well. Quantitatively, Dymore+VPM-based prediction matches measurement data in the regions directly below the rotor disk but is over-estimated in the region that is near the retreating side but away from the rotor disk. Overall, the results render sufficient confidence in the ability of the Dymore+VPM framework to capture the dominant BVI effects. Additionally, the ability of PSU-WOPWOP post-processing framework to then predict the noise emissions is also considered to be validated.

---

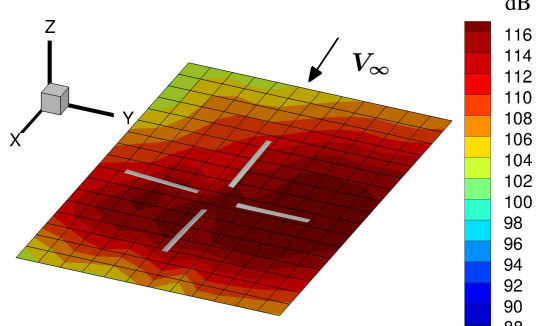
<sup>1</sup>Appropriate permissions have been obtained from Springer Nature to reproduce the Fig. 5.25(a) from Ref. [256].



(a) Experiment [256]

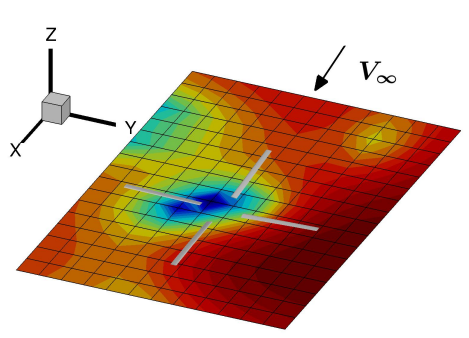


(b) Dymore

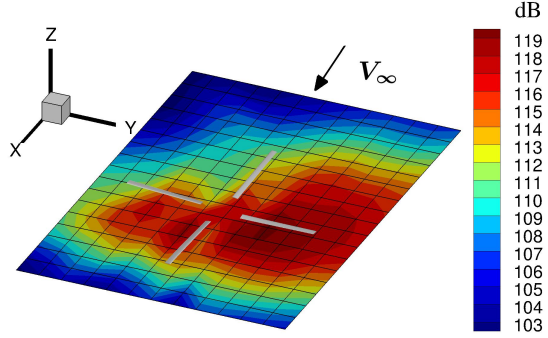


(c) Dymore+VPM

Figure 5.25.: Comparison of the predicted noise levels for the HART II BL case using the different simulation frameworks used in the current work and the experimental data reported in Ref. [256].



(a) Dymore



(b) Dymore+VPM

Figure 5.26.: Re-scaled predicted noise levels for the HART II BL case for a qualitative assessment of the results obtained using the different simulation frameworks used in the current work.

## 5.6. Active Bo 105 Rotor

The validated full-scale Bo 105 rotor from Sec. 5.4 was further used to demonstrate the capability of the current analysis framework to model active rotors. For this purpose, the rotor model definition of the Bo 105 was simply augmented using compound airfoil tables as detailed in Sec. 2.5.5. It is worth noting that the study in Ref. [300] showed that the flexibility inherent in the FishBAC mechanism had a non-negligible effect on the section aerodynamics. However, in the current work, the morphing mechanism was considered stiff enough that prescribed actuation matched the desired deflection profile. Throughout this study, the active camber deflection was prescribed, and the dynamics of the FishBAC actuation system were neglected.

It has already been demonstrated in Ref. [16] that small deflections of the FishBAC mechanism can cause significant changes in the 2D airfoil aerodynamic properties. For example, a deflection of  $2.3^\circ$  at  $M = 0.4$  changes the airfoil  $L/D$  from 14.67 to 33.23 and the  $C_m$  from -0.0084 to -0.045. In addition to that, continuous trailing-edge flaps, which are in principle similar to the FishBAC mechanism, were investigated in Ref. [264] for the purposes of primary rotor control. Here, it was shown that a maximum deflection of  $5.4^\circ$  was sufficient for rotor primary control<sup>2</sup>. Therefore, small FishBAC deflections are deemed sufficient to demonstrate the influence of active camber morphing on rotor aeromechanics. Active camber morphing was accomplished using harmonic trailing-edge actuation at 1P given by Eq. 5.6. Here  $\delta_0$  represents the amplitude of actuation, and  $\phi$  denotes the input phase delay. Different camber morphing profiles were considered using  $\delta_0 = 0.5^\circ, 1.0^\circ, 1.5^\circ$  together with a sweep of phase delay  $\phi = [0^\circ, 360^\circ]$ . The objective was to investigate the impact of active rotor morphing on rotor power, hub vibrations, and aeroacoustic noise output. The cruise speed operating condition of Run 26 point 11 from Table A.3 was used for this purpose.

$$\delta = \delta_0 \sin(2\pi t/T + \phi) \quad (5.6)$$

Theoretically, the rotor acts as a filter by allowing forces and moments only at integer multiples of  $N_b P$  to be transferred at the non-rotating rotor hub. In reality, non-integer multiples of  $N_b P$  forces can be experienced at the rotor hub due to slight dissimilarities in the rotor blades, but that is not the subject of this work. Since the contribution due to vibrations at higher multiples of  $N_b P$  can be much smaller in magnitude, it is common practice to use only the  $N_b P$  vibratory loads in order to represent vibrations due to the rotor [217][85][83]. This corresponds to a frequency of 4P for the four-bladed Bo 105 rotor. A helicopter airframe was not modeled in the current study, so the effect of airframe dynamics and the aerodynamic effect of rotor wake that periodically impinges on the fuselage were not accounted for. Vibration indices,  $J_1$  and  $J_2$ , were used as a cumulative measure of the harmonic forces and moments transferred from the rotor to the non-rotating hub. Eqs. 5.7 and 5.8 show the two different metrics used. Eq. 5.7 represents the hub vibration index containing all the components of the dominant 4P vibratory loads, and moments. This vibration index was chosen based on a combination of the different vibration indices suggested in Refs.

---

<sup>2</sup>The airfoil tip deflection is provided in inches in the study. The value of  $5.4^\circ$  was evaluated assuming the deflection begins at three quarter-chord.

[217], [85] and [83]. The loads and moments were weighted with the corresponding baseline rotor values, indicated using  $F_{4x0}, F_{4y0}$  etc. Note that all the vibratory components in Eq. 5.7 have equal weighting. Since dominant vibrations tend to occur along the shaft axis, another metric  $J_2$  (Eq. 5.8) was defined such that it contained only the vibratory components along the Z-axis.

$$J_1 = \sqrt{\left(\frac{F_{4x}}{F_{4x0}}\right)^2 + \left(\frac{F_{4y}}{F_{4y0}}\right)^2 + \left(\frac{F_{4z}}{F_{4z0}}\right)^2 + \left(\frac{M_{4x}}{M_{4x0}}\right)^2 + \left(\frac{M_{4y}}{M_{4y0}}\right)^2 + \left(\frac{M_{4z}}{M_{4z0}}\right)^2} \quad (5.7)$$

$$J_2 = \sqrt{\left(\frac{F_{4z}}{F_{4z0}}\right)^2 + \left(\frac{M_{4z}}{M_{4z0}}\right)^2} \quad (5.8)$$

Since there is no experimental data available for a rotor fitted with the FishBAC mechanism, the active rotor results obtained in this section could not be validated by comparing against measurement data. It is for this purpose that the validation presented in the foregoing sections in this chapter was conducted in order to render confidence in the predictive nature of the simulation frameworks.

### 5.6.1. Impact on performance and loads

The effect of active camber morphing on rotor power, mean rotor hub loads and vibratory hub loads is discussed here. Figures 5.27-5.29 show rotor aeromechanical quantities associated with the Bo 105 rotor, obtained at different  $\delta_0$  and  $\phi$  input. Figures 5.27(a)-5.27(c) show the variation of the rotor control angles in order to arrive at the trim conditions of Run 26 point 11 for different camber morphing actuations. By and large, the predictions made using Dymore (depicted using solid lines) and Dymore+VPM (depicted using dashed lines) follow the same trends. The maximum difference in the predicted control angles by the two frameworks hovers around  $0.5^\circ$ . The results presented in Figs. 5.27(d)-5.27(f) show that the controller was generally successful in trimming the rotor to operating conditions of the baseline rotor. Finally, Fig. 5.27(g) shows the variation in predicted rotor power consumption. While the results obtained using Dymore and Dymore+VPM cluster around a different mean predicted power consumption, the qualitative variation over  $\phi$ -sweep is largely similar. The VPM-based framework predicted a maximum reduction in power consumption of 9.1% compared to 9.6% by the Peters-He model-based framework. This maximum reduction in the former occurs close to  $\phi = 240^\circ$  while it occurs close  $\phi = 270^\circ$  for the latter. In either case, the actuation amplitude was  $\delta_0 = 1.5^\circ$ .

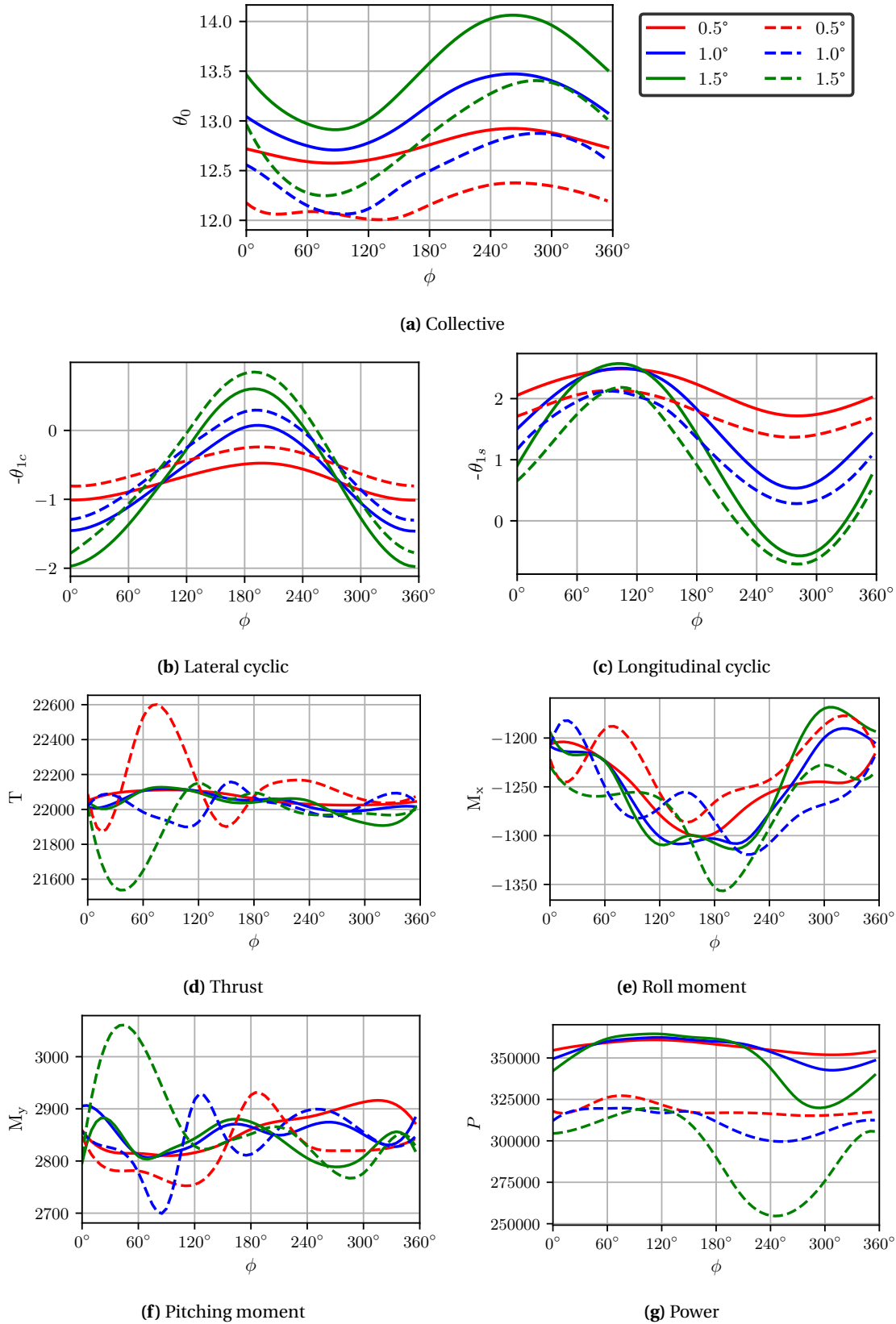
An analysis of the rotor aerodynamics for the case with  $\delta_0 = 1.5^\circ$  and  $\phi = 270^\circ$  in Fig. 5.28 shows that the change in rotor performance was brought about by a variation in the blade section angle of attack  $\Delta\alpha$  over the rotor disk. In Figs. 5.28(a) and 5.28(b), the angle of attack was decreased on the lateral sides of the rotor disk and increased on the fore and aft sections. This led to the corresponding shift in the normal lift force from the lateral to the fore and aft sections of the rotor disk (see Figs. 5.28(e) and 5.28(f)). Figures 5.28(g) and 5.28(h) show that the drag force increased on the advancing side, despite the decrease in angle of attack in that region. This can be attributed to the camber morphing profile with  $\phi = 270^\circ$ , which indicates that the active blade sections have a non-

zero deflection on the advancing side. Non-zero camber morphing, either upward or downward deflection, increases the section drag coefficient (see Ref. [16]). Together with the high dynamic pressure on the advancing side, this led to increased drag force on the advancing side. Near the blade tip, where the blade profile remained the same as the baseline, a large reduction in drag was obtained congruent with the change in angle of attack. Overall, this redistribution had a favorable effect on power consumption, as obtained in Fig. 5.27(g).

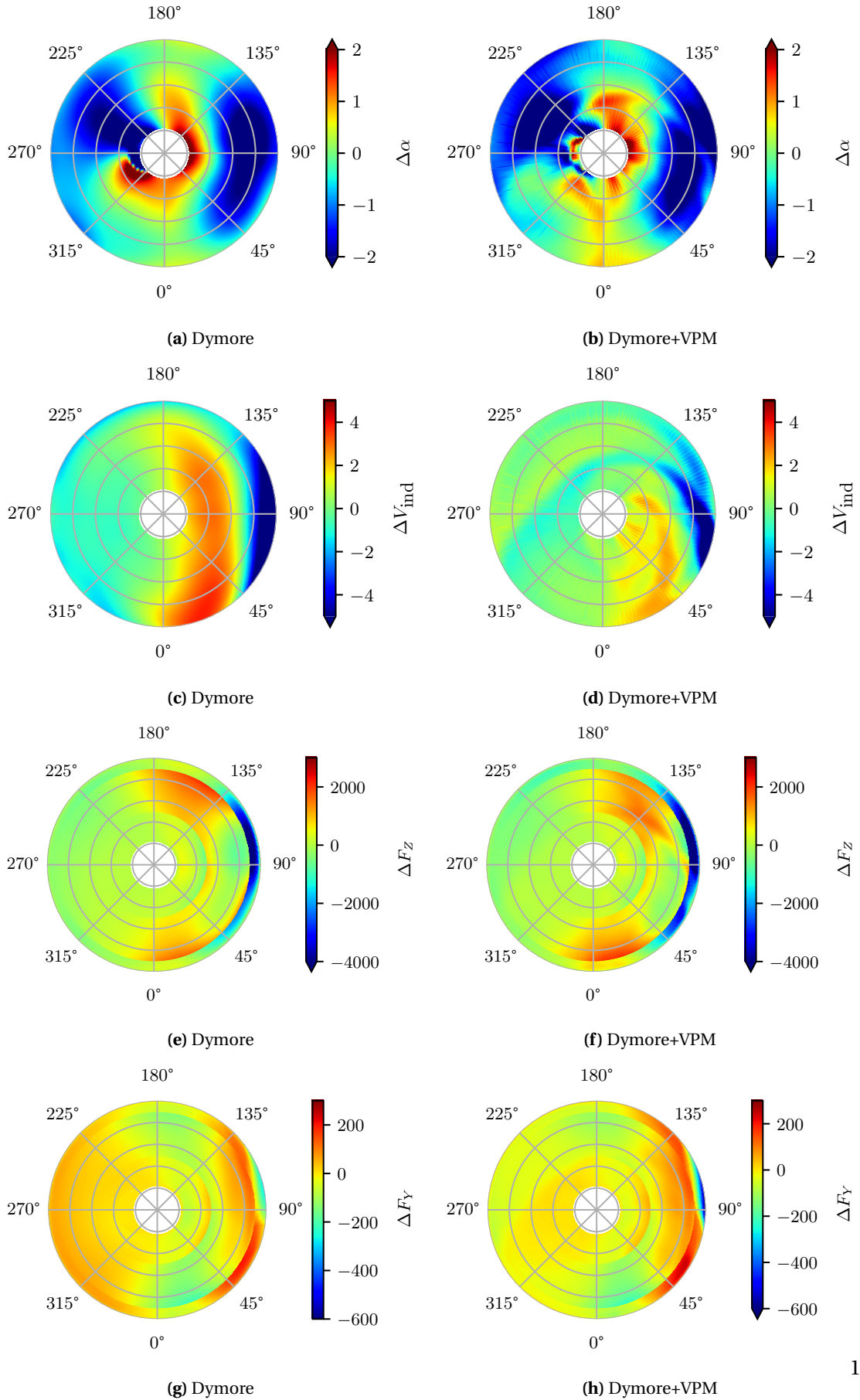
Figure 5.29 shows the vibratory 4P forces and moments generated on the active rotor for different camber deflection amplitude  $\delta_0$  and phase delay  $\phi$ . Results are shown for both the simulation frameworks—Dymore (solid lines) and Dymore+VPM (dashed lines). From Figs. 5.29(a)-5.29(f), it can be seen that similar trends are predicted by both frameworks. As already mentioned in the context of discussing the results of Fig. 5.16, this is likely a consequence of the operating conditions used. At  $\mu = 0.3$ , the effect of wake-induced inflow on the rotor aerodynamics is reduced since the wake vorticity is quickly washed away from the rotor. In the case of the 4P thrust force  $F_{4z}$ , 4P pitching moment  $M_{4x}$  and the 4P roll moment  $M_{4y}$ , there is a near-constant offset between the sets of results generated using Dymore and Dymore+VPM. The exact source of this disparity is difficult to ascertain since the 4P harmonic loads and moments are a byproduct of fluid-structure interaction involving higher harmonic airloads as well as the blade elastic motion. However, some of the discrepancies can be attributed to the inability of the Peters-He model to capture the high-frequency variations in the induced inflow velocity, given only six states were used in the current study. The number of inflow states was chosen for the baseline rotor so that the overall power requirement was correctly predicted, and this input parameter was left unchanged for the active rotor study.

Figure 5.29(g) and 5.29(h) show the combined effect of the different vibration indices presented earlier in Eqs. 5.7 and 5.8, respectively. The black horizontal line indicates the value corresponding to the baseline case. Consequently, results below this line indicate lower overall vibrations brought about by camber morphing using the FishBAC mechanism. From Fig. 5.29(g), it can be seen that the Peters-He model-based framework predicts no vibration reduction while the VPM-based framework results in a nominal reduction of 6.1% for  $\delta = 0.5^\circ \sin(2\pi t + 60^\circ)$ . An analysis of the  $J_2$  coefficient in Fig. 5.29(h) shows a similar result where Peters-He model-based results showed no reduction in vibratory loads but the VPM-based framework resulted in a maximum reduction of 32.8% in the vibrations index  $J_2$ .

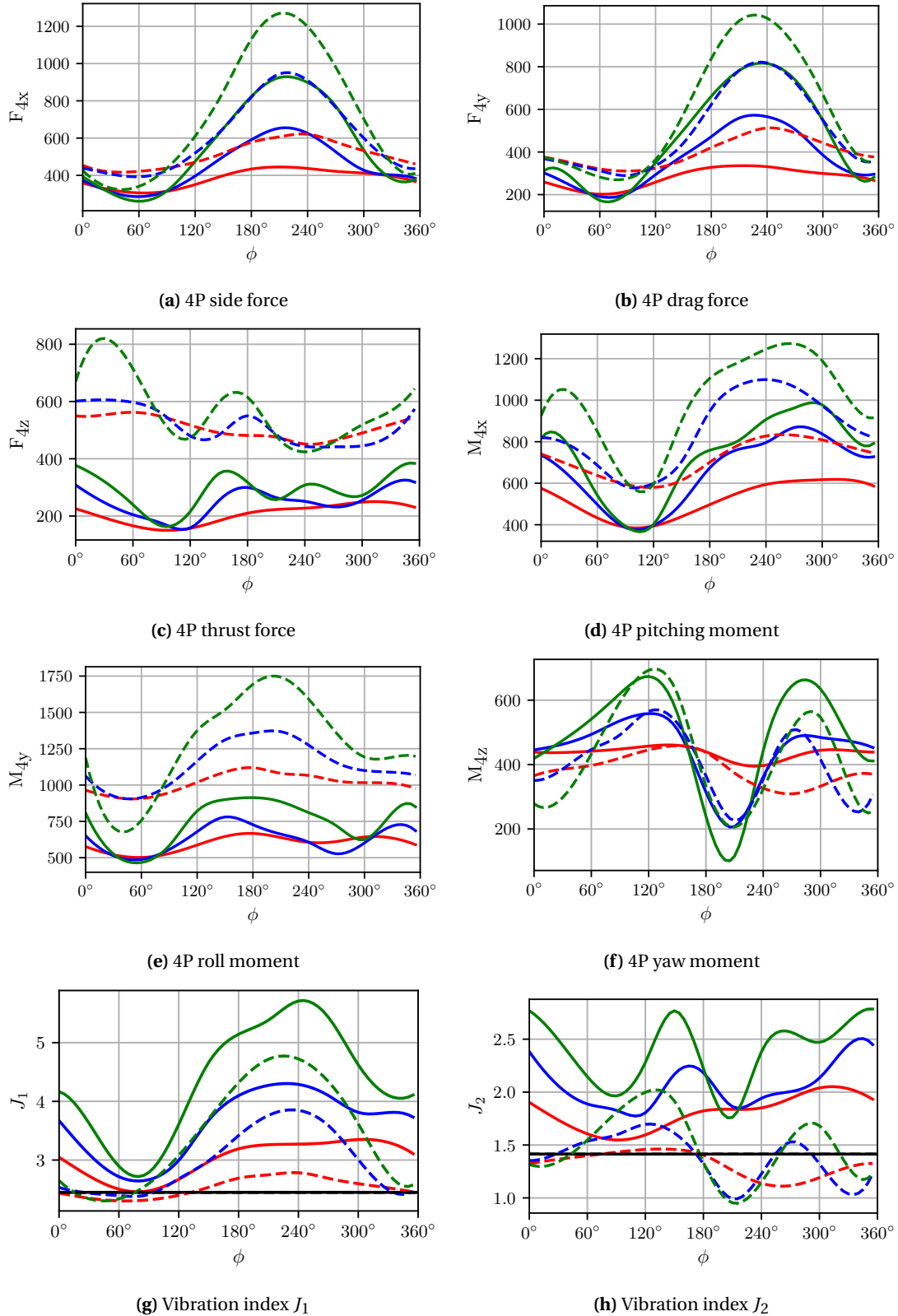
Based on the active rotor results discussed above, it is apparent that the two simulation frameworks used in the current study—standalone Dymore and Dymore+VPM—both predict qualitatively similar trends of mean as well as oscillatory aeromechanical results. Quantitatively, the two sets of results generally exhibit an offset between each other. In lieu of experimental measurement data of an active rotor with the FishBAC concept, the source of this disparity could not be completely resolved. From a physical modeling perspective, however, it is likely that the Dymore+VPM framework makes more accurate predictions since the VPM-based wake model captures more rotor wake physics than the Peters-He wake model. Code-to-code comparison of predicted results using a different simulation framework is another approach that could help put the relative accuracy of the two frameworks in perspective. However, this is beyond the scope of the current work.



**Figure 5.27.:** Comparison of rotor control angles, thrust, mean hub moments, and power obtained using Dymore (solid lines) and Dymore+VPM (dashed lines) simulations. The results are obtained at the trim condition of Run 26 point 11 ( $\mu = 0.3$ ) case for different amplitudes ( $\delta = 0.5^\circ, 1.0^\circ, 1.5^\circ$ ) and phase angles ( $\phi = [0^\circ, 360^\circ]$ ) of active camber actuation at 1P.



**Figure 5.28.:** Comparison of the change in aerodynamic quantities and blade section loads, obtained using standalone Dymore and Dymore+VPM simulation frameworks, for active rotor input of  $\delta = 1.5^\circ \sin(2\pi * t/T + 270^\circ)$  with respect to the baseline results of Run 26 point 11 in Fig. 5.16.



**Figure 5.29.:** Comparison of rotor 4P hub forces, moments and vibration indices, obtained using Dymore (solid lines) and Dymore+VPM (dashed lines) simulations. The results are obtained at the trim condition of Run 26 point 11 ( $\mu = 0.3$ ) case for different amplitudes ( $\delta_0 = 0.5^\circ, 1.0^\circ, 1.5^\circ$ ) and phase angles ( $\phi = [0^\circ, 360^\circ]$ ) of active camber actuation at 1P(see Fig. 5.27(a) for legend).

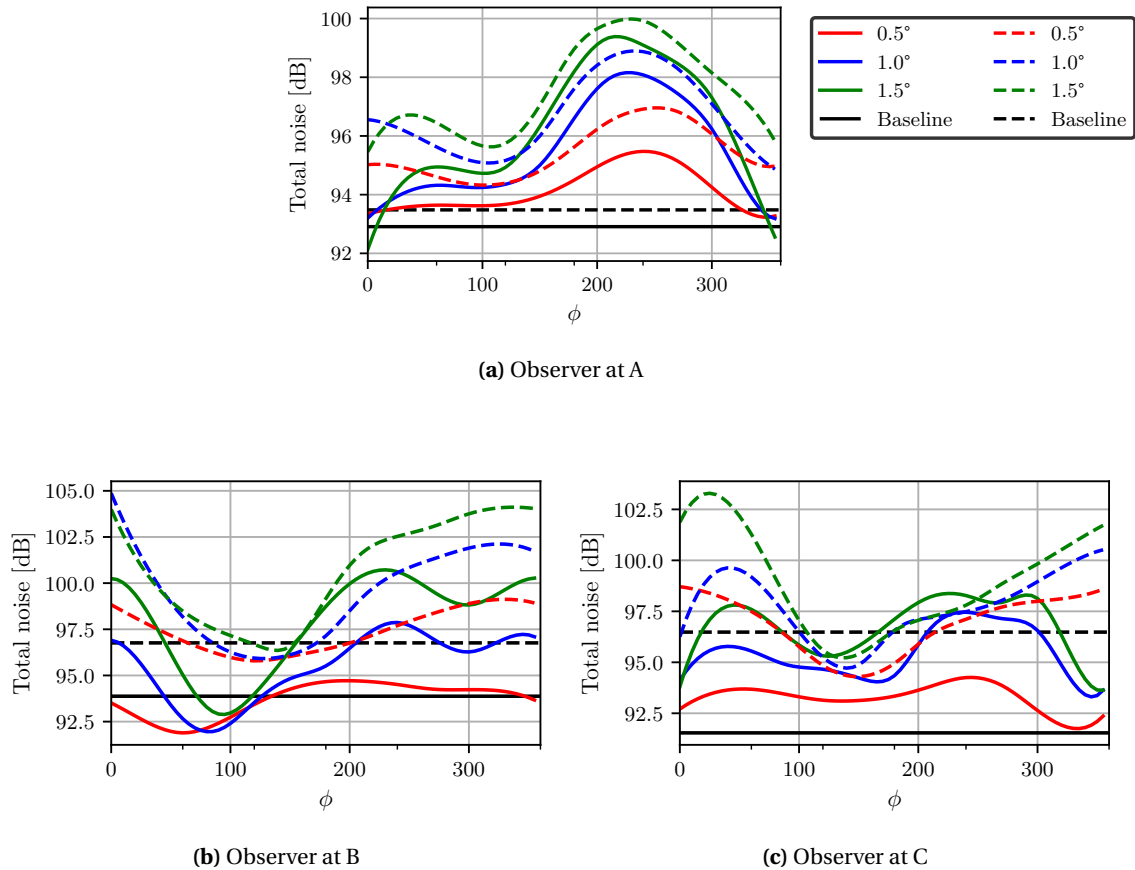


## 5.6.2. Impact on aeroacoustic noise

In order to obtain the effect of active camber actuation on the footprint of rotor noise, i.e., directivity and magnitude, the total rotor noise was calculated at several locations. These were placed on a hemispherical front that was centered at the rotor hub and moved with it. Relative acoustic effects occurred due to changes in sectional blade geometry and aerodynamic drag and lift due to morphing. The maximum change in rotor noise could be influenced to different degrees of success for different observers over the hemisphere. Three locations, viz. A, B, and C, were chosen such that they were roughly in-plane, out-of-plane and below the rotor disk, respectively. Further details about the observer locations can be referred to from Sec. 4.3.1.

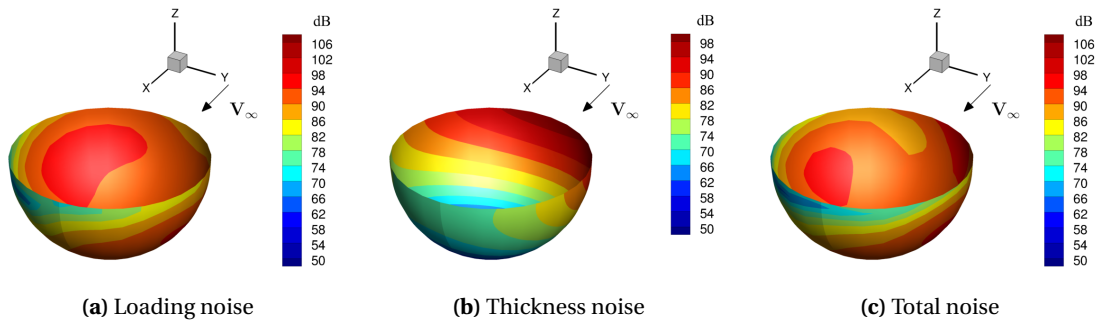
Figure 5.30 shows the total noise results obtained at the three observer locations A, B, and C. Results obtained using Dymore output to PSU-WOPWOP are shown in solid lines, and those obtained using Dymore+VPM output are shown in dashed lines. In addition to the active rotor noise results obtained for different camber actuation amplitudes  $\delta_0$  and phase angles  $\phi$ , the baseline rotor results are also shown (black lines). Since both simulation frameworks result in slightly different noise predictions, the corresponding baseline rotor noise prediction was used to assess whether noise emission increased or decreased at a given input. From Fig. 5.30(a), it can be seen that there was only a nominal decrease in in-plane rotor noise at A. The reduction in noise predicted using Dymore results, was about 1 dB. In contrast, Dymore+VPM results showed an increase in noise over the entire spectrum of morphing scheduling and amplitudes. At location B, both simulation frameworks showed that noise reduction of 1.5-2.5 dB was possible. However, the results from Dymore framework indicated that this reduction occurred at  $\phi = 90^\circ$  while Dymore+VPM showed that minimum noise occurred at  $\phi = 150^\circ$ . At location C, where the dominant component of aeroacoustic perturbations was loading noise, only the Dymore+VPM framework exhibited a maximum reduction in noise of 2 dB. Standalone Dymore-based simulation results led to no reduction in total rotor noise at C.

Figures 5.31 and 5.32 show the hemispherical contour plots of the different noise components obtained using Dymore and Dymore+VPM frameworks, respectively. Comparing the corresponding sub-figures, it can be seen that the two sets of results mainly differ in the loading noise prediction while the thickness noise distribution is largely the same. Since rotor in-plane noise at location A is predominantly composed of thickness noise, the predicted results using Dymore and Dymore+VPM at that location (see Fig. 5.30(a)) are very close to each other. For regions below the rotor disk plane, the loading noise component dominates. This is why the total noise distribution mimics the loading noise distribution over nearly the entire hemisphere. Figure 5.33 shows some example cases, with different camber morphing profiles, that exhibit significant variations in noise emissions. The objective here was to simply show the overall impact that the FishBAC mechanism can have on total noise emissions, even with small actuation amplitudes. Comparing the baseline rotor noise result of Fig. 5.32(c) with the active rotor results of Figs. 5.33(a)-5.33(c), it is apparent that active camber morphing can have a significant impact on total noise emissions, both qualitatively and quantitatively. Based on the specific locations where noise reduction is desired, different actuation profiles can be deemed useful in achieving that target. Similarly, Figs. 5.33(d)-5.33(f) show that similar behavior is also exhibited for the ground plane noise.

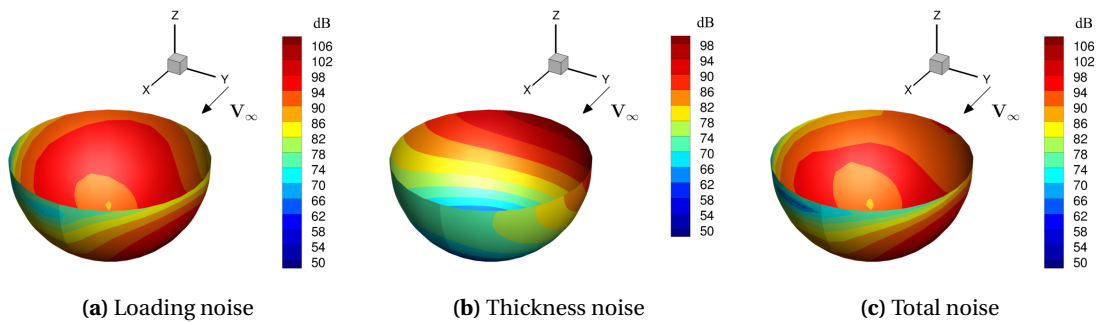


**Figure 5.30.:** Comparison of the total noise at observer locations A, B, and C (see Fig. 4.3(a)), obtained using Dymore (solid lines) and Dymore+VPM (dashed lines) simulations. The results are obtained at the trim condition of Run 26 point 11 case for different amplitudes ( $\delta_0 = \{0.5^\circ, 1.0^\circ, 1.5^\circ\}$ ) and phase angles ( $\phi = [0^\circ, 360^\circ]$ ) of active camber actuation at 1P.

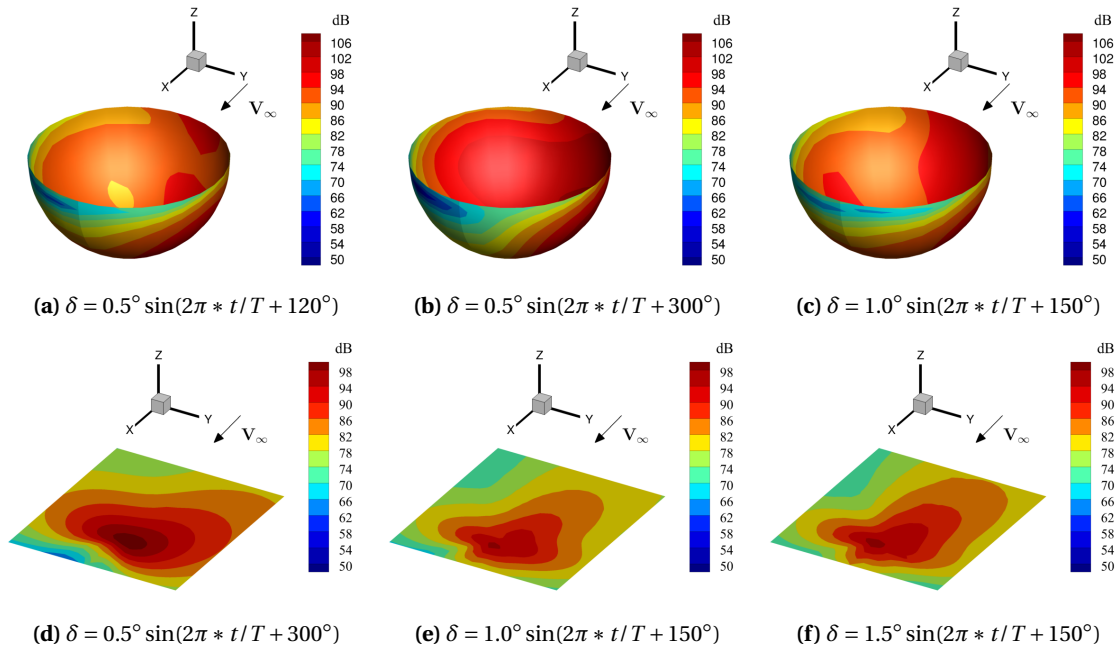
It is worth emphasizing that the presented results showcase the behavior of the FishBAC mechanism only within the scope of the different actuation profiles investigated. The results are not a reflection of the overall ability of the FishBAC concept to reduce rotor noise since no optimization study was undertaken to identify the actuation profile that led to minimum noise. It is likely that a more exhaustive investigation of the input actuation profiles could lead to discovery of different noise emission trends. Additionally, in order to truly quantify rotor noise reduction, a global metric could be more beneficial. Such a metric would need to take into account not just the change in the rotor noise at a given location but also add appropriate weighting to it to incorporate human sensitivity to the change in noise. Investigation of such a noise metric was beyond the scope of the current study but is deemed necessary for aeroacoustics investigations involving active rotors.



**Figure 5.31.:** Baseline rotor noise at Run 26 point 11 conditions obtained using standalone Dymore output.



**Figure 5.32.:** Baseline rotor noise at Run 26 point 11 conditions obtained Dymore+VPM output.



**Figure 5.33.:** Variation in rotor total acoustic noise footprint over a hemisphere and a plane below the rotor, at different actuation profiles of active camber mechanism, obtained using Dymore+VPM output.

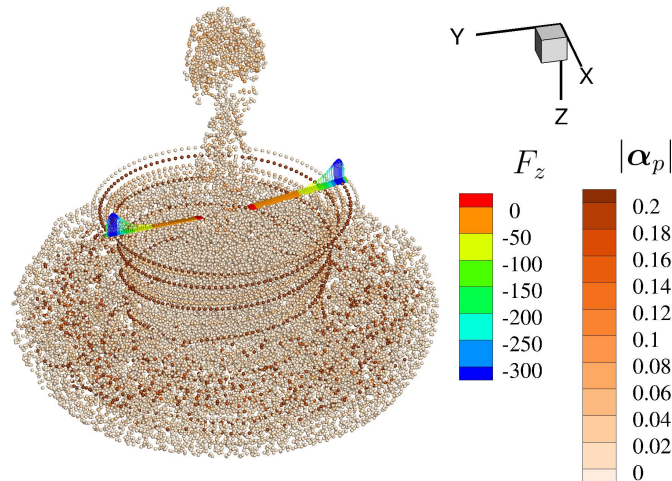
## 5.7. UT Austin Rotors

As detailed in Sec. 2.5.4, the rotor systems tested at UT Austin [207] were simulated in this study and the obtained results are presented in this section. The objective of this exercise was multifold—(a) validate the VPM framework for hovering rotors, (b) verify the framework for analysis of coaxial rotors, and (c) showcase the ability of the FishBAC mechanism to reduce vibratory loads due to blade passage effect in coaxial rotors. Single rotor designs, for which measurement data is available, were simulated using both Dymore and Dymore+VPM. The designs include a two-bladed rotor as well as a four-bladed rotor. The coaxial rotor system was simulated only using the VPM wake model since the Peters-He inflow model is incapable of modeling interacting rotor wake systems. The geometries of the different rotor systems in this study were already described in Sec. 2.5.4. The rotor blades were modeled sufficiently stiff so that they can be assumed to be rigid. Based on Eq. 2.6, a tip loss factor of 0.964 was used for the two- and four-bladed rotors. For the coaxial rotor system, a tip loss factor of 0.961 was used.

### 5.7.1. Fountain effect at blade root

In the Dymore+VPM coupled framework results, presented until now in this work, the VPM-based wake model was able to capture the dominant wake characteristics without any undue physical effects. The same strategy, however, posed some challenges for the hovering rotor cases. Note that the Run 15 point 5 case simulated using the Bo 105 rotor was not strictly a hover case since a forward velocity of 3.19 m/s was involved. Figure 5.34 shows the unphysical upflow of the rotor wake from the center of the rotor encountered for the isolated two-bladed UT Austin rotor case. The cause of this phenomenon is related to the practice adopted in the current work of completely bypassing any inflow modeling until particles were introduced once the VPM solver was engaged. Thereafter, the inflow velocity slowly built up to a periodic or steady value, based on the operating condition of the rotor, after the rotor had undergone sufficient number of revolutions. This meant that blade sections experience no inflow velocity until the VPM coupling had begun. Even after the coupling was started, there was no substantial induced inflow velocity during the first few revolutions of the rotor since the wake was not fully developed yet. As a consequence, the root vortex particles formed a ring that has the tendency to self-convect above the rotor disk plane.

A literature review on the subject led to the understanding that a majority of the studies either do not observe this computational phenomenon or shy away from presenting details about how this non-physical effect was handled. Limited studies where this phenomenon was indeed observed each suggested different ways in which they resolved the issue. Ref. [182] used simple free wake analyses to show that the effect of the root vortex on the blade loads could be neglected without incurring much error. The cause of this shortcoming of the simulation setup to represent reality, where no such upflow close to the blade root is observed, was postulated to result from a lack of hub or blade root fixtures. This reference further suggested that this led to a non-physical presence of a strong root vortex that was the cause of the obtained upflow. Ref. [241] suggested a gradual spanwise suppression factor to ensure that the vorticity at the root reduced to zero, thereby ensuring that the root vortex was artificially damped. Ref. [60] conducted simulations of a hovering rotor using free wake with parametric curves instead of linear filaments and suggested the strategy of gradually increasing rotor RPM to avoid the non-physical phenomenon of rotor upflow.



**Figure 5.34.:** VPM simulation of the two-bladed UT Austin isolated rotor, at 1200 RPM and  $6^\circ$  collective, exhibiting fountain effect when no special treatment is undertaken to solve for the rotor wake.

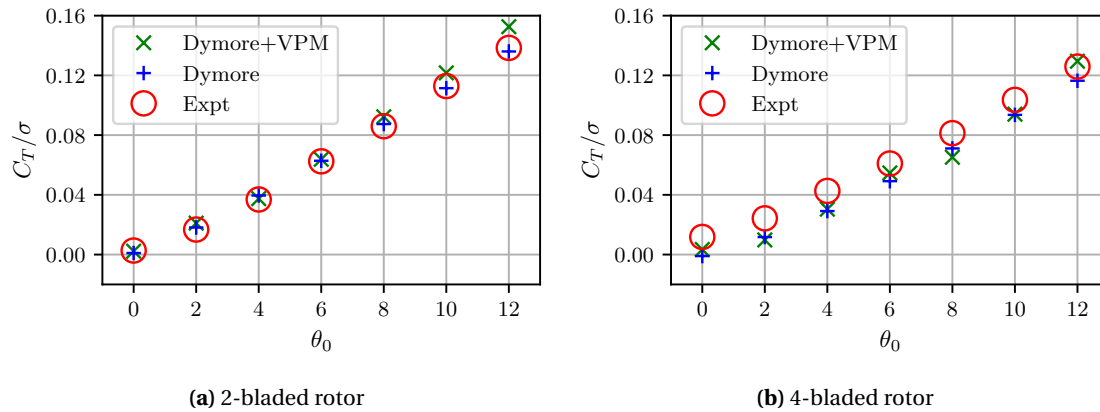
In the current study, a combination of the above-suggested strategies was found to work best. The rotor was initially run up from the rest position to reference RPM over 0.1 s and the VPM coupling was established from the beginning of the simulation itself. The trailing vorticity near the root of the blades was artificially suppressed and slowly increased to its full value over about five rotor revolutions. In addition, an artificial linearly decaying far wake flow field was assumed for these initial revolutions that washed the initial vortex particles away from the rotor. Thereafter, the rotor simulation proceeded normally for an additional ten rotor revolutions in order to obtain steady-state results.

### 5.7.2. Two-bladed/four-bladed isolated rotors

Figure 5.35 shows the thrust and power variation of two- and four-bladed rotors with the collective pitch angle. The experimental measurement data were taken from Ref. [113]. Error bars were also reported in Ref. [113] but are not shown here since they were small enough such that the conclusions of this study are not affected. It can be observed that both the Peters-He inflow model and the VPM-based wake model match the measurement data very well. The number of inflow states for the Peters-He inflow model was chosen to be six such that the predicted thrust output matches measurement data for a minimal number of states. The thrust output for the case of the four-bladed rotor was slightly under-predicted. It is worth mentioning that a better match with measurement data was also not possible in a validation study presented in Ref. [113].

Figures 5.36-5.38 further discuss the results of an example case from the validation study presented in Fig. 5.35. Figure 5.36 shows the spanwise variation of relevant rotor simulation quantities for an example case of two-bladed rotor with  $12^\circ$  collective. A comparison is made between the Peters-He inflow model-based results and those obtained using the VPM-based wake model. Figure 5.36(a) shows the variation of induced velocity over the blade span. It can be seen that the trend of the inflow velocity differs significantly between the two frameworks, particularly towards the blade tips. The characteristic trend of the Dymore+VPM result is due to the formation of a

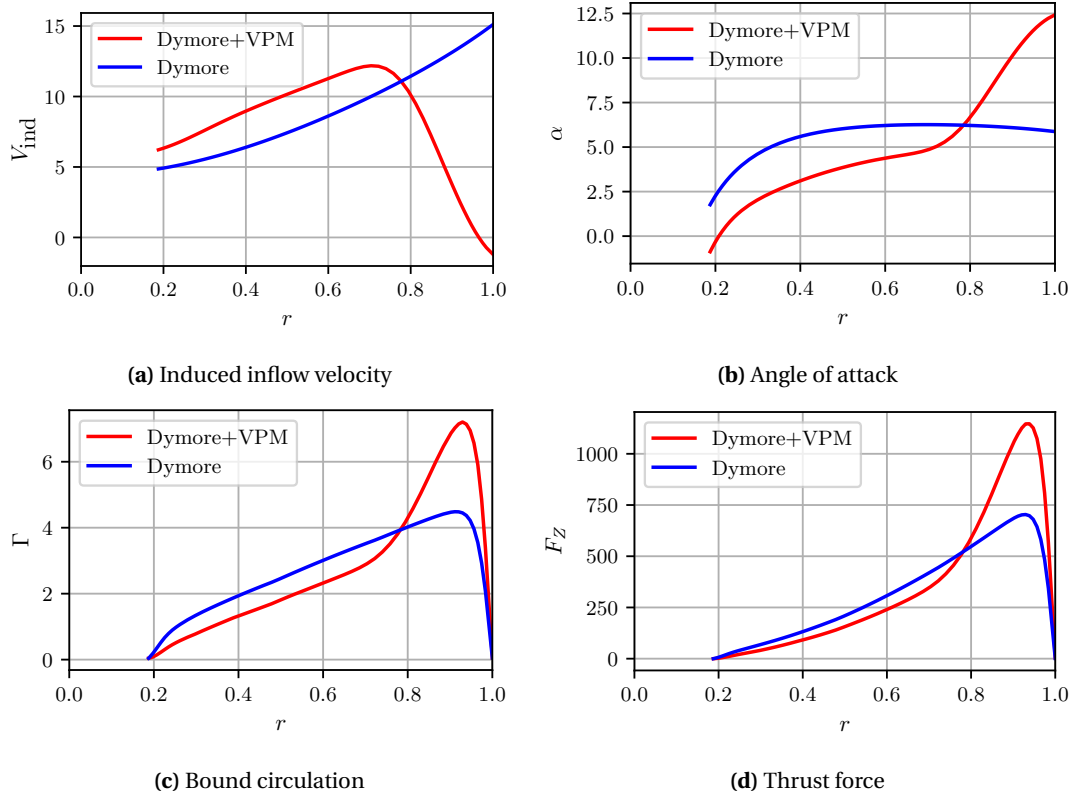
strong trailing vortex near the tip of the rotor blades (see Fig. 5.37). Consequently, the induced velocity is higher in the regions inboard of the tip vortex compared to the outboard region. Since the tip vortex is not formed perfectly at the blade tips but rather at a slightly inboard location, the resulting behavior of induced velocity is obtained. In contrast, the potential flow theory-based Peters-He inflow model is unable to capture this circulatory flow effect. The primary difference between the simulation frameworks, Dymore and Dymore+VPM, arises from the manner in which the induced inflow velocity is modeled. Therefore, the quantities shown in Figs. 5.36(b)-5.36(d) can be explained as a direct result of the distribution of the induced inflow velocity itself.



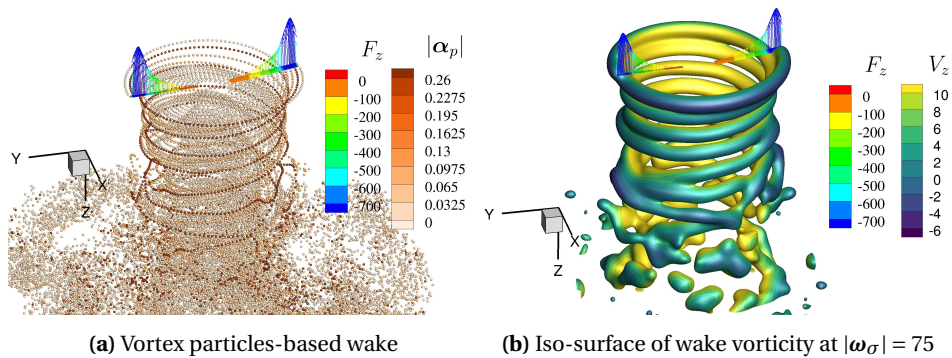
**Figure 5.35.:** Comparison of predicted rotor performance, obtained using the different simulation strategies used in the current work, against measurement data from Ref. [113] for prescribed collective inputs to the UT Austin two- and four-bladed single rotors.

Since the rotor collective was prescribed and the stiff rotors blades were modeled as stiff, any variation in the angle of attack was directly related to the induced inflow velocity (see Fig. 2.1). Figure 5.36(c) shows the variation in the bound circulation over the entire span. It is worth noting that a tip loss factor has been implemented in order to ensure that zero aerodynamic lift was generated at the blade tips. Since, bound circulation is directly proportional to the oncoming flow velocity, both models captured the near-linear increase in  $\Gamma$  in the inboard sections of the rotor blade. At the blade tip, however, the blade section lift coefficient varied sufficiently dramatically due to variation in  $\alpha$ , such that a sharp peak was obtained in the Dymore+VPM case. The variation in blade section thrust force in Fig. 5.36(d) can be directly explained by the variation in bound circulation. Since the overall rotor thrust produced using either simulation framework was the same (see Fig. 5.35(a)), the area under the  $F_Z$  curve is the same in each case. It is worth mentioning that the characteristic peak in  $\Gamma$  and  $F_Z$  towards the rotor tip, obtained using VPM, is qualitatively similar to the hover results of the NASA/Army/MIT active twist rotor (ATR) presented in Ref. [191].

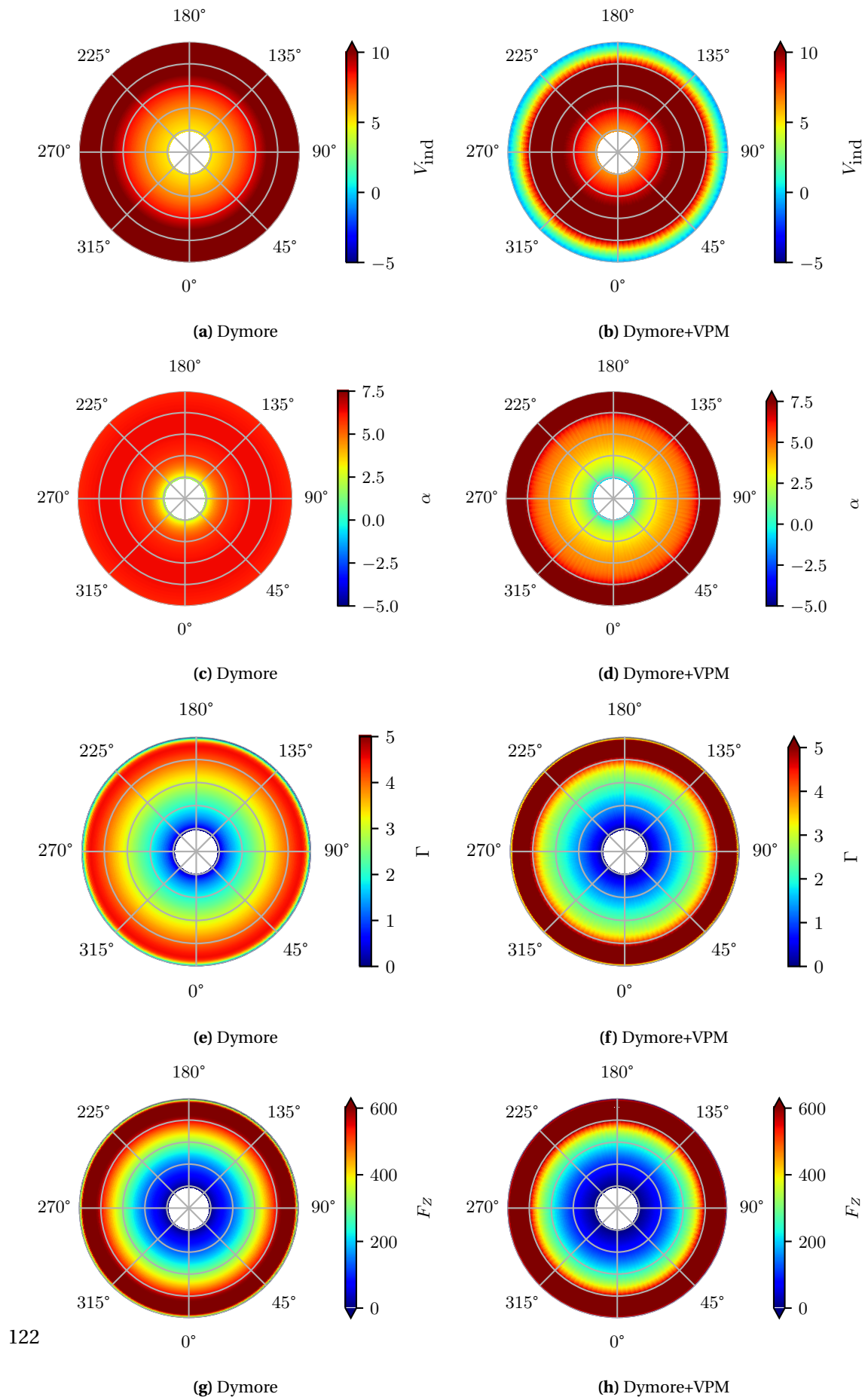
Figure 5.37 illustrates the particles-based wake and the corresponding vorticity modeled in the rotor wake. It is evident that most of the vorticity is captured near the blade tips which led to the behavior of  $V_{ind}$ ,  $\alpha$ ,  $\Gamma$  and  $F_Z$  observed in Fig. 5.36. For completeness, Fig. 5.38 shows the contour plots corresponding to the results of Fig. 5.36.



**Figure 5.36.:** Comparison of blade spanwise variation of rotor simulation quantities for the UT Austin two-bladed single rotor case at rotation rate of 1200 RPM and 12° collective.



**Figure 5.37.:** Visualization of the vortex wake of the UT Austin two-bladed single rotor case, at rotation rate at 1200 RPM and 12° collective, obtained using VPM wake modeling.



**Figure 5.38.:** Comparison of predicted rotor aerodynamic parameters and blade section loads using standalone Dymore and Dymore+VPM simulation frameworks for the UT Austin two-bladed single rotor case at 1200 RPM and 12° collective input.



### 5.7.3. Coaxial rotor

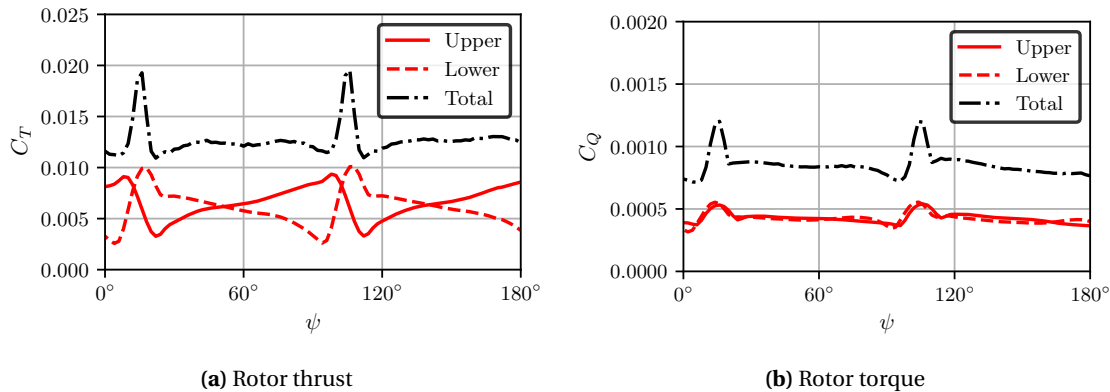
In comparison to isolated hovering rotors, two major effects take place on coaxial rotors due to the proximity of the component rotors to each other - (a) inter-rotor blade passage interactions when blades from one rotor pass close to the blades from the other rotor, (b) effect of induced velocity due to wake mixing. Essentially, the proximity of the upper and the lower rotors leads to aerodynamic interference between them. As the blades from the two rotors pass close to one another, an impulsive loading takes place due to the blade-blade interactions during crossover. This phenomenon has been well-documented in the literature; for example, see Ref. [113]. In the current study, these blade interaction effects were modeled using the computational framework laid down in Sec. 3.4.1. In addition to that, since the lower rotor operates in the wake of the upper rotor, the magnitude of the wake-induced velocity on either rotor is different from the isolated rotor case.

The objective of the current study was to simulate the UT Austin coaxial rotor system at a prescribed collective angle using the VPM-based wake model. Since the Peters-He inflow model is incapable of modeling coaxial rotor inflow, standalone Dymore results are not presented. The coaxial rotor geometry is provided in Table C.1, and the rotor setup was simulated at an RPM of 900 and a prescribed collective pitch angle of  $12^\circ$ . The resulting aerodynamics of the upper and lower rotors has been discussed in the following and the dominant effects are highlighted.

Figure 5.39 shows the rotor thrust and torque predictions for the upper and lower rotors separately, as well as the combined total results. The sudden variation in the individual rotor thrust is evident in Fig. 5.39(a) around the azimuth locations at which blade crossover occurs, i.e.  $\psi = 0^\circ, 90^\circ, 180^\circ$  and  $270^\circ$ . For clarity, results are presented only for half rotor revolution which is why only two crossover events are evident. Due to the staggered vertical placement of the rotors, the blades on the upper rotor and the lower rotor experience opposite effects. For example, the lift of the upper rotor blades decreases and increases on the blades of the lower rotor. This leads to significant net rotor thrust oscillations even in steady-state hover conditions. Figure 5.39(b) shows the effect of coaxial rotor interactions on the rotor torque. Here too, the blade passage effect has a similar pulsating influence on the shaft torque. In order to identify the underlying physics responsible for this rotor response, the polar contour plots of relevant simulation results are discussed next.

Figure 5.40 shows coaxial rotor system quantities over the upper and lower rotor disks. Figures 5.40(a) and (b) compare the angle of attack distribution over the rotor disks. It can be seen that the lower rotor disk experiences lower angles of attack due to the additional downflow from the wake of the upper rotor. The pulsating changes in angle of attack are also evident for both rotors, which ultimately are responsible for the corresponding effects on rotor thrust. Additionally, it can be observed that the blade tip sections on both rotors experience increased angles of attack. This was also obtained in the case of isolated rotors in hover and discussed in the context of Fig. 5.36(b) earlier. However, it can be seen that this effect is amplified in the case of the lower rotor. This is likely the result of the compounded effect of the trailing vortices from the lower rotor and the trailing vortices emanating from the upper rotor. This assertion is supported by the distribution of induced velocity in Figs. 5.40(c) and 5.40(d). The sudden changes in induced velocity due to blade crossover can be clearly seen. Also evident in the figures is that peak positive (i.e., downwards)

induced velocity occurs first on the lower rotor and then on the upper rotor. This explains the drop in rotor thrust first occurring on the lower rotor and then on the upper rotor, as shown in Fig. 5.39(a). Simple lifting-line theory-based models can help explain this phenomenon, which has been documented very well in Ref. [113]. Figures 5.40(e)-5.40(f) and Figs. 5.40(g)-5.40(h) show the variation of thrust and drag force, respectively, over the rotor disks. Again, the pulsating character of the drag force can be seen in Figs. 5.40(g)-5.40(h) which leads to the corresponding effect in net rotor torque as shown in Fig. 5.39(b).

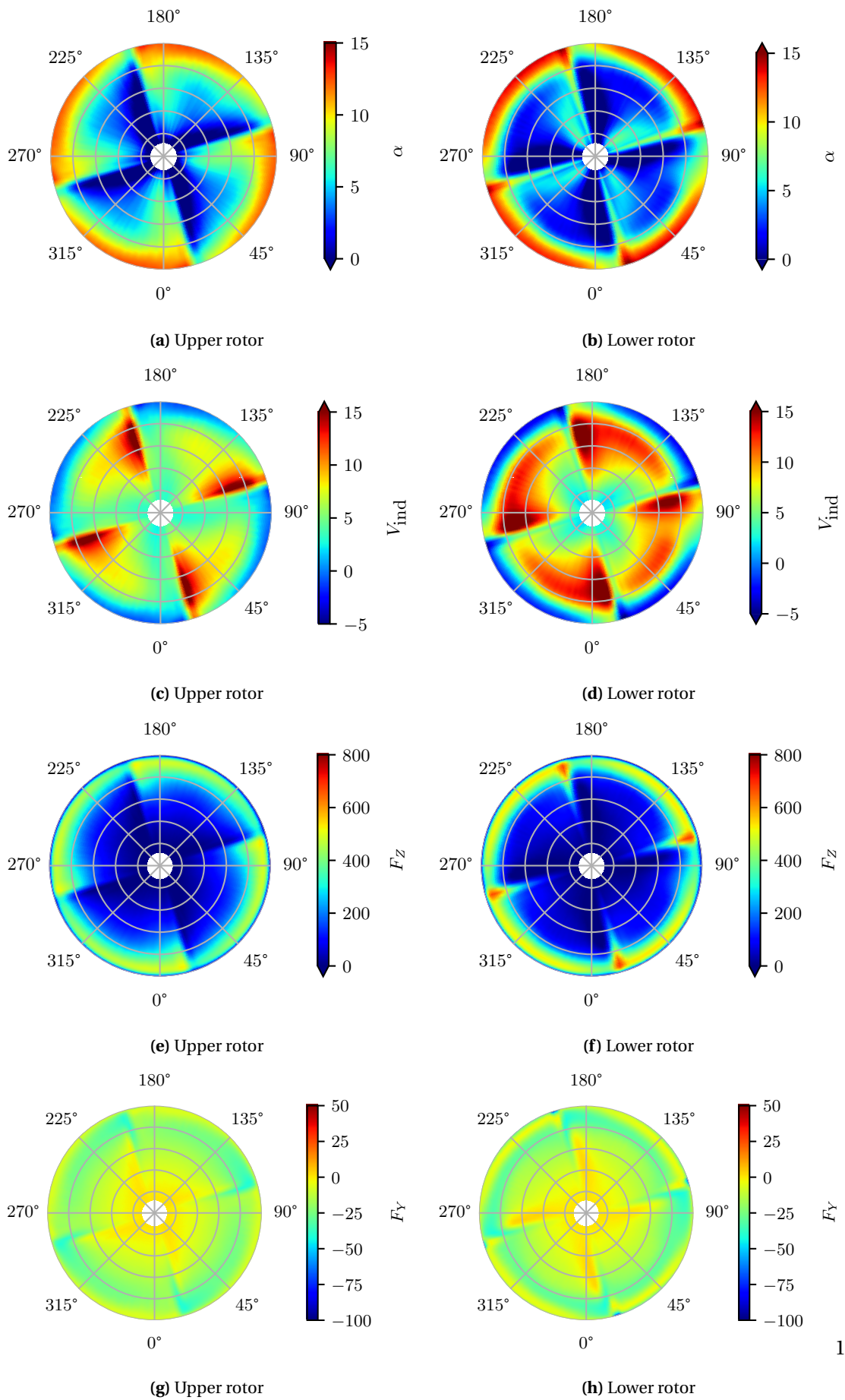


**Figure 5.39.:** Comparison of rotor thrust and torque variation for the baseline coaxial contra-rotating rotor.

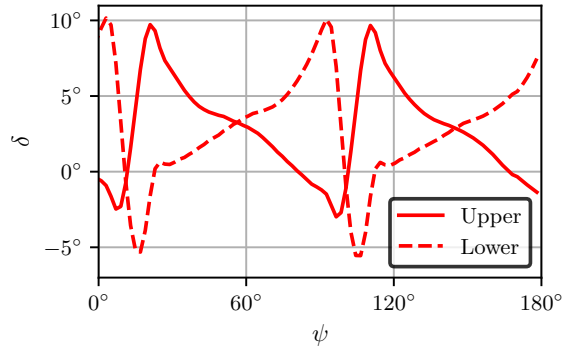
## 5.8. Active UT Austin Coaxial Rotor

The coaxial contra-rotating rotor results shown in Sec. 5.7.3 correctly predicted the presence of oscillatory rotor lift and drag forces that occur due to blade passage effects. They lead to significant vibratory loads on the rotor even in steady-state hover conditions. Single main rotor designs do not suffer from this condition, and this situation is unique to coaxial rotors. Due to the sudden and large variations in aerodynamic loading, it is likely that the coaxial rotor acoustic noise emissions also increase. Therefore, the current study investigated the potential of the FishBAC mechanism to ameliorate rotor vibrations as well as noise emissions. In this section, the coaxial UT Austin rotor was simulated using the FishBAC concept. Here, the active mechanism was placed from  $r = 0.50$ - $0.95$  section of the rotor blades on both upper and lower rotors. A periodic morphing profile was prescribed over the rotor azimuth in order to counter the aforementioned blade passage oscillatory load effects. The resulting rotor thrust and torque are presented, together with a distribution of a number of rotor simulation quantities. Additionally, the acoustic noise emissions of the baseline coaxial rotor are compared to the emissions from the active rotor system.

Figure 5.41 shows the active camber morphing profile used in the current study. Unlike the harmonic profile inputs used in active Bo 105 rotor study, the actuation in the current study was obtained based on the waveform exhibited by the thrust variation on the rotors (see Fig. 5.39(a)). This was inspired by the objective to minimize the oscillations experienced by the individual rotors, which would, in turn, reduce these effects on the combined rotor system. It is worth mentioning that a similar actuation profile can also be obtained based on the variation of rotor torque in Fig. 5.39(b) or some combination of the two profiles to simultaneously minimize oscillations in both quantities.



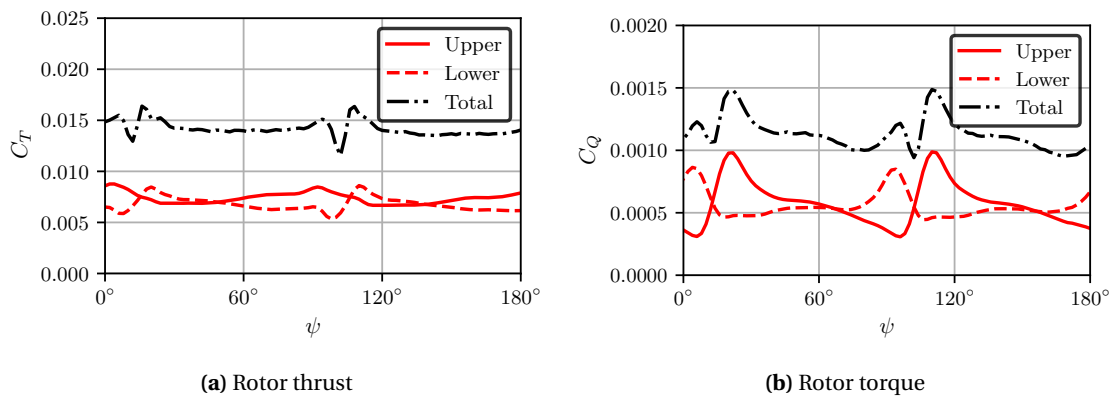
**Figure 5.40.:** Comparison of predicted rotor simulation quantities obtained using Dymore+VPM framework for the baseline coaxial contra-rotating rotor system.



**Figure 5.41.:** Actuation profile of the FishBAC concept on the upper and lower rotor blades of the coaxial contra-rotating rotor system.

### 5.8.1. Impact on blade passage loads

Figure 5.42 shows the cumulative rotor thrust and moment obtained using the active camber morphing actuation profile of Fig. 5.41. It can be seen from Fig. 5.42(a) that the oscillatory loads have been reduced on the upper rotor and, albeit to a lesser extent, on the lower rotor. The net effect was a reduction in the impact of blade passage effects on the rotor thrust loads. However, this led to an increase in the oscillatory yaw moments on each rotor, as shown in Fig. 5.42(b). This is not particularly surprising since the camber morphing actuation profile was based on the waveform of thrust variation. As suggested earlier, a different actuation profile is likely required to minimize torque oscillations but this was not investigated further in this work.



**Figure 5.42.:** Comparison of rotor thrust and torque variation for the active coaxial contra-rotating rotor.

Figure 5.43 shows the rotor simulation quantities for the active rotor. When the active rotor results in Fig. 5.43 are compared to the corresponding baseline rotor results in Fig. 5.40, the effect of camber morphing actuation is apparent. The intensity and the pulsating character of the blade passage effects is smeared out in Fig. 5.43, in the active rotor results of angle of attack, induced

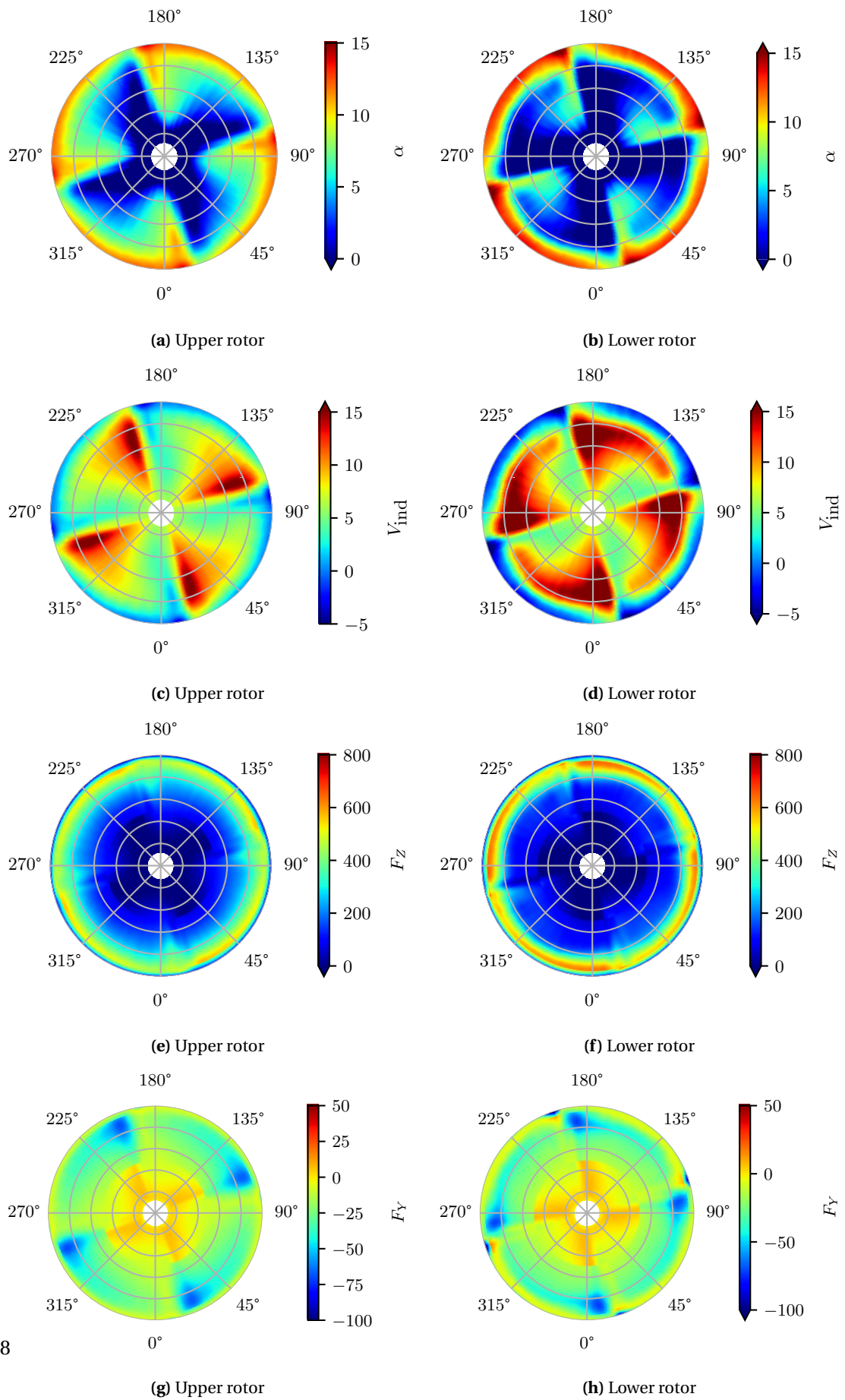
velocity and rotor thrust force. Much like the results of Fig. 5.42(a), this effect is more apparent in the upper rotor than in the lower rotor. This is because the upper rotor is less affected by the lower rotor's operation than the lower rotor is by the upper rotor. Since the lower rotor is in the wake of the upper rotor, the actuation profile based on the baseline coaxial rotor is not ideally suited to yield non-oscillating hover lift results. The impact on increased rotor torque is also evident from Figs. 5.43(g) and (h). Here, active camber morphing led to an increase in blade section drag, which manifested as increased rotor torque.

### 5.8.2. Impact on aeroacoustic noise

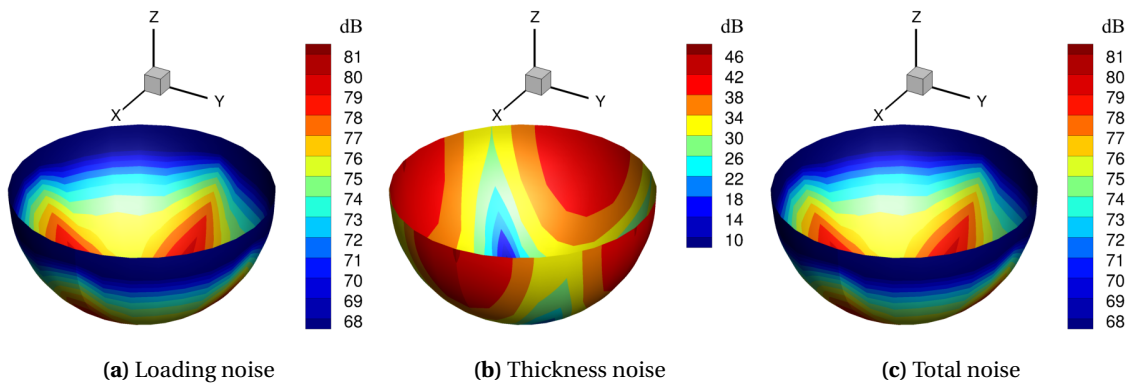
The impact of active camber morphing, using the actuation profile shown in Fig. 5.41, on rotor acoustic noise emissions was also investigated. This section describes the results of the coaxial rotor aeroacoustic noise obtained using the Dymore+VPM simulation framework and PSU-WOPWOP.

Figures 5.44 and 5.45 show the different components of the baseline and the active coaxial rotor noise emissions. Comparing Figs. 5.44 and 5.45, it is evident that the loading noise emissions of the active rotor are significantly reduced. In contrast, the thickness noise is higher in the case of the active rotor and the obtained pattern of noise distribution is largely a consequence of the morphing of the blade profile shape. This is because the rotors were held at a fixed collective angle, so the only contribution to change in rotor thickness noise could come from blade profile change due to FishBAC actuation. However, the magnitude of the thickness noise dwarfs in comparison to the loading noise. Therefore, the total noise footprint is only a reflection of the loading noise distribution. For a better comparison of rotor noise emissions, Fig. 5.46 shows the top view of the total noise results. It can be seen that a reduction of 6-10 dB is obtained over a large portion of the hemisphere below the rotor disk.

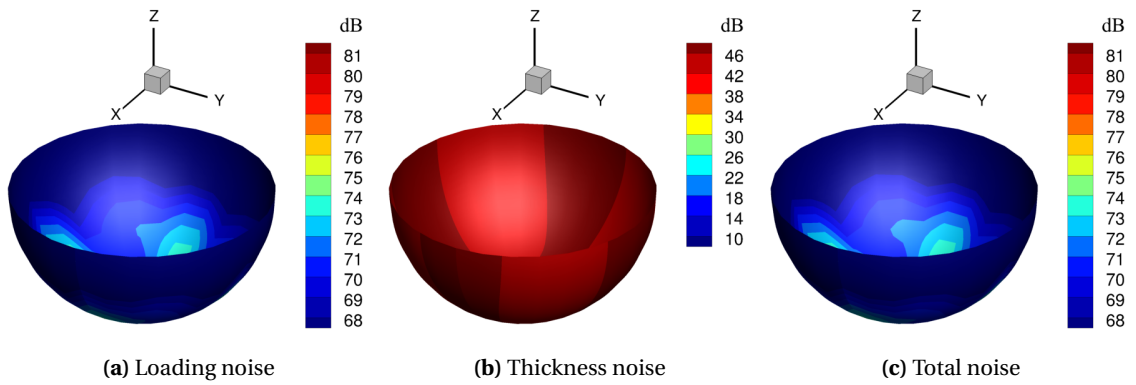
Figures 5.47 and 5.48 further show the different noise components obtained for observers distributed over the ground plane (see Fig. 4.3(b)). Qualitatively, the same conclusions can be drawn between the two sets of figures, as those made using Figs. 5.44 and 5.45. There is a significant reduction in the loading noise component, which forms the dominant component of overall noise. Even though a large increase in thickness noise was obtained below the rotor disk region, this does not affect the total noise result, which exhibits a decrease in total rotor noise by up to 10 dB below the rotor. The greater degree of influence of the FishBAC mechanism on rotor noise emissions from the coaxial rotor system can be attributed to the adopted custom actuation profile of Fig. 5.41. Instead of a harmonic actuation, this actuation profile was directly able to redress the underlying issue of oscillatory airloads. To that end, the current study differed from that of the active Bo 105 in two major ways - (a) the active FishBAC actuation occurred at the blade passage frequency of 4P instead of 1P, and (b) the actuation amplitude was also higher. It serves to indicate that a wider study of the Bo 105 rotor at higher actuation amplitudes and frequencies would likely result in greater performance benefits than those that were obtained in this work. This could be a fertile ground for detailed future investigations.



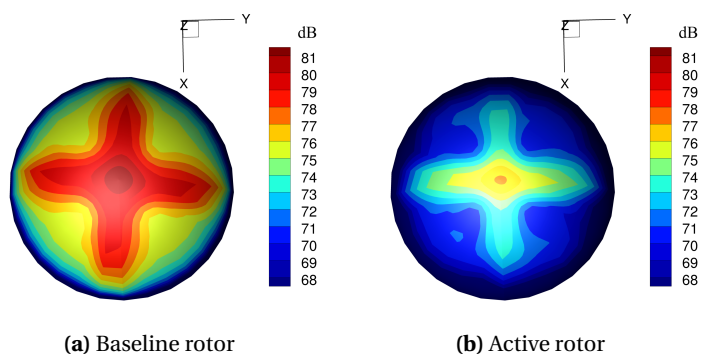
**Figure 5.43.:** Comparison of predicted rotor simulation quantities obtained using Dymore+VPM framework for the active coaxial contra-rotating rotor system.



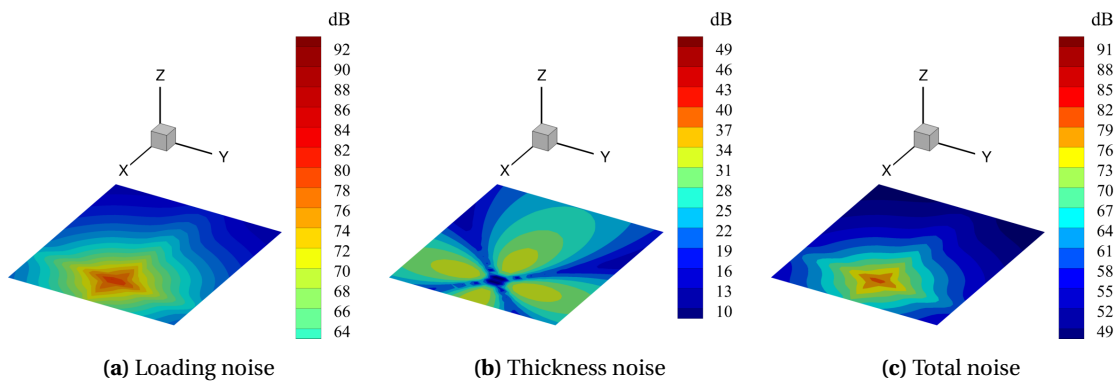
**Figure 5.44.:** Baseline coaxial rotor noise hemispheres obtained using PSU-WOPWOP and Dymore+VPM.



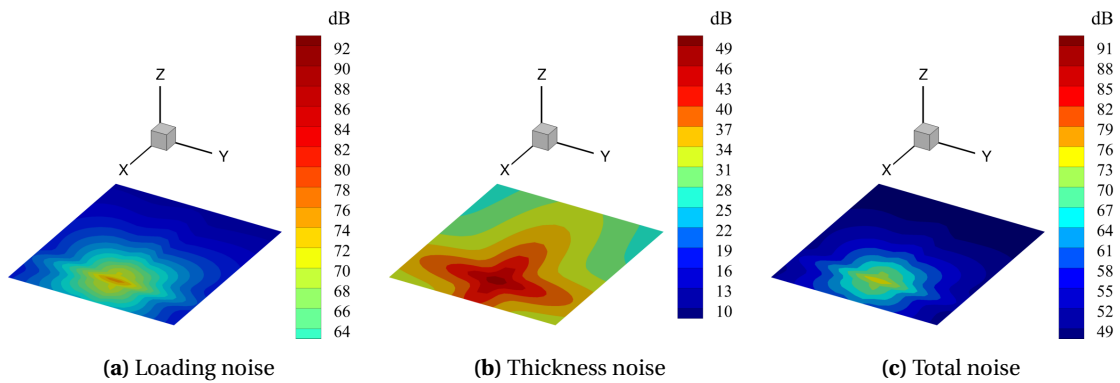
**Figure 5.45.:** Active coaxial rotor noise hemispheres obtained using PSU-WOPWOP and Dymore+VPM.



**Figure 5.46.:** Comparison of the baseline and active coaxial contra-rotating rotor total noise results from a top view of the hemisphere.



**Figure 5.47.:** Baseline coaxial contra-rotating rotor noise results over the ground plane obtained using PSU-WOPWOP and Dymore+VPM output results.



**Figure 5.48.:** Active coaxial contra-rotating rotor noise results over the ground plane obtained using PSU-WOPWOP and Dymore+VPM output results.



## 6. Summary and Conclusions

### 6.1. Summary

The overarching purpose of the current work was to establish a reliable analysis framework that was capable of accurately predicting the aeromechanical response of passive as well as active rotors. Of particular focus was the overall rotor power consumption, high-frequency vibratory loads at the rotor hub, and the aeroacoustic noise emitted as a result. In pursuit of these objectives, an extensive simulation and analysis framework was created. Baseline and active rotor simulations were conducted using the comprehensive analysis framework Dymore, which afforded detailed multibody modeling of the control system and flexible blade analysis. The blade aerodynamics were solved using the approach of first-order lifting-line theory. The rotor wake effects on the blade were solved using a potential flow theory-based dynamic inflow model for computational efficiency.

In order to accurately predict rotor airloads and blade loads, it is required that the dynamics of the flexible rotor blades, as well as the three-dimensional aerodynamic effects, be modeled with a reasonable degree of fidelity. Resorting to lower fidelity analysis methods, in lieu of fast solvers, has been the mainstay of rotorcraft modeling strategies. Within the Dymore analysis framework, for example, the Peters-He finite-state dynamic inflow model is used for quick simulations. This inflow model, however, does not directly model vorticity in the rotor wake and cannot model effects such as BVI, wake contraction, etc. Therefore, a novel vortex particle method (VPM) was implemented to improve the overall fidelity of the wake solution. It also relied on GPU-based hardware acceleration to reduce computation time. A robust coupling framework was established between the rotor dynamics solver Dymore and the VPM solver. The coupled framework with improved fidelity in rotor wake modeling was envisaged to result in better accuracy of rotor aeromechanics simulations compared to the standalone Dymore setup. This coupled framework operated by solving for the blade aerodynamics using an airfoil tables-based approach within Dymore, and the resulting blade-bound circulation was used as an input to the VPM solver. The generation and development of the wake was then dictated by fundamental fluid mechanics theories—for example, Kelvin's theorem and Prandtl's theory of circulation—and vortex particle evolution.

An aeroacoustics analysis framework was created to use comprehensive analysis output for post-processing in order to predict rotor noise emissions. The formulation FIA-based acoustics solver PSU-WOPWOP was used for this purpose and a robust interface was established between the aeromechanics solvers and the acoustics solver using a framework created for this purpose, called *HeliNoise*.

A number of test cases were devised to meticulously validate the different aspects of the simulation frameworks. Results were obtained using both the Peters-He model as well as the VPM inflow model and compared against measurement data or analytical results. A notable exception here was the coaxial contra-rotating rotor results, for which no simulation results are available for the Peters-He inflow model since it is incapable of modeling interactional rotor aerodynamics. Simple rigid finite span wings and two-dimensional airfoil cases were examined using the Dymore+VPM framework and compared against predictions using analytical aerodynamic theories. In this manner, the predictive capability of the VPM framework was validated by factoring out added complexity due to elastic structural deformation. The cases investigated include static elliptical wings, pitching and morphing airfoil sections, and a pitching finite wing. Next, different isolated rotors were simulated in hover, forward, and descent flight operating conditions. Based on the accessibility to publicly available measurement data, the obtained aeromechanical and aeroacoustic noise results were compared with test data to further validate the overall simulation framework. The following summarizes the different studies that formed part of the validation effort-

1. 2D pitching/morphing airfoil

The objective of this study was to use different unsteady airfoil motion profiles and verify whether the VPM solver was able to quantitatively match results based on analytical theory. A comparison was made between the predicted unsteady airfoil lift  $C_l$  and moment  $C_m$  using Peters 2D inflow theory and the VPM-based wake model. In addition, the Theodorsen theory results were also used for qualitative comparison. Minor differences in the results were encountered, which could be attributed to the manner in which the airfoil wake is idealized in the analytical theories. Overall, the VPM-based wake model was able to capture the unsteady  $C_l$  and  $C_m$  for all the cases investigated, both qualitatively and quantitatively.

2. Elliptical wing

An elliptical wing was one of two finite wing cases that were studied to further validate the performance of the VPM solver. Here, the objective was to match the theoretical result of uniform wake-induced inflow velocity over the entire wing span. For this purpose, a finite span wing with an elliptical planform was simulated at a steady angle of attack in oncoming flow conditions. The wing wake, modeled using VPM, resulted in a near-uniform induced inflow velocity over the wing span and matched well with the theoretical prediction. This test case helped verify the implementation of trailing vorticity in VPM and validate certain aspects of the Dymore+VPM framework.

3. Pitching finite wing

The second finite wing case simulated was a rectangular wing of aspect ratio  $AR = 5$  and oscillating harmonically in steady oncoming flow. This test case was based on experimental measurement data and computational simulation results available in the literature. The predicted cyclic wing lift  $C_L$  was compared to results reported in the literature in order to validate the VPM solver, simulating both shed and trailing vortices in the wake. The predictions matched well with measurement data when a tip loss factor was assumed. Since lifting-line model-based wing aerodynamics analyses are incapable of accounting for tip loss effects, this was accomplished by using this empirical parameter. All the studies involving finite wings, which also includes rotor blades, in this work incorporated lift loss effects at the tips using a tip loss factor.

#### 4. Full-scale Bo 105

In an effort to test the impact of the active FishBAC mechanism on a helicopter rotor, the full-scale Bo 105 rotor was chosen as the baseline. First, this rotor was extensively validated using measurement test data available in literature. The study was based on a full-scale Bo 105 rotor in level flight conditions over a range of advance ratios  $\mu = 0.01 - 0.45$ . In order to validate the rotor model, the following quantities were used—rotating blade natural frequencies in a vacuum, trim control angles, hub forces and moments, and mean and half-peak-to-peak blade loads. A fair correlation was obtained between the simulation results using the two different frameworks that have been used in the current work—Dymore and Dymore+VPM.

The aeromechanical rotor output data was also post-processed to predict rotor noise emissions using FW-H equation-based solver PSU-WOPWOP. A low-speed ( $\mu = 0.1$ ) case with BVI was chosen for this purpose. It was found that the Dymore output-based rotor noise predictions were significantly lower compared to measurement data. The reason behind this was the inability of the Peters-He inflow model to capture oscillatory airloads caused due to BVI. The Dymore+VPM simulation output-based noise results matched better, but there was still a discrepancy of 3-5 dB at some microphone locations. Due to the limited availability of experimental data on rotor noise, it was challenging to precisely ascertain whether the shortcomings were a result of the modeling framework itself or other factors. For this purpose, another rotor test setup (HART II) was investigated.

#### 5. HART II

Using the HART II rotor setup, the ability of the current analysis framework to accurately model blade aerodynamic forces and acoustic pressure was established. The baseline HART II rotor with elastic blades was simulated in BVI conditions. Unlike the Bo 105 rotor study, the control inputs to the HART II rotor were prescribed. The difference between the results obtained using different fidelity of rotor inflow models was highlighted by comparing simulation results of blade section aerodynamic normal force with measurement data. A good correlation with the predicted blade airloads was crucial in order to predict the rotor noise correctly. The Dymore+VPM framework was able to capture the BVI events occurring on the retreating side of the rotor disk and over-predicted the wake effects on the advancing side. In contrast, standalone Dymore could only capture the mean form of the variation of loads. This is because the potential flow theory-based Peters-He inflow model cannot model the effects of circulatory flow due to encounters with tip vortices. Consequently, the oscillatory airloads at the reference blade section were not captured at all by the latter framework.

Noise prediction over a grid of observers showed that the Dymore+VPM results matched well with measurement data, while those using Dymore results significantly under-predicted the noise. This study rendered further confidence in the ability of the Dymore+VPM analysis framework to better model a generic helicopter rotor with flexible blades in BVI flight conditions.

#### 6. UT Austin two-bladed/four-bladed rotors

Isolated, two-bladed, and four-bladed rigid rotor models were simulated in hover using prescribed control input over a range of collective angles. The purpose of this study was to

validate the VPM framework for the case of hovering rotors. This objective was successfully achieved with a good match between the predicted thrust output and measurement data reported in the literature. For reference, simulations were also conducted using standalone Dymore. Here, too, the results exhibited a fair match with measurement data.

Once sufficient confidence was established in the complete aeromechanics-aeroacoustics toolchain, active rotor investigations were undertaken using an isolated full-scale Bo 105 rotor and the UT Austin coaxial rotor system. The following summarizes the key aspects of those studies-

1. Full-scale Bo 105 with active FishBAC

The validated Bo 105 rotor aeromechanics-aeroacoustics framework was used to study the potential of high-frequency camber morphing via the FishBAC mechanism to influence rotor power consumption, vibratory hub loads, and aeroacoustic noise emissions. For this purpose, the validated Bo 105 full-scale rotor model was used, and simulations were conducted using harmonic actuation of the FishBAC mechanism over a range of input amplitudes and phase angles. In the absence of measurement data for the active rotor study, the results predicted by the two simulation frameworks used in this study—Dymore and Dymore+VPM—were compared against each other. Dymore+VPM results showed a maximum power reduction of 9.1%, while standalone Dymore results showed a 9.6% reduction in rotor power consumption. This was achieved for a camber morphing profile with an amplitude of  $1.5^\circ$  and input phase such that maximum camber deflection occurred on the fore and aft sections of the rotor disk. Within the domain of camber morphing profiles investigated in this study, limited success was encountered towards vibration reduction compared to active results presented in the literature. Standalone Dymore simulations showed no reduction in hub vibrations using any of the metrics defined in the current work. A maximum of 32% reduction in rotor-induced vibrations was obtained using the Dymore+VPM framework due to oscillatory loads and moments only along the rotor shaft axis.

2. UT Austin coaxial contra-rotating rotor

Coaxial rotors suffer from rotor-rotor interference effects that occur due to the passage of blades from one rotor close to the blades of the other rotor. These effects occur at the blade passage frequency and manifest as oscillations in the rotor thrust and torque even in steady-state hover operating conditions. In this study, a coaxial rotor system in hover was investigated with the active FishBAC concept. The objective was to identify the potential of the active mechanism to reduce the aforementioned oscillations in thrust and torque, as well as the noise footprint of the entire rotor system. For this study, a FishBAC actuation profile was chosen based on the fluctuating thrust loads on the passive coaxial rotor. Based on this profile, thrust fluctuations were significantly reduced on the upper rotor as well as the lower rotor. However, the fluctuations in rotor torque got amplified due to the pulsating effect of camber morphing on rotor drag. The effect of the revised airloads distribution was a net reduction in the overall footprint of the loading noise and, by extension, the total noise of the rotor. The rotor thickness noise was increased for the active rotor case but formed a much smaller proportion of the total rotor noise. Consequently, it did not have much influence on the overall rotor noise reduction.

## 6.2. Key Conclusions

In this work, active rotor investigations were conducted using two different rotor setups and operating conditions. For the Bo 105 and the coaxial active rotor studies, a cruise speed forward flight condition and hover condition were chosen, respectively. The computational studies used a validated simulation framework as a basis to predict the influence of active camber morphing on rotor aeromechanics. No postdictive corrections were made to airfoil tables, blade section properties, or semi-empirical parameters within the simulation models. As part of the validation studies undertaken in this work, the overarching nature of correlation with experimental results was fair. This helped verify the analysis framework established in this work as well as reaffirm the validity of the physics-based models used therein.

The objective of this study was not to find the optimum camber actuation profiles that led to the most efficient rotor design. Instead, since this was the first study of its kind involving active rotors with FishBAC installed, the focus was on identifying the degree of influence that camber morphing can have on the overall rotor power requirement, rotor vibratory hub loads, and the aeroacoustic noise emissions. To that end, the results obtained within this work are not representative of the maximum benefits obtained towards desired rotor aeromechanical response or acoustics emissions that can be achieved using the FishBAC concept on rotors. Clearly, the entire investigation could be expanded to include a wider range of possible actuation profiles, including higher harmonic actuation frequencies. Alternately, an optimization study could be used to arrive at global optimum benefits afforded by FishBAC actuation. These aspects, along with other recommendations in the following Chap. 7, serve as suggestions for ways in which future active rotor investigations could build upon the current work.

The section of this work focusing on active rotor analysis contributes to the existing literature on active rotors by demonstrating the influence of the FishBAC concept on isolated and coaxial rotors. The effect on different aspects of rotor operation—required power, vibratory hub loads, and noise emissions—were investigated. A detailed analysis corresponding to each of the studies was provided in the respective sections in Chap. 5. The following provides a brief summary of those discussions-

1. The potential flow theory-based Peters-He inflow model is capable of capturing the average aerodynamic effects of rotor wake. This helps accurately predict mean rotor load trends and power consumption, even in BVI conditions. Since the unsteady aerodynamic load fluctuations are not captured by this methodology, the corresponding aeroacoustic noise is severely under-predicted. This was shown using the two rotor models investigated in the current work under BVI conditions—Bo 105 and HART II. In both cases, the noise prediction did not match measurement data either qualitatively or quantitatively. The Peters-He inflow model and dynamic inflow models, in general, can be desirable when the objective is to correctly predict only the time-averaged rotor response. The computational expense of this model is another attractive aspect since it was found to be two orders of magnitude lower than even the GPU-accelerated VPM solver.
2. Using a particle representation of the rotor wake vorticity, a novel rotor wake solution method-

ology called the vortex particle method (VPM) was implemented in order to accurately capture the unsteady rotor aerodynamic effects. The VPM solver was shown to be well capable of modeling the complex interactions between finite wings and wakes. A number of test cases with incrementally complex wake scenarios were used to systematically demonstrate this capability. Overall, the solver was able to model the time-varying effects of steady/unsteady 2D and 3D wing wakes, as well as blade wake interaction for isolated and coaxial rotors.

3. Using the HART II rotor case, it was shown that the VPM-based wake model could capture the BVI effects, leading to a more accurate prediction of blade airloads. However, the Dymore+VPM framework was still unable to predict the unsteady fluctuations in blade section  $C_m$  due to interaction with wake vortices. This is a shortcoming of the lifting-line methodology used to model the blade aerodynamics in the current work. An aerodynamic model that does not collapse the influence of the blade chordwise geometry into a single collocation point is required to capture the effect on blade section  $C_m$  accurately.
4. While the VPM-based wake solver is computationally more expensive than the Peters-He wake solver, it was used in the current work since it is capable of capturing greater physics in the rotor wake. Some of the incurred computational expense could be offset by hardware-based solver acceleration on GPUs. This was critical in order to accomplish parameter sweep studies of active rotors in a reasonable time. However, the computational costs involved were still inhibitive to further expanding the scope of the investigation. Implementation of algorithmic speed-up techniques is considered vital to the future use of coupled VPM simulations for routine comprehensive analysis investigations.
5. A FW-H equation-based solver was used in this work in order to predict active and passive rotor aeroacoustic emissions. It was shown that this solver was capable of predicting the rotor noise output correctly as long as the comprehensive analysis framework itself was able to model the rotor physics correctly. This was especially true in the case of rotor operation under BVI scenarios.
6. Within the domain of the parametric study conducted in this work, the FishBAC concept was found to have a significant impact on rotor aeromechanical behavior. The influence of harmonic active camber actuation on rotor airloads led to a redistribution such that overall rotor in-plane drag was reduced. This translated to a reduction in rotor torque and, in turn, rotor power. Based on the different vibration metrics used in the current work, a significant reduction in 4P vibratory hub loads was obtained in the case of the four-bladed Bo 105 rotor.
7. In the absence of measurement data, results obtained for the Bo 105 active rotor using the two simulation frameworks used in this work—Dymore and Dymore+VPM—were compared to each other. Qualitatively, both frameworks predicted similar trends of mean and oscillatory aeromechanical results. Quantitatively, the results generally exhibited an offset between each other. The source of this disparity between the results could not be fully resolved within the scope of this work, and further investigations are required to identify the underlying issues.
8. The VPM-based wake solver implemented in the current work can be utilized to simulate

multirotor systems without modifying the underlying physical formulation. This was demonstrated using a coaxial rotor investigation where the Dymore+VPM framework was able to capture the pulsating effect of blade-blade interactions on rotor thrust and yaw. Unlike an ideal isolated rotor in hover, these blade passage effects led to severe hub vibrations and noise emissions of a coaxial rotor.

9. The FishBAC concept was demonstrated to be capable of significantly reducing the coaxial rotor interaction effects occurring at the blade passage frequency. For this purpose, an actuation profile was chosen targeted towards reducing vibratory thrust  $T$ . This profile was successful in reducing 4P hub vibratory thrust, but 4P hub vibratory yaw was exacerbated. This was because FishBAC actuation helped reduce large excursions in the rotor thrust, but the required camber morphing increased blade profile drag. Consequently, the rotor yaw moments exhibited larger spikes in the active rotor case.
10. Finally, given the different steady and unsteady wing cases investigated in the current work, as well as the different rotor systems simulated at various operating conditions, sufficient confidence was established in the modeling strategies used herein. The entire rotor aeromechanics and aeroacoustic framework used and developed in this work for the purpose of active rotor analyses is generic enough that it can be deployed towards future investigations of other passive or active rotor designs.





## 7. Outlook

The current work was a first attempt at organizing a verified and validated simulation framework that is capable of aeromechanics and aeroacoustics analysis of an active rotor using the FishBAC camber morphing mechanism. There are a number of ways the investigative frame of the current work can be expanded for follow-up work. The following summarizes some of the vital aspects of the investigation that could not be incorporated within the current work but are considered vital to any future work on this subject.

1. In the current study, the elasticity of the FishBAC concept was not modeled. This was justified in Sec. 2.5 using the fact that the qualitative nature of the influence of the camber morphing section on the rotor performance and dynamic loads is expected to remain the same. However, in order to improve quantitative predictions, a dynamic model of the camber morphing mechanism would be useful. Such a model would slow down the overall computational speed of the active rotor simulations, so it is prudent to use this approach perhaps as a means of refining the results in a narrow domain of interest. For example, this can be done by conducting refined analysis using FishBAC dynamics in the range of phase actuations that yield the most promising improvements over baseline rotor design. Additionally, the entire investigation domain can be expanded to identify the influence of geometrical parameters of the FishBAC mechanism—for example, changes in chordwise width of the morphing section, spanwise length, mid-section location of the active concept on the rotor blade, camber curvature introduced due to actuation, etc. An investigation in Ref. [170] using active rotors with multi-element airfoils suggests that an optimized airfoil design needs to be identified rather than simply attaching the morphing section to existing airfoil profiles. Therefore, the current investigation can be expanded by further taking cues from the approach adopted in that study.
2. In the current work, a coupling was established between the rotor structural dynamics solver Dymore and the vortex particle solver using an explicit time-stepping scheme. This prevented converged rotor simulations from taking place when the simulation time step was large. The exact value depended on the rotor operating conditions, but a time step size even as low as  $\Delta\psi = 1^\circ$ , for example, led to convergence difficulties while simulating BVI conditions using the Bo 105 rotor. Consequently, smaller time steps had to be adopted for Dymore+VPM coupled simulations. This dramatically increased the overall solution time despite VPM code acceleration on GPUs. The simulation time for trimmed solutions was still longer. The procedure for trimming the rotor was based on identifying the system Jacobian matrix based on perturbation inputs to the rotor system. This made the simulations very time-intensive since multiple rotor revolutions worth of simulations needed to be carried out simply to identify the parameters within the Jacobian matrix. The actual rotor trim

could only proceed thereafter. An alternative and more promising approach is described in Ref. [303]. Here, details are provided regarding the loose coupling scheme, which is used in the commercial software FLIGHTLAB to overcome a similar challenge there when using the vortex particle method to solve for the rotor wake. It is worth noting that this scheme is not so different from the loose coupling strategy, requiring data exchange per revolution, developed to speed-up rotor trim in CFD/CSD coupled studies (for example, see Ref. [208]). It would behoove future implementations of the coupled aeromechanic simulation framework using VPM to implement a similar rotor trim strategy for improved computational efficiency.

3. Helicopter rotor blades operate in a highly unsteady aerodynamic environment. Not accounting for the related unsteady aerodynamic effects results in some degree of inaccuracy in predicting the aeromechanical state of the rotor. There are a number of unsteady aerodynamic models available for predicting the blade section loads, both within the attached flow regime and during dynamic stall. Most of these models are some variation of the potential flow theory-based model first derived by Theodorsen [263]. While these models are grounded in physics, they are highly restrictive in terms of their applicability to only low frequency, small amplitude motions of the blade sections. Additionally, since their derivation is based on potential flow theory principles, the prediction of blade drag is accounted for in an ad-hoc manner. They do not explicitly account for the 2D blade section profile. As a result, unsteady behavior predictions, from small changes in the airfoil profile, can be made only to the extent that such changes are reflected in the airfoil tables used within the simulation framework. While there are a number of limitations to the state-of-the-art unsteady aerodynamic modeling theories, they have been reasonably successful at capturing lift and moment behavior. Since drag is not treated from the first principles in these theories, it is likely that the highest error is incurred here. In Ref. [52], the system identification techniques of ERA/OKID have shown to be helpful in identifying linearized state-space models that are capable of predicting airfoil behavior even when large amplitude motions are involved. The high-fidelity results that feed into this methodology can be based on either CFD simulations or experimental results. This methodology is attractive because the entire framework can be used for accurately predicting unsteady drag (provided that the underlying unsteady airfoil simulation methods model viscous boundary layer effects) and moment as well. Ref. [52] also showed that the resulting state-space models continue to be interpretable along the same lines as well-established potential flow theory counterparts like the Theodorsen theory.
4. The convergence issues encountered during the wake simulations using VPM have already been detailed in this work. Addressing the underlying issues so that vortex stretching effects can be incorporated could potentially lead to better correlation with measurement data. In addition to that, only limited studies were conducted regarding the effect of variation of parameters such as the vortex particle spanwise resolution, particle-particle overlap, tip-loss factor, etc., and the corresponding influence on the overall rotor response. A parametric study could shed some light on the sensitivity of the entire simulation framework on these parameters.
5. One of the objectives of this work was to investigate the influence of active camber mor-

phing on rotor noise emissions. It was established that for certain phase angles of camber deflection profiles a reduction in the maximum rotor noise could be achieved. However, the overall noise redistribution was more intricate, with an increase in noise at certain locations and a decrease in others. A reduction in maximum noise would not be a particularly effective demonstration of active rotors for noise reduction if noise everywhere else in the domain increased. Compounding this is the complex nature of humans' perception of noise. Therefore, a more general metric for spatial noise assessment is needed to quantify how the noise emissions over an entire domain have been influenced.

6. Within this study, the effect of the active camber morphing mechanism on vibrations induced at the rotor hub was evaluated. In principle, this is a reliable metric for assessing its impact on rotor-induced vibrations. However, vibratory loads are a concern in the way they are experienced by the passengers occupying the helicopter fuselage as well as critical components placed inside it. It is possible that a rotor design that is successful in minimizing rotor-induced vibrations at the hub may not be equally successful in minimizing vibrations within the fuselage. Therefore, in order to truly quantify the potential of active rotors to reduce vibrations, a dynamic model of the fuselage is required. It is likely that the degree to which vibrations are influenced will vary with the type of rotor as well as the fuselage dynamics. For example, Ref. [214] shows a significant contribution of loads at 1P harmonic to the vibration spectrum as well as the broadband vibrations contributions due to tail boom shaking. The reference shows that such relatively low-frequency vibrations are relevant because humans demonstrate relatively high sensitivity to them. Additionally, control system components such as swashplate servo attachments to the airframe, as well as control pitch links, need to be modeled to accurately account for the effect of multiple paths through which vibratory loads can be introduced in the airframe. This should be a part of future studies.
  
7. It behooves the future investigators or the proponents of any active rotor mechanism to use a state-of-the-art rotor, built with modern manufacturing materials and practices, in order to credibly establish the potential of active rotor control. The rotors that went onto the Bo 105 helicopter initially had the NACA0012 profile [281]; it was later switched to the NACA23012, and this model was used as a baseline rotor in the current study. Since then, the rotor blades on the Bo 105 have been upgraded to include a suite of structural and aerodynamic enhancements, detailed in Ref. [45], while keeping the same blade radius and rotor mass. The end result was an improvement in rotor performance, reduction in vibratory hubloads, and acoustic noise of the helicopter. Based on the results presented in Ref. [45], the performance benefits from rotor upgrade appear comparable or even outstrip any improvements possible using active rotor control. Advancements on the upgraded Bo 105 helicopter, in terms of airframe vibration and noise reduction, are less apparent but certainly some improvements were achieved on those fronts as well. Additionally, state-of-the-art passive blade optimization methods have also proven to lead to considerable improvements in rotor performance and vibrations [296]. For the current work, the Bo 105 (with NACA23012 airfoil blades) was chosen since experimental measurement data, as well as blade structural properties were available in the public domain. To the extent of the author's knowledge, neither of these is true in the case of the upgraded Bo 105 rotor.

8. Studies investigating the potential of active control mechanisms in primary rotor control generally conclude that greater torsional pliability of the blades is beneficial to achieving that goal. Even when primary rotor control is established using the conventional swashplate mechanism, for active mechanisms such as active twist, limitations in existing technologies dictate that this technology would be less practical on high torsional stiffness designs [283]. In the current study, the Bo 105 rotor blade properties were kept the same as the baseline rotor throughout the investigation. It is likely that reducing torsional stiffness could bring different trends in the effect of camber deflection on rotor performance, vibratory loads, and noise. In the current work, the blade dynamics did not include the effect of the FishBAC actuation system on the active blade section. In case the torsional stiffness of the blades is reduced, incorporating the active system dynamics would be all the more prudent to ensure the aeroelastic stability of the rotor system is not compromised. All this suggests that an optimal active rotor design might have significantly different properties to existing baseline rotor designs.

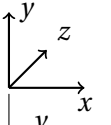
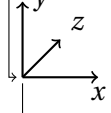
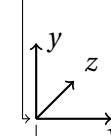
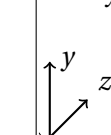
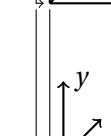
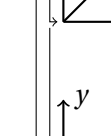
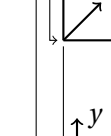
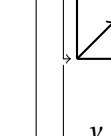
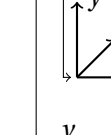
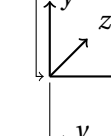
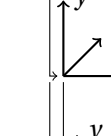
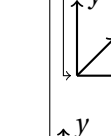
For a truly fair assessment of the capabilities of active rotor mechanisms, it is necessary to conduct an optimization study where the rotor is optimized based on the active mechanism in question. Such an exercise would include not just the blade's structural properties but also the blade planform and airfoil shape. Refs. [233] and [234] conducted some preliminary work in that direction using a comprehensive analysis simulation framework to aerodynamically optimize an active twist rotor. They used different planform parameters and arrived at different designs based on whether the targeted objective of the active rotor was power reduction, vibration reduction, maximizing blade twist response, etc. Ref. [151] also carried out a similar optimization study but focused on the blade structural properties instead. It concluded that the final optimized blade properties differed significantly based on the actuation frequency of blade twist. Similar, limited optimization studies can be found in literature corresponding to other active mechanisms [302]. Understandably, the global optimization of an active rotor is a significant undertaking but one that, to the best of the author's knowledge, has not been addressed in existing literature, even as industry and academia show no signs of giving up on the promise of active rotors.

## A. Bo 105 Rotor

**Table A.1.:** Details of the Bo 105 rotor system multibody model.

	Symbol	Value	Description
general	$N_b$	4	
	$\Omega$	44.505	
	$\sigma$	0.07	
	R	4.912 m	
	$\beta_0$	$2.5^\circ$	precone
	$\gamma$	see Table A.3	shaft tilt angle
		NACA23012	airfoil
rotor head	$\beta_0$	$2.5^\circ$	precone
	$\Delta\theta_i$	$(i-1)90^\circ$	blade $i$ , $i \in [1, N_b]$
	$x_{ph}$	0.2 m	radial location of pitchhorn
	$y_{ph}$	0.196 m	pitchhorn distance to feathering axis
	$z_{ph}$	0	pitchhorn vertical offset
	$e_p$	0.221 m	pitch bearing radial position
	pitchlink	$\Theta$	$15^\circ$
$\Phi$		$0^\circ$	
$r_{pl}$		0.2 m	
$l_{pl}$		0.30 m	
shaft	$l_{sh}$	0.3 m	
scissor	$z_{sc}$	0.1 m	
	$l_{sc,r}$	0.35 m	
	$l_{sc,v}$	0.15 m	
	$r_{sc,o}$	0.3 m	outer pickup radius
	$r_{sc,i}$	0.03 m	inner pickup radius
swashplate	$z_{sc}$	0.35 m	
	$\phi_{pl}$	$45^\circ$	
servos	$z_t$	0.07 m	

**Table A.2.:** Reference frames used to construct the Bo 105 multibody model of Fig. 2.8. Fixed points represented as •, joints as □.

Frame name	Definition	Relevant points
Inertial $I$		
Fuselage $F$	 ${}^I\vec{e}_{F,y}^T = \{0, 1, 0\}$ ${}^I\vec{e}_{F,z}^T = \{\sin(\gamma), 1, \cos(\gamma)\}$ ${}^I O_F = \{0, 0, 0\}$	
Shaft $S$	 ${}^F\vec{e}_{S,y}^T = \{0, 1, 0\}$ ${}^F\vec{e}_{S,z}^T = \{0, 0, 1\}$ ${}^F O_S = \{0, 0, 0\}$	<ul style="list-style-type: none"> <li>• <math>{}^S A_S = \{0, 0, 0\}</math></li> <li>• <math>{}^S B_S = \{0, 0, z_{sc}\}</math></li> <li>□ <math>{}^S C_S = \{0, 0, l_{sh}\}</math></li> </ul>
Root $R_i$	 ${}^S\vec{e}_{R_i,y}^T = \{\sin(\Delta\theta_i), \cos(\Delta\theta_i), 0\}$ ${}^S\vec{e}_{R_i,z}^T = \{0, 0, -1\}$ ${}^S O_{R_i} = \{0, 0, 0\}$	
Scissor $C$	 ${}^{R_i}\vec{e}_{C,y}^T = \{0, 1, 0\}$ ${}^{R_i}\vec{e}_{C,z}^T = \{0, 0, 1\}$ ${}^{R_i} O_C = \{0, 0, -z_{sw}\}$	<ul style="list-style-type: none"> <li>• <math>{}^C A_C = \{0, 0, 0\}</math></li> <li>• <math>{}^C B_C = \{0, 0, z_{sw} - z_{sc}\}</math></li> <li>□ <math>{}^C C_C = \{0.03, 0, 0.15\}</math></li> <li>□ <math>{}^C D_C = \{0.35, 0, 0.15\}</math></li> <li>□ <math>{}^C E_C = \{r_{sc}, 0, 0\}</math></li> </ul>
Swashplate $W$	 ${}^C\vec{e}_{W,y}^T = \{0, 1, 0\}$ ${}^C\vec{e}_{W,z}^T = \{0, 0, 1\}$ ${}^C O_W = \{0, 0, -z_{sw}\}$	<ul style="list-style-type: none"> <li>• <math>{}^W A_W = \{0, 0, 0\}</math></li> <li>• <math>{}^W B_W = \{0, 0, z_{sw} - z_{sc}\}</math></li> <li>□ <math>{}^W C_W = \{0.03, 0, 0.15\}</math></li> </ul>
Servo $T_i$	 ${}^W\vec{e}_{T_i,y}^T = \{0, 1, 0\}$ ${}^W\vec{e}_{T_i,z}^T = \{0, 0, 1\}$ ${}^W O_{T_i} = \{0, 0, -z_t(2 - i)\}$	
Pitch link $L$	 ${}^W\vec{e}_{L,y}^T = \{\sin(\Theta) \cdot \sin(\Phi), \cos(\Phi), \cos(\Theta) \cdot \cos(\Phi)\}$ ${}^W\vec{e}_{L,z}^T = \{\sin(\Theta) \cdot \cos(\Phi), -\sin(\Phi), \cos(\Theta) \cdot \cos(\Phi)\}$ ${}^W O_L = \{r_{pl}, 0, 0\}$	<ul style="list-style-type: none"> <li>□ <math>{}^L A_L = \{0, 0, 0\}</math></li> <li>□ <math>{}^L B_L = \{0, 0, l_{pl}\}</math></li> </ul>
Precone $P$	 ${}^{R_i}\vec{e}_{P,y}^T = \{0, 1, 0\}$ ${}^{R_i}\vec{e}_{P,z}^T = \{-\sin(\beta_0), 0, -\cos(\beta_0)\}$ ${}^{R_i} O_P = \{0, 0, 0\}$	
Attachment $A$	 ${}^P\vec{e}_{A,y}^T = \{0, 1, 0\}$ ${}^P\vec{e}_{A,z}^T = \{0, 0, 1\}$ ${}^P O_A = \{0, 0, 0\}$	<ul style="list-style-type: none"> <li>• <math>{}^P A_A = \{0, 0, 0\}</math></li> <li>• <math>{}^P D_A = \{x_{ph}, y_{ph}, 0\}</math></li> <li>□ <math>{}^P B_A = \{e_p, 0, 0\}</math></li> <li>• <math>{}^P C_A = \{x_{ph}, 0, 0\}</math></li> </ul>
Retention $R$	 ${}^A\vec{e}_{R,y}^T = \{0, 1, 0\}$ ${}^A\vec{e}_{R,z}^T = \{0, 0, 1\}$ ${}^A O_R = \{0, 0, 0\}$	<ul style="list-style-type: none"> <li>□ <math>{}^A A_R = \{0, 0, 0\}</math></li> <li>□ <math>{}^A B_R = \{0, 0, e_p\}</math></li> </ul>
Blade $B$	 ${}^A\vec{e}_{B,y}^T = \{0, 1, 0\}$ ${}^A\vec{e}_{B,z}^T = \{0, 0, 1\}$ ${}^A O_B = \{0, 0, 0\}$	<ul style="list-style-type: none"> <li>• <math>{}^A A_B = \{0, 0, 0\}</math></li> <li>• <math>{}^A B_B = \{0.93R, 0, 0\}</math></li> </ul>

**Table A.3.:** Baseline Bo 105 rotor trim conditions for cases from Ref. [111] investigated in this work.

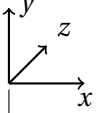
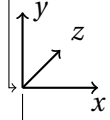
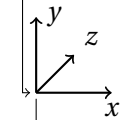
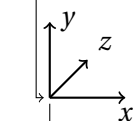
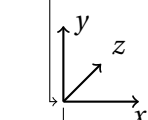
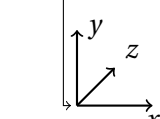
Case	Shaft tilt	Forward speed [m/s]	Thrust [N]	Roll Moment [Nm]	Pitching Moment [Nm]
Run 15 Point 5	0.0°	3.19	-19815	133	248
Run 45 Point 33	-0.4°	22.12	-22558	-435	3267
Run 42 Point 17	-0.4°	22.22	23336	-442	1907
Run 45 Point 16	-0.4°	22.17	-22242	-547	3327
Run 45 Point 26	-0.4°	22.22	-22305	-382	3283
Run 42 Point 7	-0.4°	22.27	-23380	-484	1822
Run 48 Point 5	-0.4°	23.30	-22322	-454	3229
Run 49 Point 5	-0.4°	23.30	-22256	-344	3105
Run 57 Point 7	-7.2°	52.52	22256	-386	1490
Run 43 Point 37	-7.3°	66.00	-20660	-1117	6359
Run 39 Point 5	-7.3°	66.05	-22220	-1202	1909
Run 26 Point 11	-7.3°	66.10	-22078	-1254	2853
Run 29 Point 6	-8.8°	87.30	-20998	-2199	1585
Run 57 Point 24	-8.8°	87.51	-21464	-2236	1431
Run 57 Point 8	-8.8°	87.56	-21589	-2252	1408
Run 57 Point 33	-8.8°	87.56	-21229	-2253	1204
Run 58 Point 14	-7.9°	97.85	-21202	-2261	772





## B. HART II Rotor

**Table B.1.:** Reference frames used to construct the HART II multibody model of Fig. 2.12(a). Fixed points represented as  $\bullet$ , joints as  $\square$ .

Frame name	Definition	Relevant points
Inertial $I$		
Fuselage $F$	 ${}_I\vec{e}_{F,y}^T = \{0, 1, 0\}$ ${}_I\vec{e}_{F,z}^T = \{\sin(\gamma), 1, \cos(\gamma)\}$ ${}_I O_F = \{0, 0, 0\}$	
Shaft $S$	 ${}_F\vec{e}_{S,y} = \{0, 1, 0\}$ ${}_F\vec{e}_{S,z} = \{0, 0, 1\}$ ${}_F O_S = \{0, 0, \Delta z/R\}$	
Hub-Fixed $HF$	 ${}_S\vec{e}_{HF,y} = \{0, 1, 0\}$ ${}_S\vec{e}_{HF,z} = \{0, 0, -1\}$ ${}_S O_{HF} = \{0, 0, 0\}$	
Hub-Rotating $HR$	 ${}_{HF}\vec{e}_{HR,y} = \{-\sin(\Omega t), \cos(\Omega t), 0\}$ ${}_{HF}\vec{e}_{HR,z} = \{0, 0, 1\}$ ${}_{HF} O_{HR} = \{0, 0, 0\}$	
Blade $B$	 ${}_{HR}\vec{e}_{B,y} = \{0, 1, 0\}$ ${}_{HR}\vec{e}_{B,z} = \{\sin(\beta_0), 0, \cos(\beta_0)\}$ ${}_{HR} O_B = \{0, 0, 0\}$	$\bullet {}_B A_B = \{0, 0, 0\}$ $\bullet {}_B B_B = \{R, 0, 0\}$ $\square {}_B C_B = \{r_R, 0, 0\}$

**Table B.2.:** Details of HART II rotor system multibody model.

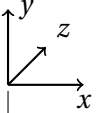
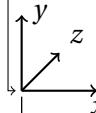
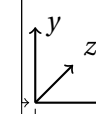
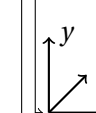
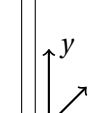

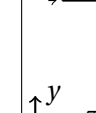
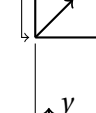
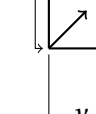
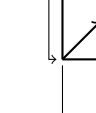
Symbol	Value	Description
$N_b$	4	number of blades
$\sigma$	0.077	solidity
$c$	0.121 m	chord
	NACA23012mod	airfoil
$\theta_{tw}$	$-8^\circ$	linear twist
$r_R$	0.22	root cutout
R	2.0 m	radius
$\beta_0$	$2.5^\circ$	precone
$\Delta\theta_i$	$90^\circ(i-1)$	blade $i$ , $i \in [1, N_b]$

## C. UT Austin Rotors

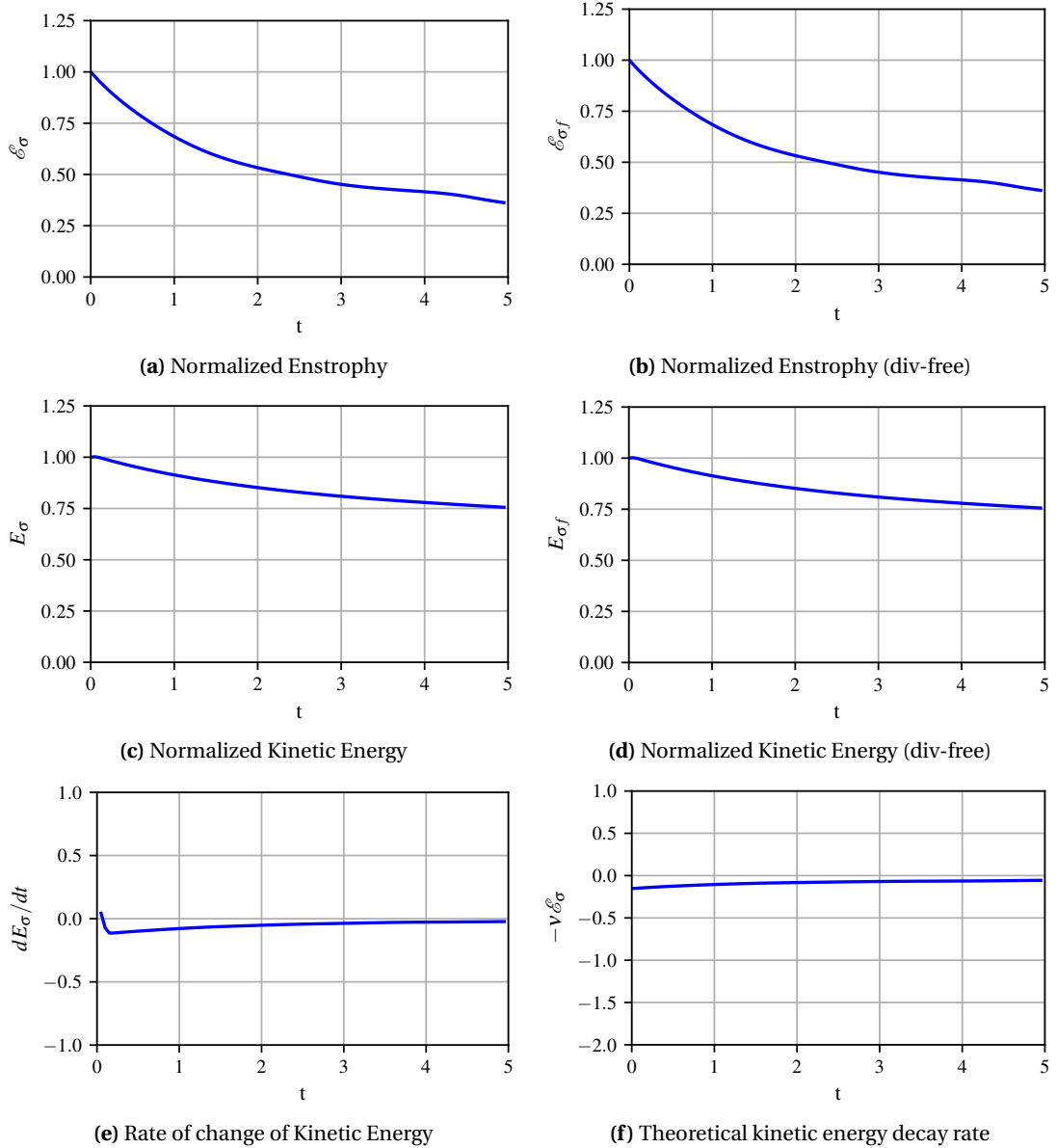
**Table C.1.:** Model parameters used for the construction of the UT Austin two- and four-bladed single rotors, and the coaxial countra-rotating rotor.

<b>Parameter</b>	<b>Single Rotor</b>	<b>Coaxial Rotor</b>
$N_b$	2 / 4	4
$\sigma$	0.04597 / 0.09193	0.10
$c$	0.08	0.08
$\Omega$	125.66 rad s <sup>-1</sup>	94.25 rad s <sup>-1</sup>
$V_{\text{tip}}$	139.26 m s <sup>-1</sup>	95.76 m s <sup>-1</sup>
$M_{\text{tip}}$	0.41	0.2816
$R$	1.108 m	1.016 m
$\gamma$	0°	0°
$\beta_0$	3°	3°
$r_R$	0.1876	0.12
$\Delta z/R$	-	0.140
Airfoil	VR-12 with tab	VR-12 with tab

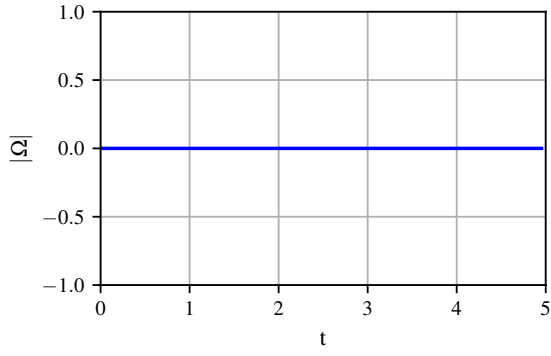
**Table C.2.:** Details of the UT Austin coaxial rotor multibody model of Fig. 2.15. Fixed points represented as  $\bullet$  and joints as  $\square$ .

Frame name	Definition	Relevant points
Inertial $I$		
Fuselage $F$	 ${}_I\vec{e}_{F,y} = \{0, 1, 0\}$ ${}_I\vec{e}_{F,z} = \{\sin(\gamma), 0, \cos(\gamma)\}$ ${}_I O_F = \{0, 0, 0\}$	
Shaft $S, r1$	 ${}_F\vec{e}_{S,r1,y} = \{0, 1, 0\}$ ${}_F\vec{e}_{S,r1,z} = \{0, 0, 1\}$ ${}_F O_{S,r1} = \{0, 0, \Delta z/R\}$	
Hub-Fixed $HF, r1$	 ${}_{S,r1}\vec{e}_{HF,r1,y} = \{0, 1, 0\}$ ${}_{S,r1}\vec{e}_{HF,r1,z} = \{0, 0, -1\}$ ${}_{S,r1} O_{HF,r1} = \{0, 0, 0\}$	
Hub-Rotating $HR, r1$	 ${}_{HF,r1}\vec{e}_{HR,r1,y} = \{-\sin(\psi_{r1}), \cos(\psi_{r1}), 0\}$ ${}_{HF,r1}\vec{e}_{HR,r1,z} = \{0, 0, 1\}$ ${}_{HF,r1} O_{HR,r1} = \{0, 0, 0\}$	
Blade $B, r1$	 ${}_{HR,r1}\vec{e}_{B,r1,y} = \{0, 1, 0\}$ ${}_{HR,r1}\vec{e}_{B,r1,z} = \{\sin(\beta_0), 0, \cos(\beta_0)\}$ ${}_{HR,r1} O_{B,r1} = \{0, 0, 0\}$	<ul style="list-style-type: none"> <li><math>\bullet {}_{B,r1} A_{B,r1} = \{0, 0, 0\}</math></li> <li><math>\bullet {}_{B,r1} B_{B,r1} = \{R, 0, 0\}</math></li> <li><math>\square {}_{B,r1} C_{B,r1} = \{r_R, 0, 0\}</math></li> </ul>
Shaft $S, r2$	 ${}_F\vec{e}_{S,r2,y} = \{0, -1, 0\}$ ${}_F\vec{e}_{S,r2,z} = \{0, 0, -1\}$ ${}_F O_{S,r2} = \{0, 0, 0\}$	
Hub-Fixed $HF, r2$	 ${}_{S,r2}\vec{e}_{HF,r2,y} = \{0, 1, 0\}$ ${}_{S,r2}\vec{e}_{HF,r2,z} = \{0, 0, -1\}$ ${}_{S,r2} O_{HF,r2} = \{0, 0, 0\}$	
Hub-Rotating $HR, r2$	 ${}_{HF,r2}\vec{e}_{HR,r1,y} = \{-\sin(\psi_{r2}), \cos(\psi_{r2}), 0\}$ ${}_{HF,r2}\vec{e}_{HR,r2,z} = \{0, 0, 1\}$ ${}_{HF,r2} O_{HR,r2} = \{0, 0, 0\}$	
Blade $B, r2$	 ${}_{HR,r2}\vec{e}_{B,r2,y} = \{0, 1, 0\}$ ${}_{HR,r2}\vec{e}_{B,r2,z} = \{\sin(\beta_0), 0, \cos(\beta_0)\}$ ${}_{HR,r2} O_{B,r2} = \{0, 0, 0\}$	<ul style="list-style-type: none"> <li><math>\bullet {}_{B,r2} A_{B,r2} = \{0, 0, 0\}</math></li> <li><math>\bullet {}_{B,r2} B_{B,r2} = \{R, 0, 0\}</math></li> <li><math>\square {}_{B,r2} C_{B,r2} = \{r_R, 0, 0\}</math></li> </ul>

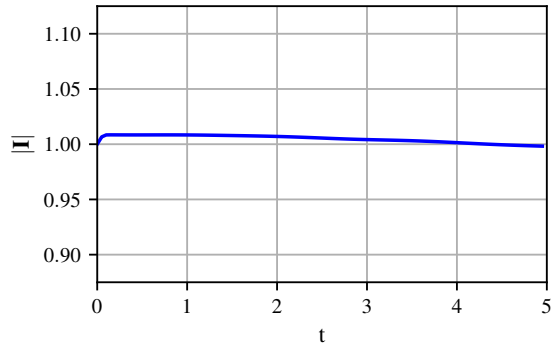
## D. VPM



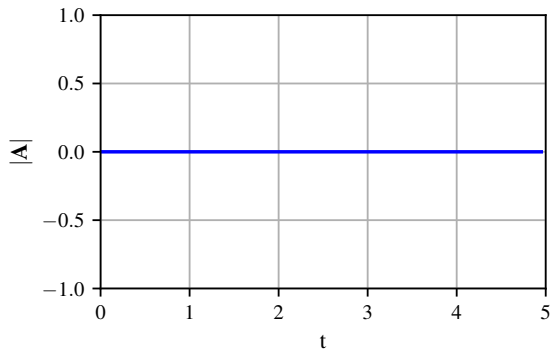
**Figure D.1.:** Quadratic flow field diagnostics of 4by80 vortex ring predicted using VPM.



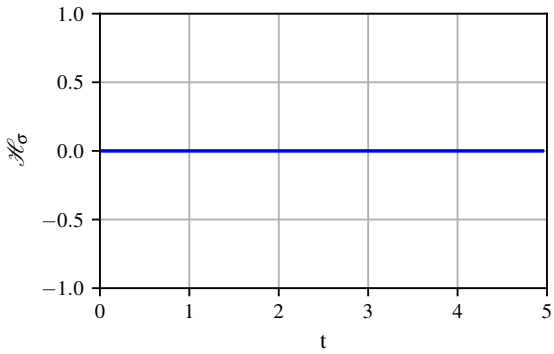
(a) Total Vorticity (4by80)



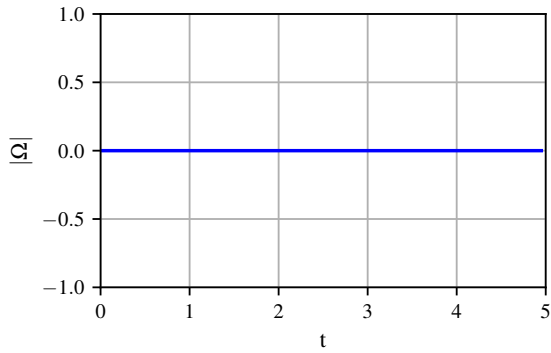
(b) Normalized Linear Impulse (4by80)



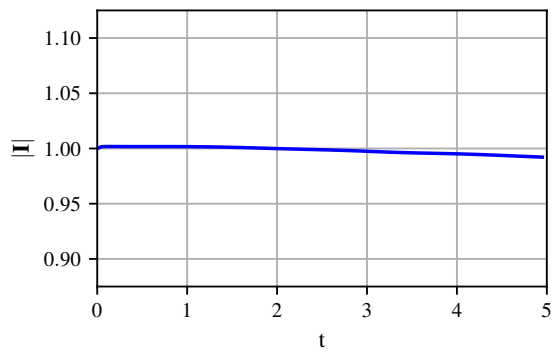
(c) Angular Impulse (4by80)



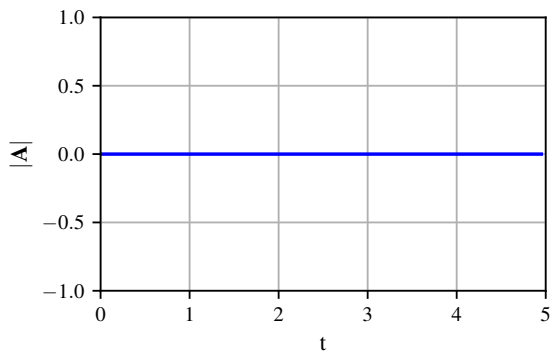
(d) Helicity (4by80)



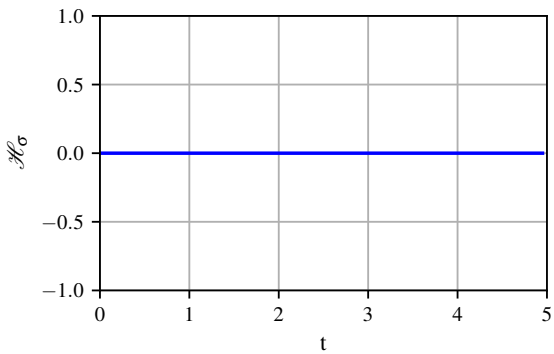
(e) Total Vorticity (5by100)



(f) Normalized Linear Impulse (5by100)

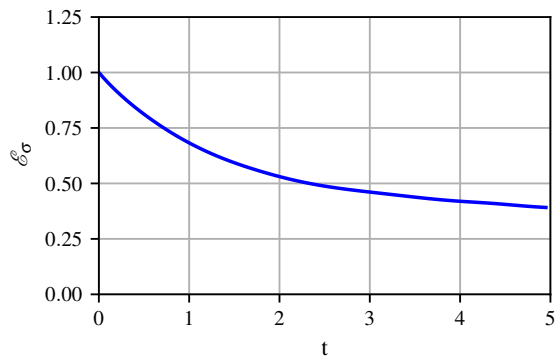


(g) Angular Impulse (5by100)

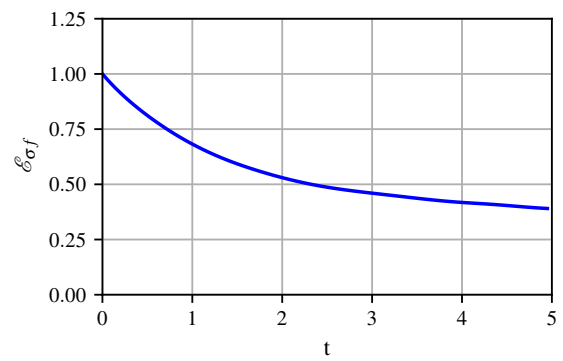


(h) Helicity (5by100)

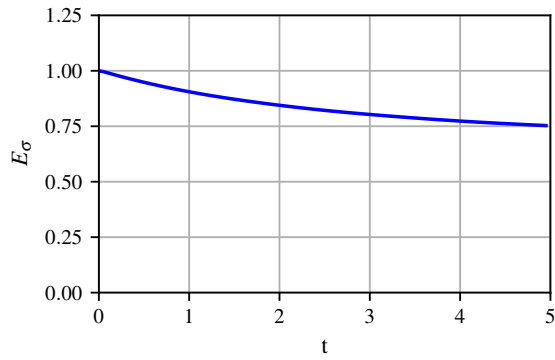
**Figure D.2.:** Linear flow field diagnostics of 4by80 and 5by100 vortex rings predicted using VPM.



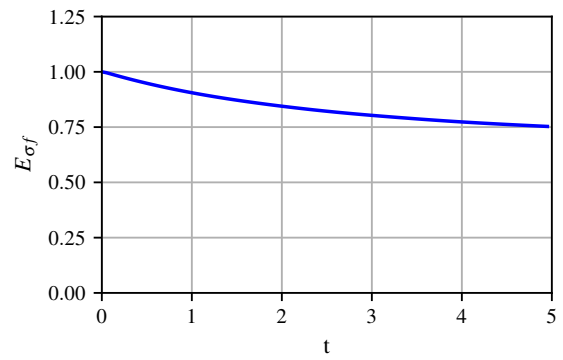
(a) Normalized Enstrophy



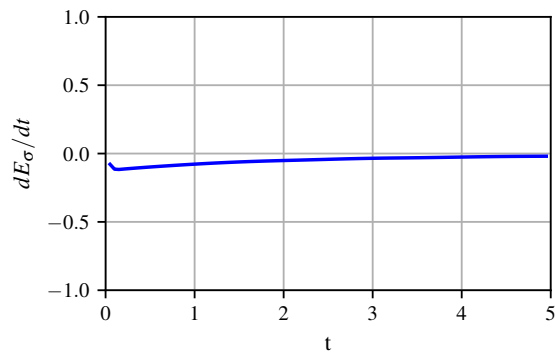
(b) Normalized Enstrophy (div-free)



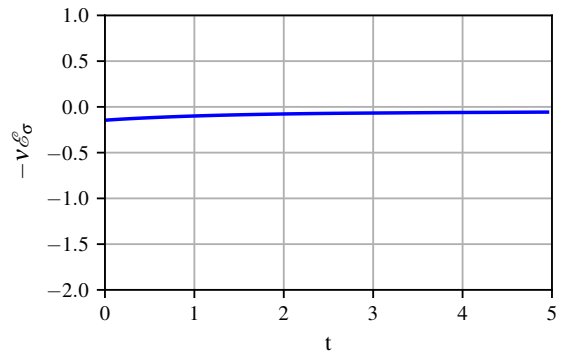
(c) Normalized Kinetic Energy



(d) Normalized Kinetic Energy (div-free)



(e) Rate of change of Kinetic Energy



(f) Theoretical kinetic energy decay rate

**Figure D.3.:** Quadratic flow field diagnostics of 5by100 vortex ring predicted using VPM.





# Bibliography

- [1] *DLR Images*. <https://www.dlr.de/en/images>. Accessed: 14-February-2024.
- [2] *DUST Aerodynamic Solver*. <https://public.gitlab.polimi.it/DAER/dust>. Accessed: 04-February-2024.
- [3] *Dymore User's Manual: Compound Air Tables*. <https://www.dropbox.com/scl/fo/97ntltncmxkdsrb5a95dk/h?rlkey=ed9yp2lnhazkupxn3nieiat3b&dl=0>. Created: 27-February-2024.
- [4] *Dymore User's Manual: Unsteady Aerodynamics*. <https://www.dropbox.com/scl/fo/97ntltncmxkdsrb5a95dk/h?rlkey=ed9yp2lnhazkupxn3nieiat3b&dl=0>. Created: 27-February-2024.
- [5] *FULL-SCALE S-76 ROTOR RESEARCH IN THE 80- BY 120-FOOT WIND TUNNEL*. <https://rotorcraft.arc.nasa.gov/Research/Programs/s76.html>. Accessed: 06-March-2024.
- [6] *Fundamentals of Helicopter Aerodynamics: Course Notes*. <https://kumar-sumeet.github.io/HeliAeroNotes/Opening.html>. Accessed: 04-February-2024.
- [7] *HART II International Workshop*. <https://www.dlr.de/en/site/hart-ii>. Accessed: 06-August-2024.
- [8] *HART II Test Documentation Reports*. <https://www.dlr.de/en/site/hart-ii/test-documentation>. Accessed: 06-August-2024.
- [9] *HeliNoise*. <https://github.com/kumar-sumeet/helinoise>. Accessed: 13-10-2022.
- [10] *Publications with HART II Data*. <https://www.dlr.de/en/site/hart-ii/publications>. Accessed: 06-August-2024.
- [11] *Raider X*. <https://www.lockheedmartin.com/en-us/products/fara-raider-x.html>. Accessed: 18-February-2024.
- [12] *SB>1 Defiant*. <https://www.lockheedmartin.com/en-us/products/sb1-defiant-technology-demonstrator.html>. Accessed: 18-February-2024.
- [13] *UH-60A INDIVIDUAL BLADE CONTROL PROJECT*. [https://rotorcraft.arc.nasa.gov/Research/Programs/UH-60\\_IBC.html](https://rotorcraft.arc.nasa.gov/Research/Programs/UH-60_IBC.html). Accessed: 06-March-2024.
- [14] *VFS Gallery*. <https://gallery.vtol.org/image/GPvOL>. Accessed: 06-March-2024.
- [15] *OpenMP*. <https://www.openmp.org/>. Accessed: 21-August-2023. 2023.
- [16] Abdelmoula, A. and Rauleder, J. "Aerodynamic performance of morphed camber rotor airfoils". In: *AIAA Scitech 2019 Forum*. San Diego, CA, Jan. 2019.
- [17] Abras, J., Smith, M., and Bauchau, O. "Rotor airload predictions using coupled finite element and free wake methods". In: *64th Annual Forum of the American Helicopter Society*. Phoenix, AZ, May 2006.

- [18] Achache, M. and Polychroniadis, M. “Development of an Experimental System for Active Control of Vibrations on Helicopters - Development Methodology for an Airborne System”. In: *12th European Rotorcraft Forum*. Garmisch-Partenkirchen, Germany, Sept. 1986.
- [19] Ahaus, L. A. “An Airloads Theory for Morphing Airfoils in Dynamic Stall with Experimental Correlation”. PhD thesis. St. Louis, May 2010.
- [20] Ananthan, S. and Leishman, J. G. “Role of filament strain in the free-vortex modeling of rotor wakes”. In: *Journal of the American Helicopter Society* 49.2 (2004), pp. 176–191.
- [21] Angulo, I. A. and Ansell, P. J. “Influence of Aspect Ratio on Dynamic Stall of a Finite Wing”. MA thesis. University of Illinois at Urbana-Champaign, 2018.
- [22] Arnold, U. T. and Fürst, D. “Closed loop IBC results from CH-53G flight tests”. In: *Aerospace Science and Technology* 9.5 (2005), pp. 421–435.
- [23] Arnold, U. T. “Recent IBC flight test results from the CH-53G helicopter”. In: (Sept. 2003).
- [24] Bagai, A. and Leishman, J. G. “Rotor Free-Wake Modeling Using a Pseudo-Implicit Technique—Including Comparisons with Experimental Data”. In: *Journal of the American Helicopter Society* 40.3 (1995), pp. 29–41.
- [25] Bain, J. J., Sankar, L. N., Prasad, J., Bauchau, O. A., Peters, D. A., and He, C. “Computational modeling of variable-droop leading edge in forward flight”. In: *Journal of aircraft* 46.2 (2009), pp. 617–626.
- [26] Bain, J. “Computational Comparisons between FW-H and Direct Acoustic Predictions”. In: *American Helicopter Society 72nd Annual Forum*. West Palm Beach, FL, May 2016.
- [27] Banerjee, T. “Dynamic Inflow-based Analysis of Pitch Changes to Hovering Rotor”. MA thesis. Nanyang Technological University, Sept. 2020.
- [28] Barba, L., Leonard, A., and Allen, C. “Advances in viscous vortex methods—meshless spatial adaption based on radial basis function interpolation”. In: *International Journal for Numerical Methods in Fluids* 47.5 (2005), pp. 387–421.
- [29] Barron, H. M., Brentner, K., Horn, J., Ozdemir, G. T., and Thorsen, A. “Acoustic Analysis of Compound Helicopters with Trim Variations”. In: *American Helicopter Society 69th Annual Forum*. Phoenix, AZ, 2013.
- [30] Basset, P.-M. and Ormiston, R. “Comparison and validation of the France/USA finite state rotor dynamic inflow models”. In: *36th European Rotorcraft Forum*. Paris, France, Sept. 2010.
- [31] Bauchau, O. A., Bottasso, C. L., and Nikishkov, Y. G. “Modeling Rotorcraft Dynamics with Finite Element Multibody Procedures”. In: *Mathematical and Computer Modelling* 33.10-11 (2001), pp. 1113–1137.
- [32] Bauchau, O. A. “DYMORE user’s manual”. In: *Georgia Institute of Technology, Atlanta* (2007).
- [33] Bauchau, O. A. “Computational schemes for flexible, nonlinear multi-body systems”. In: *Multibody System Dynamics* 2.2 (1998), pp. 169–225.
- [34] Bhagwat, M. J., Ormiston, R., Saberi, H. A., and Xiu, H. “Application of CFD/CSD coupling for analysis of rotorcraft airloads and blade loads in maneuvering flight”. In: *American Helicopter Society 63rd Annual Forum*. Virginia Beach, VA, May 2007.

- [35] Bhagwat, M. “Transient Dynamics of Helicopter Rotor Wakes using a Time-Accurate Free-Vortex Method”. PhD thesis. University of Maryland, 2001.
- [36] Bhagwat, M. “Co-rotating and counter-rotating coaxial rotor performance”. In: *AHS Aeromechanics Design for Transformative Vertical Flight* (Jan. 2018).
- [37] Biggers, J. C. and Mccloud III, J. L. *A note on multicyclic control by washplate oscillation*. Tech. rep. TM 78475. NASA, Apr. 1978.
- [38] Bisplinghoff, R. L., Ashley, H., and Halfman, R. L. *Aeroelasticity*. Mineola, New York: Dover Publications, 1996.
- [39] Bliss, D. B., Teske, M. E., and Quackenbush, T. R. *A new methodology for free wake analysis using curved vortex elements*. Tech. rep. CR-3548. NASA, Dec. 1987.
- [40] Booth, E. R. and Wilbur, M. L. “Acoustic Aspects of Active-Twist Rotor Control”. In: *Journal of the American Helicopter Society* 49.1 (2004), pp. 3–10.
- [41] Bousman, W. G. “Airfoil Design and Rotorcraft Performance”. In: *American Helicopter Society 58th Annual Forum*. Montréal, Canada, June 2002.
- [42] Bousman, W. G. “A qualitative examination of dynamic stall from flight test data”. In: *Journal of the American Helicopter Society* 43.4 (1998), pp. 279–295.
- [43] Boyd Jr, D. D. “HART-II acoustic predictions using a coupled CFD/CSD method”. In: *American Helicopter Society 65th Annual Forum*. Grapevine, TX, May 2009.
- [44] Boyd Jr, D. D. “Initial aerodynamic and acoustic study of an active twist rotor using a loosely coupled CFD/CSD method”. In: *35th European Rotorcraft Forum*. Hamburg, Germany, Sept. 2009.
- [45] Braun, D. and Humpert, A. “BO105 CBS-5: BO105 Upgrade through New Rotor Blades”. In: *19th European Rotorcraft Forum, Italy*. Sept. 1993.
- [46] Brentner, K. and Jones, H. “Noise prediction for maneuvering rotorcraft”. In: *6th Aeroacoustics Conference and Exhibit*. June 2000.
- [47] Brentner, K. S. and Farassat, F. “Modeling aerodynamically generated sound of helicopter rotors”. In: *Progress in aerospace sciences* 39.2-3 (2003), pp. 83–120.
- [48] Brès, G., Brentner, K. S., Perez, G., and Jones, H. “Maneuvering rotorcraft noise prediction”. In: *Journal of Sound and Vibration* 275.3-5 (2004), pp. 719–738.
- [49] Brentner, K. S., Edwards, B. D., Riley, R., and Schillings, J. “Predicted noise for a main rotor with modulated blade spacing”. In: *Journal of the American Helicopter Society* 50.1 (2005), pp. 18–25.
- [50] Brentner, K. S., Burley, C. L., and Marcolini, M. A. “Sensitivity of acoustic predictions to variation of input parameters”. In: *Journal of the American Helicopter Society* 39.3 (1994), pp. 43–52.
- [51] Brooks, T., Burley, C., Boyd Jr, D., and Jolly Jr, J. “Aeroacoustic codes for rotor harmonic and BVI noise-CAMRAD. Mod1/HIRES”. In: *2nd AIAA/CEAS Aeroacoustics Conference*. State College, PA, May 1996.
- [52] Brunton, S. L. “Unsteady Aerodynamic Models for Agile Flight at Low Reynolds Numbers”. PhD thesis. Princeton University, Apr. 2012.

- [53] Bryant, L. and Williams, D. "An investigation of the flow of air around an aerofoil of infinite span". In: *Philosophical Transactions of the Royal Society of London* 225.626-635 (1926), pp. 199–245.
- [54] Calabretta, J. "A Three Dimensional Vortex Particle-panel Code for Modeling Propeller-airframe Interaction". MA thesis. California Polytechnic State University, June 2010.
- [55] Calhoun, J. R. *Use of NASA STI: Disclaimers, Copyright Notice, and Terms and Conditions of Use*. <https://sti.nasa.gov/disclaimers/>. Accessed: 08-January-2024. 2024.
- [56] Caprace, D.-G., Chatelain, P., and Winckelmans, G. "Wakes of rotorcraft in advancing flight: A large-eddy simulation study". In: *Physics of Fluids* 32.8 (2020).
- [57] Cesnik, C. E. and Hodges, D. H. "VABS: a new concept for composite rotor blade cross-sectional modeling". In: *Journal of the American helicopter society* 42.1 (1997), pp. 27–38.
- [58] Chen, H.-n., Brentner, K. S., Lopes, L. V., and Horn, J. F. "An initial analysis of transient noise in rotorcraft maneuvering flight". In: *International Journal of Aeroacoustics* 5.2 (2006), pp. 109–138.
- [59] Chorin, A. J. "Numerical study of slightly viscous flow". In: *Journal of fluid mechanics* 57.4 (1973), pp. 785–796.
- [60] Chung, K. H., Kim, J. W., Ryu, K. W., Lee, K. T., and Lee, D. J. "Sound generation and radiation from rotor tip-vortex pairing phenomenon". In: *ALAA journal* 44.6 (2006), pp. 1181–1187.
- [61] Chun, T., Ryu, H., Cho Seong, H., Shin, S., Kee, Y., and Kim, D.-K. "Structural analysis of a bearingless rotor using an improved flexible multibody model". In: *Journal of Aircraft* 50.2 (2013), pp. 539–550.
- [62] Corle, E., Schmitz, S., Singh, R., Kang, H., and Floros, M. "Correlation of RCAS Load Predictions for an Active Flap Rotor". In: *AHS Specialists' Conference on Aeromechanics Design for Vertical Lift*. San Francisco, CA, Jan. 2016.
- [63] Cottet, G.-H. and Koumoutsakos, P. D. *Vortex Methods: Theory and Practice*. Cambridge university press, 2000.
- [64] Crozier, P., Leconte, P., Delrieux, Y., Gimonet, B., Le Pape, A., and Mercier de Rochettes, H. "Wind-tunnel tests of a helicopter rotor with active flaps". In: *32nd European Rotorcraft Forum*. Maastricht, the Netherlands, Sept. 2006.
- [65] Dadone, L. *US Army Helicopter Design Datcom Volume I-Airfoils*. Tech. rep. USAAMRDL CR 76-2. US Army Air Mobility Research and Development Laboratory, 1976.
- [66] Datta, A. and Chopra, I. "Validation of Structural and Aerodynamic Modeling Using UH-60A Airloads Program Data". In: *Journal of the American Helicopter Society* 51.1 (2006), pp. 43–58.
- [67] Datta, A., Nixon, M., and Chopra, I. "Review of rotor loads prediction with the emergence of rotorcraft CFD". In: *Journal of the American Helicopter Society* 52.4 (2007), pp. 287–317.
- [68] Der Wall, B. G. van et al. "Smart Twisting Active Rotor (STAR)-Pre-Test Predictions". In: *48th European Rotorcraft Forum*. Winterthur, Switzerland, Sept. 2022.
- [69] Dieterich, O., Enenkl, B., and Roth, D. "Trailing edge flaps for active rotor control aeroelastic characteristics of the ADASYS rotor system". In: *American Helicopter Society 62nd Annual Forum*. Phoenix, Az, 2006.

- [70] Ding, L. and Shen, J. “Helicopter Rotor Infield Tracking with a Trailing-edge Flap and Adaptive Closed-loop Regulator”. In: *American Helicopter Society 74th Annual Forum*. Phoenix, AZ, May 2018.
- [71] Ding, L. and Shen, J. “Multibody Dynamics Modeling of a Helicopter Rotor with Active Continuous Trailing-edge Flap”. In: *AHS International Technical Meeting Aeromechanics Design for Transformative Vertical Flight*. San Francisco, CA, Jan. 2018.
- [72] Du Val, R. and He, C. “Validation of the FLIGHTLAB virtual engineering toolset”. In: *The Aeronautical Journal* 122.1250 (2018), pp. 519–555.
- [73] Dürrwächter, L., Keßler, M., and Krämer, E. “Numerical assessment of open-rotor noise shielding with a coupled approach”. In: *AIAA Journal* 57.5 (2019), pp. 1930–1940.
- [74] Escobar, D. and Yeo, H. “Performance and Loads of a Wing-Offset Compound Helicopter”. In: *Journal of the American Helicopter Society* 68.3 (2023).
- [75] Ezzat, H. *MAE 239: Dynamics of Unsteady Flows*. Youtube. 2018. URL: [https://www.youtube.com/watch?v=MEWVd7FpnOg&list=PLCheZLRn7G\\_ynSVQc9X8hClVxvNlf6hjW&pp=iAQB](https://www.youtube.com/watch?v=MEWVd7FpnOg&list=PLCheZLRn7G_ynSVQc9X8hClVxvNlf6hjW&pp=iAQB).
- [76] Fage, A. and Simmons, L. F. G. “An investigation of the air-flow pattern in the wake of an aerofoil of finite span”. In: *Philosophical Transactions of the Royal Society of London. Series A, Containing Papers of a Mathematical or Physical Character* 225.626-635 (1926), pp. 303–330.
- [77] Farassat, F. and Succi, G. P. “A review of propeller discrete frequency noise prediction technology with emphasis on two current methods for time domain calculations”. In: *Journal of Sound and Vibration* 71.3 (1980), pp. 399–419.
- [78] Farassat, F. and Brentner, K. S. “The acoustic analogy and the prediction of the noise of rotating blades”. In: *Theoretical and computational fluid dynamics* 10.1 (1998), pp. 155–170.
- [79] Farassat, F. *Derivation of Formulations 1 and 1A of Farassat*. Tech. rep. NASA TM-2007-214853. Langley Research Center, 2007.
- [80] Ffowcs Williams, J. E. and Hawkings, D. L. “Sound generation by turbulence and surfaces in arbitrary motion”. In: *Philosophical Transactions of the Royal Society of London. Series A, Mathematical and Physical Sciences* 264.1151 (1969), pp. 321–342.
- [81] Friedmann, P. P. “On-blade control of rotor vibration, noise, and performance: Just around the corner?” In: *Journal of the American Helicopter Society* 59.4 (2014), pp. 1–37.
- [82] Gandhi, F., Frecker, M., and Nissly, A. “Design optimization of a controllable camber rotor airfoil”. In: *AIAA journal* 46.1 (2008), pp. 142–153.
- [83] Ganguli, R. “Optimum design of a helicopter rotor for low vibration using aeroelastic analysis and response surface methods”. In: *Journal of Sound and Vibration* 258.2 (2002), pp. 327–344.
- [84] Gessow, A. *Aerodynamics of the Helicopter*. New York, NY: Frederik Ungar Publishing Co., 1985.
- [85] Glaz, B., Friedmann, P. P., and Liu, L. “Surrogate Based Optimization of Helicopter Rotor Blades for Vibration Reduction in Forward Flight”. In: *Structural and Multidisciplinary Optimization* 35.4 (2008), pp. 341–363.

- [86] Glauert, H. "Airplane propellers". In: *Aerodynamic theory*. Ed. by H. H. Hubbard. Springer, 1935, pp. 169–360.
- [87] Gopalan, G. and Schmitz, F. "Far-field near-in-plane harmonic main rotor helicopter impulsive noise reduction possibilities". In: *American Helicopter Society 64th Annual Forum*. Montréal, Canada, May 2008.
- [88] Gopalan, G. and Schmitz, F. H. "Helicopter Thickness Noise Reduction Possibilities Through Active On-Blade Acoustic Control". In: *Journal of Aircraft* 47.1 (2010), pp. 41–52.
- [89] Greenberg, J. M. *Airfoil in sinusoidal motion in a pulsating stream*. Tech. rep. NACA TN 1326. Langley Memorial Aeronautical Lab, 1947.
- [90] Grohmann, B. et al. "Design, evaluation and test of active trailing edge". In: *American Helicopter Society 67th Annual Forum Proceedings*. Virginia Beach, VA, May 2011.
- [91] Guner, F., Prasad, J., He, C., and Peters, D. "Fidelity Enhancement of a Multicopter Dynamic Inflow Model via System Identification". In: *Journal of the American Helicopter Society* 67.2 (2022).
- [92] Hall, S. R., Anand, R. V., Straub, F. K., and Lau, B. H. "Active flap control of the SMART rotor for vibration reduction". In: *American Helicopter Society 65th annual forum and technology display*. Grapevine, TX, May 2009.
- [93] Hamers, M. and Basset, P.-M. "Application of the finite state unsteady wake model in helicopter flight dynamic simulation". In: (Sept. 2000).
- [94] Hammond, C. E. "Higher Harmonic Control: A Historical Perspective". In: *Journal of the American Helicopter Society* 66.2 (2021), pp. 1–14.
- [95] Ham, N. D. "Helicopter Stall Alleviation Using Individual-Blade Control". In: *10th European Rotorcraft Forum, Netherlands*. Aug. 1984.
- [96] Hariharan, N. and Leishman, J. G. "Unsteady aerodynamics of a flapped airfoil in subsonic flow by indicial concepts". In: *Journal of Aircraft* 33.5 (1996), pp. 855–868.
- [97] He, C. and Zhao, J. "Modeling rotor wake dynamics with viscous vortex particle method". In: *AIAA journal* 47.4 (2009), pp. 902–915.
- [98] He, C. and Rajmohan, N. "Modeling the aerodynamic interaction of multiple rotor vehicles and compound rotorcraft with viscous vortex particle method". In: *AHS International 72nd Annual Forum & Technology Display*. West Palm Beach, FL, May 2016.
- [99] He, C. "Development and Application of a Generalized Dynamic Wake Theory for Lifting Rotors". PhD thesis. Georgia Institute of Technology, July 1989.
- [100] Heller, H. "Into the physics of rotor aeroacoustics—highlights of recent European helicopter noise research". In: *Fifth international congress on sound and vibration*. Adelaide, Australia, 1997.
- [101] Hennes, C. C. and Brentner, K. S. "The effect of blade deformation on rotorcraft acoustics". In: *Journal of the American Helicopter Society* 53.4 (2008), pp. 398–411.
- [102] Hennes, C., Lopes, L., Shirey, J., Erwin, J., Goldman, B. A., and Brentner, K. S. "PSU-WOPWOP 3.4.3 User's Guide". In: *The Pennsylvania State University, University Park, PA* (2015).

- [103] Ho, J. C., Yeo, H., and Ormiston, R. A. “Investigation of Rotor Blade Structural Dynamics and Modeling Based on Measured Airloads”. In: *Journal of Aircraft* 45.5 (2008), pp. 1631–1642.
- [104] Ho, J. C. and Yeo, H. “Assessment of comprehensive analysis predictions of helicopter rotor blade loads in forward flight”. In: *Journal of Fluids and Structures* 68 (2017), pp. 194–223.
- [105] Ho, J. C. and Yeo, H. “Considerations in the Selection of Inflow States with Finite-State Dynamic Inflow”. In: *AIAA Journal* 59.7 (2021), pp. 2800–2805.
- [106] Ho, J. C. and Yeo, H. “Evaluation of Finite-State Dynamic Inflow for Rotors”. In: *Journal of Aircraft* 58.5 (2021), pp. 1068–1082.
- [107] Hodges, D. H. *Nonlinear composite beam theory*. Reston, Virginia: American Institute of Aeronautics and Astronautics, 2006.
- [108] Hodges, D. H. “Geometrically exact equations for beams”. In: *Encyclopedia of Continuum Mechanics* (2020), pp. 1042–1049.
- [109] Houghton, E. L., Carpenter, P. W., Collicott, S. H., and Valentine, D. T. *Aerodynamics for Engineering Students*. Sixth. Elsevier, 2013.
- [110] Isik, A. A. and Bilen, M. E. “Automated model based conceptual design approach for composite helicopter rotor blades”. In: (Sept. 2019).
- [111] Jacklin, S. A. et al. *Investigation of a Helicopter Individual Blade Control (IBC) System in Two Full-Scale Wind Tunnel Tests: Volume I*. Tech. rep. TP-20205003457 Vol I. NASA, July 2020.
- [112] Jacklin, S. A. et al. *Investigation of a Helicopter Individual Blade Control (IBC) System in Two Full-Scale Wind Tunnel Tests: Volume II—Tabulated Data*. Tech. rep. TP-20205003457 Vol II. NASA, July 2020.
- [113] Jacobellis, G., Singh, R., Johnson, C., Sirohi, J., and McDonald, R. “Experimental and computational investigation of stacked rotor performance in hover”. In: *Aerospace Science and Technology* 116 (2021).
- [114] Jacklin, S. A., Blaas, A., Teves, D., Kube, R., and Warmbrodt, W. “Reduction of Helicopter BVI noise, Vibration, and Power consumption through Individual Blade Control”. In: *AHS 51st Annual Forum and Technology Display*. Fort Worth, TX, May 1994.
- [115] Jacklin, S. A., Nguyen, K. Q., Blass, A., and Richter, P. “Full-Scale Wind Tunnel Test of a Helicopter Individual Blade Control System”. In: *50th Annual Forum of the American Helicopter Society*. Washington, DC, May 1994.
- [116] Jacklin, S. A., Blass, A., Swanson, S. M., and Teves, D. “Second Test of a Helicopter Individual Blade Control System in the NASA Ames 40- by 80-Foot Wind Tunnel”. In: *American Helicopter Society 2nd International Aeromechanics Specialists’ Conference, Bridgeport, CT*. Oct. 1995.
- [117] Jain, R., Yeo, H., and Chopra, I. “Computational Fluid Dynamics – Computational Structural Dynamics Analysis of Active Control of Helicopter Rotor for Performance Improvement”. In: *Journal of the American Helicopter Society* 55.4 (2010).
- [118] Jain, R., Yeo, H., and Chopra, I. “Examination of Rotor Loads Due to On-Blade Active Controls for Performance Enhancement”. In: *Journal of Aircraft* 47.6 (2010), pp. 2049–2066.

- [119] Jain, R., Yeo, H., and Chopra, I. “Investigation of Trailing-Edge Flap Gap Effects on Rotor Performance Using High Fidelity Analysis”. In: *Journal of Aircraft* 50.1 (2012), pp. 140–151.
- [120] Jayasundara, D., Jung, Y. S., and Baeder, J. “CFD and Aeroacoustic Analysis of Wingtip-Mounted Propellers”. In: *76th Annual Forum of the Vertical Flight Society*. Virtual, Oct. 2020.
- [121] Jia, Z. and Lee, S. “Aeroacoustic Analysis of a Side-by-Side Hybrid VTOL Aircraft”. In: *76th Annual Forum of the Vertical Flight Society*. Virtual, Oct. 2020.
- [122] Johnson, W. *Rotorcraft Aeromechanics*. New York, NY: Cambridge University Press, 2013.
- [123] Johnson, W. *CAMRAD II Manual Volume II: Components Theory*. Tech. rep. Release 4.10. Johnson Aeronautics, 2017.
- [124] Johnson, W. “Technology Drivers in the Development of CAMRAD II”. In: *American Helicopter Society Aeromechanics Specialists Conference*. San Francisco, CA, Jan. 1994.
- [125] Johnson, W. “A general free wake geometry calculation for wings and rotors”. In: *American Helicopter Society 51st Annual Forum*. Fort Worth, TX, May 1995.
- [126] Jones, H. E. and Kunz, D. L. “Comprehensive Modeling of the Apache with CAMRAD II”. In: *American Helicopter Society Structure Specialists’ Meeting*. Williamsburg, VA, 2001.
- [127] Jose, A. I., Leishman, J. G., and Baeder, J. D. “Unsteady Aerodynamic Modeling with Time-Varying Free-Stream Mach Numbers”. In: *Journal of the American Helicopter Society* 51.4 (2006), pp. 299–318.
- [128] Jose, A. I. *Investigation into the aerodynamics of washplateless rotors using CFD-CSD analysis*. 2012.
- [129] Jung, S. N., You, Y. H., Lau, B. H., Johnson, W., and Lim, J. W. “Evaluation of rotor structural and aerodynamic loads using measured blade properties”. In: *Journal of the American Helicopter Society* 58.4 (2013), pp. 1–12.
- [130] Jung, S. N., You, Y. H., Dhadwal, M. K., Hagerty, B. P., Riemenschneider, J., and Keimer, R. “Blade property measurement and its assessment on air/structural loads of HART II rotor”. In: *Proc. AHS Int. 70th Annual Forum & Technology Display*. Montréal, Canada, May 2014.
- [131] Karman, T. H. von and Sears, W. R. “Airfoil theory for non-uniform motion”. In: *Journal of the Aeronautical Sciences* 5.10 (1938), pp. 379–390.
- [132] Kessler, C. “Active Rotor Control for Helicopters: Individual Blade Control and Swashplateless Rotor Designs”. In: *CEAS Aeronautical Journal* 1 (2011), pp. 23–54.
- [133] Kessler, C. “Active Rotor Control for Helicopters: Motivation and Survey on Higher Harmonic Control”. In: *CEAS Aeronautical Journal* 1.1-4 (2011), pp. 3–22.
- [134] Kim, H. W., Duraisamy, K., and Brown, R. “Aeroacoustics of a coaxial rotor in level flight”. In: *64th American Helicopter Society Annual Forum*. Montréal, Canada, May 2008.
- [135] Kinzel, M. P., Maughmer, M. D., and Lesieutre, G. A. “Miniature Trailing-Edge Effectors for Rotorcraft Performance Enhancement”. In: *Journal of the American Helicopter Society* 52.2 (2007), pp. 146–158.
- [136] Kinzel, M. P., Maughmer, M. D., and N. Duque, E. P. “Numerical Investigation on the Aerodynamics of Oscillating Airfoils with Deployable Gurney Flaps”. In: vol. 48. 7. 2010, pp. 1457–1469.



- [137] King, F., Maurice, J.-B., Fichter, W., Dieterich, O., and Konstanzer, P. “In-flight rotorblade tracking control for helicopters using active trailing-edge flaps”. In: *Journal of Guidance, Control, and Dynamics* 37.2 (2014), pp. 633–643.
- [138] Kinner, W. “Die kreisförmige Tragfläche auf potentialtheoretischer Grundlage”. In: *Ingenieur-Archiv* 8.1 (1937), pp. 47–80.
- [139] Kirchhart, M. “Vortex Particle Redistribution and Regularisation”. PhD thesis. Keio University, Aug. 2017.
- [140] Komp, D., Kumar, S., Abdelmoula, A., Hajek, M., and Rauleder, J. “Investigation of Active Rotor Design and Control for Performance Improvement”. In: *Vertical Flight Society 75th Annual Forum*. Philadelphia, PA, 2019.
- [141] Komp, D., Kumar, S., Hajek, M., and Rauleder, J. “Effect of Active Camber Morphing on Rotor Performance and Control Loads”. In: *Aerospace Science and Technology* (2020).
- [142] Kong, Y.-B., Prasad, J., and He, C. “Finite State Coaxial Rotor Inflow Model Enhancements Using VVPM-Extracted Influence Coefficients”. In: *Journal of the American Helicopter Society* 65.2 (2020), pp. 1–17.
- [143] Kong, Y.-B., Prasad, J., Sankar, L. N., and He, C. “Finite state inflow flow model for coaxial rotor configuration”. In: *Journal of the American Helicopter Society* 65.3 (2020).
- [144] Kottapalli, S., Hagerty, B., and Salazar, D. *Boeing SMART rotor full-scale wind tunnel test data report*. Tech. rep. TM—2016–216048. NASA Ames Research Center, 2016.
- [145] Kottapalli, S., Swanson, S., LeMasurier, P., and Wang, J. “Full-scale higher harmonic control research to reduce hub loads and noise”. In: *49th Annual Forum of the American Helicopter Society*. St. Louis, MI, May 1993.
- [146] Kottapalli, S. “Enhanced correlation of smart active flap rotor loads”. In: *52nd AIAA/ASME/ASCE/AHS/ASC Structures, Structural Dynamics and Materials Conference*. Denver, CO, Apr. 2011.
- [147] Kretz, M., Aubrun, J., and Larche, M. “Wind tunnel tests of the Dorand DH 2011 jet flap rotor Vol. I”. In: *NASA CR-114693* (1973).
- [148] Krzysiak, A. and Narkiewicz, J. “Aerodynamic loads on airfoil with trailing-edge flap pitching with different frequencies”. In: *Journal of aircraft* 43.2 (2006), pp. 407–418.
- [149] Kuik, G. v. *The Fluid Dynamic Basis for Actuator Disc and Rotor Theories*. Amsterdam, The Netherlands: IOS Press, 2018.
- [150] Kumar, D., Glaz, B., Mok, J., Friedmann, P. P., and Cesnik, C. E. S. “Determination of optimum camber distribution in rotating wings with deformable airfoils for vibration reduction and performance enhancement using surrogate modeling”. In: *36th European Rotorcraft Forum, France*. 2010.
- [151] Kumar, D. and Cesnik, C. E. “New optimization strategy for design of active twist rotor”. In: *AIAA journal* 53.2 (2015), pp. 436–448.
- [152] Kumar, S., Komp, D., Hajek, M., and Rauleder, J. “Integrated Rotor Performance Improvement and Vibration Reduction Using Active Camber Morphing”. In: *ASME Conference on Smart Materials, Adaptive Structures and Intelligent Systems*. Louisville, KY, Sept. 2019.

- [153] Kumar, S., Komp, D., Hajek, M., and Rauleder, J. “Effect of Active Camber on Rotor Noise, Power and Hub Vibration”. In: *AIAA Scitech 2021 Forum*. Virtual Event, Jan. 2021.
- [154] Kumar, S., Rauleder, J., and Yavrucuk, I. “Towards Active Rotor Analysis using Viscous Vortex Particle Method”. In: *European Rotorcraft Forum*. Bueckeburg, Germany, 2023.
- [155] Kunz, D. “Comprehensive Rotorcraft Analysis: Past, present, and future”. In: *46th AIAA/ASME/ASCE/AHS/ASC Structures, Structural Dynamics and Materials Conference*. Austin, Texas, Apr. 2005.
- [156] Küssner, H. and Schwartz, I. *The oscillating wing with aerodynamically balanced elevator*. Tech. rep. NACA TM 991. National Advisory Committee for Aeronautics, 1941.
- [157] Leconte, P., Rapin, M., and Wall, B. G. van der. “Main rotor active flaps: Numerical assessment of vibration reduction”. In: *57th Annual Forum & Technology Display of the Vertical Flight Society*. Washington, DC, May 2001.
- [158] Lee, S., Brentner, K. S., Farassat, F., and Morris, P. J. “Analytic formulation and numerical implementation of an acoustic pressure gradient prediction”. In: *Journal of Sound and Vibration* 319.3-5 (2009), pp. 1200–1221.
- [159] Lee, H.-K., Viswamurthy, S., Park, S. C., Kim, T., Shin, S. J., and Kim, D.-K. “Helicopter rotor load prediction using a geometrically exact beam with multicomponent Model”. In: *Journal of aircraft* 47.4 (2010), pp. 1382–1390.
- [160] Lee, D. J. and Na, S. U. “High Resolution Free Vortex Blob Method for Highly Distorted Vortex Wake Generated from a Slowly Starting Rotor Blade in Hover”. In: *21st European Rotorcraft Forum*. St. Petersburg, Russia, 1995.
- [161] Leishman, G. J. *Principles of helicopter aerodynamics*. New York, NY: Cambridge university press, 2006.
- [162] Li, S. K. and Lee, S. “Prediction of rotorcraft broadband trailing-edge noise and parameter sensitivity study”. In: *Journal of the American Helicopter Society* 65.4 (2020), pp. 1–14.
- [163] Lim, J. and Strawn, R. “Prediction of HART II rotor BVI loading and wake system using CFD/CSD loose coupling”. In: *45th AIAA Aerospace Sciences Meeting and Exhibit*. Jan. 2007.
- [164] Lim, J. W. et al. “Aeromechanical evaluation of smart-twisting active rotor”. In: *40th European Rotorcraft Forum*. Southampton, UK, Sept. 2014.
- [165] Lim, J. W. *Summary of NACA 23012 mod Application to HART II Blade*. Tech. rep. AFDD, USA, July 2001.
- [166] Lim, J. W. “Improved Performance Prediction for Bo105 Model Rotor in Cruise using Computational Fluid Dynamics”. In: *37th European Rotorcraft Forum*. Italy, Sept. 2011.
- [167] Liu, L., Friedmann, P. P., Kim, I., and Bernstein, D. S. “Rotor Performance Enhancement and Vibration Reduction in Presence of Dynamic Stall Using Actively Controlled Flaps”. In: *Journal of the American Helicopter Society* 53.4 (2008), pp. 338–350.
- [168] Liu, L., Padthe, A. K., and Friedmann, P. P. “Computational Study of Microflaps with Application to Vibration Reduction in Helicopter Rotors”. In: *AIAA journal* 49.7 (2011), pp. 1450–1465.
- [169] Liu, L., Padthe, A. K., Friedmann, P. P., Quon, E., and Smith, M. J. “Unsteady aerodynamics of an airfoil/flap combination on a helicopter rotor using computational fluid dynamics and approximate methods”. In: *Journal of the American Helicopter Society* 56.3 (2011).

- [170] Lorber, P. F., Bagai, A., and Wake, B. E. "Design and Evaluation of Slatted Airfoils for Improved Rotor Performance". In: *62nd Annual Forum and Technology Display of the American Helicopter Society International*, Phoenix, AZ. May 2006.
- [171] Lorber, P., Hein, B., Wong, J., and Wake, B. "Rotor aeromechanics results from the Sikorsky active flap demonstration rotor". In: *American Helicopter Society 68th Annual Forum*. Fort Worth, TX, May 2012.
- [172] Maier, T. H., Sharpe, D. L., and Lim, J. W. "Fundamental investigation of hingeless rotor aeroelastic stability, test data and correlation". In: *American Helicopter Society 51st Annual Forum*. Fort Worth, TX, May 1995.
- [173] Mangler, K. and Squire, H. B. *The induced velocity field of a rotor*. Tech. rep. R& M No. 2642. Aeronautical Research Council, 1950.
- [174] Marchevsky, I., Ryatina, E., and Kolganova, A. "Fast Barnes–Hut-based algorithm in 2D vortex method of computational hydrodynamics". In: *Computers & Fluids* 266 (2023), p. 106018.
- [175] Matalanis, C. G., Wake, B. E., Opoku, D., Min, B.-Y., Yeshala, N., and Sankar, L. "Aerodynamic Evaluation of Miniature Trailing-Edge Effectors for Active Rotor Control". In: *Journal of Aircraft* 48.3 (2011), pp. 995–1004.
- [176] Maurice, J.-B., King, F., Fichter, W., Rabourdin, A., and Konstanzer, P. "Helicopter rotor in-plane stability enhancement using trailing-edge flaps". In: *Journal of Guidance, Control, and Dynamics* 36.5 (2013), pp. 1477–1489.
- [177] McColl, C., Palmer, D., Chierichetti, M., Bauchau, O., and Ruzzene, M. "Comprehensive UH-60 loads model validation". In: *American Helicopter Society 66th Annual Forum*. Phoenix, Arizona, May 2010.
- [178] McCloud III, J. L. and Kretz, M. "Multicyclic Jet-Flap Control for Alleviation of Helicopter Blade Stresses and Fuselage Vibration". In: *Proceedings of the AHS/NASA-Ames Specialist's Meeting on Rotorcraft Dynamics*. Feb. 1974.
- [179] Mccloud III, J. L. and Weisbrich, A. L. "Wind-tunnel test results of a full-scale multicyclic controllable twist rotor". In: *American Helicopter Society 34th Annual Forum*. Washington D.C., May 1978.
- [180] Miao, W., Kottapalli, S., and Frye, H. "Flight demonstration of higher harmonic control (HHC) on S-76". In: *42nd Annual Forum of the American Helicopter Society*. Washington, DC, June 1986.
- [181] Milgram, J. and Chopra, I. "A Parametric Design study for actively controlled trailing edge flaps". In: *Journal of the American Helicopter Society* 43.2 (1998), pp. 110–119.
- [182] Miller, R. "Rotor hovering performance using the method of fast free wake analysis". In: *Journal of Aircraft* 20.3 (1983), pp. 257–261.
- [183] Min, B.-Y., Sankar, L. N., Rajmohan, N., and Prasad, J. "Computational investigation of Gurney flap effects on rotors in forward flight". In: *Journal of Aircraft* 46.6 (2009), pp. 1957–1964.
- [184] Morillo, J. A., Singh, R., and Wasikowski, M. "Model Development and Integration of DYMORE at Bell Helicopter". In: *64th Annual Forum of the American Helicopter Society*. Montréal, Canada, Apr. 2008.

- [185] Morse, P. M. and Feshbach, H. *Methods of theoretical physics: Part I*. McGraw-Hill Book Company, 1953.
- [186] Murakami, Y. “A new appreciation of inflow modelling for autorotative rotors”. PhD thesis. University of Glasgow, Oct. 2008.
- [187] Myrtle, T. and Friedmann, P. “Unsteady compressible aerodynamics of a flapped airfoil with application to helicopter vibration reduction”. In: *38th Structures, Structural Dynamics, and Materials Conference*. Kissimmee, FL, Apr. 1997, pp. 224–240.
- [188] Nguyen, K., Betzina, M., and Kitaplioglu, C. “Full-Scale Demonstration of Higher Harmonic Control for Noise and Vibration Reduction on the XV-15 Rotor”. In: *Journal of the American Helicopter Society* 46.3 (2001), pp. 182–191.
- [189] Nguyen, K. “Active Control of Helicopter Blade Stall”. In: *Journal of Aircraft* 35.1 (1998), pp. 91–98.
- [190] Norman, T. R., Theodore, C., Shinoda, P., Fuerst, D., Arnold, U. T., Makinen, S., Lorber, P., and O’Neill, J. “Full-scale wind tunnel test of a UH-60 individual blade control system for performance improvement and vibration, loads, and noise control”. In: *American Helicopter Society 65th Annual Forum*. Grapevine, TX, May 2009.
- [191] Opoku, D. G., Triantos, D. G., Nitzsche, F., and Voutsinas, S. G. “Rotorcraft Aerodynamic and Aeroacoustic Modelling using Vortex Particle Methods”. In: *23rd Congress of International Council of the Aeronautical Sciences*. Toronto, Canada, Sept. 2002.
- [192] Padthe, A. K., Friedmann, P. P., Chia, M. H., and Liu, L. “Comprehensive Numerical Assessment of Rotorcraft Vibration and Noise Control Using Microflaps”. In: *Journal of Aircraft* 53.4 (2016), pp. 1113–1130.
- [193] Palacios, J., Kinzel, M., Overmeyer, A., and Szefi, J. “Active Gurney Flaps: Their Application in a Rotor Blade Centrifugal Field”. In: *Journal of Aircraft* 51.2 (2014), pp. 473–489.
- [194] Park, J.-S., Jung, S. N., Park, S. H., and Yu, Y. H. “Correlation study of a rotor in descending flight using DYMORE with a freewake model”. In: *Journal of mechanical science and technology* 24 (2010), pp. 1583–1594.
- [195] Park, J.-S. and Jung, S. “Comprehensive multibody dynamics analysis for rotor aeromechanics predictions in descending flight”. In: *The Aeronautical Journal* 116.1177 (2012), pp. 229–249.
- [196] Park, J.-S., Sa, J.-H., Park, S.-H., You, Y.-H., and Jung, S. N. “Loosely coupled multibody dynamics–CFD analysis for a rotor in descending flight”. In: *Aerospace Science and Technology* 29.1 (2013), pp. 262–276.
- [197] Patil, M. and Datta, A. “A scalable time-parallel solution of periodic rotor dynamics in X3D”. In: *Journal of the American Helicopter Society* 66.4 (2021).
- [198] Patil, M., Lumba, R., Jayaraman, B., and Datta, A. “An Integrated Three-Dimensional Aeromechanical Analysis for the Prediction of Stresses on Lift Offset Coaxial Rotors”. In: *49th European Rotorcraft Forum*. Bückeburg, Germany, Sept. 2023.
- [199] Perez, G., Brentner, K. S., Bres, G. A., and Jones, H. E. “A first step toward the prediction of rotorcraft maneuver noise”. In: *Journal of the American Helicopter Society* 50.3 (2005), pp. 230–237.

- [200] Perry III, B. *Re-Computation of Numerical Results Contained in NACA Report No. 496*. Tech. rep. 2015.
- [201] Peters, D. A., Hsieh, M.-c. A., and Torrero, A. “A State-Space Airloads Theory for Flexible Airfoils”. In: *Journal of the American Helicopter Society* 52.4 (2007), pp. 329–342.
- [202] Peters, D. A. and He, C. J. “Finite state induced flow models. II-Three-dimensional rotor disk”. In: *Journal of Aircraft* 32.2 (1995), pp. 323–333.
- [203] Peters, D. A., Barwey, D., et al. “A general theory of rotorcraft trim”. In: *Mathematical Problems in Engineering* 2 (1996), pp. 1–34.
- [204] Peters, D. A. “Two-dimensional incompressible unsteady airfoil theory—An overview”. In: *Journal of Fluids and Structures* 24.3 (2008), pp. 295–312.
- [205] Peters, D. A. “How dynamic inflow survives in the competitive world of rotorcraft aerodynamics”. In: *Journal of the American Helicopter Society* 54.1 (2009).
- [206] Pflumm, T., Garre, W., and Hajek, M. “A Preprocessor for Parametric Composite Rotor Blade Cross-Sections”. In: *44th European Rotocraft Forum*. Delft, The Netherlands, Sept. 2018.
- [207] Platzer, S. “Aerodynamic Influences of Non-Parallel Ground Effect, Rotor-Rotor Interference, and Dynamic Actuation on Rotors in Hover”. PhD thesis. Technische Universität München, 2021.
- [208] Potsdam, M., Yeo, H., and Johnson, W. “Rotor airloads prediction using loose aerodynamic/structural coupling”. In: *Journal of Aircraft* 43.3 (2006), pp. 732–742.
- [209] Potsdam, M., Fulton, M. V., and Dimanlig, A. “Multidisciplinary CFD/CSD analysis of the smart active flap rotor”. In: *American Helicopter Society 66th Annual Forum*. Phoenix, AZ, May 2010.
- [210] Potsdam, M., Fulton, M. V., Yeo, H., Ormiston, R., Sim, B., and Dimanlig, A. “Advancing State-of-the-Art Unsteady, Multidisciplinary Rotorcraft Simulations”. In: *DoD High Performance Computing Modernization Program Users Group Conference*. IEEE. 2010, pp. 115–122.
- [211] Quackenbush, T., Wachspress, D., Moretti, L. R., Barwey, D., Lewis, R. H., and Brentner, K. “Aeroacoustic modeling of an eVTOL slowed rotor winged compound aircraft”. In: *Vertical Flight Society’s 75th Annual Forum and Technology Display*. Philadelphia, PA, May 2019.
- [212] Rabourdin, A., Maurice, J., Dieterich, O., and Konstanzer, P. “Blue Pulse active rotor control at Airbus Helicopters—New EC145 demonstrator and flight test results”. In: *American Helicopter Society 70th Annual Forum*. Montréal, Canada, May 2014.
- [213] Rajmohan, N., Manivannan, V., Sankar, L., Costello, M., and Bauchau, O. “Development of a methodology for coupling rotorcraft aeromechanics and vehicle dynamics to study helicopters in maneuvering flight”. In: *AHS 65th Annual Forum*. Grapevine, TX, May 2009.
- [214] Rath, T. and Fichter, W. “A closer look at the impact of helicopter vibrations on ride quality”. In: *73rd Annual Forum of the American Helicopter Society*. Fort Worth, TX, USA, May 2017.
- [215] Rauch, P., Gervais, M., Cranga, P., Baud, A., Hirsch, J., Walter, A., and Beaumier, P. “Blue edge: The design, development and testing of a new blade concept”. In: *67th Annual Forum of the American Helicopter Society*. Virginia Beach, VA, May 2011.

- [216] Rauleder, J., Wall, B. G. van der, Abdelmoula, A., Komp, D., Kumar, S., Ondra, V., Titurus, B., and Woods, B. K. S. "Aerodynamic Performance of Morphing Blades and Rotor Systems". In: *74th Annual Forum of the American Helicopter Society, Phoenix, AZ*. May 2018.
- [217] Ravichandran, K., Chopra, I., Wake, B. E., and Hein, B. "Trailing-Edge Flaps for Rotor Performance Enhancement and Vibration Reduction". In: *Journal of the American Helicopter Society* 58.2 (Apr. 2013).
- [218] Ravichandran, K. and Chopra, I. "Open-Loop Control of Performance and Vibratory Loads Using Leading-Edge Slats". In: *Journal of the American Helicopter Society* 61.3 (2016), pp. 1–9.
- [219] Rex, W., Pflumm, T., and Hajek, M. "UH-60A Rotor and Coupled Rotor-Fuselage Simulation Framework Validation and Analysis". In: *45th European Rotorcraft Forum, Poland*. Sept. 2019.
- [220] Richter, P. and Blass, A. "Full Scale Wind tunnel Investigation of an Individual Blade Control System for the BO 105 Hingeless Rotor". In: *19th European Rotorcraft Forum, Italy*. Sept. 1993.
- [221] Rivero, A. E., Fournier, S., Manolesos, M., Cooper, J. E., and Woods, B. "Wind Tunnel Comparison of Flapped and FishBAC Camber Variation for Lift Control". In: *AIAA SciTech Forum, Orlando, FL*. Jan. 2020.
- [222] Roark, S. H. "Comparison of free vortex wake models for a sub-scale rotor at low speeds". MA thesis. 2007.
- [223] Robinson, A. and Laurmann, J. A. *Wing Theory*. Cambridge University Press, 2013.
- [224] Roget, B. and Chopra, I. "Individual blade control methodology for a rotor with dissimilar blades". In: *Journal of the American Helicopter Society* 48.3 (2003), pp. 176–185.
- [225] Roget, B. "Simulation of active twist and active flap control on a model-scale helicopter rotor". In: *24th AIAA Applied Aerodynamics Conference*. San Francisco, CA, 2006.
- [226] Roth, D., Dieterich, O., Bebesel, M., Pongratz, R., Kube, R., and Munser, H. "Individual blade root control demonstration: Recent activities". In: (Sept. 2001).
- [227] Roth, D., Enenkl, B., and Dieterich, O. "Active rotor control by flaps for vibration reduction-full scale demonstrator and first flight test results". In: (Sept. 2006).
- [228] Roth, D. "Advanced Vibration Reduction by IBC Technology". In: *30th European Rotorcraft Forum*. Marseilles, France, Sept. 2004.
- [229] Saetti, U., Horn, J., Brentner, K., Villafana, W., and Wachspress, D. "Rotorcraft Simulations with Coupled Flight Dynamics, Free Wake, and Acoustics". In: *Vertical Flight Society's 75th Annual Forum and Technology Display*. Philadelphia, PA, May 2019.
- [230] Schmaus, J. H. "Aeromechanics of a High Speed Coaxial Helicopter Rotor". PhD thesis. University of Maryland, 2017.
- [231] Schmitz, F. H. "Rotor Noise". In: *Aeroacoustics of Flight Vehicles, Theory and Practice, Vol. 1: Noise Sources*. Ed. by H. H. Hubbard. NASA TR 90-3052, Aug. 1991. Chap. 2.
- [232] Schmitz, F. H. "Reduction of Blade-Vortex Interaction (BVI) Noise through X-Force Control". In: *Journal of the American Helicopter Society* 43.1 (1998), pp. 14–24.

- [233] Sekula, M. K., Wilbur, M. L., and Yeager Jr, W. T. “Aerodynamic design study of an advanced active twist rotor”. In: *American Helicopter Society 4th Decennial Specialist’s Conference on Aeromechanics, San Francisco, CA*. Jan. 2003.
- [234] Sekula, M. K. and Wilbur, M. L. “Optimization of an Active Twist Rotor Blade Planform for Improved Active Response and Forward Flight Performance”. In: *Journal of the American Helicopter Society* 62.3 (2017), pp. 1–12.
- [235] Sengupta, T. K. *Theoretical and Computational Aerodynamics*. John Wiley & Sons, 2015.
- [236] Sharma, K., Corle, E., Brentner, K. S., and Anusonti-Inthra, P. “Robust and automated coupling of RCAS and PSU-WOPWOP”. In: *AHS International Technical Meeting on Aeromechanics Design for Transformative Vertical Flight*. San Francisco, CA, Jan. 2018.
- [237] Shaw, J. and Albion, N. “Active control of the helicopter rotor for vibration reduction”. In: *Journal of the American Helicopter Society* 26.3 (1981), pp. 32–39.
- [238] Shaw, J., Albion, N., Hanker, E. J., and Teal, R. S. “Higher harmonic control: Wind tunnel demonstration of fully effective vibratory hub force suppression”. In: *Journal of the American Helicopter Society* 34.1 (1989), pp. 14–25.
- [239] Shen, J., Roget, B., Masarati, P., Piatak, D., Singleton, J., and Nixon, M. “Modeling a stiff-inplane tiltrotor using two multibody analyses: a validation study”. In: *64th Annual Forum of the American Helicopter Society*. Montréal, Canada, Apr. 2008.
- [240] Shen, J., Liu, Y., Thornburgh, R. P., Kreshock, A. R., and Wilbur, M. L. “Design and optimisation of an aerofoil with active continuous trailing-edge flap”. In: *The Aeronautical Journal* 120.1231 (2016), pp. 1468–1486.
- [241] Sheen, G., Yin, M., Wang, X., and Baoyin, H. “Aerodynamic interference and unsteady loads for a hovering intermeshing rotor”. In: *Physics of Fluids* 34.6 (2022).
- [242] Shin, S.-J. and Cesnik, C. “Forward flight response of the active twist rotor for helicopter vibration reduction”. In: *AIAA/ASME/AHS Adaptive Structures Forum*. Seattle, Washington, 2001.
- [243] Shin, S. and Cesnik, C. “Helicopter vibration reduction in forward flight using blade integral twist control”. In: *43rd AIAA/ASME/ASCE/AHS/ASC Structures, Structural Dynamics, and Materials Conference*. Denver, CO, 2002.
- [244] Shinoda, P. M., Norman, T. R., Jacklin, S. A., Yeo, H., Bernhard, A., and Haber, A. “Investigation of a full-scale wide chord blade rotor system in the NASA Ames 40-by 80-foot wind tunnel”. In: *American Helicopter Society 4th Decennial Specialist’s Conference on Aeromechanics*. San Francisco, CA, 2004.
- [245] Shirey, J., Brentner, K., and Chen, H.-n. “A Validation Study of the PSU-WOPWOP Rotor Noise Prediction Code”. In: *45th AIAA Aerospace Sciences Meeting and Exhibit*. Reno, NV, Jan. 2007.
- [246] Sim, B. W., Potsdam, M. A., Conner, D. A., and Watts, M. E. “Direct CFD predictions of low frequency sounds generated by a helicopter main rotor”. In: *American Helicopter Society 66th Annual Forum*. Phoenix, AZ, May 2010.
- [247] Sim, B. W., Potsdam, M., Kitaplioglu, C., LeMasurier, P., Lorber, P., and Andrews, J. “Localized, non-harmonic active flap motions for low frequency in-plane rotor noise reduction”. In: *American Helicopter Society 68th Annual Forum*. Fort Worth, TX, May 2012.

- [248] Sim, B. W., JanakiRam, R. D., and Lau, B. H. “Reduced In-Plane, Low-Frequency Noise of an Active Flap Rotor”. In: *Journal of the American Helicopter Society* 59.2 (2014).
- [249] Sim, B. “Suppressing in-plane, low frequency helicopter harmonic noise with active controls”. In: *American Helicopter Society San Francisco Bay Area Chapter’s Aeromechanics Specialist’s Meeting*. Fisherman’s Wharf, CA, 2008.
- [250] Singh, P. and Friedmann, P. P. “A Computational Fluid Dynamics–Based Viscous Vortex Particle Method for Coaxial Rotor Interaction Calculations in Hover”. In: *Journal of the American Helicopter Society* 63.4 (2018), pp. 1–13.
- [251] Singh, P. and Friedmann, P. P. “Application of vortex methods to coaxial rotor wake and load calculations in hover”. In: *Journal of Aircraft* 55.1 (2018), pp. 373–381.
- [252] Singh, P. and Friedmann, P. P. “Dynamic stall modeling using viscous vortex particle method for coaxial rotors”. In: *Journal of the American Helicopter Society* 66.1 (2021), pp. 1–16.
- [253] Singh, P. “Aeromechanics of Coaxial Rotor Helicopters using the Viscous Vortex Particle Method”. PhD thesis. University of Michigan, Oct. 2020.
- [254] Singh, P. “Aeromechanics of Coaxial Rotor Helicopters using the Viscous Vortex Particle Method”. PhD thesis. University of Michigan, Oct. 2020.
- [255] Skladanek, Y., Hocquette, J., and Cranga, P. “H160 Dynamics Development: Setting New Standards”. In: *American Helicopter Society 75th Forum*. Philadelphia, USA, May 2019.
- [256] Smith, M. J. et al. “An assessment of CFD/CSD prediction state-of-the-art using the HART II international workshop data”. In: *68th Annual Forum of the American Helicopter Society, Ft. Worth, TX*. 2012.
- [257] Smith, M. J. et al. “The HART II international workshop: An assessment of the state of the art in CFD/CSD prediction”. In: *CEAS Aeronautical Journal* 4 (2013), pp. 345–372.
- [258] Stacey, S., Connolly, N., Court, P., Allen, J., Monteggia, C., and Oliveros, J. M. “Leonardo Helicopters Active Rotor programmes to improve helicopter comfort & performance”. In: *AHS International 74th Annual Forum and Technology Display*. Phoenix, AZ, May 2018.
- [259] Staley, J. A. *Validation of rotorcraft flight simulation program through correlation with flight data for soft-in-plane hingeless rotors*. Tech. rep. USAAMRDL-TR-75-50. US Army Air Mobility Research and Development Laboratory, 1976.
- [260] Su, A. “Application of a state-space wake model to elastic blade flapping in hover”. In: (Aug. 1989).
- [261] Sullivan, B. M., Edwards, B. D., Brentner, K. S., and Booth, E. R. “A subjective test of modulated blade spacing for helicopter main rotors”. In: *Journal of the American Helicopter Society* 50.1 (2005), pp. 26–32.
- [262] Teves, D. and Klöppel, V. “Development of active control technology in the rotating system”. In: (Sept. 1992).
- [263] Theodorsen, T. *General theory of aerodynamic instability and the mechanism of flutter*. Tech. rep. NACA Report No. 496. Langley Memorial Aeronautical Lab, 1940.
- [264] Thornburgh, R. P., Kreshock, A. R., Wilbur, M. L., Sekula, M. K., and Shen, J. “Continuous trailing-edge flaps for primary flight control of a helicopter main rotor”. In: *American Helicopter Society 70th Annual Forum*. Montréal, Canada, May 2014.



- [265] Torok, M. S. and Goodman, R. K. “Analysis of Rotor Blade Dynamics Using Model Scale UH-60A Airloads”. In: *Journal of the American Helicopter Society* 39.1 (1994), pp. 63–69.
- [266] Truong, K.-V., Yeo, H., and Ormiston, R. A. “Structural dynamics modeling of rectangular rotor blades”. In: *Aerospace Science and Technology* 30.1 (2013), pp. 293–305.
- [267] Tugnoli, M., Montagnani, D., Syal, M., Droandi, G., and Zanotti, A. “Mid-fidelity approach to aerodynamic simulations of unconventional VTOL aircraft configurations”. In: *Aerospace Science and Technology* 115 (2021).
- [268] Uehara, D., Sirohi, J., Feil, R., and Rauleder, J. “Blade passage loads and deformation of a coaxial rotor system in hover”. In: *Journal of Aircraft* 56.6 (2019), pp. 2144–2157.
- [269] Uehara, D., Sirohi, J., and Bhagwat, M. J. “Hover Performance of Corotating and Counter-rotating Coaxial Rotors”. In: *Journal of the American Helicopter Society* 65.1 (2020).
- [270] Valentin, J., Moretti, R., and Bernardos, L. “Development of an Aerodynamic Simulation Technique Based on the Vortex Particle Method”. In: *PEGASUS Conference*. Pise, Italy, Apr. 2022.
- [271] Valentin, J. and Bernardos, L. “Validation of a new solver based on the vortex particle method for wings, propellers and rotors”. In: *European Rotorcraft Forum*. Bueckeburg, Germany, Sept. 2023.
- [272] Van Zante, D., Nark, D., and Fernandez, H. “Propulsion Noise Reduction Research in the NASA Advanced Air Transport Technology Project”. In: *International Society of Air Breathing Engines*. Manchester, UK, Sept. 2017.
- [273] Wachspress, D. A., Quackenbush, T. R., and Boschitsch, A. H. “Rotorcraft interactional aerodynamics with fast vortex/fast panel methods”. In: *Journal of the American Helicopter Society* 48.4 (2003), pp. 223–235.
- [274] Wachspress, D. A., Michael, K. Y., and Brentner, K. S. “Rotor/airframe aeroacoustic prediction for EVTOL UAM aircraft”. In: *Vertical Flight Society's 75th Annual Forum and Technology Display*. Philadelphia, PA, May 2019.
- [275] Wall, B. G. van der, Kessler, C., Delrieux, Y., Beaumier, P., Gervais, M., Hirsch, J., Pengel, K., and Crozier, P. “From ERATO Basic Research to the Blue Edge™ Rotor Blade”. In: *American Helicopter Society 72nd Annual Forum, West Palm Beach, Florida*. 2016.
- [276] Wall, B. G. van der. *2nd HHC aeroacoustic rotor test (HART II)-Part I: Test Documentation*. Tech. rep. IB 111-2003/31. German Aerospace Center (DLR), 2003.
- [277] Wall, B. G. van der. *SABRE Deliverable D1.1: Selection of the Baseline Rotor*. Tech. rep. Project No: 723491. DLR Institute of Flight Systems, 2017.
- [278] Warmbrodt, W. and Peterson, R. L. *Hover Performance and Dynamics of a Full-Scale Hingeless Rotor*. Tech. rep. TM 85990. NASA, Aug. 1984.
- [279] Weiss, F. and Kessler, C. “Drivetrain influence on the lead-lag modes of hingeless helicopter rotors”. In: *CEAS Aeronautical Journal* 11 (2020), pp. 67–79.
- [280] Weiss, F. and Kessler, C. “Load prediction of hingeless helicopter rotors including drivetrain dynamics”. In: *CEAS Aeronautical Journal* 12 (2021), pp. 215–231.
- [281] Weiland, E. F. “Development and Test of the BO 105 Rigid Rotor Helicopter”. In: *Journal of the American Helicopter Society* 14.1 (1969), pp. 22–37.

- [282] Wheatley, J. B. *An aerodynamic analysis of the autogiro rotor with a comparison between calculated and experimental results*. Tech. rep. 487. NACA, 1934.
- [283] Wilbur, M. L., Yeager Jr, W. T., Wilkie, W. K., Cesnik, C. E., and Shin, S. “Hover testing of the NASA/ARMY/MIT active twist rotor prototype blade”. In: *American Helicopter Society 56th Annual Forum*. Virginia Beach, VA, May 2000.
- [284] Wilbur, M. L., Mirick, P. H., Yeager, W. T., Langston, C. W., Cesnik, C. E., and Shin, S. “Vibratory Loads Reduction Testing of the NASA/Army/MIT Active Twist Rotor”. In: *Journal of the American Helicopter Society* 47.2 (2002), pp. 123–133.
- [285] Winckelmans, G. and Leonard, A. “Contributions to vortex particle methods for the computation of three-dimensional incompressible unsteady flows”. In: *Journal of Computational Physics* 109.2 (1993), pp. 247–273.
- [286] Winckelmans, G. S. “Topics in vortex methods for the computation of three- and two-dimensional incompressible unsteady flows”. PhD thesis. California Institute of Technology, Feb. 1989.
- [287] Woods, B. K. S. and Friswell, M. I. “Preliminary investigation of a fishbone active camber concept”. In: *Smart Materials, Adaptive Structures and Intelligent Systems*. Vol. 45103. 2012, pp. 555–563.
- [288] Woods, B. K., Bilgen, O., and Friswell, M. I. “Wind Tunnel Testing of the Fish Bone Active Camber Morphing Concept”. In: *Journal of Intelligent Material Systems and Structures* 25.7 (2014).
- [289] Woods, B. K., Dayyani, I., and Friswell, M. I. “Fluid/structure-interaction analysis of the fish-bone-active-camber morphing concept”. In: *Journal of Aircraft* 52.1 (2015), pp. 307–319.
- [290] Wood, E. R., Powers, R. W., Cline, J. H., and Hammond, C. E. “On developing and flight testing a higher harmonic control system”. In: *Journal of the American Helicopter Society* 30.1 (1985), pp. 3–20.
- [291] Yang, C. and Aoyama, T. “Effect of computation parameters on BVI noise prediction using HART II motion data”. In: *34th European Rotorcraft Forum*. Liverpool, UK, Sept. 2008.
- [292] Yang, T., Brentner, K. S., Corle, E., and Schmitz, S. “Study of Active Rotor Control for In-Plane Rotor Noise Reduction”. In: *Journal of Aircraft* 56.1 (2019), pp. 179–190.
- [293] Yeo, H. and Lim, J. W. “Application of a slotted airfoil for UH-60A helicopter performance”. In: *AHS Aerodynamics, Acoustics and Test and Evaluation Technical Specialist Meeting*. San Francisco, CA, 2002.
- [294] Yeo, H., Romander, E. A., and Norman, T. R. “Investigation of Rotor Performance and Loads of a UH-60A Individual Blade Control System”. In: *Journal of the American Helicopter Society* 56.4 (2011), pp. 1–18.
- [295] Yeo, H. and Potsdam, M. “Rotor structural loads analysis using coupled computational fluid dynamics/computational structural dynamics”. In: *Journal of Aircraft* 53.1 (2016), pp. 87–105.
- [296] Yeo, H. “Assessment of Active Controls for Rotor Performance Enhancement”. In: *Journal of the American Helicopter Society* 53.2 (2008).

- [297] Yeo, H. “UH-60A rotor structural loads analysis with fixed system structural dynamics modeling”. In: *Journal of Aircraft* 56.2 (2019), pp. 669–684.
- [298] Yin, J., Wall, B. G. van der, and Wilke, G. A. “Investigation of a simplified aerodynamic modelling technique for noise predictions using FW–H propagation”. In: *CEAS Aeronautical Journal* 7 (2016), pp. 551–566.
- [299] Yokota, R. and Barba, L. “FMM-based vortex method for simulation of isotropic turbulence on GPUs, compared with a spectral method”. In: *Computers & Fluids* 80 (2013), pp. 17–27.
- [300] Yurt, M. K., Abdelmoula, A., John, J., and Yavrucuk, I. “Fluid Structure Interaction Investigation of the Aerodynamic Characteristics of A Dynamic Camber Morphing and Pitching Airfoil”. In: *European Rotorcraft Forum*. Bueckeburg, Germany, 2023.
- [301] Yurt, M. K., Abdelmoula, A., and John Jonas and Yavrucuk, I. “Fluid Structure Interaction Investigation of the Aerodynamic Characteristics of a Dynamic Camber Morphing and Pitching Rotor Airfoil”. In: *49th European Rotocraft Forum*. Bückebug, Germany, Sept. 2023.
- [302] Zhang, J., Smith, E. C., and Wang, K. W. “Active-Passive Hybrid Optimization of Rotor Blades with Trailing Edge Flaps”. In: *Journal of the American Helicopter Society* 49.1 (2004), pp. 54–65.
- [303] Zhao, J. and He, C. “A viscous vortex particle model for rotor wake and interference analysis”. In: *Journal of the American Helicopter Society* 55.1 (2010).
- [304] Zhongqi, J., Lee, S., Sharma, K., Brentner, K. S., et al. “Aeroacoustic Analysis of a Lift-Offset Coaxial Rotor Using High-Fidelity CFD/CSD Loose Coupling Simulation”. In: *Journal of the American Helicopter Society* 65.1 (2020).